Technische Universität München
Lehrstuhl für Technische Chemie II

Nanostructured Sulfur Traps for the protection of high performance NO_x storage/reduction catalysts in low emission engine applications

Hendrik Dathe

Vollständiger Abdruck der von der Fakultät für Chemie der Technischen Universität München zur Erlangung des akademischen Grades eines

Doktors der Naturwissenschaften (Dr.rer.nat.)

genehmigten Dissertation.

Vorsitzender: Univ. Prof. Dr. W. Domcke

Prüfer der Dissertation:

1. Univ. Prof. Dr. J.A. Lercher
2. Univ. Prof. Dr. U. K. Heiz
3. Univ. Prof. Dr. K. Köhler

Die Dissertation wurde am 27.09.2005 bei der Technischen Universität München eingereicht und durch die Fakultät für Chemie am 10.11.2005 angenommen.

"It doesn't matter how beautiful your theory is, it doesn't matter how smart you are.
If it doesn't agree with experiment, it's wrong"

Richard Feynman

Acknowledgements

Finally, the SO_2 is trapped and it's time to thank a lot of people who were part of the successful chase.

First of all, I would like to thank Prof. J. A. Lercher who offered me a PhD position (as the first East German ;)) in combination with a very interesting work. I thank you, Johannes, for the supervision and guidance of this work. I learnt a lot from you especially the way to present data in a special layout. You managed to push me to the limits with great success and my sincere thanks were always at the end. I am grateful for all the experience we shared, not only in the scientific way like in Italy. This period of time has certainly influenced my own life in a significant way.

My further thanks go to Andreas Jentys, who went through countless XAFS nights all over Germany. Thank you for the discussions, corrections and hints on my practical and theoretical problems. I will keep our pragmatic way of working in the last years, not understood from everybody, always in good memory and it improved my quality of work a lot.

All my "group" members the MOF lady Elvira, without you a great part would be missing, smoking Virginia, the coffee and calls in Hamburg always kept me awake and finally "I can calculate this" Peter, I enjoyed all periods of time working with you. You were a great benefit for my personality and for this work. Always remember "There is always a master and an apprentice, and only a master and an apprentice". This brings me to my "be my guide" Chirag introducing me in Indian culture, movies and food with a great profit for my whole live. Furthermore my thanks go to all my students Richard, Philippe, Oliver, Udo, Anastasia Claudia and Olga during this thesis.

I also want to thank all members of TC II supporting me over the whole time. Maria B., Carsten, Toshi (he really works whole nights;)), Hiroaki, Philipp, Iker, Christian S., Christian W., Su, Thomas, Ayumu, Roberta, Benjamin, Wolfgang, Wolfram, Helen, Manuel, Peter S., Andreas, Felix, Lay Hwa, Oriol, Christoph, Ansurang, Chintan, Krishna, Rhino, Olga (Great and fast corrections), Alex, Xuebing, Maria –

Florencia (By the way I guess still tired), Andreas F. thanks for the support, the nice atmosphere and the fellowship at work.

My special thanks go to Stefan (always the first option for a good coffee), Jan-Olaf (still owes me a dinner), Renate (still the IR queen), Josef, Malaika (the second option coffee), all gave me great support in life and work.

For the great technical and practical support through the whole time I want to thank Andreas M., Xaver, Martin, Heidi, the TC 2 technical workshop and Heike (always a cookie somewhere around).

Last but not least I want to thank the partners (Gabriele, Rolf, Robert, Bob, Fred) in my project and the European Union for funding. I appreciated not only our discussions also the social events were great all over Europe.

Beside my work I want to thank all persons in my private life for their great support. First I'm grateful for my whole family which had given me great strength in all times. Katrin I want to thank you in special for the good times we spent and the support in all questions of life and science. Heiko and Claudia I want to thank you especially for the great time in the beginning which still lasts and which had given me an easy start in Bavaria. Your home is always a nice place for Sunday breaks.

Finally my biggest thanks to Elli, thanks a lot for standing my mood even if I refuse to have one ;). For all times in Greece I'm really grateful and I appreciate every Frappe – everywhere -. You were the base for a lot of sunny moments in the last years. ευχαριστήσω παρα πολι μικρόυλι μου.

Table of Content

1 GENERAL INTRODUCTION 9

1.1 INTRODUCTION 10
1.2 COMPOSITION AND INFLUENCE OF POLLUTANTS EMISSION 11
1.3 LIMITATIONS OF EMISSIONS 16
1.4 REDUCTION OF EMISSION 18
1.4.1 Cleaning of exhaust gas streams from Otto engines 18
1.4.2 Removal of pollutants in gas streams with oxygen excess 19
1.5 SULFUR IN FUEL 21
1.6 DEACTIVATION THE NSR THROUGH SO_x 24
1.7 SULFUR MANAGEMENT FOR NSR CATALYSTS 26
1.8 METAL ORGANIC FRAMEWORK MATERIALS 29
1.9 SPECTROSCOPIC METHODS FOR INVESTIGATION OF SO_2 INTERACTION 31
1.9.1 IR spectroscopy 31
1.9.2 X-ray absorption spectroscopy – XAS 33
1.10 SCOPE OF THE THESIS 37
1.11 REFERENCES: 38

2 METAL ORGANIC FRAMEWORKS BASED ON CU^{2+} AND BENZENE-1,3,5-TRICARBOXYLATE AS HOST FOR SO_2 TRAPPING AGENTS 43

2.1 INTRODUCTION 44
2.2 EXPERIMENTAL 46
2.2.1 Synthesis of materials 46
2.2.2 Characterization 47
2.2.3 SO_x uptake 48
2.3 RESULT AND DISCUSSION 50
2.3.1 Composition, morphology and porosity of the materials 50
2.3.2 State of copper cations 54
2.3.3 Storage capacity for SO_2 57
2.4 CONCLUSIONS 59
2.5 ACKNOWLEDGEMENTS 61
2.6 REFERENCES 62

3 SULFATE FORMATION ON SO_X TRAPPING MATERIALS STUDIED BY CU AND S K-EDGE XAFS 64

3.1 INTRODUCTION 65
3.2 EXPERIMENTAL 66
3.2.1 Material 66
3.2.2 Physicochemical characterization 67
3.2.3 Uptake measurements 68

3.3 RESULTS 69
3.3.1 Composition, crystal structure and porosity of the materials 69
3.3.2 SO_x Storage capacity 71
3.3.3 Chemical nature of sulfur in the storage materials 72
3.3.4 Chemical state of copper cations in the storage materials 78
3.4 DISCUSSION 82
3.4.1 Structural aspects of the materials in the presence and absence of SO_x 82
3.4.2 Nature of the sulfates formed 85
3.4.3 Nature of Cu in the BTC materials 86
3.5 CONCLUSIONS 87
3.6 ACKNOWLEDGEMENTS 88
3.7 REFERENCES 90

4 *IN SITU* S K-EDGE X-RAY ABSORPTION SPECTROSCOPY FOR UNDERSTANDING AND DEVELOPING SO_X STORAGE CATALYSTS 92

4.1 INTRODUCTION 93
4.2 EXPERIMENTAL 94
4.3 RESULTS AND DISCUSSIONS 96
4.4 CONCLUSIONS 104
4.5 ACKNOWLEDGMENTS 105
4.6 REFERENCES 106

5 MECHANISTIC STUDIES OF SO_X TRAPPING ON CA-AL BASED HIGH CAPACITY SO_2 SORBENTS 108

5.1 INTRODUCTION 109
5.2 EXPERIMENTAL 112
5.2.1 Materials 112
5.2.2 Physicochemical characterization of fresh materials 112
5.2.3 Temperature programmed reaction 112
5.2.4 Uptake Experiments 113
5.2.5 Infrared Spectroscopy + 2D Correlation Analysis 113
5.2.6 XAFS experiments 113
5.3 RESULTS 114
5.3.1 Physicochemical Characterization of the fresh material 114
5.3.2 CO_2 desorption profiles 116
5.3.3 Total SO_x uptake capacity 117
5.3.4 Temperature programmed reaction 119
5.3.5 Physicochemical Characterization after SO_2 adsorption 120
5.3.6 Infrared spectroscopy 122
5.3.7 In situ Infrared spectroscopy in absence of H_2O 123
5.3.8 In situ IR spectra in presence of H_2O 126
5.3.9 2D Correlation analysis 130

5.3.10 Sulfur K-edge X-ray absorption spectroscopy *133*
5.3.11 In situ S K-edge XANES *134*
5.4 DISCUSSION 137
5.5 CONCLUSIONS 142
5.6 ACKNOWLEDGMENTS 143
5.7 REFERENCES 144

6 IDENTIFICATION OF TRANSIENT SULFUR SPECIES UNDER LEAN-RICH CYCLING CONDITIONS ON POTENTIAL SO_X STORAGE MATERIALS 148

6.1 INTRODUCTION 149
6.2 EXPERIMENTAL 154
6.2.1 Materials *154*
6.2.2 In situ IR experiments *154*
6.2.3 Matlab programs *155*
6.3 RESULTS 155
6.3.1 Properties of the materials *155*
6.3.2 SO_2 uptake experiments *156*
6.3.3 In situ IR experiments *160*
6.4 DISCUSSION 181
6.4.1 Identification of the sulfur species *181*
6.4.2 Influence of Pt on the SO_2 storage process *183*
6.4.3 Influence of water on the SO_x storage *183*
6.4.4 Influence of the time of rich conditions *184*
6.5 CONCLUSIONS 186
6.6 ACKNOWLEDGMENTS 186
6.7 REFERENCES 187

7 SUMMARY 190

7.1 SUMMARY 191
7.2 ZUSAMMENFASSUNG 196

8 CURRICULUM VITAE 202

9 WISSENSCHAFTLICHE PRÄSENTATIONEN 203

10 WISSENSCHAFTLICHE PUBLIKATIONEN 204

Chapter 1

General Introduction

Abstract:

This chapter describes the current state of vehicle emissions and outlines future trends in regulation. Concepts for NO_x removal are discussed with special emphasis on the potential deactivation of the catalytic systems in presence of sulfur. Solutions for advanced NO_x reduction systems that are applicable under these conditions are pointed out and concept of sulfur storage traps is described in detail. Potential materials for SO_x trapping are introduced as well as spectroscopic methods to investigate the storage process are discussed.

1.1 Introduction

Mobility (Lat. capable of being moved) - the ability and willingness to move or change is a major driving force in human history. The invention of the combustion engines by the German engineers Nikolaus Otto and Rudolf Diesel in the 19th century provided human mankind a degree of mobility never known before and gave an important contribution to the development of our modern society.

The main difference between the engine concepts of Otto and Diesel is the ratio of air to fuel under operating conditions expressed by the value λ [1]. If λ is below 1 the fuel mixture is called fuel rich, due to excess of fuel compared to oxygen, whereas above 1 the mixture is called lean, due to an excess of oxygen with respect to the fuel. At $\lambda = 1$ the air/fuel ratio is stoichiometric. Otto engines operate in a range of λ values between 0.98 – 1.02, while diesel engines typically operate above 1.02. The advantage for customers of the diesel engines compared to the petrol operating engines is the higher fuel efficiency. This originates from the direct injection of air (oxygen excess) to the fuel in the combustion chamber, where in comparison to the petrol engines a air/fuel mixture is introduced. Furthermore the higher compression ratio of the air in the diesel engine contributes to a higher efficiency consequently leading to approx. 35% less CO_2 emitted compared to the Otto engines. As it is well known that carbon dioxide is the main contributor to global warming (greenhouse effect) the reduction of CO_2 contributed by the transportation is an important step to reach the requirements for the Kyoto protocol [2, 3].

However, the burning of fossil fuels in combustion engines always leads to the formation of pollutants (NO_x, SO_x, CO, HC and PM). They are mainly result from the incomplete combustion, the high pressure in the engines and the additional reaction of Nitrogen/Sulfur components in the fuel at this high temperature. The pollutants influence the environmental conditions along with human health especially in congested areas. A general scheme of emission sources, their transport in the atmosphere, the natural removal options as well as the areas which are mainly affected by them is shown in Fig. 1.1.

Exhaust gas streams are complex mixtures containing various amounts of a wide range of organic and inorganic materials, in gaseous and particulate forms, from the engine combustion processes.

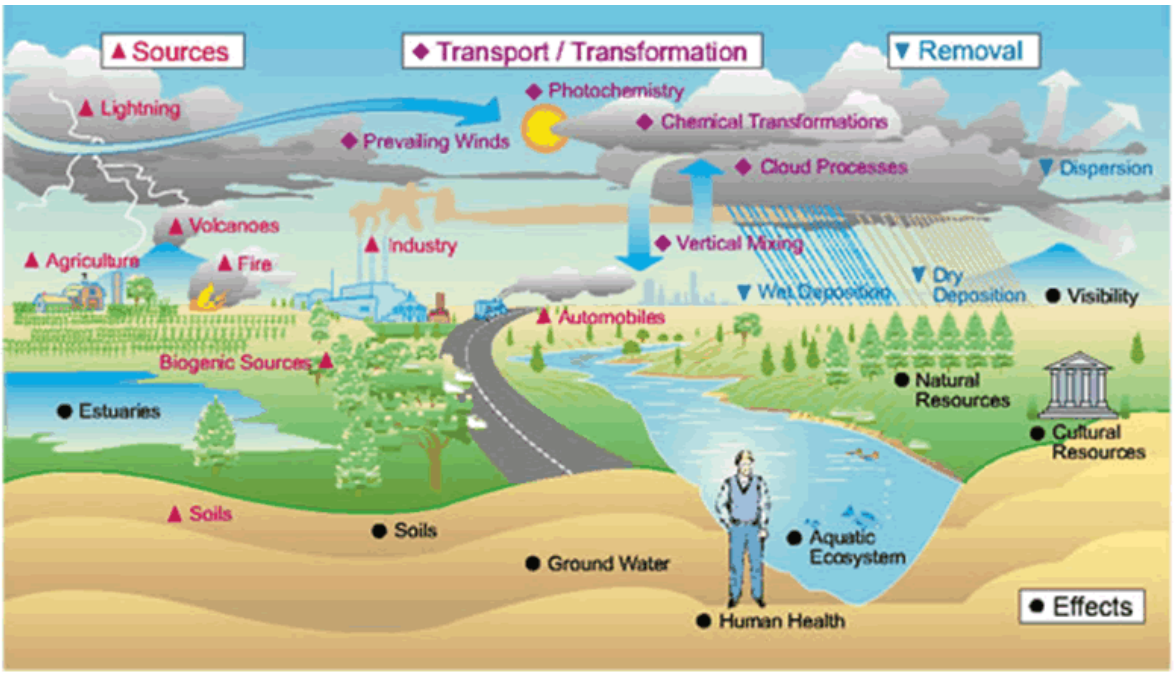

Fig. 1.1 : Sources, transport and effects of emissions.

1.2 Composition and influence of pollutants emission

The typical emissions released by diesel engines are shown in Fig. 1.2 as well as the several impacts on the global and local environment is summarized in Tab. 1.1 and discussed in detail below.

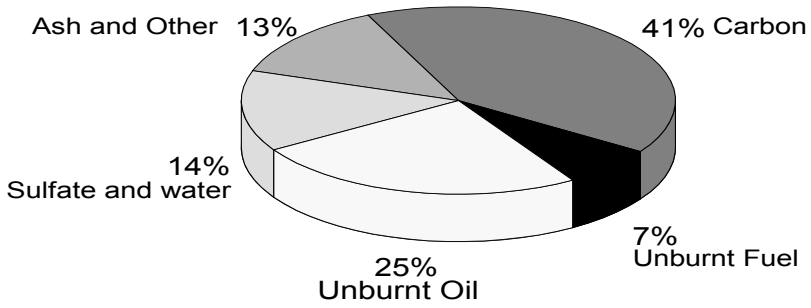

Fig. 1.2 Typical particle composition for a heavy-duty diesel engine tested in a heavy-duty transient cycle [4].

Tab. 1.1 Summary of major pollutants from transportation sources [5].

Pollutants	Local Impacts	Global Impacts	Comments
CO	• Aggravates existing cardiovascular diseases, impairs visual perception and dexterity	• Indirect influence on warming through competition with methane for oxidation	• Transportation can be responsible for up to 95% of CO emissions in urban areas. • Globally distributed gas
HC	• Range of health impacts including respiratory, neurological & carcinogenic • Photochemical smog precursor	• Class of compounds includes methane, a potent greenhouse gas • Indirect warming influence through ozone formation	• A range of natural and anthropogenic sources ensures that HC species are generally available as ozone precursors
NO_x	• Respiratory irritant • Visibility impairment • Acid precursor • Photochemical smog precursor	• Indirect warming influence through ozone formation	• Acid and ozone production impacts of NO_x can be widely distributed through long-range transport of reservoir species
O_3	• Primary constituent of photochemical smog • Severe respiratory impacts • Material & crop damage	• Global warming impacts due to increasing background concentrations • Strong oxidation agent	• O_3 has no direct emissions sources—NO_x, HC, and sunlight are required for production
SO_x	• Respiratory irritant • Visibility impairment • Acid precursor	• Sulfate has some cooling impact due to light scattering	• SO_2 has a relatively long atmospheric lifetime leading to widespread acid impacts
PM (Particular Matter)	• Cardiovascular & respiratory impacts • Visibility impairment • Includes acid species	• Particles can influence warming or cooling, depending on carbon content & scattering abilities	• Atmospheric lifetime varies with particle size
GHG (Green house Gases)		• Leading to global warming through long-term atmospheric accumulation	• Transportation is a major source of CO_2 but less important for methane & N_2O

The solid parts (particles) of the emissions are typically described as diesel particulate matter (DPM). They consist of an elemental carbon core with organic compounds, sulfates, heavy metals, trace elements and irritants (such as acrolein, ammonia and acids) adsorbed on the surface. 90% of the diesel particles have a diameter of less then 1μm and at least 94% are less than 2.5μm as approximated by the U.S. Environmental protection agency (EPA).

The gaseous fraction contains mainly nitrogen, oxygen, carbon dioxide and water vapor. However, many toxic substances such as CO, unburned HC and SO_2 are present as summarized in Tab. 1.2. The complex reactions of these pollutants in our environment are depicted in Fig. 1.3. It illustrates the reactions between the various primary emissions (e.g. from exhaust gases), the environment resulting in secondary pollutants (H_2SO_4, HNO_3).

Tab. 1.2 : Typical composition of diesel emissions.

CO [vppm]	HC [vppm]	DPM [g/m^3]	NO_x [vppm]	SO_2 [vppm]
5-1,500	20-400	0.1-0.25	50-2,500	10-150

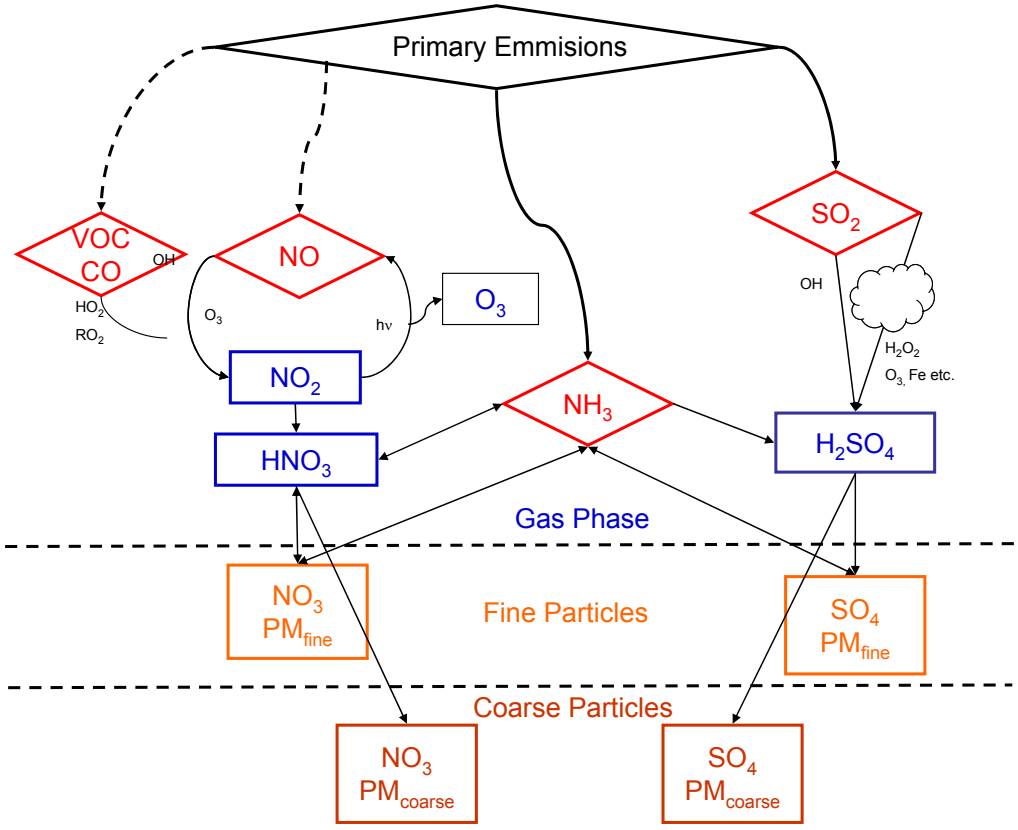

Fig. 1.3 : Cross- Effects of primary emissions with pollutants present in the environment [6].

The unburned HC in the exhaust gas stream lead to the formation of smog as shown in the early 1950s by Haagensmit *et al.* in California [7, 8].
Carbon monoxide is a very toxic gas, which preferentially binds to hemoglobin in place of oxygen and leads to a permanent damage of human health and finally to death.

NO and NO_2 contribute to ground-level ozone formation, nutrient pollution of waterways, secondary (i.e., atmospheric) formation of particulate matter and to the formation of acid rain. The complex cycle of NO on the environment is shown in Fig. 1.4 [9, 10].

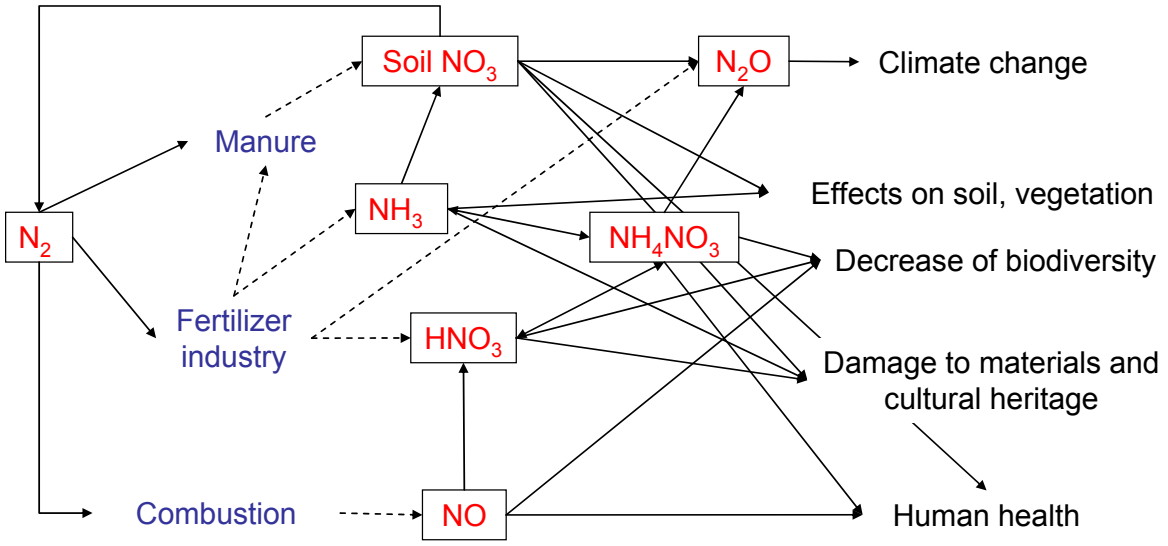

Fig. 1.4 : Different sources and effects of nitrogen in the environment and their relation [9].

Sulfur dioxide (MAK 5 mg/m^3) a colorless gas with a sharp irritating odor and Air/SO_2 mixtures with a content of 0.03% SO_2 cause poisoning symptoms, such as labored breathing, opacifying of the cornea and inflammation of respiratory organs. Higher concentrations can even lead to death.
Thermodynamically the formation of SO_3 from SO_2 and O_2 is favored at low temperatures. However, significant rates for the oxidation of SO_2 to SO_3 can only be achieved at temperatures above 950K.

SO_3 forms in contact with water sulfuric acid, which mainly contributes to the formation of acid rain. This is mainly responsible for damaging buildings, as well as the strong influence on wood leading to the deforestation [11]. The acid rain was first noted by R. A. Smith in his book “Air and rain: the beginning of a chemical climatology“ in 1872, where he already observed that the concentrations

of sulfate (SO_4^{2-}) were greater in rain collected near cities and particularly coal-burning facilities [12].

The wet and dry deposition from acidic pollutants is generally described as acid deposition. Sulfur dioxide contributes up to 60 –70% to the global acid deposition, with more than 90% of atmospheric SO_2 is of human origin. The main sources are coal and oil burning, smelting of metal sulfide ores to obtain the pure metals, volcanic eruptions and organic decay. The highest monitored concentrations of SO_2 have been recorded in the vicinity of large industrial facilities. Recent observations indicate that the reduction of SO_2 is not accompanied by an equivalent decline of acidic precipitation. Wet deposition ions have a different specific effect on vegetation soils and surface water reservoirs. Thus, the evaluation of wet deposition solely by hydrogen concentrations is inappropriate [13]. Brydges and Summer defined a concept of “acidifying potential” (AP) of wet deposition as the effective amount of acid delivered to a terrestrial or aquatic system as shown in Equation 1.1 [14]:

$$AP = [SO_4^{2-}] - ([Ca^{2+}] + [Mg^{2+}])$$

Equation 1.1 : Calculation of the acidifying Potential.

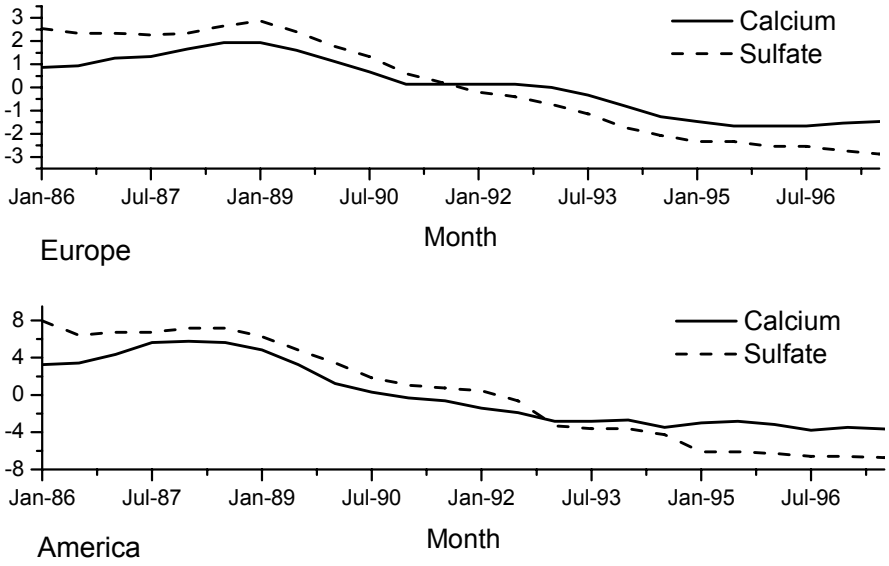

Fig. 1.5 : Reduction of sulfate and calcium (a) for Europe, and (b) for eastern USA since 1986 [13].

Fig. 1.5 shows a similar behavior for both sulfate and calcium ions, as they decrease simultaneously and independently of the region.This is due to the fact that calcium is the main counter ion associated to sulfate in rain water [15]. Conclusively, the reduction of SO_2 emissions leads to a decrease of sulfates in rain water, but simultaneously also of calcium, so that the effect on AP is negligible.

1.3 Limitations of Emissions

The contribution of the various sources to the total NO and SO_2 emissions in 2002 are compared in Fig. 1.6. The high contribution of transportation to the total NO_x and SO_x emissions shows the importance of emission reduction in this sector. With increasing amount of cars (in 2000 500 million passenger cars were present [16]), the pollutants emitted will also be increasing tremendously over the next century.

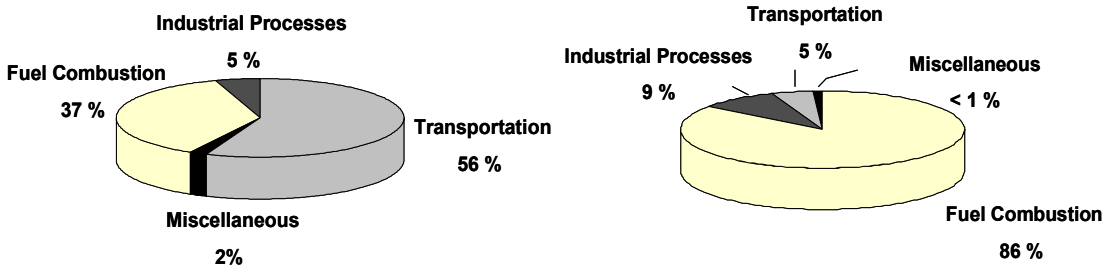

Fig. 1.6 : Contribution of NO and SO_2 to the environment [11].

The resulting legislative pressure to prevent the harmful impact of the passenger car sector on human health started in the USA (1966) where the Tier 1 regulations were finally was established at 1997 for all new light duty vehicles, such as passenger cars, light duty trucks, minivans and pick-up trucks. However, the NO_x limits for diesel cars were more relaxed compared to petrol cars. The stricter Tier 2 tailpipe standards will be phased-in between 2004 and 2009 and will lead to a significant reduction of all emissions relative to the Tier 1 regulation. In addition, the same emission standards will be applied to all vehicles. Beside the Tier regulations even stricter emission regulations (LEV) were established in California.

In the European Community, the first law defining limit values for the emissions from motor vehicles was the Directive 70/220/EEC, approved by the Council in 1970. In December 1998 the Directive 98/69/EC was published, which

limits the emissions for passenger cars and light commercial vehicles from January 2000 (Euro III stage) and from January 2005 (Euro IV stage). The even stricter Euro V norm is still under discussion.

Fig. 1.7 summarizes the actual and planned emission limits in the USA, Japan and Europe. The significantly stronger reduction in every new legislation step will finally lead 2010 to approx. 10% of the emissions from 2000/2001 which is an important step forward for cleaner environment. Fig. 1.8 depicts the actual distribution of the various restrictions in the world. As an increase in the efficiency of fuel utilization is inevitable (e.g. lean burn engines), but often leads to an increase in the emission of NO_x species. This problem has to be addressed due to environmental and legislative reasons.

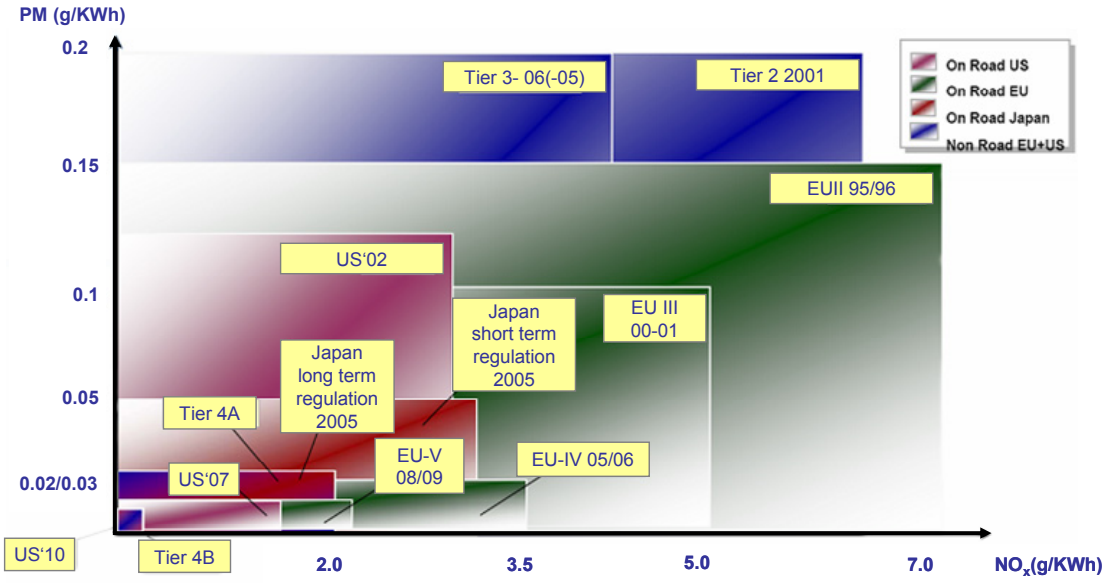

Fig. 1.7 : Legislation of emissions in the world present – future [17].

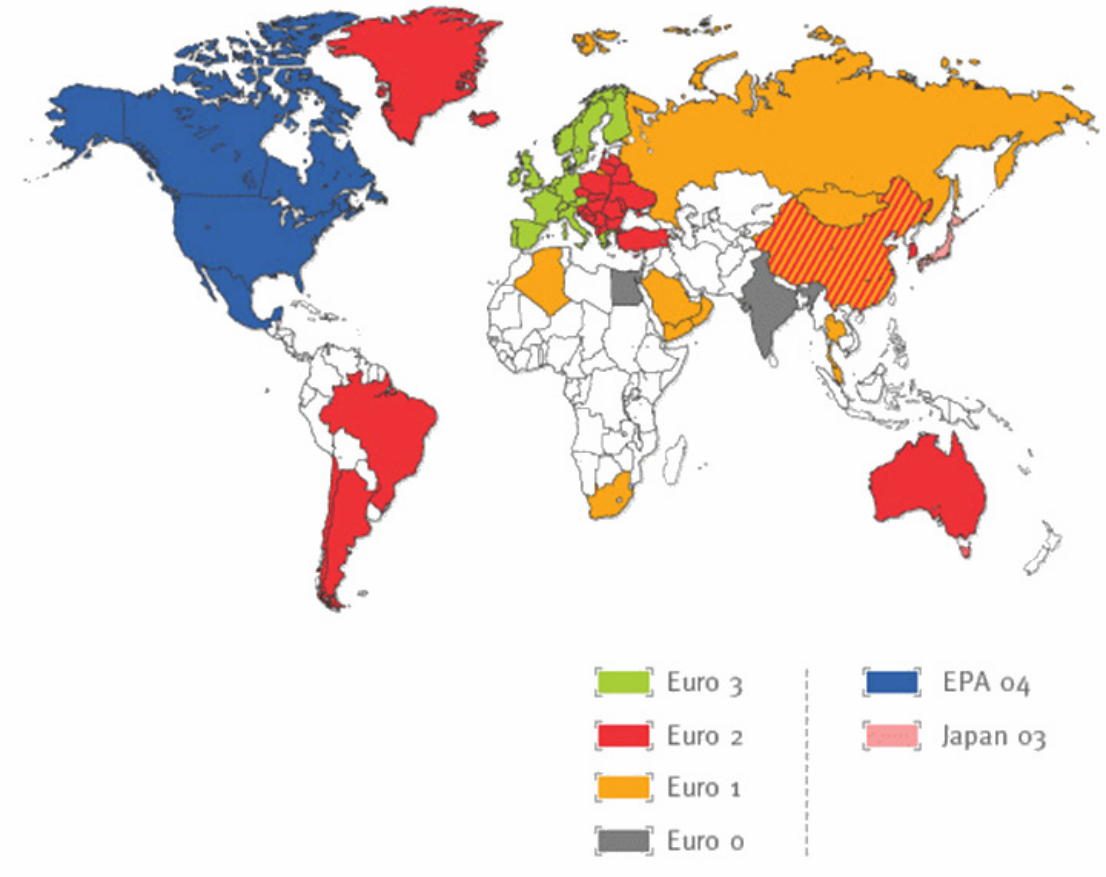

Fig. 1.8 : Actual emission restrictions in the world [18].

1.4 Reduction of Emission

1.4.1 Cleaning of exhaust gas streams from Otto engines

The increasing necessity for strong reduction of the NO_x and CO emissions led to the development and introduction of an additional exhaust gas treatment. The different operation conditions (see above lambda value) for Otto and Diesel engines requires also the presence of different cleaning applications for exhaust gas streams. On petrol burning engines, due to the stoichiometric air:fuel ratio, it is possible to clean the exhaust gas stream by a Three way catalyst (TWC). Fig. 1.9 represents the TWC removal efficiency with respect to the operating λ value. The TWC is a noble metal coated monolith removing CO, NO and HC from the exhaust gas stream [20, 21]. Nowadays also more and more metal structures are used as support for the active phases. The sufficient concentration of reducing agents (HC) and oxidation agents in the petrol engines exhaust gas stream allows a the reduction of the pollutants as shown in Equation 1.2.

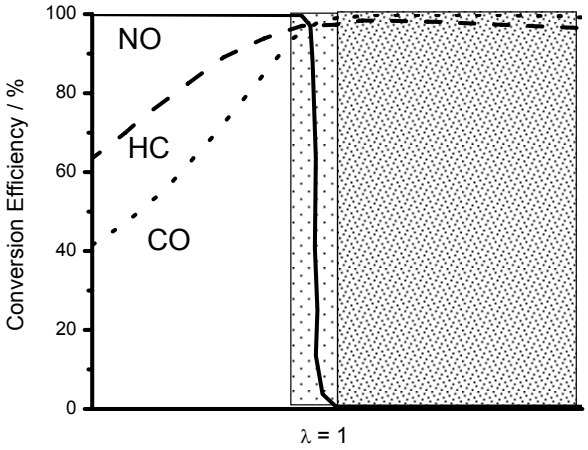

Fig. 1.9 : Three way catalyst performance determined by lambda range (Otto engine = less dotted area, diesel engine = full dotted area) [19].

$$2\ CO + O_2 \longrightarrow 2\ CO_2$$
$$(HC) + O_2 \longrightarrow CO_2 + H_2O$$
$$NO_x + CO \longrightarrow N_2 + CO_2$$

Equation 1.2 : Reaction sequences on the TWC to remove the pollutants.

On the more fuel efficient diesel engines (Fig. 1.9 full dotted area), due to the oxygen excess during combustion, the reducing agent (HC) is not present anymore in the exhaust gas. Consequently, new approaches are necessary for the removal of the emitted pollutants (NO_x and Carbon particles).

1.4.2 Removal of pollutants in gas streams with oxygen excess

The removal of the particulate matter, which could cause cancer, is nowadays realized by particle filter systems, as described by various authors [22-25].
Common to all systems for the NO_x removal developed for the automotive sector is the necessity of adding a reducing agent. At present hydrocarbons "**Hydrocarbon - Selective Catalytic Reduction (HC-SCR)"** or ammonia (Urea-SCR, **Ammonia - SCR**) are tested as potential reducing agents. Typically Ammonia - SCR utilizes urea as a NH_3 source which is transformed in an on-board unit to NH_3. The urea solution can be refilled during the normal maintenance rate [26-28].

Another promising approach is the **NO_x storage and reduction catalyst (NSR)** introduced by Toyota and widely investigated and tested in automobile

industry [29-32]. Fig. 1.10 illustrates the trapping and release of NO_x by a NSR catalyst. During lean operation, the nitrogen oxides in the exhaust are stored on the catalyst, and during rich or stoichiometric operation, the stored NO_x are reduced to nitrogen. This concept utilizes a catalyst with dual functionality: a NO_x storage function, typically on Ba-oxides and a reduction/oxidation component, typically Pt [33-35]. Barium oxide is often added to alumina supported catalysts to improve the catalysts performance under severe hydrothermal conditions [36, 37]. The promotional effect of barium lies in its capacity to retain large surface areas of alumina effectively, because the cations occupy the surface sites or bulk sites thus preventing atomic diffusion, which brings about the α-phase transformation [37, 38]. The NO_x species are stored as nitrates on e.g. Barium oxide according to Equation 1.3

$$2\ NO_2 + O + BaO \rightarrow Ba(NO_3)_2$$

Equation 1.3 : Formation of $Ba(NO_3)_2$ while the NO_x storage process on a typical NSR storage material.

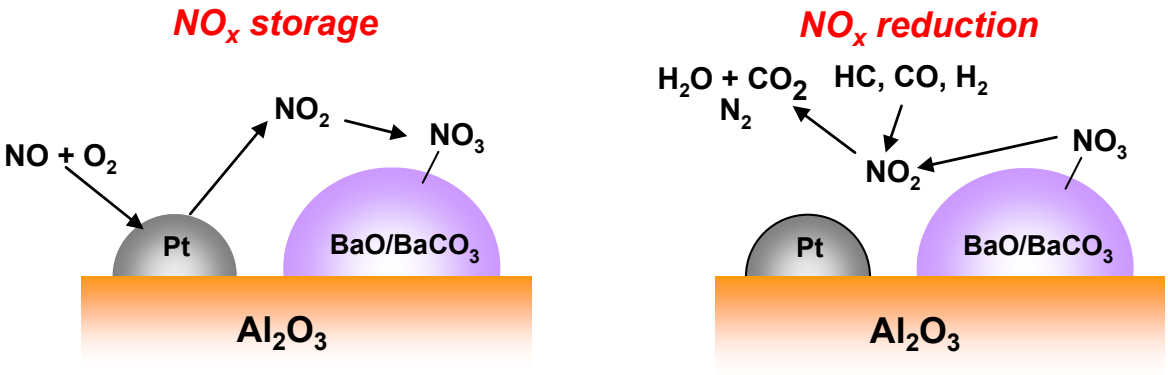

Fig. 1.10 : NO_x storage and reduction mechanism on the NSR catalysts

However, it is proposed that Equation 1.3 is the sum of several elementary steps [39]. The elementary oxygen on the left side of Equation 1.3 has to be provided on the surface of the material, either from a metal oxide or from the oxygen / reduction component (Pt) in the system as shown by Fridell *et al.* [35]. Another mechanism involving the NO adsorption on the storage material has also been proposed by Sedlmair *et al.* [33]. It was shown that the adsorption of NO and NO_2 and the formation of different NO_x species occurs not only on the surface of the oxidation component, but also on the alkali metal oxide [33]. NO can be adsorbed on the surface by :

- Molecular adsorption of NO by formation of nitrites on BaO sites
- (Partial) replacement of Ba carbonates by NO, resulting in the formation of Ba nitrites
- Formation of hyponitrites on BaO sites
- Formation of bridging and chelating bidentate nitrates on Al oxide via the formation of cation vacancy sites on the Al oxide surface.

The adsorption of NO_2 can also occur via different pathways leading to different NO_x species [33]:

- Bridged nitrites form via adsorption of NO_2 on two adjacent metal sites
- Linear nitrites form via a dissociative adsorption of NO_2
- Nitrites are oxidized by gas phase NO_2 or directly replaced by nitrates after extended exposure

However, the experimental evidences show clearly that nitrates are the main species present on the surface [33]. The burst of NO_x at the beginning of each rich regeneration cycle suggests that the decomposition of metal nitrates is probably the first step in the reduction mechanism. Upon reacting with hydrocarbons or other appropriate reductants during the regeneration, $Ba(NO_3)_2$ appears to first decompose to release NO_x which is then reduced to N_2 (see Fig. 1.10).

Many experimental studies on the NSR catalyst have been carried out and some theoretical models for this reaction have been developed, however the main problem that still remains, is the deactivation of the catalysts [40, 41]. The thermal deterioration is due to reaction of the NO_x storage material with compounds within the wash-coat and particle growth of both the precious metals and the NO_x storage material [42]. The presence of sulfur in the fuel leading to a permanent deactivation is the most difficult problem to be solved for the NSR catalysts [10, 32, 43-53].

1.5 Sulfur in fuel

Lower sulfur-content in petrol and diesel fuels directly leads to lower sulfur content in the exhaust gases. Therefore, the sulfur content is also limited by the legislation of the European Community. Tab. 1.3 shows the content of the sulfur present in the fuel as well as the further reduction planned in the future in the European Union. In Germany already now 10ppm sulfur are present in the fuel. The

distribution of the fuel with respect to the sulfur content over the world is depicted in Fig. 1.11.

Tab. 1.3 : Petrol and diesel fuel sulfur contain in European Community (mg/kg) [54].

	1996(EURO II)	2000(EURO III)	2005(EURO IV)	2009(EURO V)
Petrol	500	150	50	10
Diesel	500	350	50	10

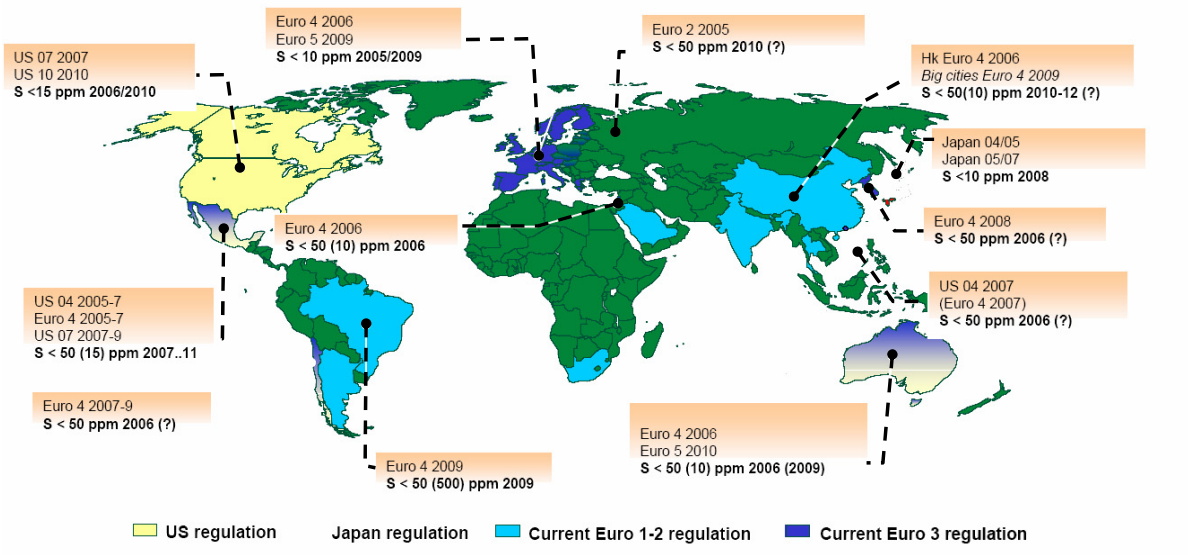

Fig. 1.11 : Distribution of the fuel with respect to the sulfur content planned for the next period of time.

However, the costs for the reduction of sulfur concentration if fuel are quite substantial and include the expense of upgrading and modernizing refineries, modifying petroleum distribution systems and installing and maintaining emission control systems. Refinery costs will vary due to differing refining and processing technologies, differences among the types of crude oil used, labor costs and other local factors. It is logical to assume that oil companies and others in the fuel supply chain will pass the cost of the transition to low-sulfur diesel fuel to their consumers. However, according to the U.S. EPA, the average consumer cost of reducing sulfur levels to 15ppm in the United States will be no more than five cents ($0.05) per gallon [55]. Indeed, shortly after the U.S. EPA report was released, British Petrol announced that it would begin selling low-sulfur diesel fuel in the western U.S. at a comparable incremental cost [56]. Since the beginning of 2005, the sulfur

content of both petrol and diesel fuels has been reduced (see Tab. 1.3) leading to ultra low sulfur diesel e.g. by implementing new dehydrodesulfurization techniques in the refineries [57].

Although a further reduction of the sulfur content in the fuel is desirable. Moreover, due to the 'sulfur contaminated' production sites, a sulfur free fuel achieved by *ultra deep* HDS would be re-contaminated on the way through the production site and/or transportation vessels. However, an effective sulfur management before the NSR catalysts would still be necessary because even with the availability of 15ppm sulfur diesel fuel deactivation does take place. Additionally to fuel sulfur, lube sulfur must also be regarded in sulfur loading and degeneration of the catalyst. These include sulfurs derived from the sulfurized detergents and sulfur containing antioxidants [58]. Tab. 1.3 provides a summary of available diesel and petrol emissions control technologies that are impacted by fuel sulfur [5].

Tab. 1.4 : Sulfur Impacts on emissions control technologies [5].

Technology	Pollutants	Sulfur Levels	Benefits	Applications
Petrol Vehicle Technologies				
TWC	NO_x, HC, CO	< 50ppm recommended	• Reductions from 18% for HC & CO and 9% NO_x with 50ppm. • Up to 55% for HC & CO and 77% for NO_x with 15 pm.	Existing vehicles.
Advanced TWC	NO_x, HC, CO	< 30ppm recommended	• Increasing emissions benefits, durability and fuel economy.	New and upcoming vehicles.
NO_x Trap	NO_x	< 15ppm required	• 90-95% reduction in NO_x from uncontrolled emissions. • Allows for significant increases in fuel economy.	Future vehicles, required to meet GHG reduction targets.
Diesel Vehicle Technologies				
No Controls	PM	< 50ppm recommended	• PM reduction of 14% for 50 ppm and 50% for 15ppm.	Existing vehicles.
DOC	PM, HC, CO	At least below 150ppm. < 50ppm, recommended.	• Reductions of 90-100% for HC and 88-99% for CO. • Reductions of 15-31% for PM with use of less than 50ppm.	Useful as a low-cost retrofit and in integrated control systems in new vehicles.

DPF	PM, HC, CO	< 50ppm required. < 15ppm highly recommended.	• Reductions of 90-99% for PM with use of less than 15ppm. • Efficiency drops to ~50% with 50ppm. • Reductions of 58-82% for HC and 90-99% for CO.	Critical retrofit and new vehicle technology.
SCR	NO_x	< 50ppm required.	• Reductions of 80-90% for NO_x	Likely for heavy-duty but passenger vehicle use also being explored.

1.6 Deactivation the NSR through SO_x

Alkaline and alkaline earth oxides, often used as storage components in NSR catalysts, do not only possess high capability of storing NO_x as nitrates but unfortunately also have a high affinity towards sulfation [59, 60]. Obviously, when sulfur containing fuel is used, this will lead to suppression of NO_x storage. Engström *et al.* studied the effect of SO_2 on the NO_x storage capacity and oxidation/reduction activities of a model $Pt/Rh/BaO/Al_2O_3$, NSR catalyst [54]. They found that the degree of deactivation of the NO_x storage capacity was proportional to the total SO_2 concentration that the catalyst had been exposed to. XPS investigations showed that sulfur accumulates in the catalyst as sulfate. On the basis of thermogravimetric and FT-IR investigations of aged catalysts, Matsumoto *et al.* assumed sulfur poisoning of NSR catalysts to be due to two main factors [61]. First, sulfur dioxide in the exhaust gas is oxidized on precious metals and reacts with the support forming aluminum sulfate. Second, SO_x reacts with the NO_x storage components such as barium to form barium sulfate.

Investigating the effect of SO_2 on a commercial NSR catalyst containing $Pt/Ba/Al_2O_3$ under lean and rich reaction conditions, Sedlmair clearly showed that deactivation during the lean cycle was not only a result of bulk sulfate formation on the storage material but also a result of decreasing oxidation function of the noble metal [62]. Yet, in contrast to the storage capacity the oxidation function could be recovered by exposure to propene at 873K. Under rich reaction conditions an initial formation of SO_x species on the storage component as well as SO_2 adsorption on the noble metal was observed. The latter reacted with propene to sulfur species on the noble metal. These are oxidized during the rich cycle and migrate to the storage component, accelerating the deactivation [62].

In conclusion, both lean and rich reaction conditions lead to a deactivation of the storage component by adsorbing irreversibly sulfur species on the catalyst surface as well as the oxidation/reduction function [21, 32-34, 39, 63]. The general deactivation concept is shown in Fig. 1.12.

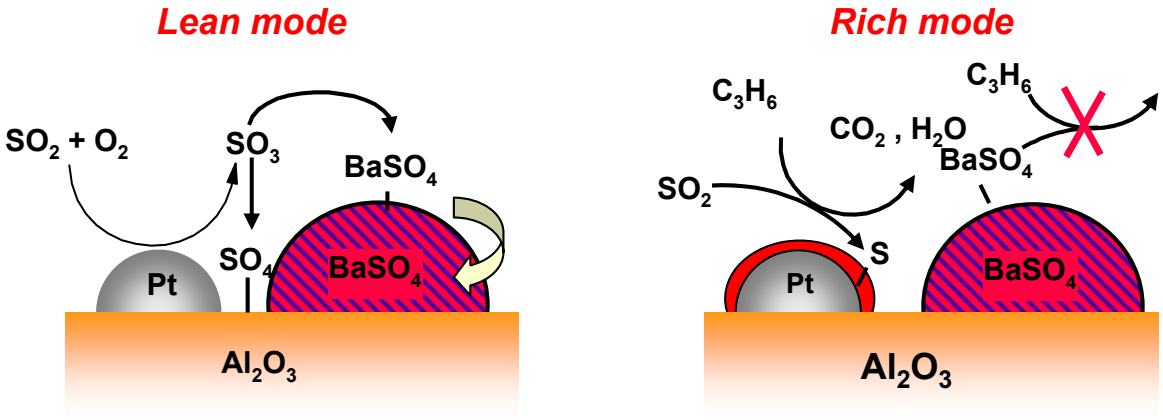

Fig. 1.12 : Deactivation mechanism of a NSR catalyst by formation of $BaSO_4$ and PtS [62].

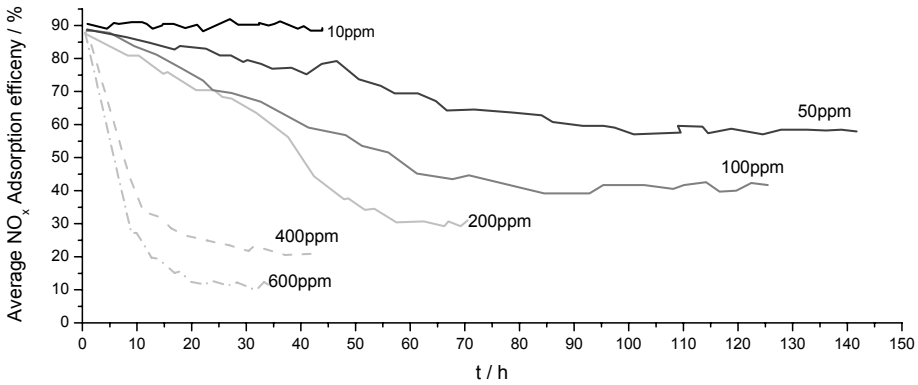

Fig. 1.13 : NO_x storage catalyst conversion efficiency as a function of sulfur content of fuel – Ford [64].

An integrated approach with a combination of a sulfur removal concept upstream with respect to the NSR catalyst leading to low and stable emission values has been proposed by numerous authors [30, 44, 45, 65-67]. To assist the NSR catalysts with respect to the influence of sulfur content, regulations are being proposed to reduce the amount of allowable sulfur in diesel fuel. Although 30ppm was initially suggested, current data (see Fig. 1.13) indicate that some catalysts have almost zero tolerance for sulfur, so zero sulfur diesel fuel is being considered.

However, while the deactivation of the storage component is mainly irreversible, the oxidation function can be partially regenerated. Fig. 1.14 shows the distance of desulfurization of the NO_x storage catalyst compared to the sulfur content in the fuel obtained by BMW indicating that only below 10ppm a secure operation of the catalyst is guaranteed.

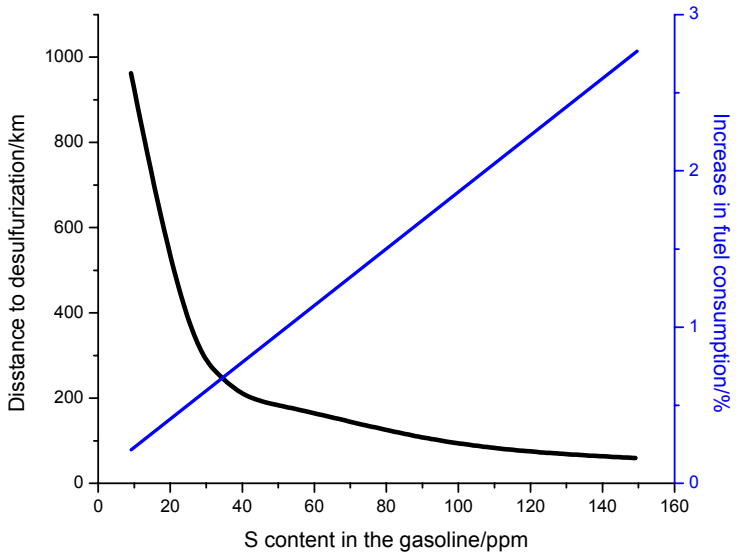

Fig. 1.14 : The effect of fuel sulfur on distance between desulfurisations and hence the effect on fuel consumption – BMW [64].

1.7 Sulfur Management for NSR catalysts

There are two general approaches to sulfur management with respect to the NO_x storage and reduction catalyst. The first is the use of diesel fuel injection in the exhaust and high temperature desulfation strategy to remove the sulfates from the NO_x trapping device and consequently recover the NO_x trapping efficiency [48, 68-70]. However, several arguments have been formulated against this technique. First, the necessity of designing a system in which in addition to the lean-rich cycles temperature cycles need to be engineered is a complicated matter. Second, for the complete removal of sulfates the rich cycle has to run for several minutes, increasing the total fuel consumption. Third, high concentrations of SO_2 and H_2S are emitted in a short space of time during regeneration, requiring further after-treatment. Finally, the thermal aging can have significant effects on the NO_x trapping system [71, 72].

A much more promising approach is the use of a disposable sulfur trap that adsorbs SO_x upstream of the NSR catalyst from the raw exhaust gas of the engine, and that can be replaced or restored offline periodically [30, 44, 47, 58, 73]. The optimal sulfur trap would adsorb all engine-out SO_x for the entire lifetime of the exhaust after-treatment device and thus avoid recovering it from sulfur deactivation through a difficult deSO_x process. However, a sulfur trap designed to last the entire lifetime of the NSR catalyst would require a very large volume and make the device impractical. A realistic SO_x trap will have a fixed volume with a limited uptake capacity and will have to be replaced when saturated. Requirements for an effective disposable sulfur trap are the removal of at least 90% SO_x from the raw exhaust gases of a lean burn engine for over 20,000km vehicle operation using fuels having 10ppm or lower sulfur content (Fig. 1.15). Furthermore the sulfur trap must be able to operate in a wide temperature range (473 - 873K). Fig. 1.15 depicts a comparison between the durability of sulfur storage a monolith with a standard volume of 2l and a 3% wash coat of active material with the sulfur content in the fuel. It shows that for 30ppm sulfur in the fuel, the maximum use of a state-of-the-art sulfur trap monolith is around 4,000km, a value too low for possible commercialization.

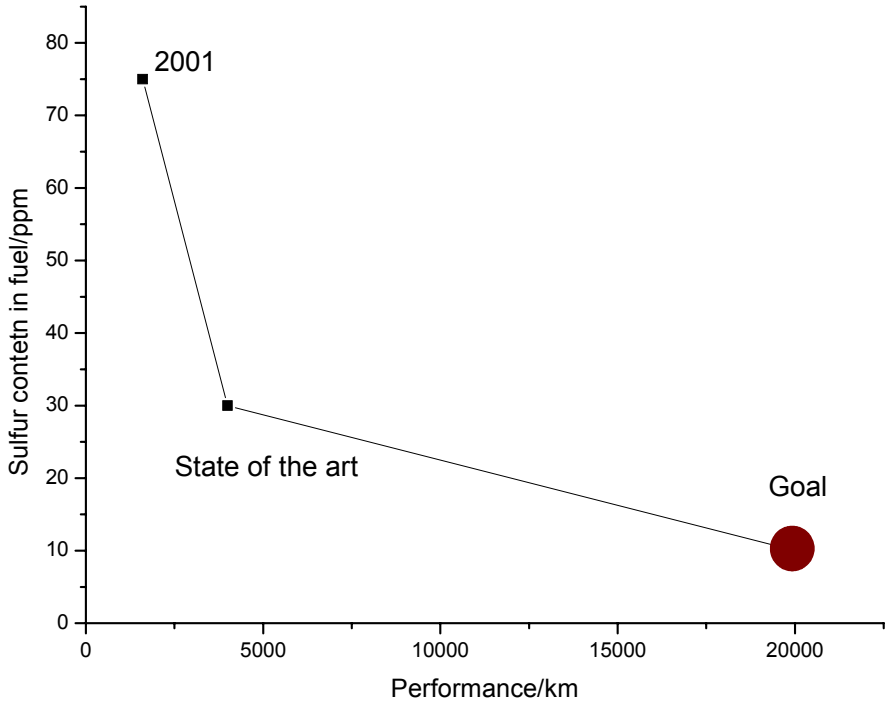

Fig. 1.15 : Sulfur trap performance in km according to the fuel sulfur content.

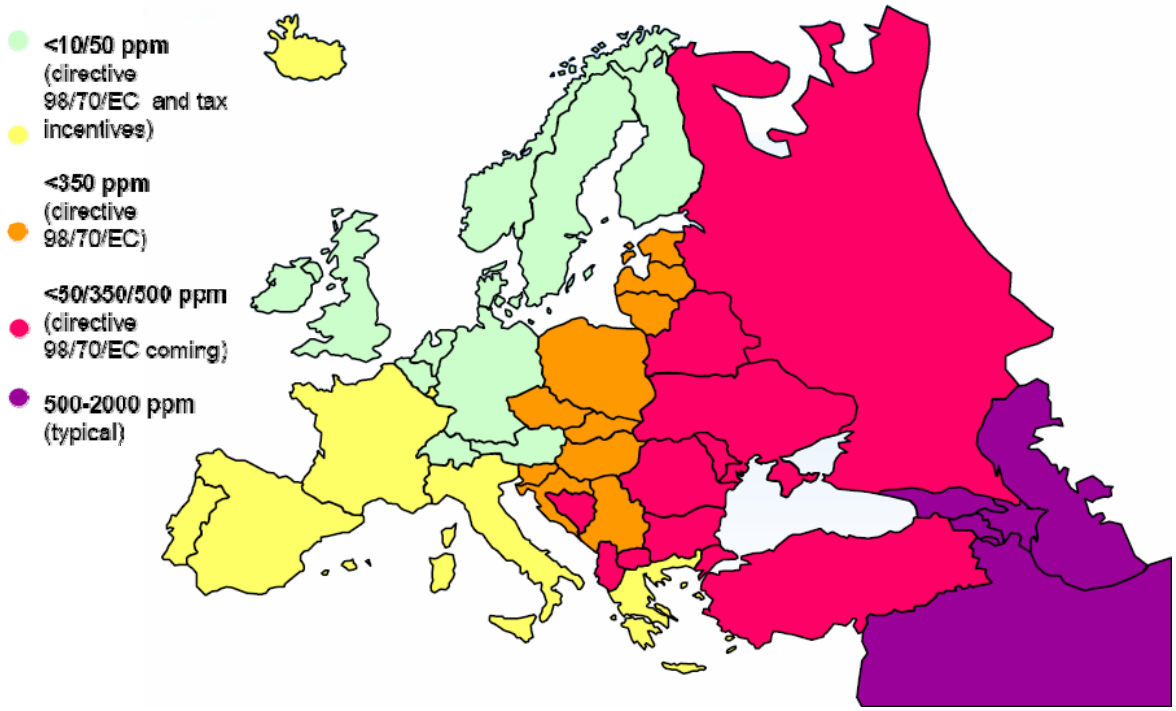

Fig. 1.16 : Distribution of the fuel with respect to the sulfur content in Europe.

Fig. 1.16 shows the actual distribution of petrol with respect to the sulfur content in Europe, indicating the potential of sulfur traps application in the whole of Europe.The industry offers different types of SO_x trap materials [74-79]. The typical composition of a sulfur trap contains an oxidation component to convert all sulfur dioxide to sulfur trioxide. In most cases this is achieved by precious metals, typically Pt. Furthermore, sulfur traps must contain a storage element, for instance barium, to immediately trap the sulfur trioxide in the form of a sulfate. A second storage component increases the capacity of sulfate storage, as the sulfate can migrate from the first to the second component. Finally, a structural element, for example α-Al_2O_3, Ce_2O_3 and ZrO_2, is necessary to act as a support and preserve the pore structure during the sulfation process. The operating method with respect to the various conditions of a sulfur trap is illustrated in Fig. 1.17.

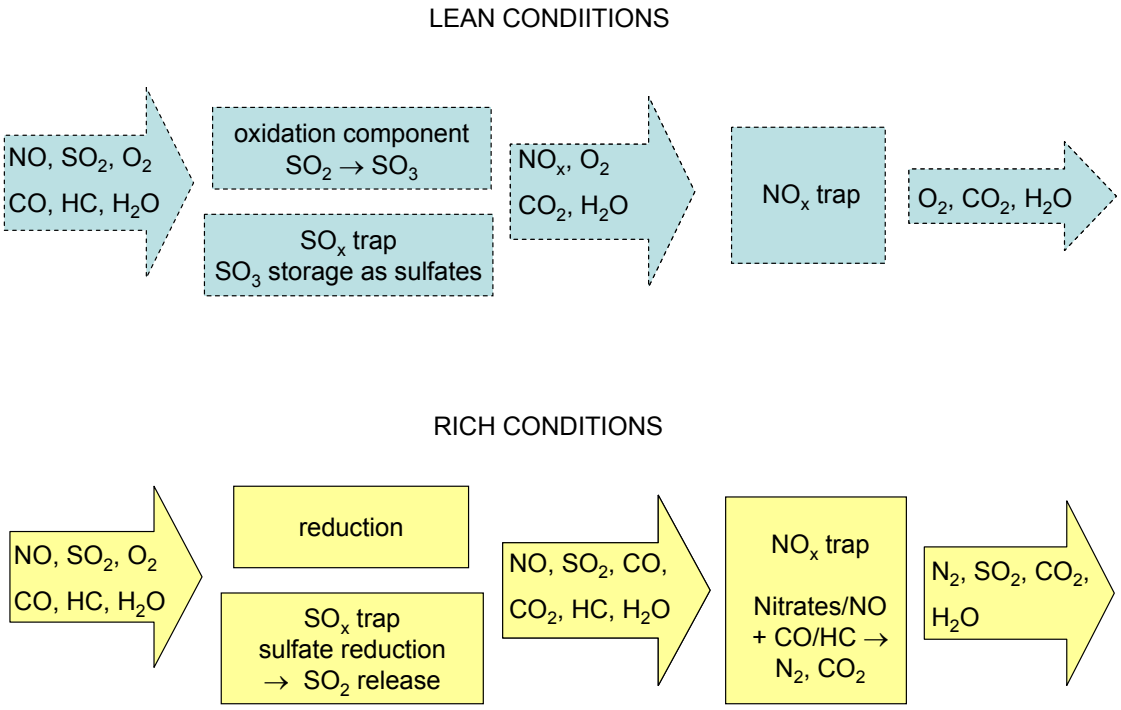

Fig. 1.17 : Operating mechanism of a sulfur trap placed upstream of a NO_x-SR catalyst.

Important properties of successful sulfur traps are a high specific surface area, thermal stability, high dispersion of the oxidation and storage component with a strong basicity of the latter [65]. To achieve these properties different types of materials can be applied.

Beside high surface area mixed metal oxides prepared with various methods (sol-gel etc.) as shown by Lin *et al.* also zeolites are useful [80, 81]. They offer a well-defined pore system in combination with a high surface area. A mesoporous pore system is necessary for a fast transport to the potential storage component. This can be integrated into the structure in a highly dispersed form (MCM-36, MCM-22 and ITQ-2) as shown by Barth *et al.* [82]. However, the low loading of potential storage component (Ba, Mg) and the complete loss of the material structure during the integration of the storage component led to no further development with zeolitic materials [83, 84].

1.8 Metal organic framework materials

Metal organic framework materials constitute a new class of materials, which offers a high dispersion of the metal integrated in the organic network. Currently, the synthetic design of metal-organic frameworks (also known as coordination polymers) is a very active research area [85-89]. Many new porous materials synthesized in the past several years belong to this family. Unlike zeolites that

have an inorganic host framework, in metal-organic frameworks the three-dimensional connectivity is established by linking metal cations or clusters with bidentate or multidentate organic ligands. As metals, typically Zn, Cu, Co, Ru, Os and rare earth metals are used [90, 91]. As ligands, O-bridging linkers, e.g. 1,3,5,-benzenetricarboxylate (BTC), N-bridging linkers, e.g. 4,4'-bipyridine and S-bridging linkers, e.g. biphenyldisulfonic acid, are common. The synthesis of metal-organic frameworks is achieved under mild conditions (e.g. solution chemistry, solvothermal synthesis) and, in the simplest case, involves reaction of a transition metal ion, which acts as a node, with an organic ligand, which acts as a bridge, to form an infinite one-, two-, or three dimensional framework [92-95]. The resulting frameworks are hybrid frameworks between inorganic and organic units and should be distinguished from porous materials in which organic amines are encapsulated in the cavities of purely organic frameworks. The development of metal-organic framework materials began in the early 1990s and was apparently an extension of the earlier work on three-dimensional cyanide frameworks [96, 97]. MOFs may provide new opportunities for practical applications due to their specific properties (e.g. large pore volume) in catalysis, adsorption impurities from liquids and gases, gas storage and molecular recognition [85, 91, 98-100]. The storage of H_2 as well as noble gases is state of the art [101-103]. However, the understanding of the clear mechanism is still under investigation. One of the main focuses in the industrial application of MOF materials presently is the reversible storage of potential energy sources (CH_4, H_2) for the fuel cell technology. Furthermore, the ultra-large pore volume makes these materials ideal candidates for supporting a second phase inside the pores, which allows creating multifunctional materials with keeping an appreciable reaction volume. As shown by Moon *et al.* the deposition of Ag in Ni-MOF materials offers a multifunctional material with a porous structure and redox active centre [104].

A rational development of effective SO_x storage materials can be only achieved by a deep insight into the mechanisms by which the oxidation and the storage component influence the storage capacity. However, despite the deep scientific knowledge of the SO_x interaction, the understanding of the sulfur dioxide chemistry under dynamic lean-rich cycling conditions is still unclear.

1.9 Spectroscopic methods for investigation of SO_2 interaction

Several techniques could be used for getting a deeper insight in the sulfate formation on surfaces. In the following paragraphs, IR spectroscopy and X-ray absorption spectroscopy are discussed in detail, due to the main utilization in the thesis.

1.9.1 IR spectroscopy

Infrared spectra originate in transitions between discrete vibrational and rotational energy levels of molecules. While applying IR radiation the molecule absorbs the energy from the photon. If the energy of the photon corresponds to the energy between the ground and the high-energy states of the molecule, energy absorption is observed leading to a band or peak [105, 106]. The position of the various vibrational modes (bending, deformation, torsion) associated with a molecule are defined by the mechanical motion of the molecule and depend on the force constants of the bonds between the atoms and the masses of these. The intensity is determined by electrical factors such as dipole moments and polarizibility [107].
The possibility for a change in the dipole moment depends e.g. on the symmetry of the molecule. In the gas phase, a molecule has 3*N*-6 or 3*N*-5 degrees of freedom (*N* denoting the number of atoms), depending on the structure of the molecule. While adsorbing on a surface, the symmetry is usually lowered which could lead to a change in structure resulting different spectra compared to the gas phase. In solid state, the degrees of freedom assigned to translational or rotational modes result in lattice vibrations (frustrated translations and rotations) [108].
When SO_4^{2-} with a high symmetry (tetrahedral symmetry T_d) in gas or liquid phase is bound to a surface, the symmetry is reduced to a C_{3v} or C_{2v} depending on the bonding of the sulfate ion on the surface [105, 109-111]:

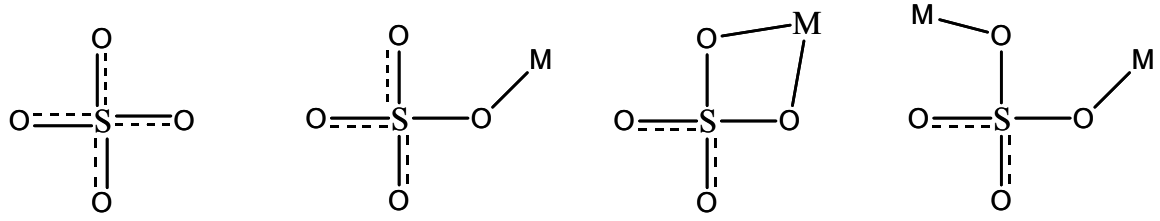

Free ion, T_d | Unidentate binding, C_{3v} | Bidentate complex, C_{2v} | Bridged bidentate complex, C_{2v}

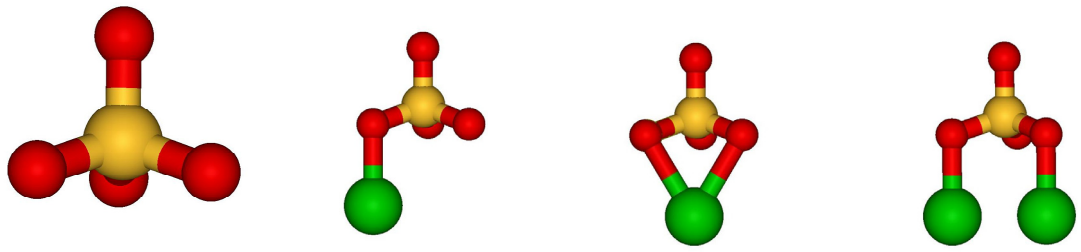

Free ion, T_d | Unidentate binding, C_{3v} | Bidentate complex, C_{2v} | Bridged bidentate complex, C_{2v}

Fig. 1.18 : Symmetry of different SO_4^{2-} species. Sulfur atoms are pictured in yellow, oxygen in red and the Metal atom in green color.

Changes in the local environment and/or symmetry of the sulfate ions may cause a shift in the position of the corresponding peak, or can generate new vibrations [105].

Tab. 1.5 depicts a short summary of various peak positions assigned to the sulfur species. It is clearly observed that especially on mixed metal oxide surface a clear distinction between the various sorption sites is rather challenging.

Tab. 1.5 : IR active vibrational modes of SO_4^{2-} and SO_3^{2-} species with different symmetry.

Wavenumber range [cm^{-1}]	**S-species**	**reference**
860-1230	SO_3^{2-} species	[112]
940-1240	SO_4^{2-} species	[112]
940-960	ν_1 chelating bidentate SO_4^{2-}	[112]
940-985	ν_1 SO_3^{2-} bound to a metal through the sulfur atom	[112]
960-990	ν_1 bridged bidentate SO_4^{2-}	[112]
975-1000	ν_3 organic sulfates	[112]
975-1000	organic sulfates	[112]
995-1035	ν_3 chelating bidentate SO_4^{2-}	[112]
1030-1035	ν_3 bridged bidentate SO_4^{2-}	[112]
1030-1050	ν_1 organic sulfites	[112]
1031-1044	ν_3 monodentate SO_4^{2-}	[112]
1035-1043	Sulfuric acid monohydrate, $H_3O^+HSO_4^-$	[113]
1040	$Al_2(SO_4)_3$	[34, 63]
1050-1120	ν_3 SO_3^{2-} bound to a metal through the sulfur atom	[112]
1060	$BaSO_4$ surface	[34, 63]

1086-1193	bidentate sulfate on Ba and Ca	[110]
1090-1125	ν_3 chelating bidentate SO_4^{2-}	[112]
1105-1110	ν_3 bridged bidentate SO_4^{2-}	[112]
1117-1147	ν_3 unidentate SO_4^{2-}	[112]
1120	$BaSO_4$ surface	[34, 63]
1126-1134	bidentate sulfate on Mg/Al	[109]
1150-1220	ν_3 vibration of SO_4^{2-} on Cu	[114]
1150-1230	ν_3 organic sulfates	[112]
1155	$BaSO_4$ bulk	[34, 63]
1160-1195	ν_3 bridged bidentate SO_4^{2-}	[112]
1180-1250	organic sulfites	[112]
1230-1240	ν_3 chelating bidentate SO_4^{2-}	[112]
1248	$BaSO_4$ bulk	[34, 63]
1326-1330	Adsorbed SO_2 on Al_2O_3	[115]
1338-1372	SO_2	[116]
1338-1372	reversibly adsorbed SO_2 on Al_2O_3	[116]
1350	$Al_2(SO_4)_3$	[34, 63]
1350-1460	ν_3 organic sulfates	[112]

1.9.2 X-ray absorption spectroscopy – XAS

X-ray absorption spectroscopy is a non destructive bulk technique that reveals useful information about the local atomic environment. XAS is especially useful for deriving conclusions about the oxidation state, the interatomic distances, the number of the next neighbors, the atomic species present in the sample and their structural and electronical properties [117].

In situ XAS measurements are in widespread use in heterogeneous catalysis for gaining deeper insight on the chemical behavior of the catalyst under reaction conditions [118-123]. XAS measurements can be performed in transmission or in fluorescence mode. At energies > 5keV and high concentrations of the species investigated, transmission mode is mainly applied. However, high X-ray adsorption coefficients at low energies and at low elemental concentrations have led to the application of fluorescence detectors.

The main goal of an XAS experiment is to determine the absorption coefficient μ as a function of the energy of the x-ray beam. The X-ray beam has to fulfill the Lambert-Beer's law [124]:

$$I_t = I_0 * e^{-\mu(E)x}$$

Equation 1.4 : Lambert Beer's Law

(with *I* being the intensity and *x* being the path length i.e. the thickness of the sample).

When the energy of the monochromatic X-ray beam corresponds to the energy necessary to excite one of the core electrons (K, L or M electron), a sharp increase in the absorption coefficient is observed (absorption edge). For every atom this binding energy is well defined which makes it possible to select the element of interest by changing the energy of the beam. Fig. 1.19 shows the photoelectric effect, i.e. the excitation of an electron by X-ray radiation (left) and the influence of the neighboring atoms and shells which allows drawing a conclusion about the interatomic distances and the number of neighbors [124]. The outgoing electron can be seen as a spherical wave scattering with the neighboring atoms. The interference pattern can range from a constructive interference to total destruction and is strongly influenced by the interatomic distance.

A typical X-ray absorption spectrum is depicted in Fig. 1.20. The main feature of the spectrum is the distinctive edge (here: Cu K-edge) at 8979eV. There are two regions of interest in an XA spectrum: the XANES and the EXAFS region. The data recorded in the EXAFS region contain information about the scattering behavior of the next neighbor shells of the atom monitored. In contrast, the XANES region contains information about the local structure of the investigated atom. The interpretation of the XANES spectrum can be performed straight from the μ-eV-spectrum. The spectral features of interest are the pre-edge, the position of the main edge and the position of the so-called "white line".

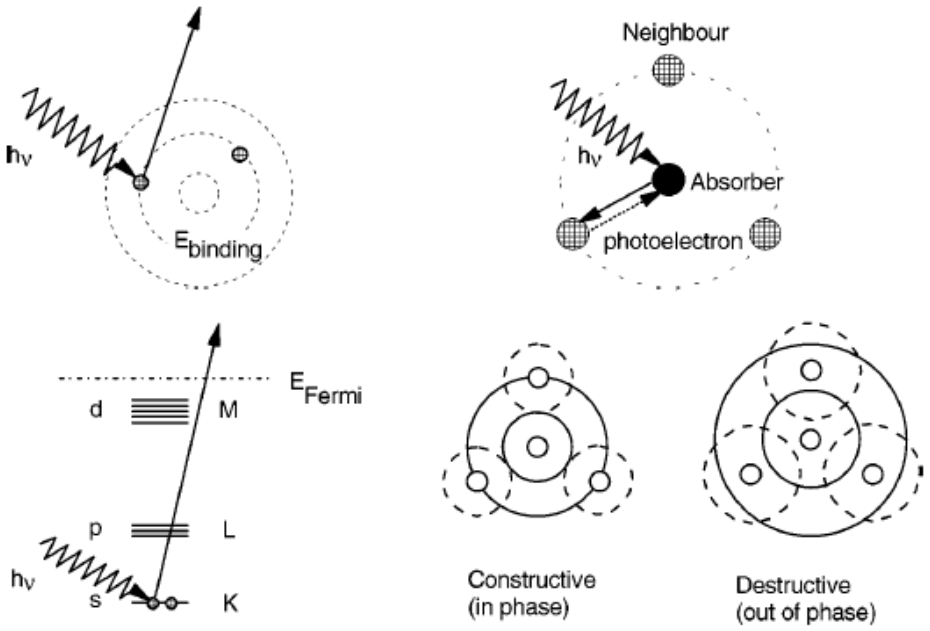

Fig. 1.19 : Excitation of an electron by X-ray radiation and influence of the neighboring atoms [124].

Pre-edge features can be observed when a dipole forbidden (s → d for the K-edge) transition takes place and are highly dependant on the local geometry [125]. The position of the main edge allows a conclusion on the oxidation state of the atom under study. In general, the lower the oxidation state, the further the spectrum is shifted to lower energies. The name “white line” therefore originates from former times when XA spectra were recorded on photographic paper: A white line denoting the highest intensity appeared short after the edge energy was reached. The white line is proposed to monitor the density of the empty states at the Fermi level. Thus, it is affected by the oxidation state and the ligands of the atom. Although the oxidation state affects the white line intensity, there is not necessarily a monotonic correlation of the white line intensity and the oxidation state [120, 126-128].

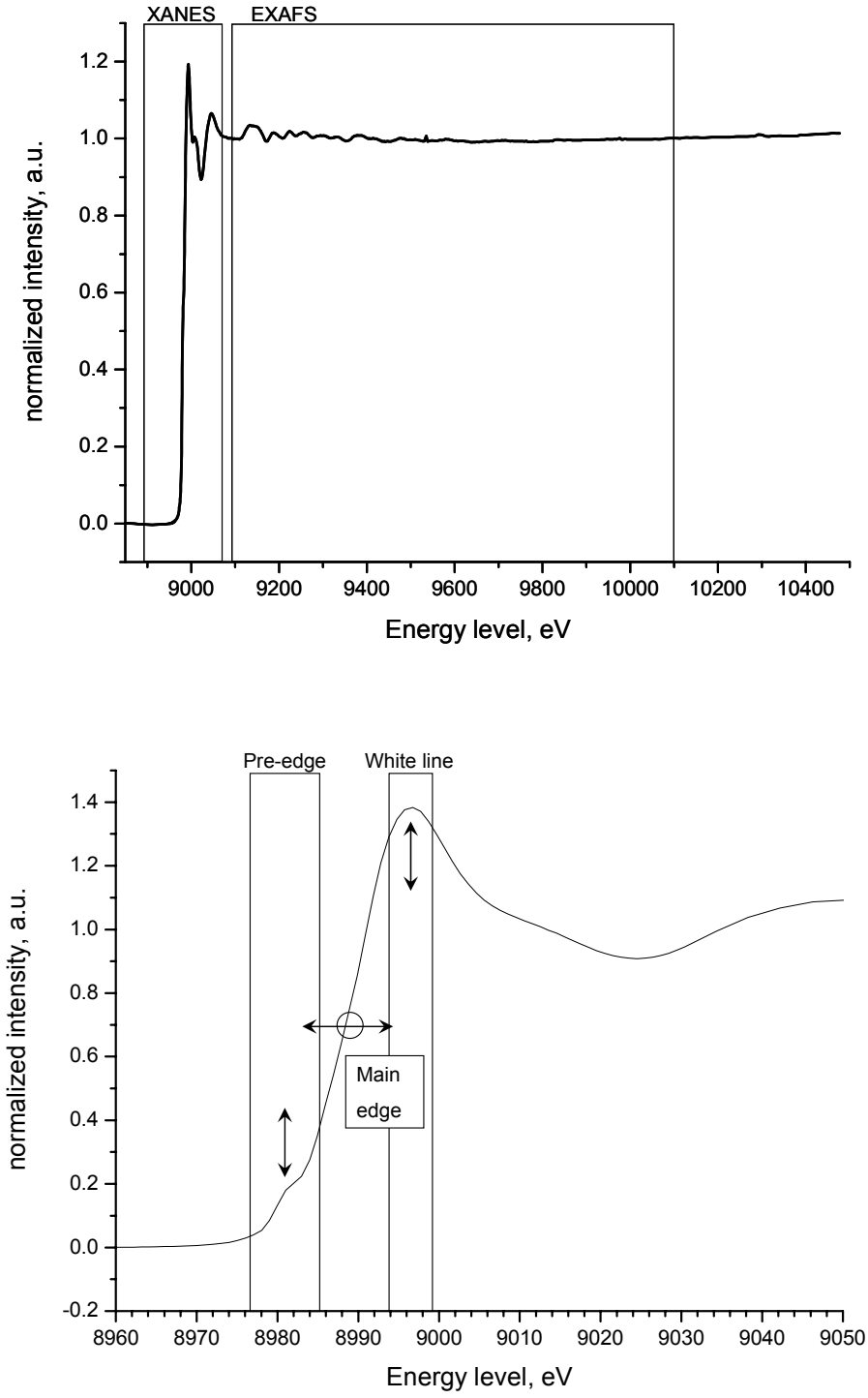

Fig. 1.20 : EXAFS and XANES absorption-energy spectra.

1.10 Scope of the Thesis

In this thesis, Metal-organic Framework materials (MOF) and various mixed metal oxides were evaluated in exhaust gas catalysis and the key factors influencing the SO_x storage capacity were identified. The influence of the gas composition on the SO_x storage process was evaluated. Furthermore, the application of a *in situ* technique (S K XANES) and the combination of advanced chemometric methods led to a complete understanding of the SO_x storage process under dynamic conditions.

After a general introduction in Chapter 2 of the thesis, copper containing MOF materials modified with various Ba sources were evaluated with respect to the storage capacity compared to a standard SO_x trap. Various physicochemical methods were applied to investigate the influence of the Ba source on the properties of the material. The application of S K-edge XANES and Cu K-edge XANES as a non destructive technique to investigate the sulfur and copper species on the MOF materials with respect to temperature is discussed in Chapter 3. The application of S K-edge XANES under reaction conditions on a second generation SO_x trapping material is shown in Chapter 4. There, the influence of the gas composition (oxidizing/reducing conditions) on this trapping material is discussed. Chapter 5 focuses on the evaluation of the storage performance of a noble metal free material. The characterization and identification of the key factors with respect to the impregnating component, as well as the influence of water on the storage process, are discussed. Chapter 6 deals with the application of 2D correlation analysis and principal component analysis on dataset obtained by means of *in situ* IR spectroscopy. The influence of lean-rich cycling conditions as well as the presence of water in the gas stream on the materials (Pt and Pt free) was investigated under plug flow conditions and by *in situ* IR spectroscopy. Chapter 7 gives a summary of the major results and conclusions of this thesis.

1.11 References:

[1] J. Brettschneider, *BOSCH TECH BERICHTE,* 1970, **6**, 4.
[2] A. F. Hollemann, E. Wiberg and N. Wiberg, Lehrbuch der Anorganischen Chemie, de Gruyter, Berlin.
[3] S. Pischinger, *Topics in Catalysis,* 2004, **30-31**, 5.
[4] D. B. Kittelson, *Journal of Aerosol Science,* 1998, **29**, 575.
[5] K. O. Blumberg, M. P. Walsh and C. Pera, Low sulfur gasoline & diesel: the key to lower vehicle emissions, Meeting of the international council on clean transportation (ICCT), Napa, California*,* **2003**.
[6] L. D. Robin, Air Quality Modeling of Ammonia: A Regional Modeling Perspective, Ammonia Workshop, Washington, D.C.*,* **2003**.
[7] A. J. Haagensmit, *Industrial And Engineering Chemistry,* 1952, **44**, 1342.
[8] A. J. Haagensmit, C. E. Bradley and M. M. Fox, *Industrial And Engineering Chemistry,* 1953, **45**, 2086.
[9] J. W. Erisman, P. Grennfelt and M. Sutton, *Environment International,* 2003, **29**, 311.
[10] M. A. Gomez-Garcia, V. Pitchon and A. Kiennemann, *Environment International,* 2005, **31**, 445.
[11] E. P. Agency, <http://www.epa.gov/airtrends >, 19.09. 2005.
[12] R. A. Smith, Air and rain: the beginning of a chemical climatology, Longmans, Green and Co., London.
[13] L. Gimeno, E. Marin, T. del Teso and S. Bourhim, *Science of the Total Environment,* 2001, **275**, 63.
[14] T. G. Brydges and P. W. Summers, *Water Air And Soil Pollution,* 1989, **43**, 249.
[15] J. H. Seinfeld and S. N. Pandis, Atmospheric chemistry and physics of air pollution, Wiley-Interscience,
[16] R. M. Heck and R. J. Farrauto, *Applied Catalysis A-General,* 2001, **221**, 443.
[17] J. P. Fayolle, An european prospective of EURO 5 / US 07 HD enginges technologies and their related consequences, DEER, Coronada, California*,* **Year**.
[18] P. A. G. C. KG, <http://www.purem.de/>, 19.09. 2005.
[19] T. Kreuzer, E. S. Lox, D. Lindner and J. Leyrer, *Catalysis Today,* 1996, **29**, 17.
[20] J. Kaspar, P. Fornasiero and N. Hickey, *Catalysis Today,* 2003, **77**, 419.
[21] S. I. Matsumoto, *Catalysis Today,* 2004, **90**, 183.
[22] D. D. Jayaseelan, S. Ueno, H. Kita, N. Kondo and T. Ohji, *Journal Of Porous Materials,* 2005, **12**, 47.
[23] D. Fino, G. Saracco and V. Specchia, *Industrial Ceramics,* 2002, **22**, 37.
[24] J. P. A. Neeft, M. Makkee and J. A. Moulijn, *Fuel Processing Technology,* 1996, **47**, 1.
[25] M. K. Khair, *Society of Automotive Engineers, [Special Publication] SP,* 2003, **SP-1791**, 57.
[26] A. Fritz and V. Pitchon, *Applied Catalysis B-Environmental,* 1997, **13**, 1.
[27] P. L. T. Gabrielsson, *Topics in Catalysis,* 2004, **28**, 177.
[28] M. Koebel, M. Elsener and M. Kleemann, *Catalysis Today,* 2000, **59**, 335.

[29] K. Nakanishi, S. Iguchi, T. Inoue, K. Kato, T. Kihara, H. Muraki and H. Nohira, Exhaust emission control device for internal combustion engine, EU 0573672, **1993**.
[30] R. Mital, J. Li, S. C. Huang, B. J. Stroia, R. C. Yu, J. A. Anderson and K. Howden, *Society of Automotive Engineers, [Special Publication] SP,* 2003, **SP-1754**, 31.
[31] H. L. Fang, S. C. Huang, R. C. Yu, C. Z. Wan and K. Howden, *Society of Automotive Engineers, [Technical Paper] TP,* 2002, **2002-01-2889**,
[32] W. S. Epling, L. E. Campbell, A. Yezerets, N. W. Currier and J. E. Parks, *Catalysis Reviews-Science and Engineering,* 2004, **46**, 163.
[33] C. Sedlmair, K. Seshan, A. Jentys and J. A. Lercher, *Journal of Catalysis,* 2003, **214**, 308.
[34] C. Sedlmair, K. Seshan, A. Jentys and J. A. Lercher, *Catalysis Today,* 2002, **75**, 413.
[35] E. Fridell, M. Skoglundh, B. Westerberg, S. Johansson and G. Smedler, *Journal of Catalysis,* 1999, **183**, 196.
[36] M. F. M. Zwinkels, S. G. Jaras, P. G. Menon and T. A. Griffin, *Catalysis Reviews-Science And Engineering,* 1993, **35**, 319.
[37] S. Suhonen, M. Valden, M. Pessa, A. Savimaki, M. Harkonen, M. Hietikko, J. Pursiainen and R. Laitinen, *Applied Catalysis A-General,* 2001, **207**, 113.
[38] F. Klingstedt, H. Karhu, A. K. Neyestanaki, L. E. Lindfors, T. Salmi and J. Vayrynen, *Journal of Catalysis,* 2002, **206**, 248.
[39] E. Fridell, H. Persson, L. Olsson, B. Westerberg, A. Amberntsson and M. Skoglundh, *Topics in Catalysis,* 2001, **16**, 133.
[40] W. Bogner, M. Kramer, B. Krutzsch, S. Pischinger, D. Voigtlander, G. Wenninger, F. Wirbeleit, M. S. Brogan, R. J. Brisley and D. E. Webster, *Applied Catalysis B-Environmental,* 1995, **7**, 153.
[41] J. S. Hepburn, E. Thanasiu, D. Dobson and W. L. Watkins, *SAE Technical Papers,* 1996, **962051**,
[42] M. Takeuchi and S. Matsumoto, *Topics in Catalysis,* 2004, **28**, 151.
[43] A. Amberntsson, B. Westerberg, P. Engstrom, E. Fridell and M. Skoglundh, *Studies in Surface Science and Catalysis,* 1999, **126**, 317.
[44] J. Parks, A. Watson, G. Campbell, G. Wagner, M. Cunningham, N. Currier, T. Gallant and G. Muntean, *Society of Automotive Engineers, [Special Publication] SP,* 2001, **SP-1631**, 63.
[45] T. V. Johnson, *Society of Automotive Engineers, [Special Publication] SP,* 2004, **SP-1835**, 1.
[46] I. Hachisuka, H. Hirata, Y. Ikeda and S. Matsumoto, *Society of Automotive Engineers, [Special Publication] SP,* 2000, **SP-1196**,
[47] O. H. Bailey, D. Dou and M. Molinier, *Society of Automotive Engineers, [Special Publication] SP,* 2000, **SP-1533**, 257.
[48] J. R. Asik, G. M. Meyer and D. Dobson, *Society of Automotive Engineers, [Special Publication] SP,* 2000, **SP-1200**, 219.
[49] K. Arakawa, S. Matsuda and H. Kinoshita, *Society of Automotive Engineers, [Special Publication] SP,* 1998, **SP-1353**, 111.
[50] J. Li, J. R. Theis, W. Chun, C. T. Goralski, R. J. Kudla, W. L. Watkins and R. H. Hurley, *Society of Automotive Engineers, [Special Publication] SP,* 2001, **SP-1637**, 47.
[51] Y. Cheng, J. V. Cavataio, W. D. Belanger, J. W. Hoard and R. H. Hammerle, *Society of Automotive Engineers, [Special Publication] SP,* 2004, **SP-1861**, 47.

[52] Y. Takahashi, Y. Takeda, N. Kondo and M. Murata, *Society of Automotive Engineers, [Special Publication] SP,* 2004, **SP-1860**, 141.
[53] N. Kono, T. Uchiyama, M. Hirose, K. Akasofu and H. Takeda, *Society of Automotive Engineers, [Special Publication] SP,* 2003, **SP-1801**, 73.
[54] P. Engstrom, A. Amberntsson, M. Skoglundh, E. Fridell and G. Smedler, *Applied Catalysis B-Environmental,* 1999, **22**, L241.
[55] E. P. Agency, Control of Air Pollution From New Motor Vehicles: Heavy-Duty Engine and Vehicle Standards and Highway Diesel Fuel Sulfur Control Requirements; Final Rule, Environmental Protection Agency, p. 5093.
[56] B. Amoco, June 15, 2000.,
[57] K. G. Knudsen, B. H. Cooper and H. Topsoe, *Applied Catalysis A-General,* 1999, **189**, 205.
[58] H. L. Fang, J. C. Wang, R. C. Yu, C. Z. Wan and K. Howden, *Society of Automotive Engineers, [Special Publication] SP,* 2003, **SP-1801**, 185.
[59] P. S. Lowell, Schwitzg.K, T. B. Parsons and K. J. Sladek, *Industrial & Engineering Chemistry Process Design and Development,* 1971, **10**, 384.
[60] D. W. Deberry and K. J. Sladek, *Canadian Journal of Chemical Engineering,* 1971, **49**, 781.
[61] S. Matsumoto, Y. Ikeda, H. Suzuki, M. Ogai and N. Miyoshi, *Applied Catalysis B-Environmental,* 2000, **25**, 115.
[62] C. Sedlmair, *Elemantary reaction steps of NO_x trapping ad SO_x deactivation of NO_x storage reduction,* **2002**, University of Twente, Phd. thesis.
[63] C. Sedlmair, K. Seshan, A. Jentys and J. A. Lercher, *Research on Chemical Intermediates,* 2003, **29**, 257.
[64] ACEA, ACEA data of the sulphur effect in advanced emission control technologies,Brussels European Automobile Manufacturers Association., **2000**.
[65] L. Limousy, H. Mahzoul, J. F. Brilhac, P. Gilot, F. Garin and G. Maire, *Applied Catalysis B-Environmental,* 2003, **42**, 237.
[66] L. Limousy, H. Mahzoul, J. F. Brilhac, F. Garin, G. Maire and P. Gilot, *Applied Catalysis B-Environmental,* 2003, **45**, 169.
[67] H. Mahzoul, L. Limousy, J. F. Brilhac and P. Gilot, *Journal of Analytical and Applied Pyrolysis,* 2000, **56**, 179.
[68] M. Molinier, *Society of Automotive Engineers, [Special Publication] SP,* 2001, **SP-1581**, 79.
[69] M. Molinier, Method for sulfur protection of nitrogen oxide adsorber in exhaust gas purification, US 6758036, **2004**.
[70] R. M. Smaling, Method and apparatus for purging SO_x from NO_x trap, US 2004/050035, **2004**.
[71] J. P. Breen, M. Marella, C. Pistarino and J. R. H. Ross, *Catalysis Letters,* 2002, **80**, 123.
[72] R. Burch, *Catalysis Reviews-Science And Engineering,* 2004, **46**, 271.
[73] L. Y. Li and D. L. King, *Industrial & Engineering Chemistry Research,* 2004,
[74] W. Strehlau, U. Gobel, R. Domesle, E. Lox and T. Kreuzer, Sulfur oxide storage material for exhaust gas catalytic converters, EP 99-105440 945165, **1999**.
[75] A. N. Chigapov, A. A. Dubkov, B. P. Carberry, C. N. Montreuil, G. W. Graham, R. W. McCabe and W. Chun, SO_x trap for diesel and lean burn gasoline automotive applications, EP 1374978 A1 20040102, **2004**.
[76] A. Berris, J. Li, M. S. Chattha and W. L. H. Watkins, Vehicle sulfur oxide trap and related method, US 2003/159435, **2003**.

[77] L. Li and D. L. King, Sulfur oxide adsorbents and emissions control, US 2005/0169826, **2005**.
[78] R. McCabe, W. Chun, G. Graham, C. Montreuil, B. Carberry, A. Chigapov and A. Dubkov, SO_x trap for diesel and lean-burn gasoline automotive applications, US 2005/145827, **2005**.
[79] J. S. Feeley, R. J. Farrauto and M. Deeba, Regenerable catalyzed trap and apparatus, and method of using the same for waste gases, US 7195 9743034, **1997**.
[80] Y. S. Lin and S. G. Deng, *Studies in Surface Science and Catalysis,* 1999, **120A**, 653.
[81] Y. S. Lin and S. G. Deng, Sol-gel preparation of nanostructured adsorbents, Elsevier Science Publ B V, Amsterdam, p. 653.
[82] J. O. Barth, J. Kornatowski and J. A. Lercher, *Journal of Materials Chemistry,* 2002, **12**, 369.
[83] V. Roberts, *Mechanistic studies of SO_2-adsorption on metal oxides incorporated in porous networks,* **2004**, TU Munich, Diploma thesis.
[84] E. Peringer, *New materials for the adsorption of SO_2 in oxygen rich atmosphere,* **2004**, TU Munich, Diploma thesis.
[85] F. Fajula, A. Galarneau and F. D. Renzo, *Microporous and Mesoporous Materials,* 2005, **82**, 227.
[86] J. L. C. Rowsell and O. M. Yaghi, *Microporous and Mesoporous Materials,* 2004, **73**, 3.
[87] M. J. Rosseinsky, *Microporous and Mesoporous Materials,* 2004, **73**, 15.
[88] C. Janiak, *Dalton Transactions,* 2003, 2781.
[89] B. L. Chen, M. Eddaoudi, S. T. Hyde, M. O'Keeffe and O. M. Yaghi, *Science,* 2001, **291**, 1021.
[90] C. N. R. Rao, S. Natarajan and R. Vaidhyanathan, *Angewandte Chemie-International Edition,* 2004, **43**, 1466.
[91] O. M. Yaghi, M. O'Keeffe, N. W. Ockwig, H. K. Chae, M. Eddaoudi and J. Kim, *Nature,* 2003, **423**, 705.
[92] O. M. Yaghi, C. E. Davis, G. M. Li and H. L. Li, *Journal of the American Chemical Society,* 1997, **119**, 2861.
[93] K. Ohtsuka, *Chemistry of Materials,* 1997, **9**, 2039.
[94] M. Eddaoudi, J. Kim, N. Rosi, D. Vodak, J. Wachter, M. O'Keefe and O. M. Yaghi, *Science,* 2002, **295**, 469.
[95] S. R. Batten, *Current Opinion in Solid State & Materials Science,* 2001, **5**, 107.
[96] G. B. Gardner, D. Venkataraman, J. S. Moore and S. Lee, *Nature,* 1995, **374**, 792.
[97] B. F. Hoskins and R. Robson, *Journal of the American Chemical Society,* 1990, **112**, 1546.
[98] H. Li, M. Eddaoudi, M. O'Keeffe and O. M. Yaghi, *Nature,* 1999, **402**, 276.
[99] Q. M. Wang, D. Shen, M. Bulow, M. L. Lau, F. R. Fitch and S. G. Deng, Metallo-organic polymers for gas seperation and purification, US 6491740 B1, **2002**.
[100] H. K. Chae, D. Y. Siberio-Perez, J. Kim, Y. Go, M. Eddaoudi, A. J. Matzger, M. O'Keeffe and O. M. Yaghi, *Nature,* 2004, **427**, 523.
[101] U. Mueller, H. Puetter, M. Hesse and H. Wessel, Electrochemical synthesis of crystalline porous metal-organic frameworks, WO 2005/049892, **2005**.
[102] U. Mueller, Metal-organic framework material for the reversible storage of gases, WO 2005/049484, **2005**.

[103] U. Mueller, L. Lobree, M. Hesse, O. Yaghi and M. Eddaoudi, Shaped bodies containing metal-organic frameworks, US 2003/222023, **2003**.
[104] H. R. Moon, J. H. Kim and M. P. Suh, *Angewandte Chemie-International Edition,* 2005, **44**, 1261.
[105] S. C. B. Myneni, *Reviews in Mineralogy & Geochemistry,* 2000, **40**, 113.
[106] J. Ryczkowski, *Catalysis Today,* 2001, **68**, 263.
[107] L. H. Little, Infrared Spectra of Adsorbed Species,
[108] G. Busca, *Catalysis Today,* 1996, **27**, 323.
[109] J. T. Kloprogge, D. Wharton, L. Hickey and R. L. Frost, *American Mineralogist,* 2002, **87**, 623.
[110] D. Stoilova, M. Georgiev and D. Marinova, *Journal of Molecular Structure,* 2005, **738**, 211.
[111] J. A. Wang, Z. L. Zhu and C. L. Li, *Journal of Molecular Catalysis A-Chemical,* 1999, **139**, 31.
[112] T. Yamaguchi, *Applied Catalysis,* 1990, **61**, 1.
[113] K. L. Nash, K. J. Sully and A. B. Horn, *Physical Chemistry Chemical Physics,* 2000, **2**, 4933.
[114] S. Iretskaya and M. B. Mitchell, *Journal of Physical Chemistry B,* 2003, **107**, 4955.
[115] M. A. Babaeva, A. A. Tsyganenko and V. N. Filimonov, *Kinetics and Catalysis,* 1985, **25**, 787.
[116] H. C. Yao, H. K. Stepien and H. S. Gandhi, *Journal of Catalysis,* 1981, **67**, 231.
[117] J. J. Rehr and R. C. Albers, *Reviews Of Modern Physics,* 2000, **72**, 621.
[118] J. H. Bitter, K. Seshan and J. A. Lercher, *Topics in Catalysis,* 2000, **10**, 295.
[119] A. Jentys, N. H. Pham, H. Vinek, M. Englisch and J. A. Lercher, *Catalysis Today,* 1998, **39**, 311.
[120] M. L. Englisch, J.A. Haller, G.L., Supported Metal Particles, World Scientific - Singapore / New Jersey / Hong Kong, Singapore.
[121] B. I. Mosqueda-Jimenez, A. Jentys, K. Seshan and J. A. Lercher, *Journal of Catalysis,* 2003, **218**, 375.
[122] T. Ressler, J. Wienold, R. E. Jentoft, T. Neisius and M. M. Gunter, *Topics in Catalysis,* 2002, **18**, 45.
[123] G. Sankar, J. M. Thomas and C. R. A. Catlow, *Topics in Catalysis,* 2000, **10**, 255.
[124] D. C. Koningsberger, B. L. Mojet, G. E. van Dorssen and D. E. Ramaker, *Topics in Catalysis,* 2000, **10**, 143.
[125] J. C. J. Bart, *Advances in Catalysis,* 1986, **34**, 203.
[126] F. Hilbrig, H. E. Gobel, H. Knozinger, H. Schmelz and B. Lengeler, *Journal of Physical Chemistry,* 1991, **95**, 6973.
[127] F. Hilbrig, H. E. Gobel, H. Knozinger, H. Schmelz and B. Lengeler, *Journal of Catalysis,* 1991, **129**, 168.
[128] M. C. Hilbrig F., and Haller G.L., *Journal of Physical Chemistry,* 1992, **96**, 9893.

Chapter 2

Metal organic frameworks based on Cu^{2+} and benzene-1,3,5-tricarboxylate as host for SO_2 trapping agents

Abstract :

Metal organic framework materials with Cu^{2+} as central cation and benzene-1,3,5-tricarboxylate (BTC) as linker were prepared via hydrothermal synthesis and impregnated with barium salts (chloride, nitrate, acetate) to explore the role of the Ba^{2+} counter ion on the SO_2 uptake. The impregnation of the metal organic framework materials with barium salts led to a decrease of pore volume through the (intra pore) formation of small Ba – salt crystals. The structure of the Cu-BTC material was preserved after the impregnation with acetate and nitrate, but partially destroyed during impregnation with chloride. The complete loss of the BTC structure occurred through thermal decomposition at temperatures around 573K. The sample impregnated with $BaCl_2$ showed a higher fraction of Cu^{2+} species compared to the other Ba/Cu-BTC samples.
The SO_2 uptake capacity of the Ba/Cu-BTC(Cl^-) sample was the highest at temperatures below 673K among all materials prepared and even higher compared to $BaCO_3/Al_2O_3$/Pt based material. The comparison of the theoretical uptake (based on the stoichiometric formation of $BaSO_4$) with the maximum SO_x uptake achieved on the Ba/Cu-BTC samples clearly points out that a fraction of the SO_x is stored on the Cu species being part of the metal organic framework structure. With increasing temperature the framework is (partially) decomposed and highly dispersed Cu species are released, which act as additional SO_x storage sites in the high temperature region.

2.1 Introduction

Three dimensionally linked metal-organic frameworks can lead to void structures capable of sorbing organic and inorganic molecules [1-6]. Unlike oxide based microporous molecular sieves the reticulated structure of the metal-organic frameworks is established by linking metal cations or clusters with bi- or multi-dentate organic ligands. Recently substantial progress has been made with respect to the rational synthesis of such materials and a large number of metal-organic frameworks have been made with tailored micro- and mesoporosity [7-11]. Typically metal cations of Zn, Cu, Co, Ru, Os and rare earth metals are used in combination with O-bridging linkers, e.g. benzene-1,3,5,-tricarboxylate (BTC), N-bridging linkers, e.g. 4,4'-bipyridine or S-bridging linkers, e.g. biphenyldisulfonic acid [12].

The dimensionality of the Me-BTC frameworks mainly depends on the solvent used for the synthesis and the strength of base employed for the H_3BTC deprotonation. With a strong conjugate base (e.g., the acetate anion acting as a strong coordinating ligand) and water as solvent (and strong coordinating ligand) a porous one-dimensional framework will be obtained. Using a less strongly coordinating solvent such as ethanol and a weaker base such as pyridine for deprotonation a porous two-dimensional structure will be obtained. Pyridine partly deprotonates H_3BTC and, in the absence of water, binds strongly to metal ions blocking so the extension of the framework. For three dimensional structures a stronger base, such as triethylamine, with sufficient strength to completely deprotonate H_3BTC, but with a low affinity for binding to metal ions is necessary [13].

The rigid and divergent character of the linker added, e.g. carboxylates, leads to high pore volumes (up to 91.1% of the crystal volume) and in consequence high apparent surface areas of up to 2500m^2/g for three-dimensional structures [13, 14]. The coordination chemistry allows locking the metal ions in their positions within the M-O-C clusters, referred to as secondary building units (SBUs). The SBUs serve as large rigid vertices that can be joined by rigid organic links to produce neutral charged extended frameworks without counter ions in their cavities.

MOF materials typically lose their integrity and structure above 573K. The control of the architecture by variation of the organic linkers and the

functionalization of the pores with organic groups, like –Br, $-NH_2$, $-OC_3H_7$, $-OC_5H_{11}$, $-C_2H_4$, $-C_4H_4$ allows a flexible design of these materials [3, 10]. After removal of the solvent molecules, which act as a ligand a high concentration of coordinative unsaturated coordination sites on the metal ions, accessible from all direction from the three-dimensional channels are produced.

As an example for MOF materials, the structure of copper(II) benzene-1,3,5-tricarboxylate - $[Cu_3(BTC)_2(H_2O)_3]_n$ - (denoted as Cu-BTC) will be discussed. Cu-BTC is a neutral coordination polymer composed of dimeric cupric tetracarboxylate units [8]. Twelve carboxylate oxygen atoms from two BTC ligands, which bind to the four coordination sites of the three Cu^{2+} ions present in the SBU. These copper-benzenecarboxylate units form a face-centered crystal lattice of *Fm*3*m* symmetry, which has a complex three-dimensional channel system. Terminal water ligands, bound to the copper ions, are directed towards the interior of these pore system. A crystal structure of the material is shown in Fig. 2.1.

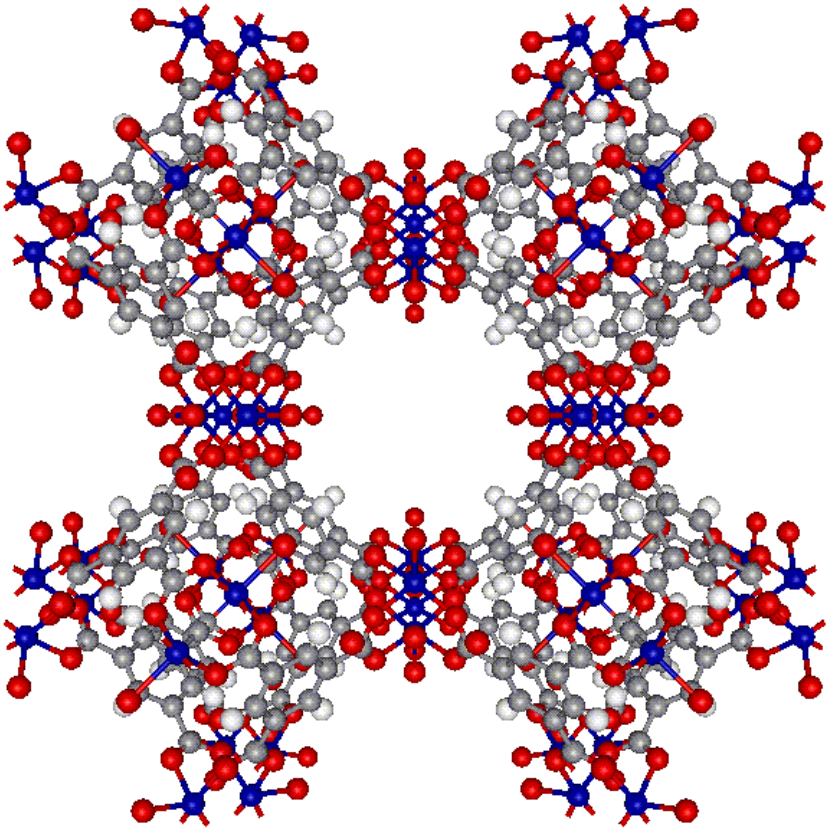

Fig. 2.1 : Crystal structure of the Cu-BTC.

The main pores of approximately 0.9nm diameter form a cubic network with additional side pockets formed by planar $C_6H_3(O_2C)_3$ segments. These

tetrahedron-shaped windows of these pockets have a diameter of about 0.35nm. This is wide enough for a penetration of small gas molecules in the network while larger organic molecules are excluded [12]. Promising applications of MOF materials include gas sorption, e.g. hydrogen storage, gas separation and catalysis [9, 10, 15-17].

The ultra-large pore volume makes these materials ideal candidates for supporting a second phase inside the pores, which allows creating multifunctional materials with keeping an appreciable reaction volume. In the work presented we focus on describing the synthesis, characterization and testing of novel sulfur trap materials, to be potentially used as guards for NO_x storage reduction catalysts to prevent admission of SO_x, which leads to a rapid decrease of the storage capacity by forming highly stable sulfates [18, 19]. In such "sulfur traps" SO_2 formed from the combustion of S impurities present in the fuel needs to be oxidized to SO_3 first, which in turn will be chemisorbed as sulfate by alkaline earth cations such as Ba^{2+}. In conventional oxide based materials supported barium oxide or carbonate will act as trapping agent, while Pt is added as oxidation catalyst. The materials discussed here will be based on Cu^{2+} (probably on defect sites) acting as oxidizing component, while supported barium salts will be providing sites for SO_3 chemisorption.

2.2 Experimental

2.2.1 Synthesis of materials

The synthesis method used was adapted from the synthesis route described by Vishnyakov *et al.* [12]. Benzene-1,3,5-tricarboxylic acid (12.28g, 0.059mol, Merck) was dissolved in 62.5ml ethanol (Merck) and cupric nitrate hydrate $Cu(NO_3)_2 \cdot 3H_2O$ (28.15g, 0.117mol, Merck) was dissolved in 62.5ml water. The two solutions were mixed at ambient temperature for 30min and subsequently transferred into a 120cm^3 PTFE-lined stainless steel autoclave, which was heated to 383K under hydrothermal conditions for 18h. The reaction vessel was cooled to ambient temperature and the blue crystals of Cu-BTC were isolated by filtration and washed with water. The solid product was dried overnight at 383K. The yield achieved was nearly 100% (18.13g Cu-BTC).

For the impregnation, $BaCl_2 \cdot 2\ H_2O$ (0.81g, 0.003mol, Merck), $Ba(CH_3COO)_2$ (0.76g, 0.003mol) or $Ba(NO_3)_2$ (0.78g, 0.003mol) was dissolved in 60ml alcohol/water mixture (1:1) and 2g of Cu-BTC (dried at 435K for 4h) was added to the solution. The mixture was stirred for 22.5h at ambient temperature. The solvent was removed under reduced pressure and the blue material was finally dried at 383K. For comparison a model catalyst containing (2%) Pt (oxidation/reduction components), (10%) $BaO/BaCO_3$ (SO_x storage component) on an Al_2O_3 support was used.

2.2.2 Characterization

The crystalline structure of the synthesized and modified materials was analyzed by XRD using a Philips X'Pert Pro System ($CuK_{\alpha 1}$-radiation, 0.154056nm) operating at 40kV / 40mA. Measurements were performed in a glass capillary (ø = 0.5mm) with a scan step of 0.05°/min from 5° to 80° 2θ. The morphology and particle size of the synthesized materials were examined by scanning electron microscopy using a *JEOL* 500 SEM-microscope (accelerating voltage 23kV). For SEM experiments the samples were outgassed for 2 days and sputtered with gold before collecting the images. Nitrogen adsorption measurements were collected at 77.4K with a PMI automated BET Sorptometer. For BET measurements the samples were outgassed at 473K in vacuum (10^{-3}Pa) for 24h prior to the adsorption measurements. The mesopore size distribution was obtained from the desorption branch of the isotherm using the Barret-Joyner-Halenda (BJH) method, the micropore volume was obtained from the desorption branch of the isotherm using (H-K) method [20, 21].

The thermal stability of the materials was investigated by thermogravimetric methods in a modified *Setaram TG-DSC 111* system. The samples were pressed into thin wafers and subsequently broken into small platelets. Approximately 18mg of these platelets were charged into the quartz samples holder of the balance. The samples were heated in vacuum with a temperature increment of 10K/min to 973K. Changes in weight were observed and the gases evolved were analyzed with a Balzers quadrupole mass spectrometer. The chemical composition of materials synthesized was determined by atomic absorption spectroscopy (AAS) using a *UNICAM 939 AA-Spectrometer*.

For X-ray absorption spectroscopy the samples were pressed into self supported wafers with a total absorption 2.5. X-ray absorption spectra were measured at HASYLAB, DESY (Hamburg, Germany) on beam line X1 and E4 using a Si (111) monochromator. The contributions of higher order reflections were excluded by detuning the second crystal of the monochromator to 60% of the maximum intensity. The spectrum of the corresponding metal foil was recorded simultaneously between the second and a third ionization chamber to calibrate the energy alignment of the monochromator. X-ray absorption spectra were recorded at the Cu-K edge at liquid nitrogen temperature. For the analysis of the EXAFS the oscillations were extracted from the background using a combination of a first and third order polynomial function and after weighting with k^2 the oscillations were Fourier transformed in the range between 2.1 and 15$Å^{-1}$. The local environment of the Cu atoms was determined from the analysis of the EXAFS in k-space using phase-shift and amplitude functions for Cu-O and Cu-Cu calculated assuming multiple scattering processes (FEFF Version 8.10) using the program Viper to analyze the data [22, 23].

2.2.3 SO_x uptake

The SO_x uptake rate was determined in a plug flow reactor system equipped with a fluorescence detector (Model 43C *Fa.* Thermo Environmental Instruments) to monitor the SO_2 concentration at the reactor outlet. As the detector can only monitor the SO_2 concentration in the gas stream a converter operating at 1223K was placed behind the reactor to convert SO_3 formed during the reaction to SO_2. For distinction between SO_2 and SO_3 experiments with and without converter were carried out. For the SO_2 uptake experiments 50mg of the storage material (particle size 0.3 - 0.6mm) was diluted with 100mg SiC (particle size < 0.3mm) and exposed to a flow of 50ppm SO_2 and 6% O_2 in He at a flow rate of 200ml/min. After heating up to 473K with 10K/min the SO_x breakthrough over the catalyst bed was followed at 473K, 573K, 673K and 773K. A schematic draw of the experimental setup is shown in Fig. 2.2.

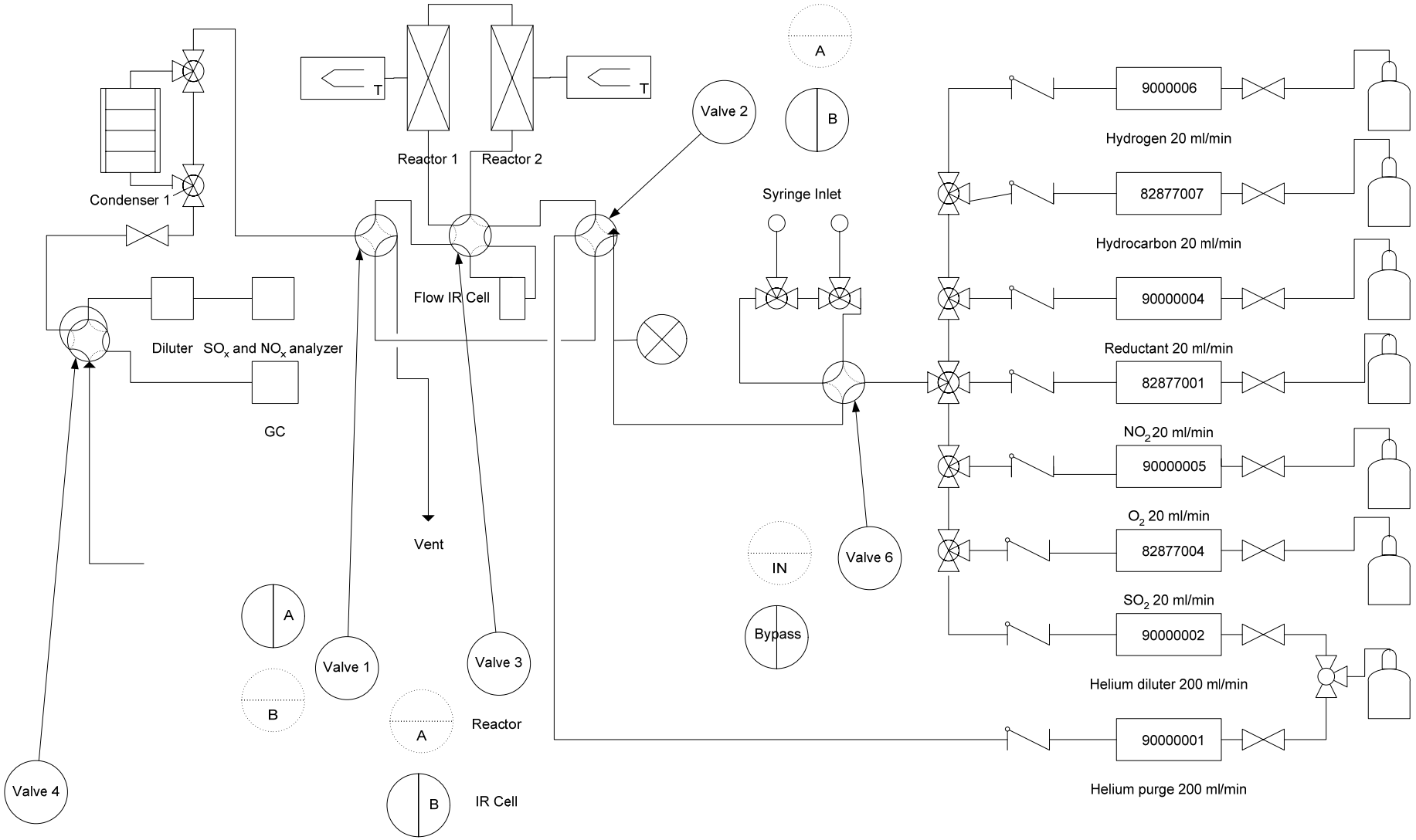

Fig. 2.2 : Flow scheme of the setup used for the SO_2 uptake measurements.

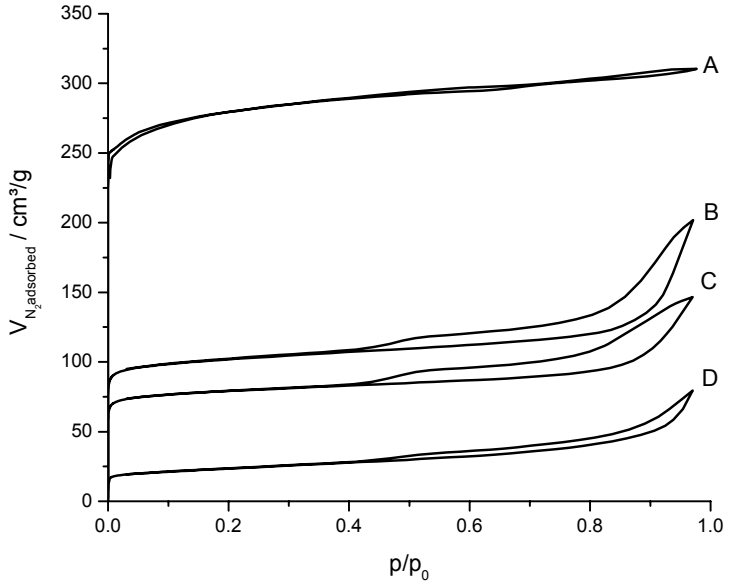

Fig. 2.3 : N_2 adsorption/desorption isotherms of the prepared MOF samples Cu-BTC (A) Ba/Cu-BTC(CH_3COO^-) (B) Ba/Cu-BTC(NO_3^-) (C) Ba/Cu-BTC(Cl^-) (D).

2.3 Result and Discussion

2.3.1 Composition, morphology and porosity of the materials

The compositions and N_2 physisorption results of the parent Cu-BTC and of the Ba^{2+} loaded materials are shown in Tab. 1. Due to the lower solubility of Ba-nitrate in the water/ethanol mixture the Ba^{2+} concentration for the Ba/Cu-BTC (NO_3^-) sample was 7.5wt.%, while for the other Ba^{2+} containing samples a loading of 15wt.% Ba was reached. The N_2 adsorption/desorption isotherms of Cu-BTC and Ba/Cu-BTC are compared in Fig. 2.3.

The isotherms of Cu-BTC correspond to a type I isotherm, typical for microporous materials, whereas the impregnated samples show a type IV isotherm typical for materials with mesopores. The highest pore volume was observed for the parent Cu-BTC, while after impregnation with the Ba salts the pore volume decreased. A comparison of the pore volumes analyzed with the different methods showed that it strongly decreased (especially the volume of the micropores) after impregnation with Ba-chloride.

The XRD patterns of the Ba^{2+} impregnated Cu-BTC samples are compiled in Fig. 2.4. The XRD of the parent Cu-BTC was in perfect agreement with the X-ray diffractogram simulated using the program MERCURY and the crystal

structure reported by Chui *et al.* [8]. After impregnation with Ba-acetate and Ba-nitrate strong reflections around 2θ = 25° and 38° were observed, which are assigned to acetate and nitrate species. In contrast for Cu-BTC impregnated with $BaCl_2$ the intensity of all XRD reflections decreased indicating a decrease in crystallinity. The basic patterns of the Cu-BTC structure observed for the samples impregnated with nitrate and acetate indicate that the metal organic framework structure was preserved, while for the $BaCl_2$ impregnated sample the smaller reflections indicate a significant reduction of the coherence in the metal organic framework structure.

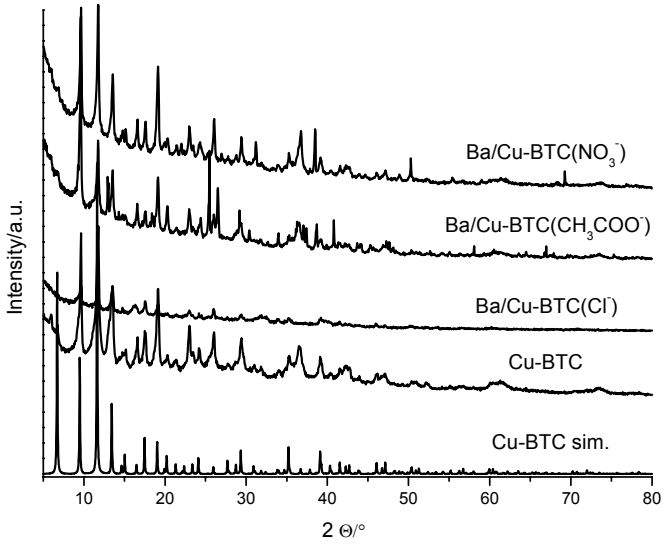

Fig. 2.4 : XRD patterns of Cu-BTC and Ba/Cu-BTC samples.

Scanning electron microscopy images from Cu-BTC and $BaCl_2$ impregnated Cu-BTC are compared in Fig. 2.5 and Fig. 2.6, respectively. Cu-BTC crystallized in double sided pyramids with an edge length in the range of 130 - 215µm and a height of 170 – 230µm. Besides these large crystals, also smaller crystals with an edge length around 15µm and height of 20µm were formed. EDAX analysis indicated that impregnation with $BaCl_2$ resulted in small Cu-BTC particles covered by barium salt with 5µm particle size, which agglomerated to bigger particles (~ 20µm, Fig. 2.6). The change in particle morphology compared to the parent Cu-BTC is in good agreement with the general decrease of the intensity of the XRD pattern of this sample.

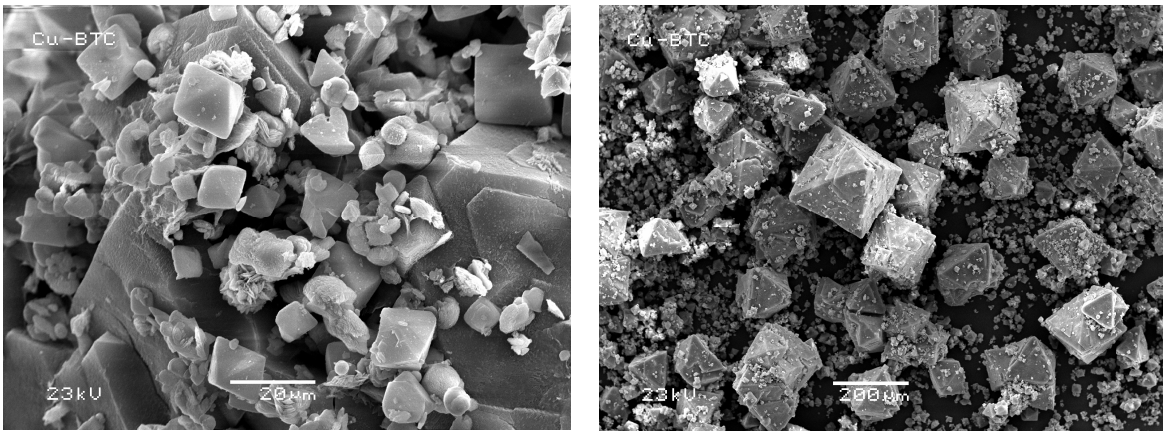

Fig. 2.5 : Scanning electron micrographs of Cu-BTC

Tab. 2.1 : AAS and N_2 physisorption results of synthesized MOF samples.

Sample	Ba [wt.%]	Cu [wt.%]	Pore Volume > 16 Å (BJH) [cm³/g]	Pore Volume 4 - 20 Å (HK) [cm³/g]
Cu-BTC	-	26.2	0.1359	0.417761
Ba/Cu-BTC (CH_3COO^-)	15.2	22.5	0.1398	0.120883
Ba/Cu-BTC (NO_3^-)	7.5	27.2	0.1997	0.155452
Ba/Cu-BTC (Cl^-)	14.9	26.3	0.1157	0.035272

The changes in sample mass and the evolution of H_2O and CO_2 during temperature increase from 273 and 973K of Cu-BTC and Ba/Cu-BTC(Cl^-) are compared in Fig. 2.7. For Cu-BTC, desorption of water (m/z = 18) was observed in the temperature range 323 - 523K with two maxima at 373 and 483K. The mass loss due to the desorption of water was 6.0wt.%, which according to the 3mol water present in the Cu-BTC. The release of CO_2 (m/z = 44) indicated that the decarboxylation of the organic linker started at 593K. The decomposition of the organic linker led to a mass decrease of 44wt.%, which is in line with the loss of the CO_2 groups from benzene-1,3,5-tricarboxylate.

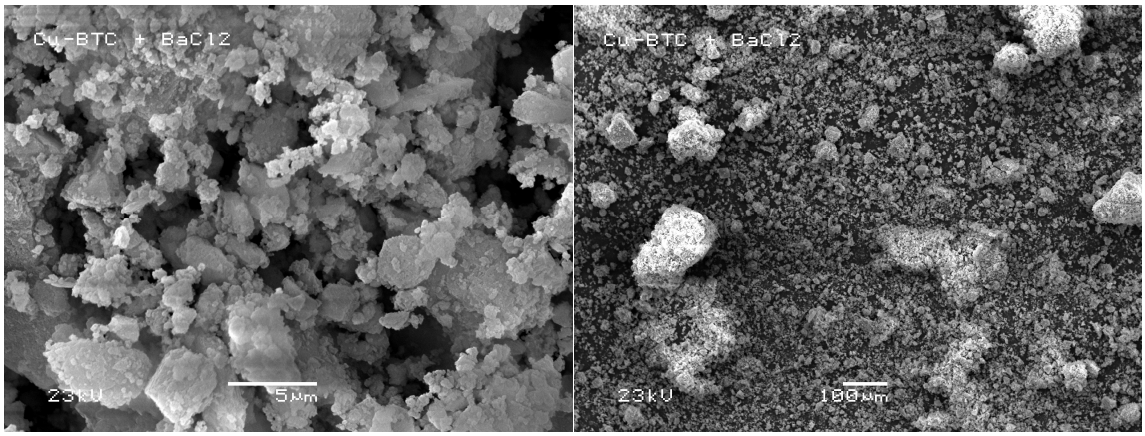

Fig. 2.6 : Scanning electron micrographs of Ba/Cu-BTC (Cl^-).

The benzene rings seem to be retained in the sample. For the $BaCl_2$ impregnated Cu-BTC sample the release of H_2O was more pronounced at the maximum around 488K (weight decrease 10wt.%), which is attributed to the removal of H_2O retained in higher concentrations by $BaCl_2$.The simultaneous appearance of the maximum for the CO_2 release and for the decrease in the weight indicates that the thermal stability of the Ba-impregnated samples was not affected by the impregnation, i.e., that decarboxylation occurred at the same temperature than with the parent sample.

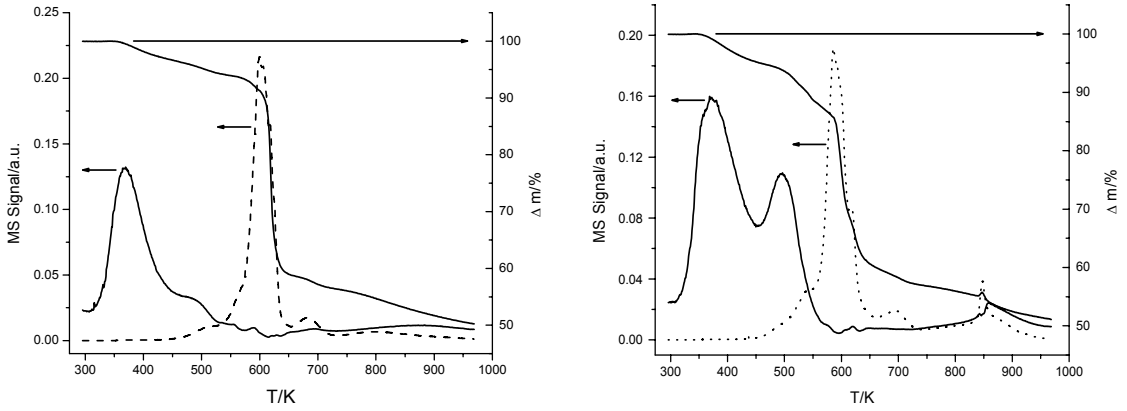

(A) (B)

Fig. 2.7 : TGA profiles of Cu-BTC (A) and Ba/Cu-BTC (Cl^-) (B) (295 – 973K, full line m/z = 18, dashed line m/z = 44).

2.3.2 State of copper cations

The XANES and the first derivative of the Cu K-edge region of different copper containing references are shown in Fig. 2.8. The oxidation state of copper can be determined from the position of the absorption edge (see Fig. 2.8), with a shift to higher energies indicating increasing oxidation state [24-26]. For Cu^{+} (8980eV) and Cu^{2+}species (square-planar symmetry, 8984eV) the edge positions differ by approx. 4eV and Cu^{2+} exhibits a further feature at 8976eV. The edge position and the appearance of specific transitions allow the differentiation between chemical state and the local symmetry of the copper species for each compound [27-30]. The absorption edge results from the dipole-allowed 1s $\rightarrow$ 4p transition. While Cu^{0} and Cu^{+} do not have a gap in the 3d orbital, Cu^{2+} compounds are in a d^{9} configuration, thus showing a weak, but characteristic pre-edge peak at 8976 – 8979eV (quadrupole-allowed 1s $\rightarrow$ 3d transition with a shoulder at 8986 - 8989eV due to the 1s $\rightarrow$ 4p transition). The 8984eV (post-edge) feature of Cu^{+} complexes has been assigned empirically to a dipole-allowed Cu 1s $\rightarrow$ 4s transition [31-34]. Cu^{2+} species (e.g. CuO) exhibit a weak pre-edge peak around 8985eV, which results from the dipole-forbidden 1s $\rightarrow$ 3d transition. Cu^{+} compounds (e.g. Cu_2O and CuCl) show an intense peak at 8980eV, which is attributed to the dipole-allowed 1s $\rightarrow$ 4p transition.

XANES and the first derivative of the Cu-K edge region for Cu-BTC and Ba salt impregnated Cu-BTC are shown in Fig. 2.9. For Cu-BTC and the series of Ba^{2+} impregnated samples an edge position of 8980eV (main maximum in the first derivative) was observed, which is characteristic for Cu^{+}. Additionally, for all compounds a second maximum in the derivative spectrum was observed at 8993eV as well as a shoulder at 8985eV. These features are assigned in all samples to Cu^{2+} in a square-planar symmetry. The differences in the area under the peaks at 8980 and 8993eV in the first derivative of the XANES between the Ba/Cu-BTC(Cl^{-}) and the other samples indicate a higher fraction of Cu^{2+} (in square-plane coordination) to be present in the $BaCl_2$ containing sample.

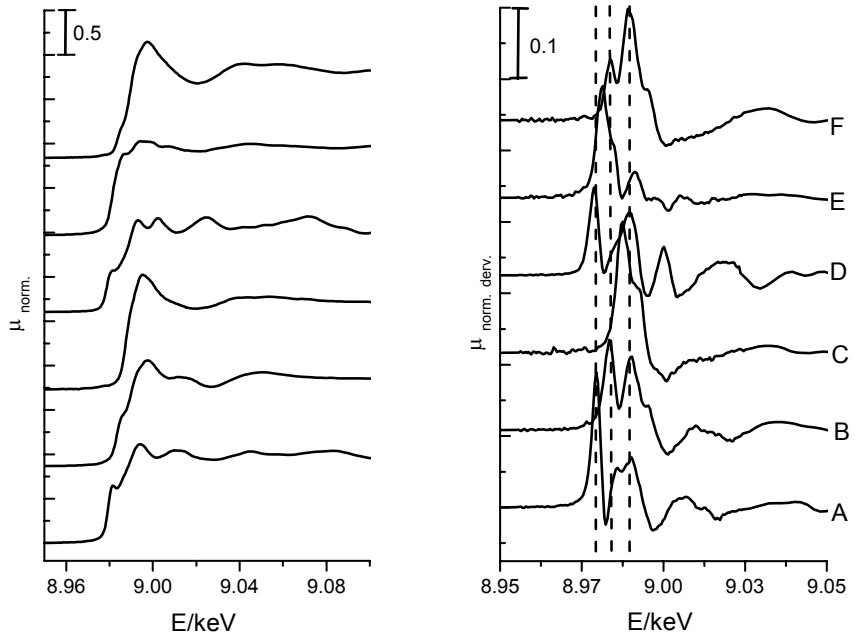

Fig. 2.8. : Cu K-edge XANES of reference materials and their first derivatives: Cu_2O (A), CuO (B), $CuSO_4$ (C), Cu (D), CuCl (E), $Cu(CH_3COO)_2$ (F)

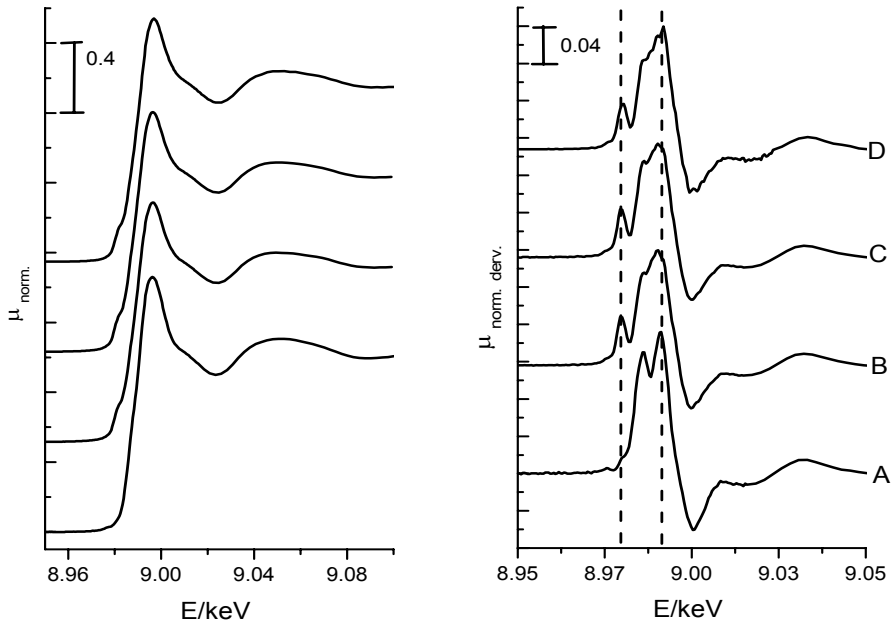

Fig. 2.9 : Cu K-edge XANES of the Ba/Cu-BTC samples and their first derivatives: Cu-BTC with $BaCl_2$ (A) Cu-BTC with $Ba(CH_3COO)_2$, (B) Cu-BTC with $Ba(NO_3)_2$, (C) Parent material (D).

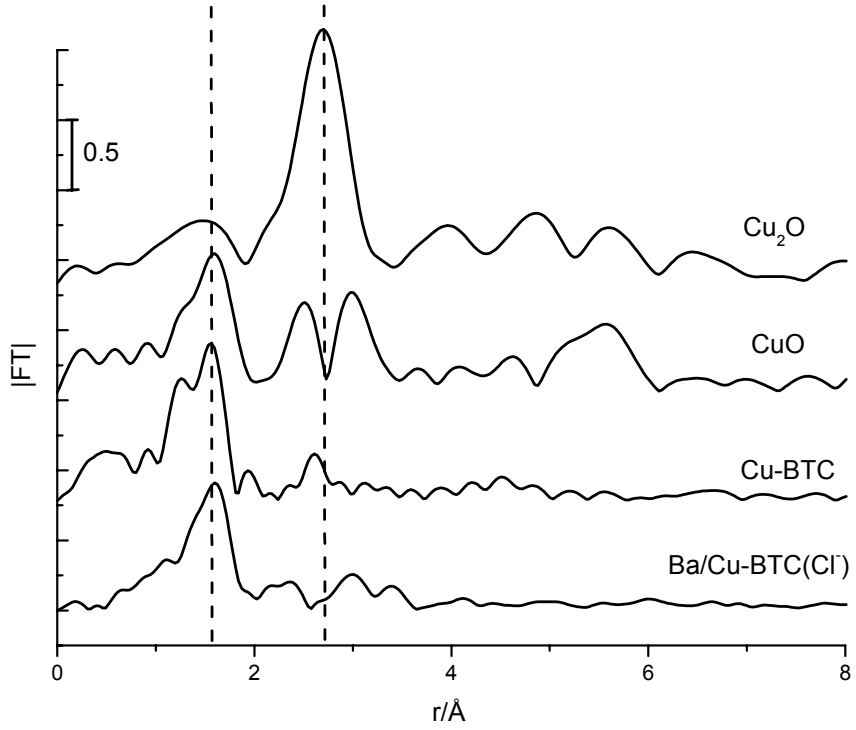

Fig. 2.10 : Fourier Transform of the EXAFS for Ba/Cu-BTC(Cl^-) and reference samples (Cu K-edge).

The radial distribution functions (obtained from the Fourier transform of the EXAFS oscillations) of Cu-BTC and Ba/Cu-BTC(Cl^-) are compared to those of CuO and Cu_2O in Fig. 2.10. The structural properties (obtained by the FEFF fitting) are summarized in Tab. 2.2. Both Cu-BTC samples showed one Cu-O contribution with the distance for r_{Cu-O} = 1.91 and 1.94Å for Cu-BTC and Ba/Cu-BTC(Cl^-), respectively. As synthesis has led to a nearly 100% yield based on the material balance, we conclude that the Cu-O distance in the carboxylates is identical with the distance in CuO. The distance between Cu-Cu in both samples was 2.67Å, with 0.97 Cu neighbors, in the Cu-BTC and 0.6 in the Ba/Cu-BTC(Cl^-), respectively. The presence of one Cu neighbor in the Cu-BTC sample is in line with the structure of the Cu-BTC structure. Therefore, we conclude that the average number of Cu-Cu neighbors in the sample impregnated with barium chloride indicates a partial destruction of the Cu-BTC structure. Thus, the characterization data indicate that impregnation with $BaCl_2$ affects the local structure of a large fraction of the Cu cations in the metal organic framework.

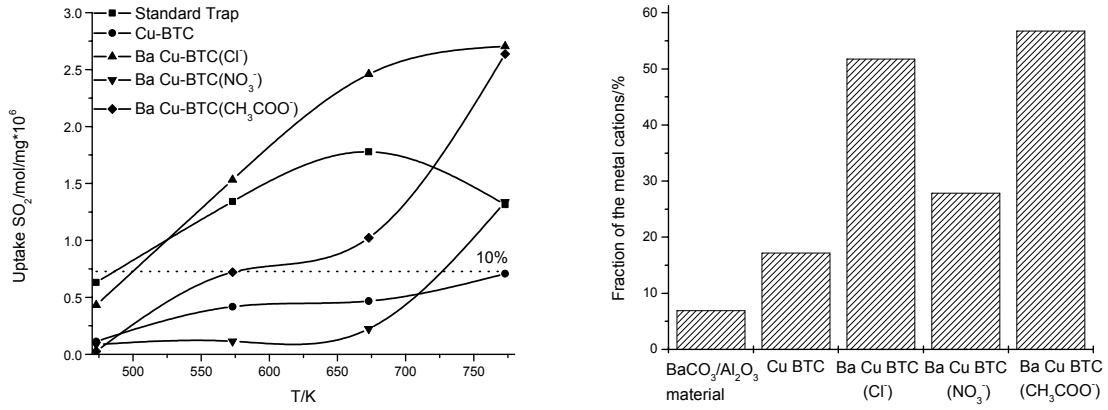

(A) (B)

Fig. 2.11 : Uptake capacity (A) and the fraction (B) of the prepared samples.

2.3.3 Storage capacity for SO_2

The SO_2 uptake capacities of the parent Cu-BTC material and the Ba-salt impregnated derivatives were explored between 473 and 773K and are compared to a conventional $BaCO_3/Al_2O_3$/Pt based material (see Fig. 2.11A).

For Cu-BTC the SO_2 uptake capacity increased with increasing the temperature from 473K to 573K. A further increase up to 673K induced only a minor SO_2 uptake. In total, a final storage capacity of $0.7*10^{-6}$ mol SO_2/mg are observed and was reached between 473K and 773K.

The materials impregnated with barium chloride and acetate showed an increasing uptake capacity during heating from 473K up to 573K, while the nitrate impregnated sample did not show a variation in the capacity compared to the parent material. By heating the samples up to 673K the uptake capacity for all samples increased. The most marked increase was observed for Cu-BTC impregnated with $BaCl_2$. From 673K to 773K the uptake increased further, with the strongest being found for the samples impregnated with barium nitrate and acetate. After this procedure the total SO_2 storage capacity of the different impregnated metal organic framework materials were similar for the samples impregnated with barium chloride and acetate, while for the nitrate impregnated sample only half of the capacity was observed.

Also the $BaCO_3/Al_2O_3$/Pt based material (as first generation storage reduction catalyst known to store SO_3) showed an increasing of the uptake

capacity during by heating up to 573 and 673K respectively. At further increasing temperatures (up to 773K) desorption of SO_2 was observed leading to the decrease of the SO_2 storage capacity.

At 473K, $BaCO_3/Al_2O_3$/Pt based material showed the highest uptake, followed by the metal organic framework material impregnated with $BaCl_2$. As the temperature increased to 573K and 673K the storage capacity increased for all samples, even though only slightly for the Cu-BTC and the nitrate impregnated sample. In the final increase to 773K the storage capacity for the $BaCO_3/Al_2O_3$/Pt based material decreased, while it increased for all MOF materials. Overall, the highest storage capacities over the entire temperature range were observed for the MOF materials impregnated with barium chloride and barium acetate.

Tab. 2.2 : Results from EXAFS analysis from the synthesized MOF samples (S_0^2=0.7).

Sample	Atoms	N	R [Å]	σ^2 [Å²]	E_0 shift [eV]
Cu-BTC	Cu-O	4.05	1.91	0.00720	-7.26
	Cu-Cu	0.97	2.67	0.01200	9.65
Ba/Cu-BTC(Cl^-)	Cu-O	4.21	1.94	0.00748	-8.01
	Cu-Cu	0.60	2.67	0.00958	-4.02

The fractions of metal cations contributing to the chemically binding of SO_2 in the presence of oxygen are compiled in Fig. 2.11B. The amount SO_2 necessary for converting all metal cations into sulfates is defined as 100%. The analysis of the concentrations of SO_2 bound and the concentration of Ba^{2+} and Cu^+/Cu^{2+} of the Ba/Cu-BTC samples shows that a significant fraction of the chelated Cu cations are converted into copper sulfates. Similarly, barium and aluminum sulfates are formed upon exposure of $BaCO_3/Al_2O_3$/Pt based material to $SO_2 + O_2$. The results suggest that the cations in the metal organic framework are better utilized than those of the $BaCO_3/Al_2O_3$/Pt based material.

The formation of the various sulfates has profound implications on the thermal stability of the loaded materials as Cu- and Al-sulfates are of lower thermal stability than $BaSO_4$. This variation in stability explains the decreased SO_x storage capacity of the $BaCO_3/Al_2O_3$/Pt based material when the temperature was

increased from 673K to 773K. In this temperature interval (surface) $Al_2(SO_4)_3$ is beginning to be instable and is decomposed to Al_2O_3 and SO_3. It is shown in Tab. 2.3 that the impregnation of the metal organic framework materials with Ba-salts leads to a higher SO_x storage capacity. The inclusion of the salt leads to the partial local destruction of the metal organic structure varying in extent with the anion used. Higher local destruction by salt impregnation is associated with higher uptake capacity at low temperature. The strongly increased SO_x uptake capacity above 673K is attributed to the gradual thermal degradation of the lattice and the resulting availability of Cu cations. XRD reveals that $CuSO_4$ and $BaSO_4$ species are formed increasing the concentration with storage temperature.

Tab. 2.3 : SO_2 uptake capacities of the prepared materials in [mol/mg*10^{-6}].

Sample	Uptake [mol/mg*10^{-6}]			
	473K	**573K**	**673K**	**773K**
$BaCO_3/Al_2O_3/Pt$	0.631	1.341	1.779	1.314
Cu-BTC	0.112	0.418	0.467	0.707
Ba/Cu-BTC (CH_3COO^-)	0.431	1.532	2.460	2.705
Ba/Cu-BTC (NO_3^-)	0.085	0.115	0.223	1.338
Ba/Cu-BTC (Cl^-)	0.026	0.721	1.023	2.637

2.4 Conclusions

Barium loaded materials impregnated with a metal function for SO_2 oxidation are excellent sorbents for SO_2 in oxygen rich atmosphere. The storage capacity of metal organic framework materials with Cu^{2+} as central cation and benzene-1,3,5-tricarboxylate(BTC) as linker subsequently impregnated with Ba using $BaCl_2$, $Ba(CH_3COO)_2$ and $Ba(NO_3)_2$ was competitive or better compared to the $BaCO_3/Al_2O_3/Pt$ based material. The deposition of the Ba salts leads to small micro-crystals of $Ba(CH_3COO)_2$ and $Ba(NO_3)_2$ in pores of the fully intact Cu-BTC together with a decrease in the pore volume. After impregnation of Cu-BTC with $BaCl_2$ the crystallinity of the metal organic framework decreases and Ba-chloride is highly dispersed in the material, therefore the high pore volume and the well defined structures of the Cu-BTC material offer as well defined and accessible support material.

The Cu-BTC decomposed around 573K, leading to a complete loss of the Cu-BTC structure. XANES indicates that for the Ba-chloride impregnated sample a significant fraction of copper was oxidized to Cu^{2+}. The other samples did not have a marked concentration of Cu^{2+} (i.e., similar to the parent Cu-BTC). Thus, we conclude that the dispersion of the Ba^{2+} species is the highest in the Ba/Cu-BTC(Cl^-) sample, that the local structure is destroyed for a significant portion of that material and that the accessibility of the Cu cations is drastically enhanced compared to other Ba/Cu-BTC samples. This reveal that the Cu-BTC framework act as a perfect support for the combination between highly dispersed barium (via impregnation with barium chloride) and a highly dispersed form of a oxidation component (partial destroyed metal organic framework).

The highest SO_2 uptake at lower temperatures (< 673K) was observed for Ba/Cu-BTC(Cl^-), while at 773K the uptake of the Ba/Cu-BTC(Cl^-) and Ba/Cu-BTC(CH_3COO^-) samples (both with the same Ba loading) were identical. The SO_2 uptake of all Ba/Cu-BTC samples exceeded the stoichiometric uptake capacity based on the Ba^{2+} concentration. It is concluded that a fraction of the SO_x is bound to Cu cations. Therefore, the high storage capacity of the Ba/Cu-BTC(Cl^-) material observed not only resulted from the high dispersion of the Ba species, but was also caused by the better accessibility of the Cu cations. At low temperatures the SO_x storage can be described as a physisorption process of SO_2 on Cu cations and the formation of Ba-sulfates, as Cu is still integrated into the metal-organic framework. At higher temperatures the metal organic framework is thermally decomposed, which leads to the formation of isolated Cu species that act as SO_x storage sites forming Cu-sulfates. Cu-BTC is a good host material which provides at low temperature a excellent support properties for the formation of highly dispersed barium, while at higher temperatures, additional storage sites due to the decomposition of the metal organic framework could be formed.

The work presented clearly indicates that impregnated metal organic framework materials are novel suitable components for irreversible SO_x storage, which can be incorporated into advanced non regenerable SO_x traps to enhance the SO_2 storage capacity especially in the low temperature region.

2.5 Acknowledgements

Funding from the European Union in the framework of project G3RD-CT2002 00793 is gratefully acknowledged. The author is also grateful to M. Neukamm for the AAS measurements, X. Hecht for the BET measurements and the staff of the beamline X1 and E4 at Hasylab DESY, Hamburg, Germany for their kind help and continuous support during the experiments.

2.6 References

[1] H. K. Chae, D. Y. Siberio-Perez, J. Kim, Y. Go, M. Eddaoudi, A. J. Matzger, M. O'Keeffe and O. M. Yaghi, *Nature,* 2004, **427**, 523.

[2] S. R. Batten, *Current Opinion in Solid State & Materials Science,* 2001, **5**, 107.

[3] M. Eddaoudi, J. Kim, N. Rosi, D. Vodak, J. Wachter, M. O'Keefe and O. M. Yaghi, *Science,* 2002, **295**, 469.

[4] G. Ferey, *Chemistry of Materials,* 2001, **13**, 3084.

[5] H. Li, M. Eddaoudi, T. L. Groy and O. M. Yaghi, *Journal of the American Chemical Society,* 1998, **120**, 8571.

[6] C. N. R. Rao, S. Natarajan and R. Vaidhyanathan, *Angewandte Chemie-International Edition,* 2004, **43**, 1466.

[7] B. L. Chen, M. Eddaoudi, S. T. Hyde, M. O'Keeffe and O. M. Yaghi, *Science,* 2001, **291**, 1021.

[8] S. S. Y. Chui, S. M. F. Lo, J. P. H. Charmant, A. G. Orpen and I. D. Williams, *Science,* 1999, **283**, 1148.

[9] M. Eddaoudi, H. L. Li and O. M. Yaghi, *Journal of the American Chemical Society,* 2000, **122**, 1391.

[10] H. Li, M. Eddaoudi, M. O'Keeffe and O. M. Yaghi, *Nature,* 1999, **402**, 276.

[11] H. L. Li, C. E. Davis, T. L. Groy, D. G. Kelley and O. M. Yaghi, *Journal of the American Chemical Society,* 1998, **120**, 2186.

[12] A. Vishnyakov, P. I. Ravikovitch, A. V. Neimark, M. Bulow and Q. M. Wang, *Nano Letters,* 2003, **3**, 713.

[13] N. L. Rosi, J. Eckert, M. Eddaoudi, D. T. Vodak, J. Kim, M. O'Keeffe and O. M. Yaghi, *Science,* 2003, **300**, 1127.

[14] M. Eddaoudi, D. B. Moler, H. L. Li, B. L. Chen, T. M. Reineke, M. O'Keeffe and O. M. Yaghi, *Accounts of Chemical Research,* 2001, **34**, 319.

[15] O. M. Yaghi, C. E. Davis, G. M. Li and H. L. Li, *Journal of the American Chemical Society,* 1997, **119**, 2861.

[16] Q. M. Wang, D. M. Shen, M. Bulow, M. L. Lau, S. G. Deng, F. R. Fitch, N. O. Lemcoff and J. Semanscin, *Microporous and Mesoporous Materials,* 2002, **55**, 217.

[17] Q. M. Wang, D. Shen, M. Bulow, M. L. Lau, F. R. Fitch and S. G. Deng, Metallo-organic polymers for gas seperation and purification, US 6491740 B1, **2002**.

[18] A. Amberntsson, M. Skoglundh, S. Ljungstrom and E. Fridell, *Journal of Catalysis,* 2003, **217**, 253.

[19] A. Amberntsson, M. Skoglundh, M. Jonsson and E. Fridell, *Catalysis Today,* 2002, **73**, 279.

[20] S. Brunauer, L. S. Deming, W. E. Deming and E. Teller, *Journal of the American Chemical Society,* 1940, **62**, 1723.

[21] G. Horvath and K. Kawazoe, *Journal of Chemical Engineering of Japan,* 1983, **16**, 470.

[22] A. L. Ankudinov and J. J. Rehr, *Physical Review B,* 2000, **62**, 2437.

[23] K. V. Klementev, *Journal of Physics D: Applied Physics,* 2001, **34**, 209.

[24] Y. J. Huang and H. P. Wang, *Journal of Physical Chemistry A,* 1999, **103**, 6514.

[25] Y. J. Huang, H. P. Wang and J. F. Lee, *Applied Catalysis B-Environmental,* 2003, **40**, 111.
[26] C. Lamberti, S. Bordiga, F. Bonino, C. Prestipino, G. Berlier, L. Capello, F. D'Acapito, F. Xamena and A. Zecchina, *Physical Chemistry Chemical Physics,* 2003, **5**, 4502.
[27] J. Y. Kim, J. A. Rodriguez, J. C. Hanson, A. I. Frenkel and P. L. Lee, *Journal of the American Chemical Society,* 2003, **125**, 10684.
[28] C. Prestipino, S. Bordiga, C. Lamberti, S. Vidotto, M. Garilli, B. Cremaschi, A. Marsella, G. Leofanti, P. Fisicaro, G. Spoto and A. Zecchina, *Journal of Physical Chemistry B,* 2003, **107**, 5022.
[29] L. S. Kau, D. J. Spirasolomon, J. E. Pennerhahn, K. O. Hodgson and E. I. Solomon, *Journal of the American Chemical Society,* 1987, **109**, 6433.
[30] F. Xamena, P. Fisicaro, G. Berlier, A. Zecchina, G. T. Palomino, C. Prestipino, S. Bordiga, E. Giamello and C. Lamberti, *Journal of Physical Chemistry B,* 2003, **107**, 7036.
[31] V. W. Hu, S. I. Chan and G. S. Brown, *Proc. Natl. Acad. Sci. U.S.A,* 1977, **74**, 3821.
[32] L. Powers, W. E. Blumberg, B. Chance, C. Barlow, J. S. Leight, Jr., J. C. Smith, T. Yonetani, S. Vik and J. Peisach, *J. Biochim. Biophys. Acta,* 1979, **546**, 520.
[33] J. M. Brown, L. Powers, B. Kincaid, J. A. Larrabee and T. G. Spiro, *Journal of the American Chemical Society,* 1980, **102**, 4210.
[34] W. Grunert, N. W. Hayes, R. W. Joyner, E. S. Shpiro, M. R. H. Siddiqui and G. N. Baeva, *Journal of Physical Chemistry,* 1994, **98**, 10832.

Chapter 3

Sulfate formation on SO_x trapping materials studied by Cu and S K-edge XAFS

Abstract:

The elementary steps during oxidative chemisorption of SO_2 by a novel composite material consisting of highly disordered benzene tri-carboxylate metal organic framework materials with Cu as central cation and $BaCl_2$ as a second component (Ba/Cu-BTC) and by a conventional $BaCO_3/Al_2O_3$/Pt based material were investigated. EXAFS analysis on the Cu K-edge in Ba/Cu-BTC indicates the opening of the majority of the Cu-Cu pairs present in the parent Cu-BTC. Compared to Cu-BTC the $BaCl_2$ loaded material hardly has micropores and higher disorder, but also better accessibility of the Cu^{2+} cations. This results from the partial destruction of the MOF structure by reaction between $BaCl_2$ and the Cu cations. The SO_2 uptake in oxidative atmosphere was higher for the Ba/Cu-BTC sample than for the $BaCO_3/Al_2O_3$/Pt based material. XRD showed that on Ba/Cu-BTC the formation of $BaSO_4$ and $CuSO_4$ occurs in parallel to the destruction of the crystalline structure. With $BaCO_3/Al_2O_3$/Pt the disappearance of carbonates was accompanied with the formation of Ba- and Al-sulfates. XANES at the S K-edge was used to determine the oxidation states of sulfur and to differentiate between the sulfate species formed. At low temperatures (473K) $BaSO_4$ was formed preferentially (53mol% $BaSO_4$, 47mol% $CuSO_4$), while at higher temperatures (and higher sulfate loading) $CuSO_4$ was the most abundant species (42mol% $BaSO_4$, 58mol% $CuSO_4$). In contrast, on the $BaCO_3/Al_2O_3$/Pt based material the relative concentration of the sulfate species (i.e., $BaSO_4$ and $Al_2(SO_4)_3$) as function of the temperature remained constant.

3.1 Introduction

The demand to lower emissions of automobiles requires the introduction of novel exhaust gas treatment technologies such as particulate traps and NO_x reduction catalysts with lean burn and diesel engines [1-6]. While diesel emission particulate filters reached market maturity, solutions for sufficient catalytic NO_x removal in diesel exhaust emissions are still in the development stage.

One of the most promising approaches for passenger cars is the NO_x storage-reduction (NO_x-SR) concept. During a (long) period in which the exhaust gas is rich in oxygen (lean fuel conditions), NO is catalytically oxidized to NO_2 and trapped (stored) in the form of nitrates. During short periods an excess of fuel is introduced (fuel rich conditions) and the stored nitrates are catalytically reduced to nitrogen [7-11].

The major hurdle for the commercialization of this technique is related to the presence of sulfur compounds in the fuel. During the long period in which the exhaust gas is rich in oxygen SO_3 is (catalytically) formed and subsequently trapped on the basic oxide materials leading to the formation of sulfates. This reduces the storage capacity for NO_x and the partial regenerability leads to an enrichment of the sulfates on the storage material and to its permanent deactivation [10, 12-15].

In part, these drawbacks are related to the fact that surface sulfates formed initially migrate into the bulk of the storage material forming very stable sulfates. Even at higher temperatures than that typically achieved in normal operation the bulk sulfates are not reducible and, thus, complete blockage of the storage material occurs with time on stream. Under fuel rich conditions (reducing atmosphere) the additional formation of sulfides on Pt was observed by EXAFS, blocking the oxidation of NO [14]. Various experimental approaches on improving the sulfur tolerance of the complex materials effective in NO_x storage-reduction have been reported [16-18]. As the sulfur level of motor fuels will be reduced to 10ppm, a conceptually intriguing approach is to trap SO_x before it reaches the NSR material, while allowing NO_x to pass [19-21].

In that context, various SO_x trapping materials have been reported in the literature [19, 22]. These materials contain an oxidation component (e.g. a noble metal) to convert the SO_2 to SO_3 and a sulfur storage component (typically oxides

of alkaline and earth alkaline metals). A refractory support such as α-Al_2O_3, Ce_2O_3 and ZrO_2 is necessary to preserve the pore structure during the sulfation process.

The approach described here - based on metal organic frameworks - uses instead the gradual and irreversible destruction of the trapping material by forming hard-to-reduce sulfate components relatively large in crystal size. These new materials consist of three-dimensionally linked metal-organic framework materials forming void structures with very high pore volumes of up to 91.1% of the crystal volume. Copperbenzene-1,3,5-tricarboxylate (Cu-BTC) is an example as already described in Chapter 2. The rigid character of the linker, e.g., carboxylates, leads to three-dimensional structures. Due to the high pore volume these materials are ideal candidates for supporting a second phase inside the pores. Thus, a storage component can be combined with the oxidation function of the metal in the framework. During the sulfate storing process the material is gradually destroyed leading to a difficult to reduce (and hence inert) substance.

In the present work, the formation of sulfates on this novel and on conventional SO_x trapping materials is qualitatively and quantitatively described. The chemical nature and location of the sulfur species are characterized by X-ray diffraction and X-ray absorption spectroscopy at the S- and Cu K-edges.

3.2 Experimental

3.2.1 Material

Cu-BTC materials were prepared as described in detail in chapter 2. Benzene-1,3,5-tricarboxylic acid was dissolved in ethanol and mixed with a solution of cupric nitrate hydrate $Cu(NO_3)_2$ $3H_2O$ in water. After stirring at ambient temperature for 30min the material was transferred into a 120cm^3 PTFE-lined stainless steel autoclave and heated to 383K under hydrothermal conditions. The reaction vessel was cooled to ambient temperature and the blue crystals of Cu-BTC were isolated by filtration and washed with water.

For impregnation, $BaCl_2 \cdot 2H_2O$ (0.81g, 0.003mol, Merck) was dissolved in 60ml alcohol/water mixture (1:1) and 2g of Cu-BTC (dried at 435K for 4h) was added to the solution. The mixture was stirred for 22.5h at ambient temperature. The solvent was removed under reduced pressure and the material was finally dried at 383K. For comparison, a model catalyst containing 2wt.% Pt (oxidation/reduction

component) and 10wt.% $BaO/BaCO_3$ (SO_x storage component) on an Al_2O_3 support was used.

3.2.2 Physicochemical characterization

The structure of the synthesized and modified materials was analyzed by X-ray diffraction using a *Philips X'Pert Pro System* ($CuK_{\alpha 1}$-radiation, 0.154056nm) operating at 40kV / 40mA. The measurements were performed in a glass capillary (ø = 0.5mm) with a scan rate of 0.05 /min from 5° to 80° 2θ. The chemical composition of materials synthesized was determined by atomic absorption spectroscopy (AAS) using a *UNICAM 939 AA-Spectrometer*.

X-ray absorption spectra were recorded at the ANKA-XAS Beamline on the Angstroemquelle Karlsruhe (ANKA). The storage ring was operated at 2.5GeV with an electron current between 100 and 200mA. A double-crystal monochromator equipped with Si (111) crystals was used for the experiments at the S K-edge (2480eV). Contributions of higher order reflections on the monochromator crystals were minimized by detuning the second crystal to 60% of the maximum intensity. For the experiments at the S K-edge (2480eV) the (monochromatic) flux rate on the sample was about $2 \cdot 10^{11}$ photons/s. Harmonic rejection was provided by a grazing incidence pre-mirror which acted as a high energy filter. All measurements were performed in transmission mode using ionization chambers (filled with 60mbar air) in front of and behind the sample. For energy calibration, the maximum of the first resonance ("white line") in the spectrum of $ZnSO_4$ was set to an energy of 2481.4eV. The samples were pressed on Kapton tape and the X-ray absorption spectra were measured with step widths of 1eV in the pre-edge region between 2447 and 2464eV, 0.2eV between 2464 and 2482eV, and 0.4eV between 2482 and 2609eV. For the removal of scattering contributions and for normalizing the spectra to the amount of material exposed to the X-ray beam a linear background was fitted to the pre-edge region (2460 – 2473eV) and the post-edge region (2506 – 2535eV) using the software Sixpack V0.5 [23]. $BaSO_4$, $CuSO_4$ and $Al_2(SO_4)_3 \cdot 18H_2O$ (Merck analytical grade) and various mixtures were measured as references to determine the relative contributions of these compounds in the materials exposed to SO_x by least square fitting of the XANES with the spectra of the individual reference compounds.

For X-ray absorption spectra on the Cu K-edge the samples were pressed into self supported wafers with a total absorption of 2.5. X-ray absorption spectra were measured at using a Si (111) monochromator. The contributions of higher order reflections were excluded by detuning the second crystal of the monochromator to 60% of the maximum intensity. The spectrum of a Cu foil was recorded simultaneously between the second and a third ionization chamber to calibrate the energy of the monochromator. X-ray absorption spectra were recorded after cooling the samples to liquid nitrogen temperature. For the analysis of the EXAFS the oscillations were extracted from the background using a combination of a first and second order polynomial function and, after weighting with k^2, the oscillations were Fourier transformed in the range between 2.4 - 16$Å^{-1}$. The local environment of the copper atoms was determined from the analysis of the EXAFS in k-space with the program WinXas V3.1 [24] using phase-shift and amplitude functions for Cu-O and Cu-Cu calculated with FEFF (Version 8.10) assuming multiple scattering processes. The values for S^2_0, were determined by fitting the first shell of Cu-oxide and kept constant during the refinement of the inter atomic distances (r), the relative mean square displacements (σ^2) of the bond length of the scattering paths (Debye–Waller factor) and the coordination numbers (CN).

3.2.3 Uptake measurements

The SO_x uptake was determined in a tubular reactor system equipped with a fluorescence detector (Model 43C *Fa.* Thermo Environmental Instruments) to monitor the SO_2 concentration at the reactor outlet. As the detector only monitors SO_2 a converter for SO_3 to SO_2 (using a Pt/Al_2O_3 catalyst operating at 1223K) was placed behind the reactor. For the SO_2 uptake experiments 50mg of the storage material (particle size 0.3 – 0.6mm) were diluted with 100mg SiC (particle size < 0.3mm) leading to a total amount of 150mg and exposed to a flow of 50ppm SO_2 and 6% O_2 in He at a flow rate of 200ml/min. After heating the materials at 473K with 10K/min in Helium the SO_x uptake was followed at 473K, 573K, 673K and 773K.

3.3 Results

3.3.1 Composition, crystal structure and porosity of the materials

The compositions and pore volumes of the Cu-BTC and Ba/Cu-BTC samples are compiled in Tab. 3.1. Both materials contain 26 wt.% copper, and the Ba/Cu-BTC sample additional 14.9 wt.% barium impregnated in the form of $BaCl_2$. The pore volume above a pore diameter of 1.6nm decreased only slightly after impregnation, while that between 0.4 – 2.0nm was reduced to less than 10% of the original value (0.41cm³/g in Cu-BTC to 0.03cm³/g in Ba/Cu-BTC). Assuming a density of 3.9cm³/g for $BaCl_2$ the corresponding volume of the $BaCl_2$ phase present in the sample is around 0.89cm³, which exceeds the amount necessary to fill the micropores of Cu-BTC. Thus, around 50% of the barium chloride must be present in any case outside the micropores.

Tab. 3.1 : AAS and N_2 physisorption results of synthesized MOF samples.

Sample	Ba [wt.%]	Cu [wt.%]	Pore Volume > 16 Å (BJH) [cm³/g]	Pore Volume 4 - 20 Å (HK) [cm³/g]
Cu-BTC	-	26.2	0.1359	0.417761
Ba/Cu-BTC	14.9	26.3	0.1157	0.035272

The X-ray diffractogram (XRD) simulated for the Cu-BTC structure is depicted together with that measured with Cu-BTC and the Ba^{2+} impregnated Cu-BTC samples in Fig. 3.2. The XRD of the parent Cu-BTC agrees well with the diffractogram simulated from the crystal structure of Cu-BTC [25]. After impregnation of Cu-BTC with $BaCl_2$ a strong decrease in the intensity of the X-ray diffraction peaks assigned to the Cu-BTC structure was observed, however, the XRD pattern was still observable. This indicates that the regular 3 dimensional MOF structure is partially destroyed, which could result from the filling of the pores with $BaCl_2$ and the subsequent formation of Cu-Cl species. The XRD of the Ba^{2+} impregnated Cu-BTC sample exposed to 50ppm SO_2 + 6% O_2 at temperatures between 473 and 773K are shown in Fig. 3.2.

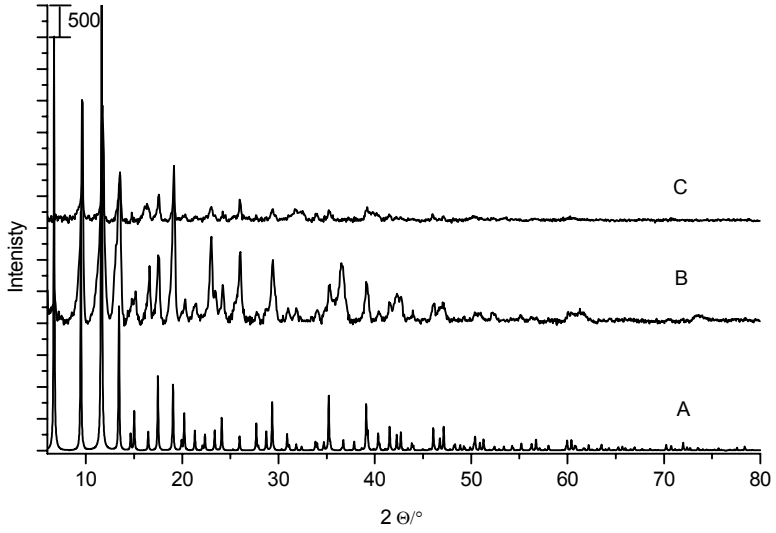

Fig. 3.1 : XRD of the simulated Cu-BTC (A), Cu-BTC (B) synthesized and Ba/Cu-BTC (C).

After exposure at 473K the material showed only X-ray diffraction peaks attributed to $BaSO_4$. At higher reaction temperatures the intensities of the diffraction peaks of $BaSO_4$ increased and starting from 573K additional peaks assigned to CuO appeared clearly and increased with increasing temperature. After exposure to 50ppm SO_2 + 6% O_2 at 673K diffraction peaks characteristic of $CuSO_4$ were observed. The XRD patterns of the fresh and treated $BaCO_3/Al_2O_3$/Pt based material during exposure to 50ppm SO_2 + 6% O_2 at temperatures up to 773K are shown in Fig. 3.3. With the fresh sample crystalline phases of $BaCO_3$ and Al_2O_3 were observed. With increasing temperature the X-ray diffraction peaks of the carbonate decreased and finally disappeared, while peaks for $BaSO_4$ and $Al_2(SO_4)_3$ appeared (see Fig. 3.3).

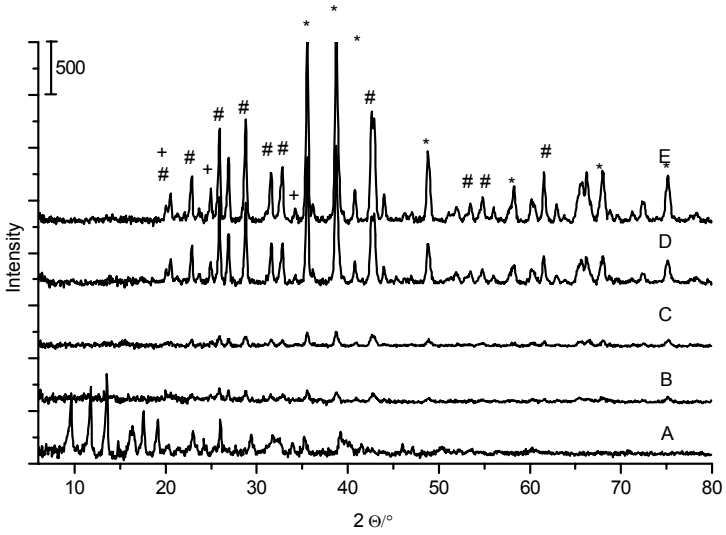

Fig. 3.2 : XRD of the fresh and SO_x/O_2 treated Ba/Cu-BTC sample: Fresh (A) 473K (B) 573K (C) 673K (D) 773K (E); # = $BaSO_4$; + = $CuSO_4$; * = CuO.

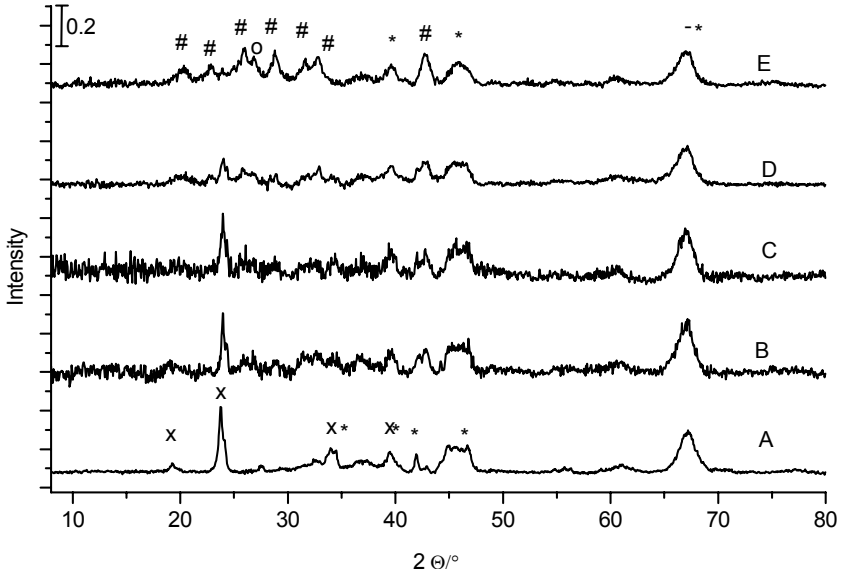

Fig. 3.3 : XRD of the fresh and treated $BaCO_3/Al_2O_3$/Pt based material: Fresh (A) 473K (B) 573K (C) 673K (C) 773K (E) # = $BaSO_4$; x = $BaCO_3$; * = Al_2O_3; o = $Al_2(SO_4)$; - = Pt.

3.3.2 SO_x Storage capacity

The SO_2 uptake of the Ba/Cu-BTC and the $BaCO_3/Al_2O_3$/Pt based material between 473 and 773K are compiled in Fig. 3.4 For Ba/Cu-BTC the SO_2 uptake capacity increased with increasing temperature and the maximum storage

capacity for Ba/Cu-BTC of $2.7 \cdot 10^{-6}$mol SO_2/mg was reached at 773K. With $BaCO_3/Al_2O_3$/Pt based material the uptake also increased with increasing temperature (see Fig. 3.4 (square symbols)). Contrary to Ba/Cu-BTC, the highest SO_2 uptake capacity of $BaCO_3/Al_2O_3$/Pt ($1.6 \cdot 10^{-6}$mol SO_2/mg) was reached at 673K. The further temperature increase up to 773K resulted in the desorption of SO_2 leading to a decrease of the SO_2 storage capacity. Assuming a complete utilization of the barium ions present the maximum SO_x uptake is $1.08 \cdot 10^{-6}$mol SO_2/mg for Ba/Cu-BTC and $7.3 \cdot 10^{-7}$mol SO_2/mg for the $BaCO_3/Al_2O_3$/Pt based material, respectively. This capacity was already reached at 573K indicating that at higher temperatures SO_3 is retained not only on sites associated with Ba^{2+} cations.

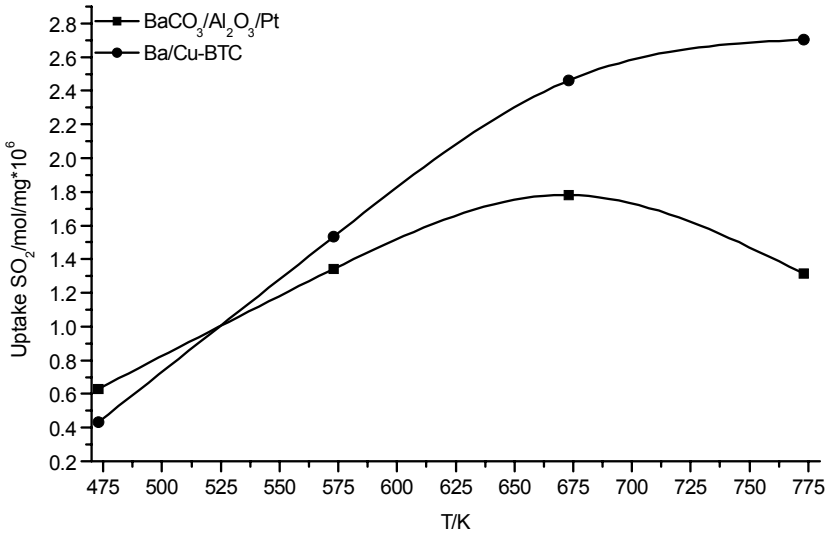

Fig. 3.4 : SO_x Uptake capacity of the prepared samples.

3.3.3 Chemical nature of sulfur in the storage materials

The X-ray absorption spectra at the S K-edge of $CuSO_4$, $BaSO_4$, $ZnSO_4$, $Fe_2(SO_4)_3 \cdot 5H_2O$, $Al_2(SO_4)_3 \cdot 18H_2O$, $MgSO_4 \cdot 7H_2O$ and the first derivative of the edge region are shown in Fig. 3.5 Unless otherwise noted the figures are focused on the main spectral features (-6 – 25eV relative to the edge position), however the normalization has been carried out on a wider energy range where only minor spectral changes were observed. The position of the strong peak (“white line”) in the spectra at 2481eV, assigned to the 1s → 3p transition, indicates the presence

of S^{+6} (SO_4^{2-}) species in all samples [26-28] .The maxima at 2481.4eV of $ZnSO_4$ was used as reference for the energy calibration.

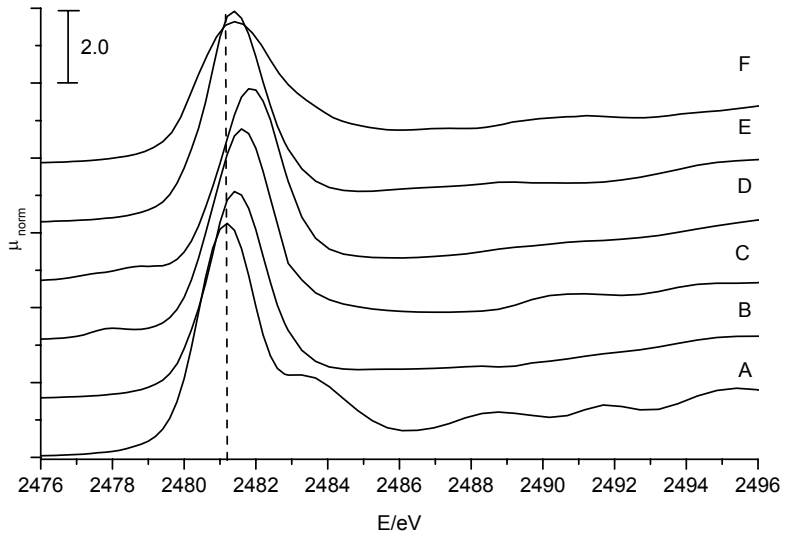

Fig. 3.5 : S K-edge spectra of different reference compounds and their first derivative: $BaSO_4$ (A) $Al_2(SO_4)_3 \cdot 18H_2O$ (B) $CuSO_4$ (C) $FeSO_4 \cdot 5H_2O$ (D) $MgSO_4 \cdot 7H_2O$ (E) $ZnSO_4$ (F).

For $MgSO_4 \cdot 12H_2O$ and $BaSO_4$ a small shift of the edge to higher energies and a more defined post edge fine structure, with a characteristic shoulder around 2484eV for $BaSO_4$, was observed. For copper sulfate and iron sulfate an additional pre-edge peak around 2478eV was observed. The fraction of $CuSO_4$ and $BaSO_4$ present in the Ba/Cu-BTC sample after exposure to SO_2/O_2 was determined by a least square fitting of the XANES in the region 2475 – 2506eV using the reference samples. The accuracy of this approach was evaluated by applying this method to the S K-edge XANES of physical mixtures of $CuSO_4$ and $BaSO_4$. An example for the XANES of a physical mixture of 82wt.% $CuSO_4$ and 18wt.% $BaSO_4$, the spectra obtained by least square fitting and the weighted reference spectra are shown in Fig. 3.6, which confirms that the XANES of physical mixtures of $BaSO_4$ and $CuSO_4$ can be perfectly fitted.

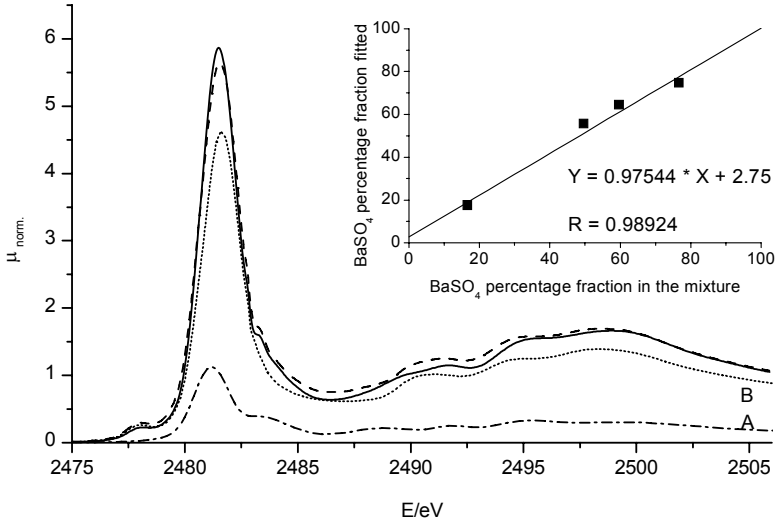

Fig. 3.6 : S K-edge spectra (full line) of a physical mixture of 82 wt.% $CuSO_4$ and 18 wt.% $BaSO_4$ and the fitted spectra (dashed line), with the weighted references: dotted line = $BaSO_4$ (A) dashed dotted = $CuSO_4$ (B).

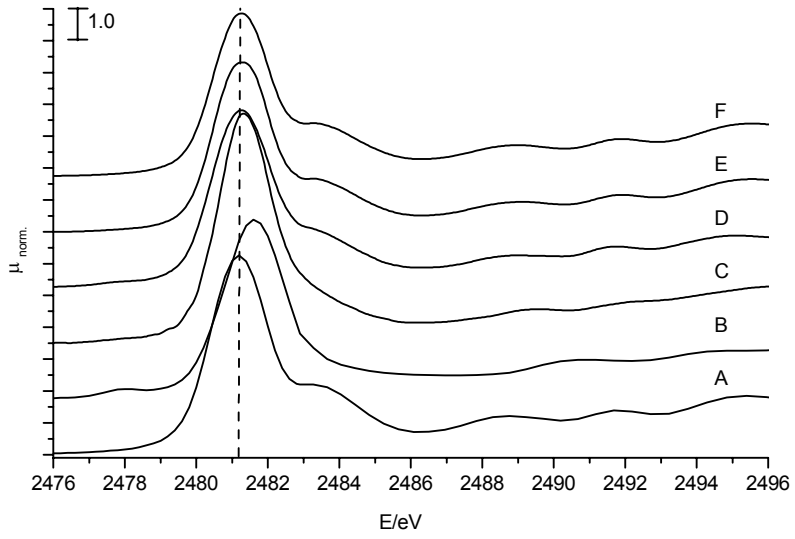

(A)

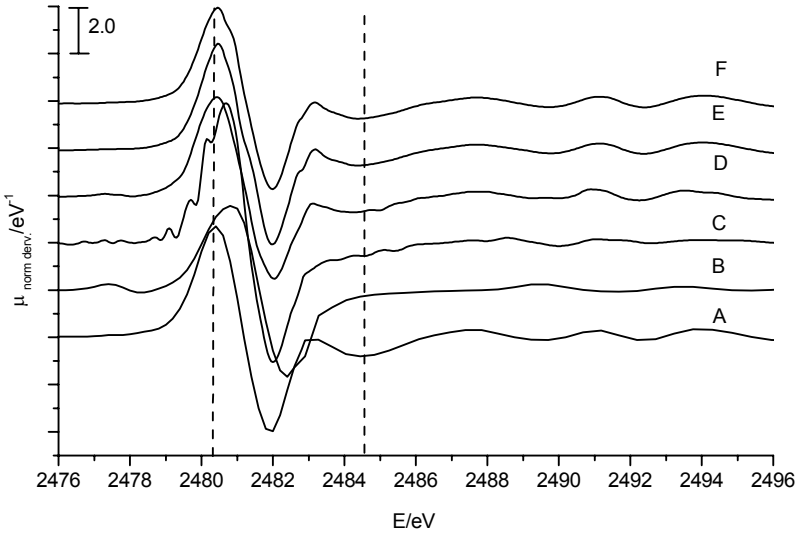

(B)

Fig. 3.7 : S K-edge spectra of Ba/Cu-BTC treated with 50ppm SO_2 + 6% O_2 at different temperatures and $BaSO_4$, $CuSO_4$ as reference samples (A) and their first derivative (B): $BaSO_4$ (A) $CuSO_4$ (B) 473K (C) 573K (D) 673K (E) 773K (F).

The concentration range evaluated was between 77wt.% and 15wt.% $BaSO_4$. The correlation between the composition and the results for the fraction of $BaSO_4$ present is shown in the inset in Fig. 3.6. The XANES and the first derivative at the S K-edge of the Ba impregnated Cu-BTC sample after exposure to 50ppm SO_2 + 6% O_2 at temperatures between 473 and 773K are shown in Fig. 3.7. Only a single peak in the spectra around 2481eV was observed at all temperatures studied. With increasing temperature a shoulder at 2484eV and a more defined fine structure in the post edge appeared. To determine the fraction of Cu and Ba sulfates present, the XANES was fitted with the corresponding reference compounds. As an example the XANES of the sample after treatment at 573K in combination with the weighted XANES of the reference compounds is given in Fig. 3.8.

The molar fraction of $BaSO_4$ and $CuSO_4$ present on the sample as function of the temperature used for the SO_2/O_2 treatment are shown in Tab. 3.2. At 473K about 58% of the sulfate was stored as $BaSO_4$ and this fraction gradually decreased to 43% at the final temperature of 773K. Using the molar fraction of $BaSO_4$ and $CuSO_4$ and the chemical compostion of the materials the utilization of the barium and copper sites for the formation of sulfates was estimated as function of the temperature. At 473K $BaSO_4$ dominates showing that only barium is utilized

to store sulfur (approximately 25% of the total capacity). At 573K, the fraction of barium used for sulfates storage increased up to 78%, while only 16% of copper was used. At 673K the maximum storage capacity of barium was reached and the further increase in the SO_x uptake at temperatures up to 773K resulted solely from the formation of $CuSO_4$.

Tab. 3.2 : Molar fraction and amount of metal used after treatment with 50ppm SO_2 + 6% O_2 at different temperatures, determined with least square fitting procedure.

T [K]	$BaSO_4$			$CuSO_4$		
	Mass Fraction	Mol Fraction	Metal used	Mass Fraction	Mol Fraction	Metal used
473	67	58	23	33	42	4
573	64	56	78	34	44	16
673	54	46	104	46	54	32
773	51	43	108	49	57	37

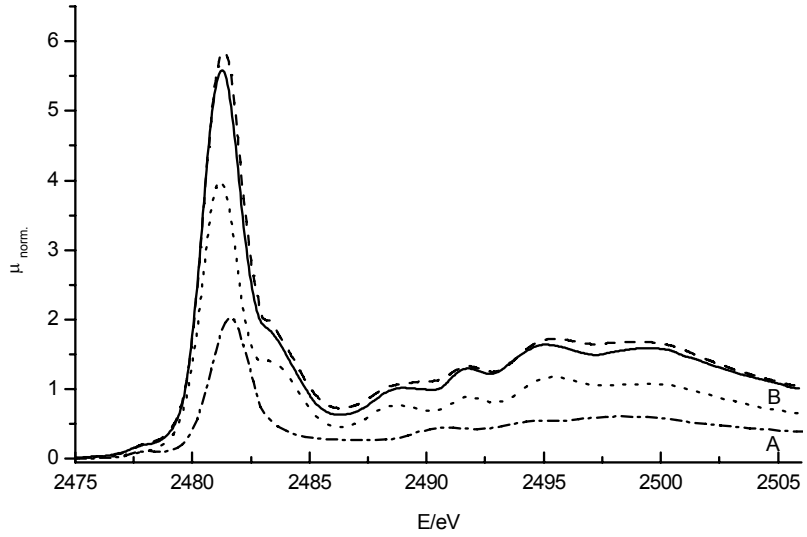

Fig. 3.8 : S K-edge spectra (full line) of the Ba/Cu-BTC treated with 50ppm SO_2 + 6% O_2 at 573K and the fitted spectra (dashed line) with the weighted references: dotted line = $BaSO_4$ (A) dashed dotted = $CuSO_4$ (B).

The sulfur XANES and the first derivative of the K-edge spectra of $Al_2(SO_4)_3 \cdot 18H_2O$ at temperatures between 273 and 773K are shown in Fig. 3.9. Between 273 and 473K the intensity of the peak above the absorption edge decreased. At 673 and 773K the fine structure became more pronounced and a small shift of the edge to higher energies (2482eV) was observed. The XANES

and the first derivative at the S K-edge region of the $BaCO_3/Al_2O_3/Pt$ based material after exposure to 50ppm SO_2 + 6% O_2 between 473 and 773K are shown in Fig. 3.10. Only a single peak in the spectra around 2481eV was observed at all temperatures studied. Post edge features with low intensity were also observed, which are similar to the post edge features present in $BaSO_4$. With increasing temperature the spectra hardly varied indicating only minor changes in the surrounding of the sulfur atoms in the sample.

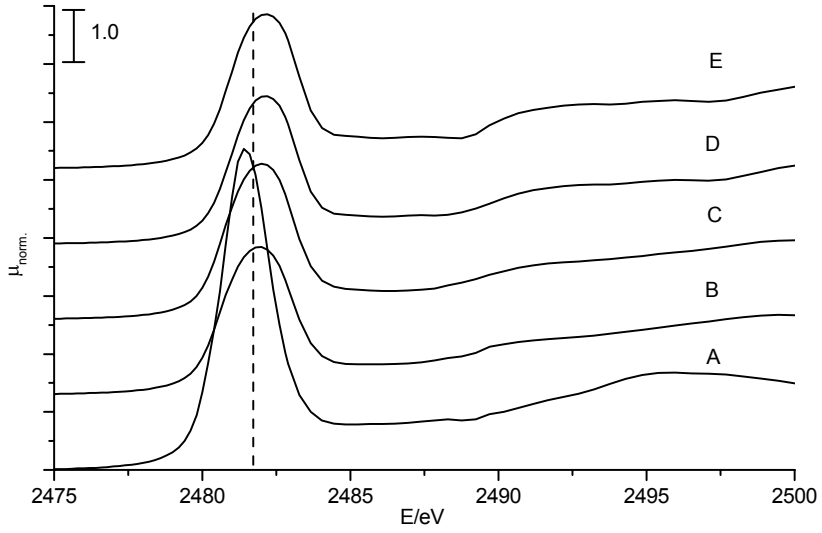

(A)

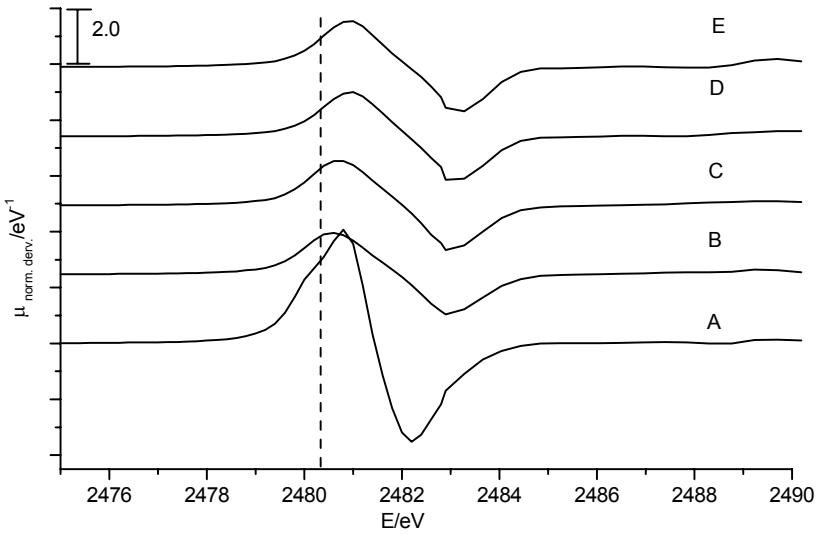

(B)

Fig. 3.9 : S K-edge spectra of $Al_2(SO_4)_3 \cdot 18H_2O$ at different temperatures and their first derivative: RT (A) 473K (B) 573K (C) 673K (D) 773K (E).

To differentiate between $Al_2(SO_4)_3$ and $BaSO_4$ in the $BaCO_3/Al_2O_3$/Pt based material, the same approach was applied as for Cu-BTC. Although the fitting of physical mixtures of $Al_2(SO_4)_3 \cdot 18H_2O$ and $BaSO_4$ at different temperature with the individual reference materials at this temperature was applied (see Fig. 3.12). However, the determination of the $Al_2(SO_4)_3$ and $BaSO_4$ contributions in the $BaCO_3/Al_2O_3$/Pt (see Fig. 3.11) was less accurate than for the other two cases (see Fig. 3.6 and Fig. 3.9).

3.3.4 Chemical state of copper cations in the storage materials

The XANES and the first derivative of the Cu K-edge region of different copper containing references and of the Ba/Cu-BTC material exposed to 50ppm SO_2 + 6% O_2 at temperatures between 473 and 773K are shown in Fig. 3.13. For the fresh Ba/Cu-BTC sample the edge position of 8983eV and a second maximum at 8990eV were observed (Fig. 3.13), which indicates the presence of Cu^{2+} in a square-planar symmetry. During treatment with SO_2/O_2 at 473K the edge shifted to 8985eV (+2eV relative to the edge of metallic Cu). After increasing the temperature to 573K the maximum of the first derivative at 8985eV increased relative to that at 8987eV. At 673 and 773K the edge position was again at 8983eV, while the energy of the second maximum did not change. The least square fitting of the XANES of the impregnated MOF sample at the Cu K-edge using reference spectra of $CuSO_4$ Cu_2O and CuO is shown in Fig. 3.14.

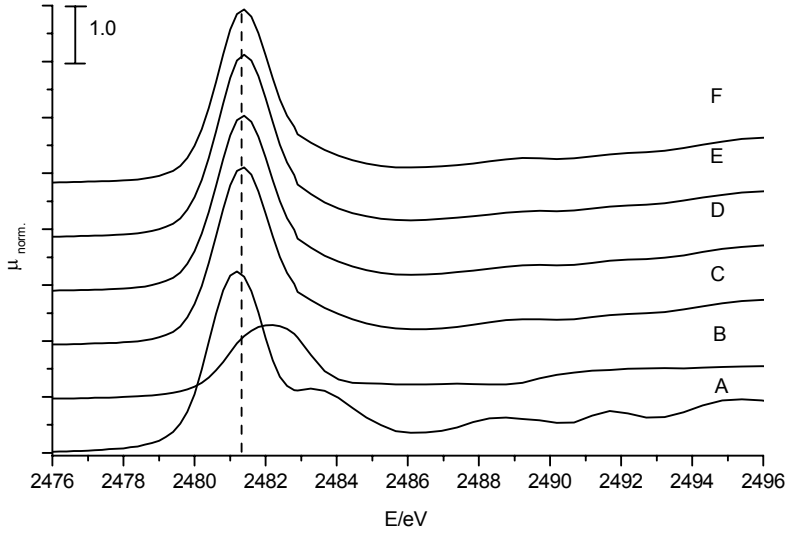

(A)

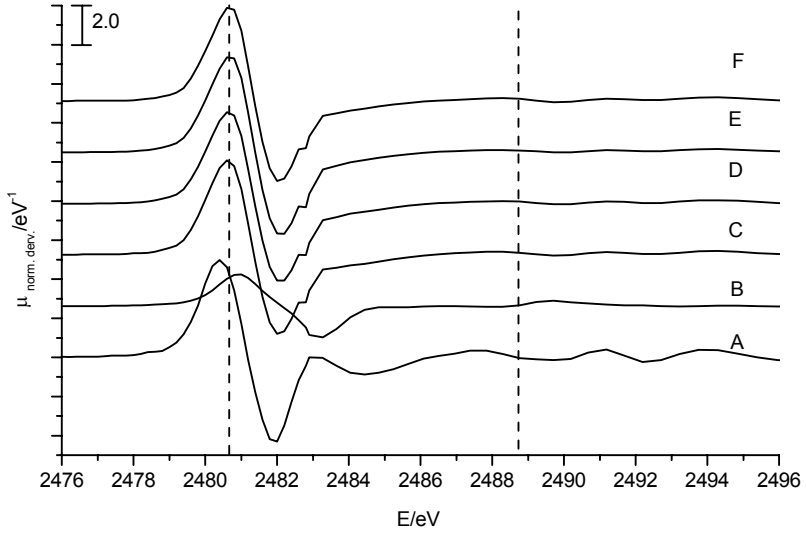

(B)

Fig. 3.10 : S K-edge spectra of the $BaCO_3/Al_2O_3$/Pt based material treated with 50ppm SO_2 + 6% O_2 at different temperatures and $BaSO_4$, $Al_2(SO_4)_3$ as reference samples and their first derivative: $BaSO_4$ (A) $Al_2(SO_4)_3$ (B) 473K (C) 573K (D) 673K (E) 773K (F).

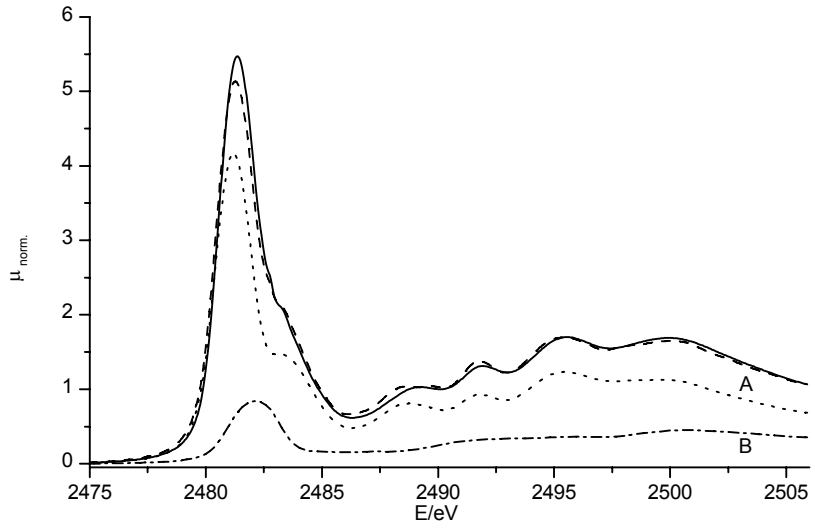

Fig. 3.11 : S K-edge spectra (full line) of a physical mixture of aluminum sulfate and barium sulfate at 673 K and the fitted spectra (dashed line) with the weighted references : dotted line = $BaSO_4$ (A) dashed dotted = $Al_2(SO_4)_3$ (B).

A perfect agreement between the measured spectra and the fit is observed. The fraction and the amount of copper sites used are summarized in Tab. 3.3. The value of 27wt.% copper sulfate is in a good agreement with the 32wt.% $CuSO_4$ determined from the XANES at the S K-edge. Note that the similarity between the

Cu K-edge spectra of the fresh Ba impregnated metal organic framework sample and $CuSO_4$ did not allow to determine the fraction of the different copper species at temperatures below 673K. The EXAFS oscillations and the radial distribution functions of Ba/Cu-BTC are compared to CuO in Fig. 3.15 and the detailed results of the analysis of the EXAFS are summarized in Tab. 3.4. At all temperatures similar numbers of neighbors for Cu-O (CN_{Cu-O}~ 4) were obtained at a distance of r_{Cu-O}=1.94Å. Note that the higher Debye-Waller factor for the Cu-O contributions in the sample after treatment at 473K (compared to the fresh sample) points to a distortion of the local environment of the Cu atoms in this sample.

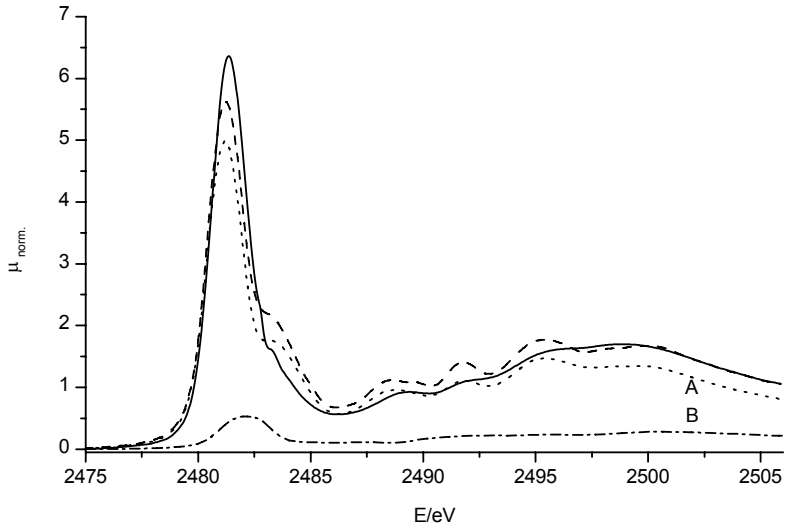

Fig. 3.12 : S K-edge spectra (full line) of the $BaCO_3/Al_2O_3$/Pt based material treated with 50ppm SO_2 + 6% O_2 at 773K and the fitted spectra (dashed line) with the weighted references ($BaSO_4$ (A), $Al_2(SO_4)_3$ (B)).

The absence of additional Cu-Cu and Cu-O neighbors at larger distances (~ 2.8Å in CuO) in the fresh sample and in the sample treated at 473K indicates that the Cu-O species are highly dispersed. In order to form Cu-O species, most of the Cu-Cu pairs of the Cu-BTC must have opened leading to the disappearance of the regular Cu-Cu distances. The EXAFS of the Cu-BTC materials and a detailed discussion of the structural properties after the impregnation with $BaCl_2$ are included in Chapter 2. Starting from 573K one additional Cu-O neighbor at r = 2.78 and Cu-Cu contributions at r = 2.90 and 3.07Å were identified. At 673 and 773K a similar number and distance of the Cu-O and Cu-Cu neighbors as in CuO was found.

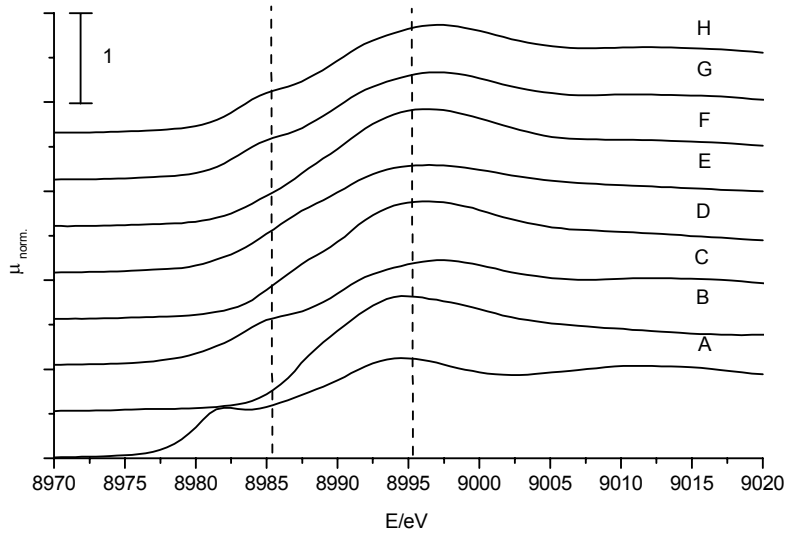

(A)

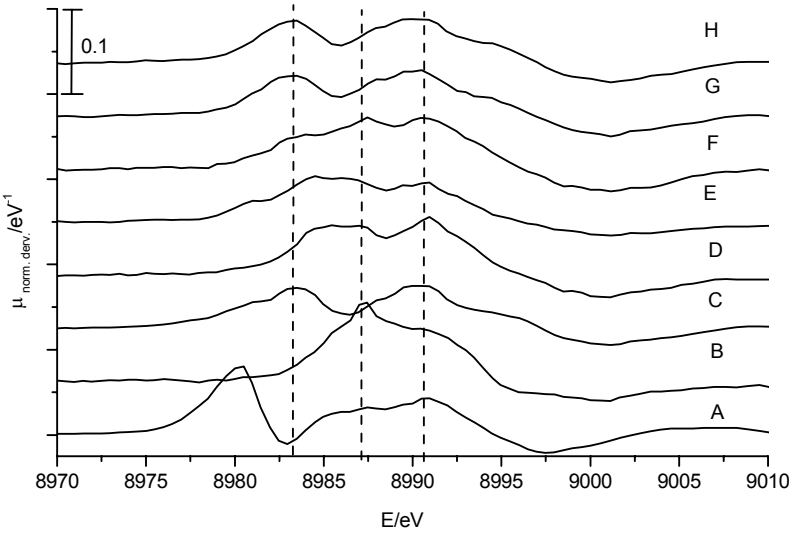

(B)

Fig. 3.13 : Cu K-edge spectra (A) and their first derivative (B) of different references and the Ba/Cu-BTC treated with 50ppm SO_2 + 6% O_2 at different temperatures: Cu_2O (A) $CuSO_4$ (B) CuO (C) fresh (D) 473K (E) 573K (F) 673K (G) 773K (H).

3.4 Discussion

3.4.1 Structural aspects of the materials in the presence and absence of SO_x

For Cu-BTC impregnated with $BaCl_2$ the intensity of all XRD reflections decreased compared to the starting material, however, the basic pattern of the Cu-BTC structure was observed. The smaller intensities of the reflections result from a significant reduction of the coherence length indicating a decrease in the crystallinity of the material. The disappearance of the Cu-Cu pair in the Cu K–edge EXAFS on the Ba impregnated sample indicates the opening of the organic framework and the formation of highly dispersed Cu-O species, in agreement with the decrease of the X-ray diffraction peaks. The absence of diffraction peaks assigned to $BaCl_2$ suggests that small Ba^{2+} particles exist. The decrease of the micropore volume in the impregnated sample indicates either the blocking of pores or the partial destruction of the MOF structure during impregnation. Thus, the characterization with XRD, N_2 physisorption reveals a partial destruction of the material after impregnation and the Cu K-edge EXAFS reveals the formation of highly dispersed Cu-O entities resulting from the reaction of the $BaCl_2$ deposited in the pores and the existence Cu cations located in the Cu-BTC structure. However the presence of highly dispersed Cu-Cl species could not be excluded. Note that the close distance between the $BaCl_2$ deposited via the impregnation in the pores and the Cu species present in the metal organic framework structure could facilitate this reaction at low temperature in the aqueous impregnation solution. This reaction caused on the one hand the partial destruction of the metal organic framework structure during impregnation with $BaCl_2$, but allowed on the other hand the formation of highly accessible Ba^{2+} and Cu^{2+} species, the active sites for SO_x storage. Note that the partial destruction of the Cu-BTC structure due to solvents containing chlorine were also observed by Schlichte *et al.* [29].

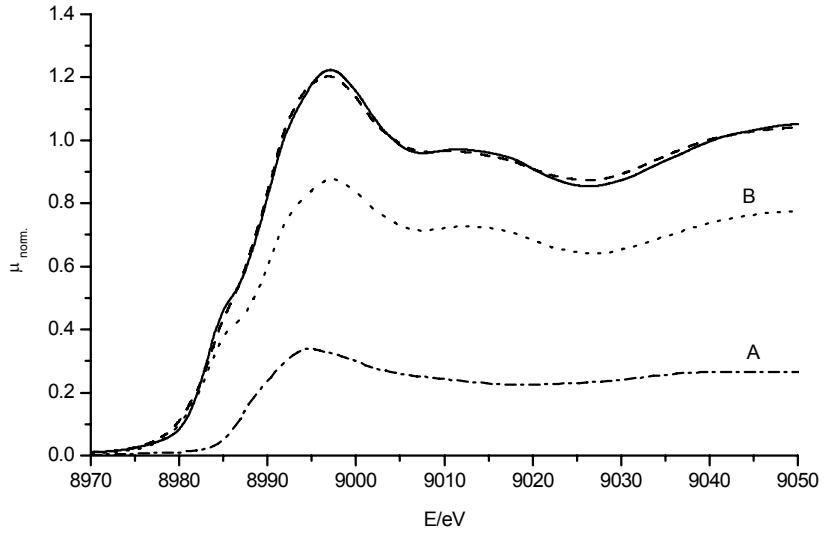

Fig. 3.14 : Cu K-edge spectra (full line) of the Ba/Cu-BTC treated with 50ppm SO_2 + 6% O_2 at 773K and the fitted spectra (dashed line) with the weighted references. $CuSO_4$ (A), CuO (B).

The significantly higher SO_x uptake capacities of both Ba containing materials at temperatures above 673K indicate that Ba, Cu and Al_2O_3 (from the support) contribute markedly to the SO_2 uptake capacity. However, the sulfates on Al_2O_3 have a lower thermal stability than $BaSO_4$, which leads to the decrease of the SO_x storage capacity of the $BaCO_3/Al_2O_3$/Pt based material above 673K. The decomposition of (surface) $Al_2(SO_4)_3$ at these temperatures leads to the evolution of SO_2 from sulfate saturated materials. The formation of bulk barium sulfate at 473K with the impregnated MOF material indicates that SO_x storage occurs in the bulk phase already at that low temperature. In contrast, for the $BaCO_3/Al_2O_3$/Pt based material the strong reflections of bulk sulfates were not observed, which indicates that SO_x is mainly stored on the surface of the material at 473K.

The formation of additional XRD peaks of $CuSO_4$ and CuO on the Ba/Cu-BTC material confirms the additional SO_x storage on the Cu^{2+} sites and the formation of CuO clusters. At 573K the weak XRD peaks for copper sulfate indicate the presence of low amounts of bulk copper sulfate, while at the same temperature Ba/Cu-BTC showed sharp peaks suggesting the formation of highly crystalline sulfate/oxide species. Thus, the weak XRD peaks of sulfates on $BaCO_3/Al_2O_3$/Pt indicate a generally low crystallinity of these sulfate species. However, the formation of bulk sulfate species on the barium and aluminum sites was observed at higher temperatures.

Tab. 3.3 : Percentage composition of the Ba/Cu-BTC obtained from least square fitting procedure.

T [K]	Percentage composition		
	CuO	**Cu_2O**	**$CuSO_4$**
673	73	0	27
773	74	0	26

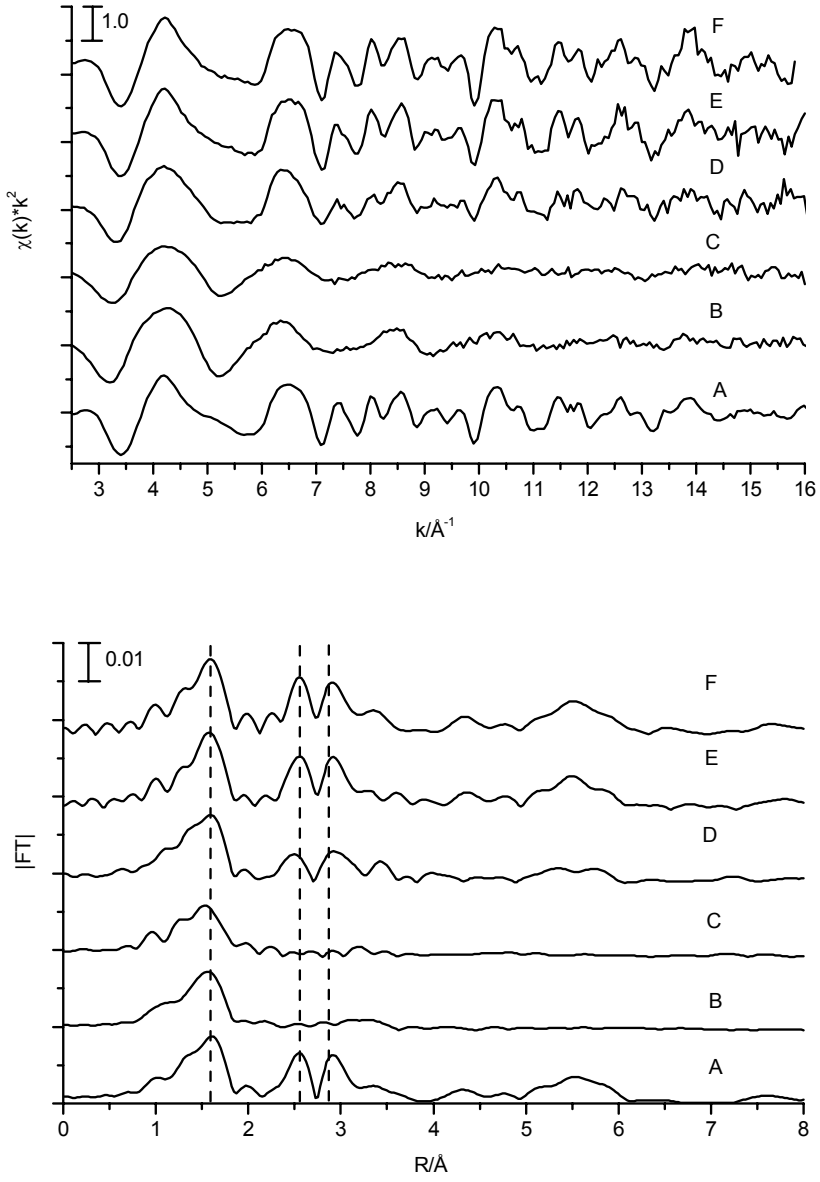

Fig. 3.15 : χ(k)*k2 and the Fourier Transform of the EXAFS for Ba/Cu-BTC and reference samples Cu K-edge: CuO (A) fresh(B) 473K(C) 573K (D) 673K (E) 773K (F).

3.4.2 Nature of the sulfates formed

The sharp peak in the absorption cross section above the S K-edge spectra is assigned to the 1s → 3p transition, while the additional maxima above the S K-edge are assigned to transitions from the 1s to unoccupied 3d like orbitals [30-32]. The differences in the positions of the "white line" and post edge structure between the sulfates of Ba and Mg result from the presence of structurally bound water molecules in $MgSO_4 \cdot 12H_2O$ and from the larger back-scattering of the photo-electrons from the heavier Ba atoms compared to Mg atoms [26].

The characteristic pre-edge peak at the S K-edge for copper sulfate and iron sulfate at 2478eV is assigned to the transition from the S 1s → ψ * state (HOMO formed from the overlap of the S 3p and the Me $3dx^2$-y^2 orbitals in the Me sulfate). If the Me 3d orbital is half filled the orbital contains, due to the localized nature, a significant contribution of the ligand 3p orbital. For the d-elements Fe^{3+} and Cu^{2+} ψ* is half filled, while for Ba^{2+} and Mg^{2+} they are completely filled. Moreover, the difference in the energy and intensity of the pre-edge peak for Fe^{3+} compared to Cu^{2+} could be due to multiplet effects, which influence the d-like final state of the ligand orbital [32, 33]. Consequently the hydbridization of the 3p orbitals of sulfur with the d orbital of the metal cation the dipole allowed 1s → 3p transition at K-edges of S provides a direct probe of the interaction between the sulfur species and the metal [34].

The single X-ray absorption at 2481.1eV, observed in the S K-edge spectra of all SO_x/O_2 treated samples, indicates that sulfur is present as sulfate (S^{+6}) and, moreover, the shoulder observed above the "white line" reveals the formation $BaSO_4$. The least square fitting of the S K-edge spectra allows differentiating between the contributions of barium and copper sulfate at temperatures of 473K and above. As the reflections of $CuSO_4$ were not detected by XRD, we would like to speculate that copper sulfate is present as (highly dispersed) surface species on this material. The higher fraction of barium sulfate present at temperatures below 673K and the almost complete utilization of the Ba^{2+} sites for the SO_x storage process confirm that barium act as main storage component in this temperature range, however, the formation of copper sulfate proves the additional contribution of copper. The preferred formation of barium sulfate results from the higher thermodynamic stability of $BaSO_4$ compared to $CuSO_4$. At low temperatures (up to 573K) copper acts as oxidation component for SO_2 and only at

temperatures above 673K, when the maximum SO_x storage capacity of Ba is reached, the formation of copper sulfate occurs. At the same temperature the thermal decomposition of the Cu-BTC structure starts (573K), which leads to the formation of highly dispersed and crystalline copper oxide species (observed in the Cu K-edge EXAFS and XRD) that further facilitates the SO_x storage.

On $BaCO_3/Al_2O_3$/Pt XRD shows the presence of $BaCO_3$ particles, however, a clear distinction between surface and bulk species is not possible. On $BaCO_3/Al_2O_3$/Pt only sulfates were detected after exposure to SO_2/O_2. The presence of a small shoulder around 2484eV and the pronounced post edge structure indicates that the main fraction of sulfur is trapped as $BaSO_4$. The minor changes in the XANES at the S K-edge of the samples exposed to SO_2/O_2 at different temperatures indicate that the local environment of the sulfates formed is independent of the temperature. While it was not possible to apply the least square fitting procedure using $BaSO_4$ or $BaSO_4/Al_2(SO_4)_3$ on the XANES of the $BaCO_3/Al_2O_3$/Pt based material XRD confirmed the presence of bulk barium sulfate. This is in agreement with the characteristic shoulder and post edge structure present in the S K–edge spectra of the SO_2/O_2 treated samples. Additionally, a fraction of an aluminum sulfate species is formed with $BaCO_3/Al_2O_3$/Pt. The presence of $Al_2(SO_4)_3$ has been identified by small reflections in the XRD, the complete utilization of Ba^{2+} ions above 573K. This species, thermally decomposing above 673K, is concluded to cause the formation of SO_2 during the uptake experiments at higher temperatures. Note that this temperature is markedly lower compared to the temperature necessary for the decomposition of bulk $Al_2(SO_4)_3$.

3.4.3 Nature of Cu in the BTC materials

The oxidation state of copper after exposure to SO_2/O_2 was determined from the position of the Cu K-edge. In general, a shift of the absorption edge to higher energies indicates a higher oxidation state [35-37]. For metallic Cu (8979eV), Cu^+ (8981eV) and Cu^{2+}species (square-planar symmetry, 8985eV) the edge positions differ by 6eV and 5eV, respectively. While for Cu^0 and Cu^+ the 3d orbital is completely occupied, Cu^{2+} compounds are in a d^9 configuration, thus showing a weak, but characteristic pre-edge peak at 8976 – 8979eV, which allows to identify the presence of Cu^{2+} species (e.g. CuO and $CuSO_4$). In addition, a weak pre-edge

peak around 8985eV, assigned to the dipole-forbidden 1s → 3d transition, is observed for Cu^{2+}, while Cu^{+} and Cu^{0} compounds (e.g. Cu_2O) show an intense peak at 8980eV attributed to the dipole-allowed 1s → 4p transition. Thus, the edge position and the appearance of specific transitions below the edge allow to differentiate between the chemical state and the local symmetry of the copper species [38-40].

The increasing intensity of the of the pre-edge peak and the formation of the shoulder around 9015eV with increasing temperature of the SO_2/O_2 treatment, indicates the formation of Cu^{2+} present as CuO and $CuSO_4$, while the absence of the peak around 8980eV confirms that Cu_2O was not formed. The increasing intensity of the maximum at 8990eV (white line) in the first derivate of the XANES with increasing temperature indicates the formation of $CuSO_4$ at elevated temperatures. Due to similar XANES of the fresh metal organic framework sample and $CuSO_4$ it was not possible to determine the fraction of the different copper species present in the sample below 673K by least square fitting of the XANES using the corresponding bulk materials as references. At higher temperatures, however, the relative fractions of CuO, Cu_2O and $CuSO_4$ present confirmed the high utilization of the Cu ions as additional SO_x storage sites in agreement with the S K-edge features. The formation of highly dispersed Cu-O species, observed in the EXAFS of the Ba/Cu-BTC materials exposed to SO_2/O_2 at 473K and at 573K, is speculated to be the cause for the higher SO_x uptake capacity of the Ba^{2+} impregnated metal organic framework materials compared to the $BaCO_3/Al_2O_3$/Pt based material. Note that highly dispersed Cu-O species have been reported enhance the oxidation capacity for SO_2 and generate additional sites for SO_3 sorption [41, 42]. At 673 and 773K, CuO with a similar structure as the bulk metal oxide forms and also acts as oxidation and additional SO_x storage component.

3.5 Conclusions

The formation of sulfates during trapping of SO_2 in $BaCl_2$ impregnated, highly disordered benzene tri-carboxylate metal organic framework materials with Cu as central cation (Ba/Cu-BTC) and on a $BaCO_3/Al_2O_3$/Pt based material was investigated by SO_x uptake measurements, X-ray diffraction and X-ray absorption spectroscopy. The analysis of the EXAFS on the Cu K-edge in Ba/Cu-BTC demonstrates the opening of the majority of the Cu-Cu pairs present in the parent

Cu-BTC and the sorption of N_2 indicates the disappearance of the micropores upon impregnation with $BaCl_2$. Although the $BaCl_2$ impregnated material has a lower micropore volume compared to Cu-BTC the formation of highly dispersed Cu species, resulting from the close interaction between the $BaCl_2$ deposited inside the pores and the Cu ions locates in the MOF structure. Partial mesoscopic opening of the structure cannot be excluded.

The SO_2 uptake in oxidative atmosphere was higher for the Ba/Cu-BTC sample than for $BaCO_3/Al_2O_3$/Pt at temperatures between 273 and 773K. For Ba/Cu-BTC XRD indicates the formation of sulfates and the total destruction of the crystalline structure while for $BaCO_3/Al_2O_3$/Pt the formation of Ba- and Al-sulfates is accompanied with the disappearance of carbonates. Considering all Ba^{2+} cations deposited the maximum SO_x uptake corresponds to the utilization of 35% of the Cu-ions and 6% of the alumina present in Ba/Cu-BTC and $BaCO_3/Al_2O_3$/Pt, respectively. Using XANES at the S K-edge the sulfates are qualitatively and quantitatively determined using least square fitting procedures. At low temperatures (473K) $BaSO_4$ is formed preferentially (53mol% $BaSO_4$, 47mol% $CuSO_4$), while at higher temperatures $CuSO_4$ is the most abundant species (42mol% $BaSO_4$, 58mol% $CuSO_4$). The maximum utilization of the barium sites is reached at 573K, at higher temperatures mainly copper sulfate formed. On the $BaCO_3/Al_2O_3$/Pt based material $BaSO_4$ and Al sulfate species could be identified by S K-edge spectroscopy. The work presented shows also that the combination of different X-ray absorption spectroscopic techniques leads to a better understanding of the storage process on the metal organic framework materials which are novel promising components for irreversible SO_x storage.

3.6 Acknowledgements

Funding from the European Union in the framework of project G3RD-CT2002 00793 is gratefully acknowledged. We acknowledge the ANKA Angstroemquelle Karlsruhe for the provision of beamtime. Specially we would like to thank Stefan Mangold for the adaptation of the ANKA-XAS beamline for the experiments at the S K-edge and for the assistance during the experiments. The authors are also grateful to M. Neukamm for the AAS measurements, X. Hecht for the BET measurements.

Tab. 3.4 : Feff Fit results from the Ba/Cu-BTC exposed to 50ppm SO_2 + 6% O_2 at various temperatures [K] and a metal oxide ($S0^2$=0.62).

		CuO structure	**CuO**	**fresh**	**473**	**573**	**673**	**773**
Cu-O	N_{Cu-O}	4	3.75	4.43	4.24	4.43	4.13	3.83
	r_{Cu-O} /Å	1.95	1.949	1.959	1.949	1.947	1.949	1.944
	σ^2/Å^2		0.0033	0.0047	0.0069	0.0036	0.0024	0.0018
	E_{shift}/eV		0.8104	-2.5494	-2.5074	-1.3050	0.4166	0.2523
Cu-O	N_{Cu-O}	2	1.50	0.67		1.59	1.62	2.30
	r_{Cu-O}/Å	2.78	2.77	2.68		2.78	2.78	2.77
	σ^2/Å^2		0.0045	0.0084		0.0500	0.0050	0.0029
	E_{shift}/eV		4.7476	4.6176		6.0000	4.2559	4.2492
Cu-Cu	N_{Cu-Cu}	4	4.38			3.03	4.13	2.80
	r_{Cu-Cu}/Å	2.9	2.91			2.90	2.90	2.89
	σ^2/Å^2		0.0040			0.00572	0.0030	0.0010
	E_{shift}/eV		2.6017			0.84675	4.4386	3.3651
Cu-Cu	N_{Cu-Cu}	4	3.44			2.00	5.11	4.12
	r_{Cu-Cu}/Å	3.08	3.07			3.08	3.08	3.07
	σ^2/Å^2		0.0021			0.0022	0.0042	0.0043
	E_{shift}/eV		6.0238			5.6508	5.0641	4.6590
Cu-Cu	N_{Cu-Cu}	2	2.31			1.02	0.88	1.53
	r_{Cu-Cu}/Å	3.17	3.17			3.17	3.18	3.18
	σ^2/Å^2		0.0012			0.0001	0.0001	0.0017
	E_{shift}/eV		4.5140			6.1083	7.5501	11.3255

3.7 References

[1] E. Jobson, *Topics in Catalysis,* 2004, **28**, 191.
[2] T. V. Johnson, *Society of Automotive Engineers, [Special Publication] SP,* 2004, **SP-1835**, 1.
[3] A. Fritz and V. Pitchon, *Applied Catalysis B-Environmental,* 1997, **13**, 1.
[4] P. L. T. Gabrielsson, *Topics in Catalysis,* 2004, **28**, 177.
[5] R. M. Heck and R. J. Farrauto, *Applied Catalysis A-General,* 2001, **221**, 443.
[6] A. Konig, W. Held and T. Richter, *Topics in Catalysis,* 2004, **28**, 99.
[7] E. Fridell, M. Skoglundh, B. Westerberg, S. Johansson and G. Smedler, *Journal of Catalysis,* 1999, **183**, 196.
[8] T. Kreuzer, E. S. Lox, D. Lindner and J. Leyrer, *Catalysis Today,* 1996, **29**, 17.
[9] N. Miyoshi, S. Matsumoto, K. Katoh, T. Tanaka, J. Harada, N. Takahashi, K. Yokota, M. Suguira and K. Kasahara, *Society of Automotive Engineers, [Special Publication] SP,* 1995, **950809**, 1361.
[10] N. Takahashi, H. Shinjoh, T. Iijima, T. Suzuki, K. Yamazaki, K. Yokota, H. Suzuki, N. Miyoshi, S. Matsumoto, T. Tanizawa, T. Tanaka, S. Tateishi and K. Kasahara, *Catalysis Today,* 1996, **27**, 63.
[11] M. Takeuchi and S. Matsumoto, *Topics in Catalysis,* 2004, **28**, 151.
[12] G. Corro, *Reaction Kinetics and Catalysis Letters,* 2002, **75**, 89.
[13] E. Fridell, H. Persson, L. Olsson, B. Westerberg, A. Amberntsson and M. Skoglundh, *Topics in Catalysis,* 2001, **16**, 133.
[14] C. Sedlmair, K. Seshan, A. Jentys and J. A. Lercher, *Journal of Catalysis,* 2003, **214**, 308.
[15] P. Engstrom, A. Amberntsson, M. Skoglundh, E. Fridell and G. Smedler, *Applied Catalysis B-Environmental,* 1999, **22**, L241.
[16] J. P. Breen, M. Marella, C. Pistarino and J. R. H. Ross, *Catalysis Letters,* 2002, **80**, 123.
[17] H. Mahzoul, L. Limousy, J. F. Brilhac and P. Gilot, *Journal of Analytical and Applied Pyrolysis,* 2000, **56**, 179.
[18] C. Sedlmair, K. Seshan, A. Jentys and J. A. Lercher, *Catalysis Today,* 2002, **75**, 413.
[19] A. N. Chigapov, A. A. Dubkov, B. P. Carberry, C. N. Montreuil, G. W. Graham, R. W. McCabe and W. Chun, SO_x trap for diesel and lean burn gasoline automotive applications, EP 1374978 A1 20040102, **2004**.
[20] L. Limousy, H. Mahzoul, J. F. Brilhac, P. Gilot, F. Garin and G. Maire, *Applied Catalysis B-Environmental,* 2003, **42**, 237.
[21] O. H. Bailey, D. Dou and M. Molinier, *Society of Automotive Engineers, [Special Publication] SP,* 2000, **SP-1533**, 257.
[22] Z. Hu, P. L. Burk and B. L. Chen, SO_x trap for enhancing NOx trap performance and methods of making and using the same, US 2002103078 A1 20020801, **2002**.
[23] *SixPack*, version 0.50; Stanford Synchrotron Radiation Laboratory: Menlo Park, **2004**.
[24] T. Ressler, *Journal of Synchrotron Radiation,* 1998, **5**, 118.
[25] S. S. Y. Chui, S. M. F. Lo, J. P. H. Charmant, A. G. Orpen and I. D. Williams, *Science,* 1999, **283**, 1148.

[26] D. Li, G. M. Bancroft, M. Kasrai, M. E. Fleet, X. H. Feng and K. Tan, *Canadian Mineralogist,* 1995, **33**, 949.
[27] S. C. B. Myneni, *Reviews in Mineralogy & Geochemistry,* 2000, **40**, 113.
[28] A. Vairavamurthy, B. Manowitz, W. Q. Zhou and Y. S. Jeon, Determination of Hydrogen-Sulfide Oxidation-Products by Sulfur K-Edge X-Ray-Absorption near-Edge Structure Spectroscopy, American Chemical Society, Washington, p. 412.
[29] K. Schlichte, T. Kratzke and S. Kaskel, *Microporous and Mesoporous Materials,* 2004, **73**, 81.
[30] S. C. B. Myneni, *Reviews in Mineralogy & Geochemistry,* 2002, **49**, 485.
[31] A. Vairavamurthy, *Spectrochimica Acta, Part A: Molecular and Biomolecular Spectroscopy,* 1998, **54**, 2009.
[32] K. R. Williams, B. Hedman, K. O. Hodgson and E. I. Solomon, *Inorganica Chimica Acta,* 1997, **263**, 315.
[33] S. E. Shadle, J. E. Pennerhahn, H. J. Schugar, B. Hedman, K. O. Hodgson and E. I. Solomon, *Journal of the American Chemical Society,* 1993, **115**, 767.
[34] N. Okude, M. Nagoshi, H. Noro, Y. Baba, H. Yamamoto and T. A. Sasaki, *Journal of Electron Spectroscopy and related Phenomena,* 1999, **103**, 607.
[35] W. Grunert, N. W. Hayes, R. W. Joyner, E. S. Shpiro, M. R. H. Siddiqui and G. N. Baeva, *Journal of Physical Chemistry,* 1994, **98**, 10832.
[36] C. Lamberti, S. Bordiga, F. Bonino, C. Prestipino, G. Berlier, L. Capello, F. D'Acapito, F. Xamena and A. Zecchina, *Physical Chemistry Chemical Physics,* 2003, **5**, 4502.
[37] M. Fernandez-Garcia, C. M. Alvarez and G. L. Haller, *Journal of Physical Chemistry,* 1995, **99**, 12565.
[38] L. S. Kau, K. O. Hodgson and E. I. Solomon, *Journal of the American Chemical Society,* 1989, **111**, 7103.
[39] C. Prestipino, S. Bordiga, C. Lamberti, S. Vidotto, M. Garilli, B. Cremaschi, A. Marsella, G. Leofanti, P. Fisicaro, G. Spoto and A. Zecchina, *Journal of Physical Chemistry B,* 2003, **107**, 5022.
[40] F. Xamena, P. Fisicaro, G. Berlier, A. Zecchina, G. T. Palomino, C. Prestipino, S. Bordiga, E. Giamello and C. Lamberti, *Journal of Physical Chemistry B,* 2003, **107**, 7036.
[41] G. Centi, N. Passarini, S. Perathoner and A. Riva, *Industrial & Engineering Chemistry Research,* 1992, **31**, 1947.
[42] S. S. Pollack, W. P. Chisholm, R. T. Obermyer, S. W. Hedges, M. Ramanathan and P. A. Montano, *Industrial & Engineering Chemistry Research,* 1988, **27**, 2276.

Chapter 4

In situ S K-edge X-ray absorption spectroscopy for understanding and developing SO_x storage catalysts

Abstract:

In situ S K-edge XANES experiments were carried out on second generation SO_x trapping materials under oxidizing and reducing conditions. The experiments clearly show that the strong release of SO_2 under rich conditions at plug flow conditions is caused by the facilitated reduction of sulfite species on Pt. In absence of Pt the sulfite species were stable under reducing conditions, while maintaining a similar total SO_2 uptake capacity. Thus, SO_x trapping materials without a noble metal are a clearly better option. The enhancing effect on the SO_x storage process of water present in the gas mixture is attributed to the formation of a higher sulfate fraction on the samples. The application of the in situ S K-edge XANES technique clearly reveals new information and insights on the behavior of the sulfur in the trapping process compared to the ex situ measurements and is therefore essential for designing new SO_x trapping materials.

4.1 Introduction

The combination of more efficient diesel engines and the tighter Euro IV emission standards for NO_x require the introduction of new exhaust gas treatment technologies for NO_x. One of the most promising approaches for diesel passenger cars is the NO_x storage-reduction (NO_x-SR) concept [1-3]. During a (long) period in which the exhaust gas is rich in oxygen (lean fuel conditions), NO is catalytically oxidized to NO_2 and stored in the form of nitrates. During short periods an excess of fuel is introduced (fuel rich conditions) and the stored nitrates are catalytically reduced to nitrogen. The successful application of this technique in automotive industry depends on solving the (complete) deactivation of the catalyst in the presence of SO_x in the exhaust gas formed by the combustion of sulfur compounds in the fuel. During the oxygen rich period the NO_x trap generally acts as oxidation catalyst, which leads to the formation of SO_3 and the subsequent formation of sulfates on the NO_x storage material, typically consisting of base oxide materials (e.g. barium oxide). The sulfates formed are thermodynamically more stable than nitrates under reducing conditions (lean mode) and, therefore, lead to a permanent deactivation of the material for NO_x storage [4-6]. A possible concept, facilitated by the low levels of sulfur in diesel and gasoline fuels (at present 10ppm or less), is the use of disposable or ex situ regenerable sulfur traps for on-site removal of sulfur from emissions prior to contact with NO_x-SR catalyst. The materials proposed for SO_x trapping in exhaust emission control contain typically an oxidation component (e.g., a noble metal) to convert the SO_2 to SO_3 and a sulfur storage component (usually oxides of alkaline and earth alkaline metals) supported on α-Al_2O_3, Ce_2O_3 and ZrO_2 [7-9]. However, limitations of the SO_x uptake rate and the applicable SO_x storage capacity limit the immediate application of such materials in the exhaust gas treatment of lean burn engines. For enhancing the performance of SO_x trap materials a deeper insight into the sulfur storage process with respect to the formation of the surface and bulk sulfur species especially under cycling (lean-rich) conditions is necessary.

Various techniques like IR, Raman or XPS give information about the state of sulfur present on the sample, however, strongly overlapping bands of bulk and surface sulfates formed (Infrared Spectroscopy) or the requirement of ultra high vacuum (X-ray photoelectron spectroscopy) limit most methods for in situ studies

of the sulfur storage reaction [10-12]. In contrast, X-ray absorption spectroscopy is frequently used for in situ studies of the chemical nature and the local structure of elements investigated [13-15]. XANES of sulfur at the K-edge (2473eV) has been shown to be very sensitive to the oxidation state of the sulfur species present in the sample [16-19].The difference in the edge position between S^{-2} and S^{+6} for example is around 10eV, which allows a direct and clear distinction between various natures of the sulfur existing [16-21]. Furthermore due to the direct probe of the interaction between the sulfur species and metal cations resulting from the hybridization of the 3p orbitals of sulfur and the 3d orbitals of the metal cations the technique reveals information about this relationship [22].

To study the chemical nature of sulfur, however, due to the low energy of the S K absorption edge advanced experimental setups and specifically designed beam lines are necessary for in situ experiments. This mainly results from the high background absorption at the relative low energy, which requires to minimize the path length of the X-rays in the gas atmosphere of the reactant gas mixture and to use vacuum outside the in situ reaction chamber. We have designed an *in situ* cell allowing to monitor the changes in the S K-edge XANES during exposure of the materials to SO_x at elevated temperatures. A similar approach was already published by Hayter *et al.*, however, the limited temperature range up to 452K made this approach not applicable for our investigations [23].

4.2 Experimental

A picture of the XAS cell used for in situ experiments at the sulfur K-edge is shown in Fig. 4.1. The sample is placed inside a reaction chamber sealed against the vacuum with a 7.5µm Kapton window to measure the fluorescence of the sample exposed to the X-ray beam. The outside of the cell was evacuated to minimize the scattering of the gas phase. Note that in this energy range the 7.5µm Kapton window leads to an absorption of 25% of the X-ray beam. The sample was heated with a heating wire (thermocoax) around the sample holder controlled by a K-type thermocouple. Special care has to be taken in the design of the sealing being a crucial part in the experimental setup, by using thermally stable graphite sheets between the metal parts of the cell and the Kapton windows. The samples were inserted as self supporting wafers. The reactant gas mixtures were controlled by electronic mass flow controllers, using a total flow of 100ml/min in the reaction

chamber. The setup allowed experiments in the temperature range between 273K and 573K at 1bar total pressure of the reactants.

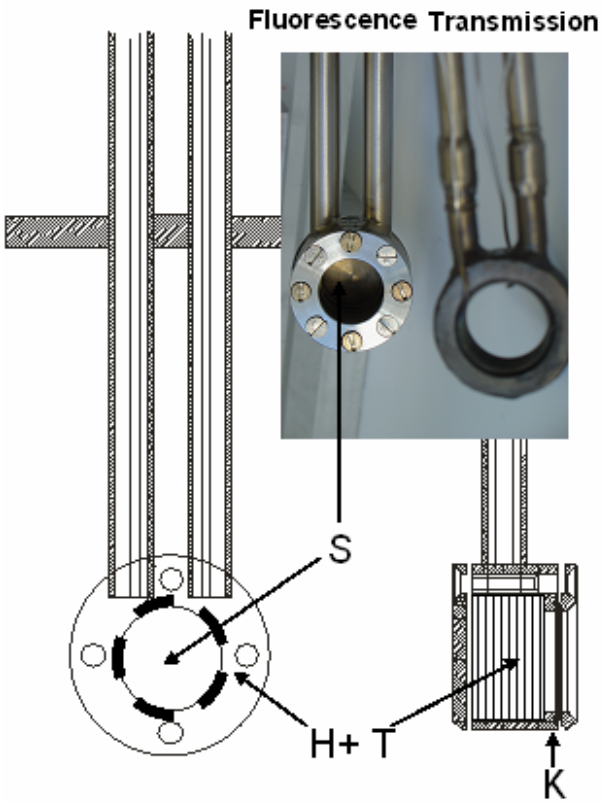

Fig. 4.1 : Experimental setup for measuring in situ time resolved XANES at the S K-edge (H = Heating; T = Thermocouple; S = Sample; K = 7.5μm Kapton).

The experiments were carried out on XAFS Beamline at the ANKA Angströmquelle Karlsruhe. The storage ring was operated at 2.5GeV with an electron current between 100 and 200mA. A double-crystal monochromator equipped with Si (111) crystals was used for the experiments at the S K-edge (2480eV). Contributions of higher order reflections on the monochromator crystals were minimized by detuning the second crystal to 60% of the maximum intensity. For the experiments at the S K-edge (2480eV) the (monochromatic) flux rate on the sample was about $2 \cdot 10^{11}$ photons/s. Harmonic rejection was provided by a grazing incidence pre-mirror which acted as a high energy filter. All measurements were performed in fluorescence mode using a Si-drift Detector (*Ketek, Munich, Germany*) with an area of $10mm^2$. For energy calibration, the maximum of the first resonance ("white line") in the spectrum of $ZnSO_4$ was set to an energy of 2481.4eV. For the removal of scattering contributions and for normalizing the spectra to the amount of material exposed to the X-ray beam a linear background was fitted to the pre-edge region (2460 – 2473eV) and the post-edge region (2506

– 2535eV) using the software Sixpack V 0.51 [24]. A least square fitting method was applied using a combination of Gaussian peaks to simulate the contributions of the electron transitions to empty orbitals of the different sulfur species and arctangent function to model the edge step feature in the XANES corresponding to 1s excitations into continuum states [25-27]. The peak position and FWHM was kept constant over a sample investigated while applying the least square fitting procedure. The relative fractions of the sulfur species present on the samples were calculated based on the area of the peaks assigned to sulfite and sulfate species as function of exposure to oxidizing and reducing conditions.

The SO_x uptake capacities of the material studied at the 523K were determined with a plug flow reaction system described in detail in Chapter 2. The material investigated was an industrial (second generation) SO_x trap material containing Ba as potential SO_x storage component on a $CuO\text{-}Al_2O_3$ support prepared by Venezia Tecnologia. To study the influence of Pt as SO_2 oxidation component on the SO_x storage process the sample was additionally impregnated with Pt. The samples are named VTNS3 for the sample without Pt and VTNS3 Pt for the sample impregnated with Pt.

4.3 Results and Discussions

The results obtained from various other characterization techniques (BET, XRD, SEM) did not show differences in the structure of the main components (support and storage component) on the sample with and without Pt. The S K-edge spectra of the ex situ prepared samples with and without Pt exposed to lean-rich cycle conditions in the plug flow reactor are compared with those of Ba and Cu sulfate (reference compounds) in Fig. 4.2.

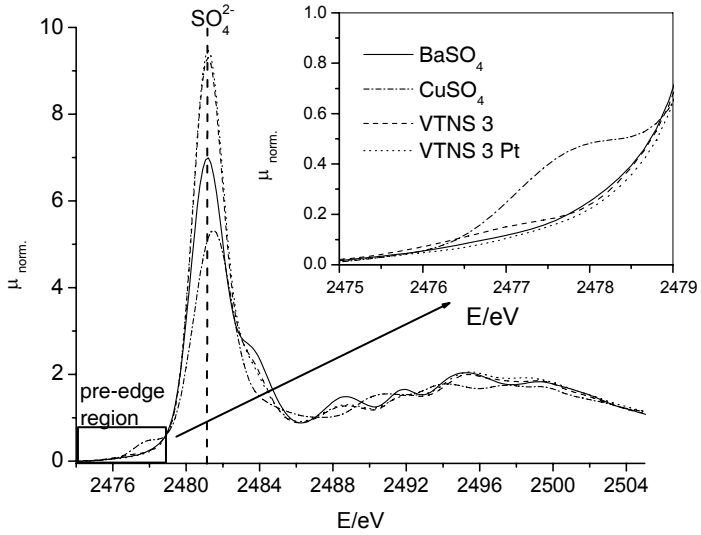

Fig. 4.2 : S K-edge spectra of the VTNS3 (dashed line) + VTNS3 Pt (dotted line) sample after treatment under dynamic conditions in the plug flow reactor (10ppm SO_2 + 12% O_2) and $CuSO_4$ (dashed-dotted line) + $BaSO_4$ (full line) as reference samples.

The position of the strong peak ("white line") in the spectra at 2480eV, assigned to the 1s → 3p transition, indicates the presence of S^{+6} (SO_4^{2-}) species in all samples [20, 28-30]. The insert shows the magnification of the pre-edge region, where an additional pre-edge peak around 2478eV was observed on $CuSO_4$ and a very weak feature around 2477eV on the Pt free sample. This characteristic pre-edge peak (2478eV) at the S K-edge for d-elements (e.g., copper sulfate) is assigned to the transition from the S 1s to the ψ^* state (SOMO formed from the overlap of the S 3p and the Me $3d_{x^2-y^2}$ orbitals in the Me sulfate) [22, 31-33]. If the Me 3d orbitals are half filled, they contain a significant contribution of the ligand 3p orbital due to their high localization. Therefore, the characteristic shape of the post edge indicates the presence of $BaSO_4$ in the samples [20]. However applying a least square fitting method to distinguish clearly the type of sulfates present on the sample, as shown in Chapter 3, was not successful.

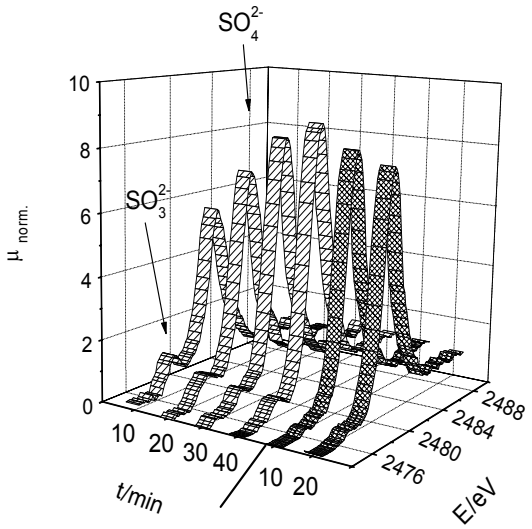

Fig. 4.3 : Time resolved *in situ* S K-edge spectra of the VTNS3 Pt at 523K exposed to 10ppm SO_2 + 12% O_2 – oxidizing conditions (medium striped ribbons) and 5% H_2 in He - reducing conditions (dense striped ribbons).

The in situ XANES of the Pt containing SO_x trap material during exposure to SO_2 under oxidative and reductive conditions are shown in Fig. 4.4. During exposure to 10ppm SO_2 in oxidative atmosphere a strong peak at 2481eV and a peak around 2477eV appeared. The peak at 2481eV, which increased in intensity with increasing SO_2 exposure, is assigned to sulfate species. The smaller peak around 2477eV showed the highest intensity at the lowest exposure time and decreased with increasing SO_2 exposure. The peak at 2477eV is compared with the pre-edge peak of copper sulfate in Fig. 4.3, and clearly shows a difference in the peak positions (determined using the first derivative of the spectrum) the SO_2 treated VTNS3 Pt sample as well as the reference $CuSO_4$.

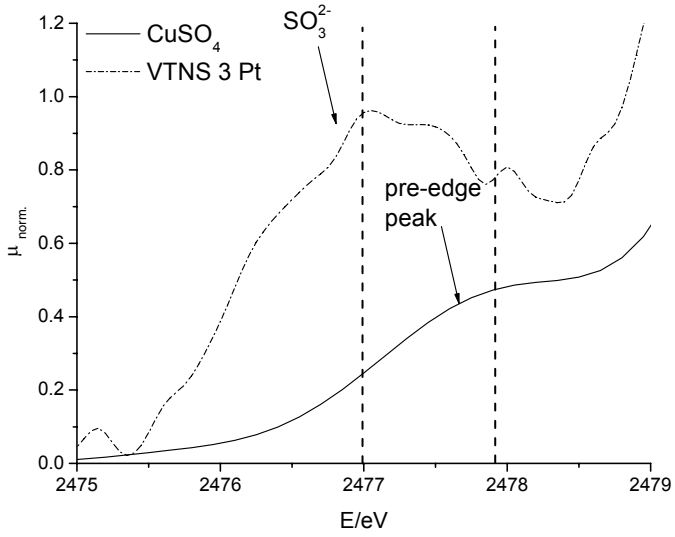

Fig. 4.4 : S K-edge spectra of the VTNS3 Pt (dashed line) at 523K 20min exposed to 10ppm SO_2 + 12% O_2 – oxidizing conditions and $CuSO_4$ as reference material.

The similar position of this peak and the peak maxima of sulfite materials identified by various authors indicate the presence of sulfur in oxidation state +4 (attributed to SO_3^{2-}) which was not observed on the ex situ treated sample [19, 34]. After switching to reducing atmosphere (5% H_2 in He, see Fig. 4.4 dense striped ribbons) the intensity of both peaks decreases with increasing reduction time. The time resolved XANES at the S K-edge of the Pt free sample under these reaction conditions are shown in Fig. 4.5. Under oxidizing conditions two peaks appear in the S K-edge region around 2481eV and 2477eV, i.e., at energies similar to those obtained with the Pt containing sample. However, with increasing SO_2 exposure the intensity of the peak assigned to sulfite species remains constant, while the intensity of the peak assigned to sulfate increases. After switching to reducing conditions a slight decrease of both peaks was observed.

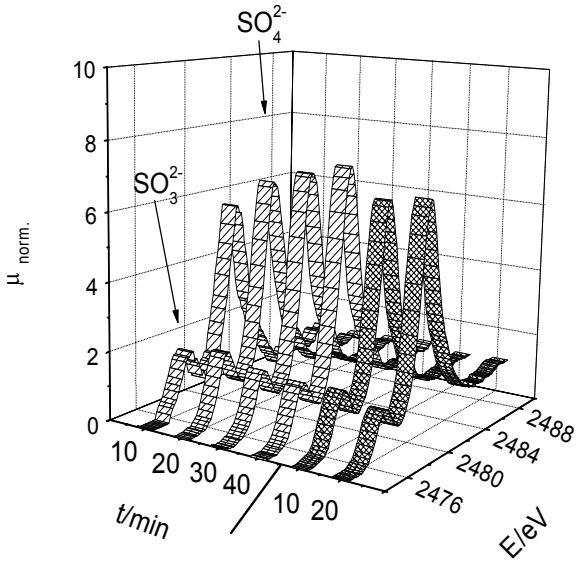

Fig. 4.5 : Time resolved in situ S K-edge spectra of VTNS3 without Pt at 523K exposed to 10ppm SO_2 + 12% O_2 – oxidizing conditions (medium striped ribbons) and 5% H_2 in He-reducing conditions (dense striped ribbons).

As mentioned in the experimental section the fraction of sulfite and sulfates were quantified by applying a least square fitting procedure. Note that the intensity of the peak assigned to the electron transitions strongly depends on the occupancy of the S p states and, therefore, the intensities of the peak for S^{+4} and S^{+6} can not directly be compared, as shown by Huffman *et al.* [25]. An example fit for the S K-edge of VTNS3 Pt after 40min exposure to 10ppm SO_2 + 12% O_2 is shown in Fig. 4.6. The relative fraction of the samples in dependence of the exposure time is shown in Tab. 4.1. After 10min of exposure to 10ppm SO_2 in 12% O_2 around 20% of the total sulfur present on the VTNS3 Pt sample is in the form of sulfite. With increasing exposure the fraction of sulfite decreases and sulfate species were formed on the Pt containing sample. After switching to reducing conditions (5% H_2 in He) a further decrease of the fraction of sulfite species was observed (from 0.05 to 0.03). On the Pt free sample, initially a higher fraction of sulfite species was observed after 10min under oxidizing conditions compared to the Pt containing material. With increasing exposure time under oxidizing conditions only a slight decrease of the sulfite concentration was observed. After switching to reducing conditions the sulfite concentration seems to be hardly influenced.

A comparison of VTNS3 Pt and VTNS3 showed that a higher concentration of sulfate species existed in the Pt containing sample. However, imposing reducing conditions subsequently hardly influenced the fraction of sulfite in the VTNS3 sample, while on the Pt containing sample the sulfite species were almost completely removed. Note that in the typical exhaust gas stream CO and hydrocarbons will be additionally present under rich conditions, however, preliminary experiments have shown that these components do not influence the formation of sulfates and sulfites during the SO_x storage process.

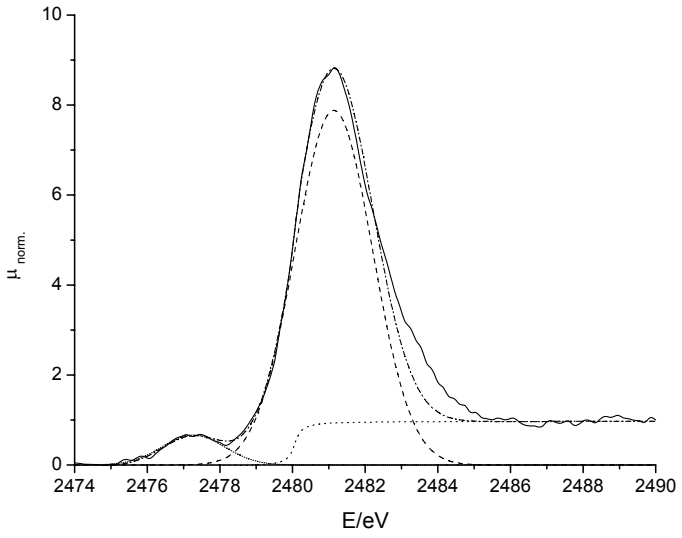

Fig. 4.6 : S K-edge spectra and least square fitted results of VTNS3 Pt after 10min 10ppm SO_2 + 12% O_2 at 523K (full line = original spectra; dashed line = sulfate species; short dotted line = sulfite species; dotted line = arc tan function; dashed-dotted line = summed simulated spectra).

Tab. 4.1 : Relative fractions of Sulfate (S^{+6}) and sulfite (S^{+4}) present on the samples at 523K.

Material	**t [min] 10ppm SO_2 + 12% O_2**								**t [min] 5% H_2 in He**			
	10		20		30		40		10		20	
	SO_3^{2-}	SO_4^{2-}	SO_3^{2-}	SO_4^{2-}	SO_3^{2-}	SO_4^{2-}	SO_3^{2-}	SO_4^{2-}	SO_3^{2-}	SO_4^{2-}	SO_3^{2-}	SO_4^{2-}
VTNS 3 Pt	0.16	0.84	0.10	0.90	0.07	0.93	0.05	0.95	0.02	0.98	0.03	0.97
VTNS 3	0.19	0.81	0.17	0.83	0.14	0.86	0.13	0.87	0.15	0.85	0.12	0.88

Provided that the metal oxide materials for SO_2/SO_3 storage have the same physicochemical properties, the results indicate that expectedly Pt enhances the activity for SO_2 oxidation/reduction. Lean-rich cycling experiments under flow conditions (not shown here) showed the formation of SO_2 under fuel rich conditions (240s lean mode/18s rich mode) for both materials, with a markedly higher amount of SO_2 released from the Pt containing material. During the typical operation conditions of a NO_x storage-reduction catalyst (i.e., periodic variation between oxidizing and reducing atmosphere) the release of SO_x from the SO_x trap observed under reducing conditions will cause deactivation of the NO_x storage catalyst. Therefore, the complete and irreversible SO_x storage is essential for a permanent protection of the catalyst.

The influence of water present in the gas mixture on both materials was investigated under plug flow experiments revealing a strongly enhanced SO_x storage capacity under lean conditions, as well as a reduced SO_2 release under reducing conditions. To investigate the influence of water on the nature of the sulfur formed during the SO_x on the storage process XANES experiments with 10% H_2O in air were carried out in the same manner. Fig. 4.8 depicts the time resolved in situ S K-edge XANES of the VTNS3 Pt sample in presence of water at 523K.

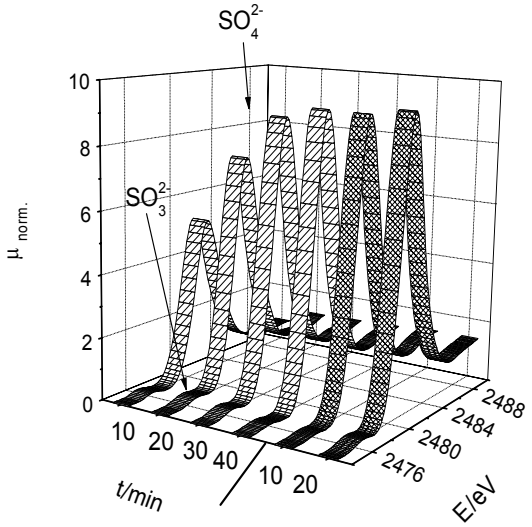

Fig. 4.7 : Time resolved *in situ* S K-edge spectra of VTNS3 without Pt at 523K exposed to 10ppm SO_2 + 12% O_2 + 10% H_2O – oxidizing conditions (medium striped ribbons) and 5% H_2 in He - reducing conditions (dense striped ribbons).

The formation of a peak at 2481.2eV is observed indicating the formation of sulfates on the material, the formation of sulfuric acid on the material however could not be ruled out. Furthermore a small contribution appears at 2476.4eV denoting the presence of sulfite type species. With respect to S K-edge XANES under dry conditions (see Fig. 4.4) and the plug flow experiments a supporting effect on the sulfate formation could be assumed; which is most likely caused by the formation of sulfuric acid. It is important to note that at 523K thermodynamic limitations on the formation of sulfuric acid do not exist. Switching to reducing conditions showed no strong influence on the nature of the sulfur formed, which could explain the lowered SO_2 release under fuel rich conditions in presence of water. The S K-edge XANES of the Pt free sample exposed to the same gas mixture is shown in Fig. 4.7.

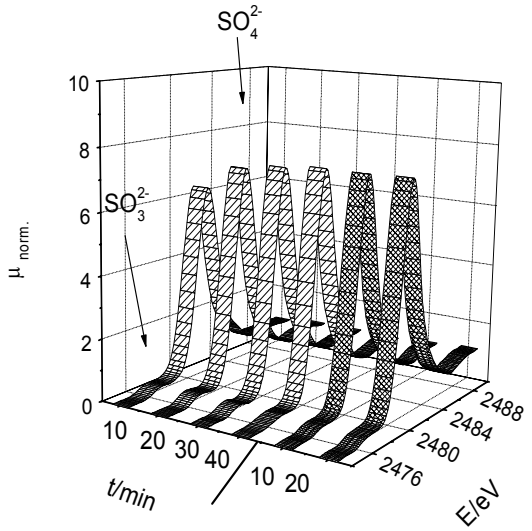

Fig. 4.8 : Time resolved in situ S K-edge spectra of the VTNS3 Pt at 523K exposed to 10ppm SO_2 + 12% O_2 + 10% H_2O – oxidizing conditions (medium striped ribbons) and 5% H_2 in He - reducing conditions (dense striped ribbons).

Clearly one adsorption band at 2481eV was observed, giving evidence for the formation of sulfates. The small band appearing at 2477eV proves the existence of sulfite type species also in the presence of water, a. Although the intensity of this peak is smaller compared to the dry conditions (see Fig. 4.5) the presence of sulfite species explains the higher SO_2 storage capacity in presence of water due to the elimination of a potential rate limiting oxidation step. The

relative fractions of the sulfate and sulfite species formed in dependence of the SO_2 exposure time is depicted in Tab. 4.2.

Tab. 4.2 : Relative fractions of Sulfate (S^{+6}) and sulfite (S^{+4}) present on the samples at 523K.

Material	t/min 10ppm SO_2 + 12% O_2 + 10% H_2O								t/min 5% H_2 in He + 10% H_2O			
	10		20		30		40		10		20	
	SO_3^{2-}	SO_4^{2-}	SO_3^{2-}	SO_4^{2-}	SO_3^{2-}	SO_4^{2-}	SO_3^{2-}	SO_4^{2-}	SO_3^{2-}	SO_4^{2-}	SO_3^{2-}	SO_4^{2-}
VTNS 3 Pt	0.02	0.98	0.02	0.98	0.02	0.98	0.01	0.99	0.01	0.99	0.02	0.98
VTNS 3	0.04	0.96	0.03	0.97	0.03	0.97	0.03	0.97	0.03	0.97	0.03	0.97

On both materials the main fraction observed is sulfate with a slightly higher sulfite fraction on the Pt free sample. Even switching to reducing conditions only hardly influences the relative fractions of the sulfur species. The obtained results in presence of water strongly suggest that water facilitate the oxidation of the sulfite species to hardly reducible sulfate species which are stable under fuel rich conditions leading to a reduced SO_2 release under cycling conditions.

4.4 Conclusions

The results obtained from the in situ S K-edge XANES experiments clearly show that the release of SO_2 under rich conditions is caused by the reduction of sulfite species present. In contrast with the Pt containing sample, the sulfite species were stable under reducing conditions in absence of Pt, while maintaining a similar total SO_2 uptake capacity. Thus, SO_x trapping materials without a noble metal are a clearly better option. Furthermore the presence of water accelerates the sulfite oxidation leading to a lower relative sulfite fraction observed, probably caused by the production of sulfuric acid. Therefore the reduced SO_2 release under fuel rich conditions could result from the higher relative fraction of the stable sulfate present. The results shown here demonstrate that monitoring of the oxidation state of sulfur by *in situ* S K-edge X-ray adsorption spectroscopy leads to a better understanding and shows the key parameters for designing SO_x trapping materials. Rational and rapid development of a new generation of such materials on the basis of complex oxide catalysts that take up SO_x rapidly, but prevent the

reduction/release during the lean-reach cycles using the leads described here is under way.

4.5 Acknowledgments

This work was supported by the European Union in the framework of project G3RD-CT2002 00793. We acknowledge the ANKA Angstroemquelle Karlsruhe for the provision of beamtime. Specially we would like to thank Stefan Mangold for the adaptation of the ANKA-XAS beamline for the experiments at the S K-edge and for the assistance during the experiments.

4.6 References

[1] T. Kreuzer, E. S. Lox, D. Lindner and J. Leyrer, *Catalysis Today,* 1996, **29**, 17.

[2] M. Takeuchi and S. Matsumoto, *Topics in Catalysis,* 2004, **28**, 151.

[3] N. Miyoshi, T. Tanziawa, K. Kasahara and S. Tateishi, Catalyst with NO_x storage component for purifying exhaust gases, EP 669157, **1995**.

[4] C. Sedlmair, K. Seshan, A. Jentys and J. A. Lercher, *Catalysis Today,* 2002, **75**, 413.

[5] E. Fridell, A. Amberntsson, L. Olsson, A. W. Grant and M. Skoglundh, *Topics in Catalysis,* 2004, **30-31**, 143.

[6] C. Sedlmair, K. Seshan, A. Jentys and J. A. Lercher, *Journal of Catalysis,* 2003, **214**, 308.

[7] A. N. Chigapov, A. A. Dubkov, B. P. Carberry, C. N. Montreuil, G. W. Graham, R. W. McCabe and W. Chun, SO_x trap for diesel and lean burn gasoline automotive applications, EP 1374978 A1 20040102, **2004**.

[8] L. Limousy, H. Mahzoul, J. F. Brilhac, P. Gilot, F. Garin and G. Maire, *Applied Catalysis B-Environmental,* 2003, **42**, 237.

[9] O. H. Bailey, D. Dou and M. Molinier, *Society of Automotive Engineers, [Special Publication] SP,* 2000, **SP-1533**, 257.

[10] J. Ryczkowski, *Catalysis Today,* 2001, **68**, 263.

[11] J. A. Lercher, V. Veefkind and K. Fajerwerg, *Vibrational Spectroscopy,* 1999, **19**, 107.

[12] M. Hunger and J. Weitkamp, *Angewandte Chemie-International Edition,* 2001, **40**, 2954.

[13] M. Fernandez-Garcia, *Catalysis Reviews-Science and Engineering,* 2002, **44**, 59.

[14] A. Jentys, N. H. Pham, H. Vinek, M. Englisch and J. A. Lercher, *Catalysis Today,* 1998, **39**, 311.

[15] T. Ressler, O. Timpe, T. Neisius, J. Find, G. Mestl, M. Dieterle and R. Schlogl, *Journal of Catalysis,* 2000, **191**, 75.

[16] G. N. George and M. L. Gorbaty, *Journal of the American Chemical Society,* 1989, **111**, 3182.

[17] M. N. Najman, M. Kasrai and G. M. Bancroft, *Wear,* 2004, **257**, 32.

[18] D. Solomon, J. Lehmann and C. E. Martinez, *Soil Science Society of America Journal,* 2003, **67**, 1721.

[19] A. Vairavamurthy, *Spectrochimica Acta, Part A: Molecular and Biomolecular Spectroscopy,* 1998, **54**, 2009.

[20] D. Li, G. M. Bancroft, M. Kasrai, M. E. Fleet, X. H. Feng and K. Tan, *Canadian Mineralogist,* 1995, **33**, 949.

[21] S. C. B. Myneni, *Reviews in Mineralogy & Geochemistry,* 2002, **49**, 485.

[22] K. R. Williams, D. R. Gamelin, L. B. LaCroix, R. P. Houser, W. B. Tolman, T. C. Mulder, S. deVries, B. Hedman, K. O. Hodgson and E. I. Solomon, *Journal of the American Chemical Society,* 1997, **119**, 613.

[23] C. E. Hayter, J. Evans, J. M. Corker, R. J. Oldman and B. P. Williams, *Journal of Materials Chemistry,* 2002, **12**, 3172.

[24] *SixPack*, version 0.50; Stanford Synchrotron Radiation Laboratory: Menlo Park, **2004**.

[25] G. P. Huffman, S. Mitra, F. E. Huggins, N. Shah, S. Vaidya and F. L. Lu, *Energy & Fuels,* 1991, **5**, 574.
[26] G. S. Waldo, R. M. K. Carlson, J. M. Moldowan, K. E. Peters and J. E. Pennerhahn, *Geochimica et Cosmochimica Acta,* 1991, **55**, 801.
[27] A. Vairavamurthy, B. Manowitz, W. Q. Zhou and Y. S. Jeon, Determination of Hydrogen-Sulfide Oxidation-Products by Sulfur K-Edge X-Ray-Absorption near-Edge Structure Spectroscopy, American Chemical Society, Washington, p. 412.
[28] D. A. McKeown, I. S. Muller, H. Gan, I. L. Pegg and W. C. Stolte, *Journal of Non-Crystalline Solids,* 2004, **333**, 74.
[29] I. J. Pickering, R. C. Prince, T. Divers and G. N. George, *FEBS Letters,* 1998, **441**, 11.
[30] H. Sekiyama, N. Kosugi, H. Kuroda and T. Ohta, *Bulletin of the Chemical Society of Japan,* 1986, **59**, 575.
[31] E. I. Solomon, B. Hedman, K. O. Hodgson, A. Dey and R. K. Szilagyi, *Coordination Chemistry Reviews,* 2005, **249**, 97.
[32] E. I. Solomon, R. K. Szilagyi, S. D. George and L. Basumallick, *Chemical Reviews,* 2004, **104**, 419.
[33] R. K. Szilagyi, P. Frank, S. D. George, B. Hedman and K. O. Hodgson, *Inorganic Chemistry,* 2004, **43**, 8318.
[34] S. C. B. Myneni, *Reviews in Mineralogy & Geochemistry,* 2000, **40**, 113.

Chapter 5

Mechanistic studies of SO_x trapping on Ca-Al based high capacity SO_2 sorbents

Abstract:

$CaO-Al_2O_3$ based materials impregnated with Na and Mn were evaluated as sulfur trapping materials at 523K. The SO_2 sorption experiments carried out showed a three times higher total storage capacity as well as a higher time of complete SO_2 removal compared to a second generation SO_x trapping material. The physicochemical characterization (BET, XRD and TPD) revealed a mesoporous material with Calcium mainly present in oxide form. With the combination of *in situ* S K-edge XANES and IR the key parameters in relation to the storage process could be identified. The prepared $CaO-Al_2O_3$ was recognized therefore as a sufficient support for depositing additional storage component - Na. The impregnation with Mn led to an appropriate oxidation capacity at the low SO_2 concentration (50ppm) as well as in absence and presence of 10% water. The transport into the bulk phase as limiting step in presence of Mn could be clearly proved by means of *in situ* S K-edge XANES. The combination of *in situ* IR and the 2D Correlation Analysis led to the identification of similar surface sulfate species on the Mn containing samples indicating a similar reaction network. The water layer on the surface influencing the transport into the bulk phase rather than the oxidation capacity was discovered to be the rate limiting step.

5.1 Introduction

The extensive use of cars for traveling or commuting is one of the major sources for the emission of hazardous and toxic gases (NO_x, SO_x) into the atmosphere. Although a significant reduction of emissions has been already achieved, further development is necessary to reduce the emission of pollutants to obtain a cleaner environment especially in congested areas [1]. The reduction of CO_2-emissions is essential as it contributes largely to the greenhouse effect. At present the most effective approach is the introduction of engines with lower fuel consumption such as Diesel and lean burn (Otto) engines, both operating under oxygen excess. However, the lean operation mode with the high compression rate of the air/fuel mixture leads to unfavorably high emission of NO_x as 3-way catalysts are not effective for NO_x reduction at λ >1. A promising approach to overcome the NO_x emission can be found in the Nitrogen-Storage-Reduction concept (NSR), which is based on a cycling operation mode of the engine and on a typical 3-way catalyst that additionally contains a NO_x storage component [2-4]. During a long cycle in oxygen excess (lean mode) the NO_x species formed are trapped on the catalyst surface. During a short fuel rich period the reduction takes place, were unburned hydrocarbons in addition to CO are used as a reducing agent for the NO_x species.

However, the NSR catalysts are severely poisoned by the presence of SO_2 in the exhaust gas stream which adsorbs irreversibly on the catalyst surface and leads to a deactivation of the NO_x sorption sites due to the formation of thermodynamically favored sulfate species [2, 3, 5]. Lowering the sulfur content in the fuel allows the development of an integrated approach combining a sulfur removal device upstream to the NSR catalyst that prevents the permanent deactivation [6, 7]. Promising materials for such a device have already been shown in Chapter 2. Nevertheless, a deeper understanding of the material properties in relation to their sulfur trapping abilities has to be gained. The typical composition of a S-trap material includes a refractory support (e.g. Al_2O_3, CeO_2, ZrO_2), an oxidation component (e.g. Pt, Rh) and a sulfur storage component (e.g. Mg, Ca, Ba) [6]. During the operation under lean conditions (oxygen excess), a fast oxidation of SO_2 to SO_3 in combination with an instantaneous adsorption of SO_3 on the storage component should be realized. Recent results showed that beside noble metals also Mn and Cu could be sufficient as oxidation components

[8]. To achieve high sulfur storage capacity for long time storage in a wide temperature range a high thermal stability of the sulfates is required. Among the earth alkaline metals Barium shows the highest sulfate decomposition temperature, however, Mg and Ca both having a lower molar weight could also be utilized as potential SO_x trapping materials as shown by Swisher *et al*. [9].

According to literature infrared spectroscopy is a suitable technique for *in situ* studying the sulfate formation which is sensitive to the structure of sulfate species and adsorption sites [10-12]. The major limitations of a straightforward application on mixed metal oxides are the strongly overlapping IR bands of bulk and surface sulfates.

A promising approach for resolving complex spectra is the Generalized 2D Correlation Analysis offering the opportunity for e.g. differentiation between overlapping peaks and identification of spectral features not readily observable in the time resolved spectra. The 2D Correlation Analysis was introduced by Noda in the late 1980s [13, 14]. There are a numerous publications of the application of 2D Correlation Analysis in all fields of chemistry [15-18]

$$\Phi(\nu_1,\nu_2) = \frac{1}{n-1} \cdot DD^T$$

$$\Psi(\nu_1,\nu_2) = \frac{1}{n-1} \cdot DND^T \qquad with \qquad N_{jk} = \begin{cases} 0 & for \quad j = k \\ \dfrac{1}{\pi \cdot (k-j)} & for \quad j \neq k \end{cases}$$

.

Equation 5.1 : Generalized 2D Correlation Analysis involving the Hilbert Transform N_{jk} is referred to as the Noda-Hilbert matrix, *n* denotes the number of spectra in the dataset.

In general the data matrix D (i.e. mean centered spectrum) is analyzed by a synchronous and asynchronous technique [19]. The synchronous 2D Correlation intensity is regarded as the overall covariance between two spectral intensity variations measured at different spectral frequencies (ν) at different times, while the asynchronous correlation intensity represents sequential or successive changes in the spectral intensities measured at ν_1 and ν_2.

The synchronous spectrum evidences simultaneous changes of spectral intensity variations measured at ν_1 and ν_2. The auto peaks (at $\nu_1 = \nu_2$) located on the diagonal line on the contour plot obtained for $\Phi(\nu_1,\nu_2)$ and cross-peaks (at $\nu_1 \neq \nu_2$) at the intersections of correlated spectral intensities represent synchronized spectral changes. Positive signs indicate a change in the same direction, whereas

negative signs indicate a change in the opposite direction The asynchronous spectrum is anti-symmetric with respect to the diagonal line, and develops cross peaks only if the intensities of two spectral features change out of phase with each other (i.e. delayed or accelerated) [20]. Therefore, the synchronous plot identifies the spectral intensities changing under the effect of the perturbation and denotes whether these intensities change in the same or in opposite directions whereas the asynchronous plot depicts the sequential or time-resolved changes occurring.
The extended interpretation rules for the synchronous and asynchronous 2D correlation plots were proposed by Noda [20, 21]. For further information about the recent developments in theory and application of the 2D Correlation Analysis, the interested reader is referred to these review articles [17, 22, 23]. One of the major limitations in the straightforward interpretation of the asynchronous spectra are frequency shifts and/or bandwidth broadening, which result in additional peaks present in the asynchronous plot not related to a physical/chemical effect caused by the perturbation. These artifacts are extensively described in literature [24, 25]. A possible solution to overcome these problems can be found in the concept of Progressive Correlation Analysis (ProCorA) as described by Haider *et al.* [15]. In ProCorA, multiple calculations of the synchronous plot are performed starting with the first two spectra. The sequence of peak change can now be set up from the evolution of peaks in the plots. As multiple calculations of the plots are performed, the ProCorA is utilized to find a compromise between employing the maximum number of spectra for maximizing the information present in the dataset and circumventing problems due to artifacts.

A promising technique for study the chemical nature of sulfur is S K-edge XAFS. The XANES of S at the K-edge (2473eV) is very sensitive to the oxidation state of the sulfur species present in the sample according to literature [26, 27]. The peaks arising at the S K-edge are assigned to the 1s → 3p transition. The exact position of the absorption edge strongly depends on the oxidation state of sulfur. The difference between S^{-2} and S^{+6} for example is around 10eV, which allows a direct and clear distinction between various oxidation states of the sulfur species on the sample [26, 28, 29]. However, due to the low energy of the S K absorption edge, advanced experimental setups and specifically designed beam lines are necessary as shown in Chapter 4.

5.2 Experimental

5.2.1 Materials

The materials were provided by the ACA in Berlin and prepared as follows. The mesoporous alumina support was synthesized by a precipitation of Disperal P2 (SASOL) and Ca nitrate. After drying at room temperature the support was calcined at 873K and at 1073K for 1h. The obtained calcium-alumina (CaO-Al_2O_3) support was modified by incipient wetness impregnation with a manganese acetate solution resulting in 3wt.% Mn loading (Mn/CaO-Al_2O_3). After drying the sample was calcined at 873K. Finally, this material was additionally modified with a Na_2CO_3 solution to obtain about 10wt.% Na on the material ($Na/Mn/CaO$-Al_2O_3). For comparison a second generation SO_x trapping material consisting of a CuO-Al_2O_3 supported Ba prepared by Venezia Tecnologia was used (Ba/CuO-Al_2O_3).

5.2.2 Physicochemical characterization of fresh materials

The crystalline structure of the materials was analyzed by XRD using a Philips X'Pert Pro System ($CuK_{\alpha 1}$-radiation, 0.154056nm) at 40kV / 40mA. The measurements were performed in a capillary (ø = 0.3 or 0.5mm) with a step scan of 0.05°/min from 10° to 80° 2Θ. The analytical composition of the samples was determined by optical emission spectroscopy with excitation by inductively coupled plasma (ICP-OES) with the spectrometer Optima 3000 XL (*Perkin Elmer*). Pore volumes and surface areas were determined by nitrogen adsorption on an ASAP 2010M facility (M*icromeritics, Germany*) applying the BET method. Temperature programmed desorption studies focused on CO_2 (m/z = 44) were performed in a flow reactor system heated with a cylindrical, ceramic oven (*Horst GmbH*). The gases evolved were monitored by a mass spectrometer (*Balzers QME 200*). Approximately 50mg of the samples were heated with a rate of 15K/min in helium with a total flow rate of 30ml/min up to 1223K.

5.2.3 Temperature programmed reaction

The influence of the temperature on the SO_2 storage process was investigated by a Temperature programmed reaction (TPR). The SO_2-TPR was performed with 50mg of the storage material starting the experiment at a temperature of 323K under continuous heating up to 873K with a heating rate of 10K/min. The feed

consisted of 50ppm SO_2, 100ppm NO, 6% O_2 and 5% CO_2 in He. During the test runs 4 cycles with periodic temperature variations between 323 and 873K with a constantly flowing feed (120ml/min) through the reactor were carried out. The composition of the exit stream was continuously analyzed by a multigas sensor *(Multor. 610, Maihak GmbH).* The amounts of stored SO_2 were determined by integration of the concentration profiles.

5.2.4 Uptake Experiments

The SO_x uptake experiments were carried out under dynamic conditions at 523K using a tubular reactor system described in Chapter 2. A typical mixture contains 50mg of the sample with a particle size of 0.1-0.3mm and 100mg SiC (< 0.3mm). The gas mixture typically contained 50ppm SO_2 + 12% O_2 with an optional addition of 10% H_2O in air and was balanced to 200ml/min with He. The SO_2 concentration in the exhaust gas stream was determined using an SO_2 analyzer (*Model 43C, Thermo Environmental Instruments*).

5.2.5 Infrared Spectroscopy + 2D Correlation Analysis

In situ IR experiments were carried out in a flow cell in transmission mode with a Perkin Elmer 2000 – FTIR spectrometer. For the IR measurements, the samples were pressed into self supporting wafers. After heating to the final temperature (523K) in helium, the sample was exposed to 10ppm SO_2 + 12% O_2 with an optional addition of 10% H_2O in air at a total flow of 200ml/min (balance He). The background correction was performed as shown by Mazet *et al.* [30]. The calculations of the synchronous and asynchronous correlation plots were performed using the method described in Equation 5.1 and compared to the results obtained with the program “2D POCHA” written by Adachi [31]. The spectra were mean-centered before the calculation

5.2.6 XAFS experiments

The S-XAFS experiments were performed at the XAS beamline at Angströmquelle Karlsruhe (ANKA). The samples were pressed into self supporting wafers and placed in the reaction chamber. All samples were measured in the fluorescence mode. The storage ring was operated at 2.5GeV with an electron current between

100 and 200mA. A double-crystal monochromator equipped with Si (111) crystals was used for the experiments at the S K-edge (2480eV). For energy calibration, the maximum of the first resonance ("white line") in the spectrum of $ZnSO_4$ was set to an energy of 2481.4eV. For the removal of scattering contributions and for normalizing the spectra to the amount of material exposed to the X-ray beam a linear background was fitted to the pre-edge region (2460 – 2473eV) and the post-edge region (2506 – 2535eV) using the software XANDA [32]. A spline smoothing procedure was applied to the background corrected spectra. For further experimental details see Chapter 4. A least square fitting method was applied using a combination of Gaussian peaks to simulate the contributions of the electron transitions to empty orbitals of the different sulfur species and a arctangent function to model the edge step feature in the XANES corresponding to 1s excitations into continuum states. The peak position and FWHM was kept constant over a sample investigated while applying the least square fitting procedure. The relative fractions of the sulfur species present on the samples were calculated based on the area of the peaks assigned to sulfite and sulfate species as function of exposure to oxidizing and reducing conditions.

5.3 Results

5.3.1 Physicochemical Characterization of the fresh material

The N_2 Isotherms as well as pore size distribution are shown in Fig. 5.1. They clearly confirm the presence of mesopores (Isotherm type IV). The corresponding BET surface area, the pore volume and the composition of the materials are summarized in Tab. 5.1. The highest pore volume was observed for the pure support (1.352cm³/g). Impregnation with Mn and Na led to a decrease of the pore volume of 30 and 70%, respectively, compared to the parent material. This indicates that the impregnation leads to a partial blockage of the pores. The average pore size of 180Å for $CaO\text{-}Al_2O_3$ increased to 250Å after the impregnation with Mn which could result from the additional performed calcination (873K). The decomposition of the $CaCO_3$ present on the material is therefore influencing strongly the pore size (Fig. 5.1B). After the final impregnation with sodium the pore size decreased to 180Å and the pore volume diminished. The $Ba/CuO\text{-}Al_2O_3$ reference material showed a uniform pore size around 60Å and a BET surface area of 174m²/g.

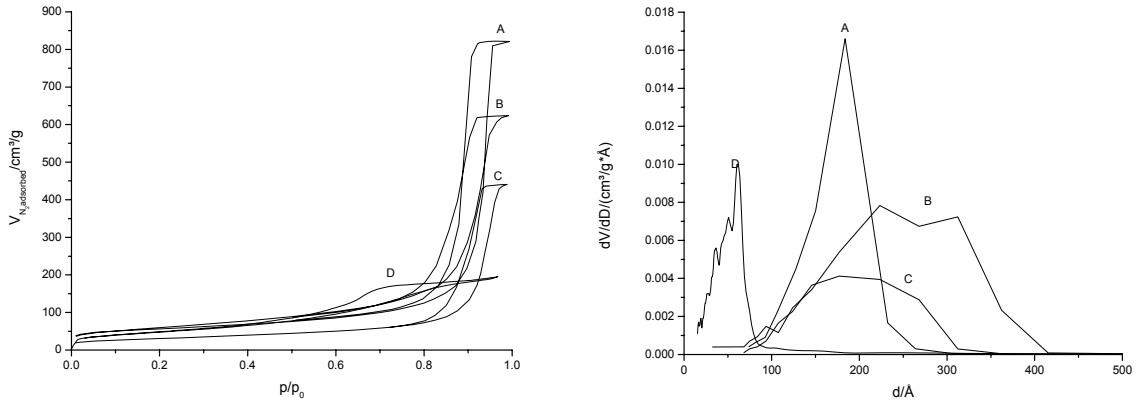

(A) (B)

Fig. 5.1 : N_2 isotherms and pore size distribution for $CaO\text{-}Al_2O_3$ (A), $Mn/CaO\text{-}Al_2O_3$ (B) $Na/Mn/Al_2O_3$ (C) and $Ba/CuO\text{-}Al_2O_3$.

The phases identified by means of XRD are summarized in Tab. 5.2. Al_2O_3 as the support material could be clearly identified on all materials. The absence of further reflections at $Mn/CaO\text{-}Al_2O_3$ indicates the presence of small MnO_2 particles. The final impregnation with sodium leads to the formation $Na_2CO_3 \cdot xH_2O$. On the Ba containing material $BaCO_3$ is present on an amorphous $CuO\text{-}Al_2O_3$ support.

Tab. 5.1 : ICP and N_2 physisorption results of synthesized samples.

Sample	Ca [wt. %]	Al [wt. %]	Mn [wt. %]	Na [wt. %]	BET [m²/g]	Pore Volume [cm³/g]
$CaO\text{-}Al_2O_3$	6.25	42.42			293	1.352
$Mn/CaO\text{-}Al_2O_3$	5.83	39.66	2.87		210	0.963
$Na/Mn/CaO\text{-}Al_2O_3$	5.48	37.33	2.82	9.15	100	0.380
$Ba/CuO\text{-}Al_2O_3$	15(Ba)			10(Cu)	174	0.301

Tab. 5.2 : Phases identified by means of XRD on the materials investigated.

Material	Phases
$CaO\text{-}Al_2O_3$	Al_2O_3
$Mn/CaO\text{-}Al_2O_3$	Al_2O_3
$Na/Mn/CaO\text{-}Al_2O_3$	Al_2O_3, $NaCO_3$
$Ba/CuO\text{-}Al_2O_3$	CuO, Al_2O_3, $BaCO_3$

5.3.2 CO_2 desorption profiles

The CO_2 desorption profiles while heating up to 1273K are shown in Fig. 5.2. For $CaO\text{-}Al_2O_3$ and the material impregnated with Mn one clear peak at 440K with a strong shoulder at 630K was observed. The maximum at the lowest temperature possibly results from the decomposition of carbonate species present on the surface and with increasing temperature bulk carbonate species are decomposed. The $Na/Mn/CaO\text{-}Al_2O_3$ revealed three desorption maxima at 530K, 610K and 970K. The peak at the highest temperature could be assigned to the decomposition of bulk Na_2CO_3. For the $Ba/CuO\text{-}Al_2O_3$ material three maxima of CO_2 formation at 453K, 723K and 930K were observed. The total amount of CO_2 released was determined by integration of the desorption profile and the theoretical amount calculated on the basis of the chemical composition is compared in Tab. 5.3.

Tab. 5.3 : Total CO_2 yields detected in the TPD experiment on the samples and the theoretical amount present.

Sample	CO_2 yield [mmol/g]	Theoretical amount [mmol/g]
$CaO\text{-}Al_2O_3$	6.70	15.60
$Mn/CaO\text{-}Al_2O_3$	6.50	14.55
$Na/Mn/CaO\text{-}Al_2O_3$	13.07	93.69
$Ba/Cu\text{-}Al_2O_3$	9.46	9.80

The far lower amount of CO_2 released in the TPD compared to the theoretical amount for the $CaO\text{-}Al_2O_3$ based materials indicates that Ca/Na as the main carbonate containing species are not completely present as carbonate. In contrast for the sample obtained from Venezia Technologia the amount of CO_2 released (9.46mmol/g) is in good agreement with the maximum amount that can be formed from the decomposition of $BaCO_3$.

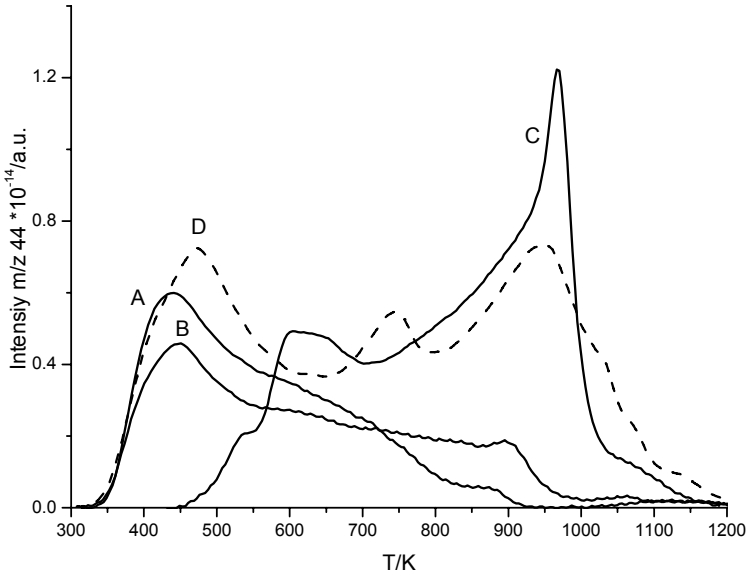

Fig. 5.2 : CO_2 desorption profiles for the $CaO\text{-}Al_2O_3$ (A), $Mn/CaO\text{-}Al_2O_3$ (B), $Na/Mn/CaO\text{-}Al_2O_3$ (C) and $Ba/CuO\text{-}Al_2O_3$ (D).

5.3.3 Total SO_x uptake capacity

The SO_2 uptake in dependence of time during the exposure to 50ppm SO_2 +12% O_2 at 523K is shown in Fig. 5.3. After a short period of complete SO_2 absorption a steep increase indicates the beginning of the breakthrough. On the $CaO\text{-}Al_2O_3$ material a complete uptake for the first 18min was observed followed by an almost linear breakthrough for the next 100min up to the initial concentration, which was reached at 700min indicating a complete saturation of the material. The $Mn/CaO\text{-}Al_2O_3$ sample showed a total sulfur dioxide adsorption for 31min, followed by an exponential increase (S-shape) to the initial concentration (at 700min). The additional impregnation with sodium led to a tremendous increase of the time for the whole SO_2 adsorption (52min) compared to the other materials. Nevertheless, the typical S-shape breakthrough behavior could be observed leading to a complete penetration of the material at 1000min. The $CuO\text{-}Al_2O_3$ based material showed complete adsorption for 21min, followed by a breakthrough finished at 500min. It can be seen that the time for complete SO_x adsorption increases in the order $CaO\text{-}Al_2O_3$ (18min) < $CuO\text{-}Al_2O_3$ (21min) < $Mn/CaO\text{-}Al_2O_3$ (31min) < $Na/Mn/CaO\text{-}Al_2O_3$ (52min). It is important to note that the Mn/Al_2O_3 material shows the same time of reaching a complete saturation with respect to the pure support. The S – shape of the breakthrough curves observed for all samples indicates that

on these materials the product diffusion through the surface layer is the limiting step at high loadings [33-35].

SO_2 storage experiments at 523K in presence of 10% H_2O in the gas mixture show a similar breakthrough behavior compared to the measurements under dry conditions. However, on the Mn and Na impregnated as well as on the Ba/CuO-Al_2O_3 sample a longer time of complete SO_2 adsorption could be observed.

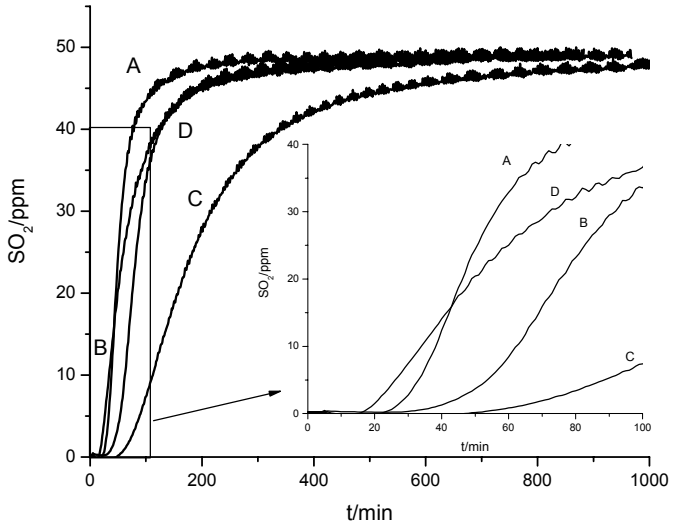

Fig. 5.3 : SO_x Uptake in dependence of time while exposure to 50ppm SO_2 + 12% O_2 at 323K at CaO-Al_2O_3 (A), Mn/CaO-Al_2O_3 (B), Na/Mn/CaO-Al_2O_3 (C) and Ba/Cu-Al_2O_3 (D).

The total SO_x uptake calculated from the area of the adsorbed SO_2 in the breakthrough-curves in absence and presence of water is shown in Fig. 5.4. It was found that the support itself, i.e. without the presence of a potential oxidation component, already shows a significant total uptake of 9.0mmol SO_2/g. The material containing Mn as oxidation component and the Na impregnated sample show a higher total uptake (13.0mmol SO_2/g, 23.7mmol SO_2/g, respectively) compared to the pure support. However, the storage capacity varies drastically in presence of water compared to dry conditions. It is found that water has a promoting effect on the Mn/CaO-Al_2O_3 (21.3mmol SO_2/g) and Na/Mn/CaO-Al_2O_3 (32.5mmol SO_2/g) samples but leads to a decrease in capacity of almost 50% for the pure support (5.1mmol SO_2/g) compared to the experiments carried out under dry conditions. Similar results are shown in literature for pure metal oxides [36, 37]. For the second generation material (Ba/CuO-Al_2O_3) only a minor influence of

the sorption capacity on the presence of water was observed. (7.3mmol SO_2/g vs. 8.20mmol SO_2/g)

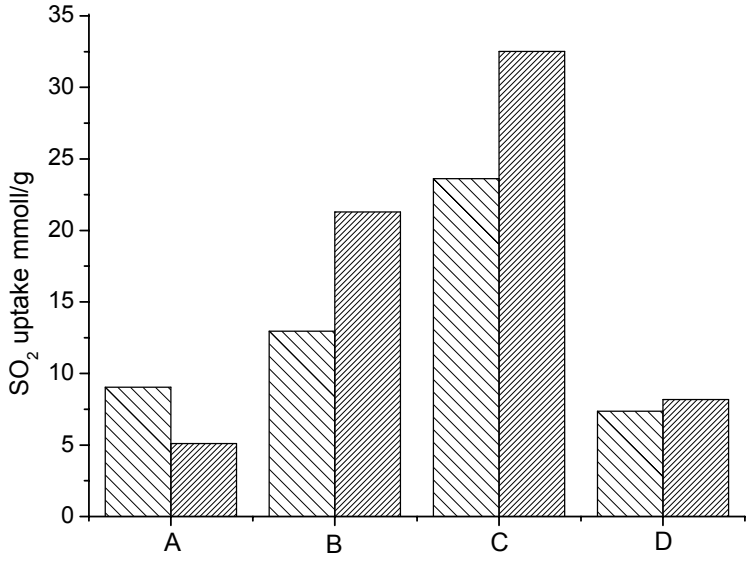

Fig. 5.4 : Total SO_x uptake of $CaO\text{-}Al_2O_3$ (A), $Mn/CaO\text{-}Al_2O_3$ (B), $Na/Mn/CaO\text{-}Al_2O_3$ (C), $Ba/CuO\text{-}Al_2O_3$.(D) (spare bar = 50ppm SO_2 + 12% O_2,dense bar= 50ppm SO_2 + 12% O_2 + 10% H_2O).

5.3.4 Temperature programmed reaction

To investigate the influence of the temperature on the SO_2 storage materials with the highest SO_2 uptake capacity ($Mn/CaO\text{-}Al_2O_3$ + $Na/Mn/CaO\text{-}Al_2O_3$) temperature programmed reactions were carried out. The dynamic SO_2 storage and release during 4 cycles of the temperature programmed reactions are shown in Fig. 5.5. SO_2 was not detected after the Mn impregnated material in the first temperature cycle (see Fig. 5.5 solid line) while heating up to 873K indicating the complete sorption. During cooling down, from 423K on a partial penetration was observed which decreased when 323K was reached. The following temperature cycles typically led to a strong SO_2 release while heating up to 423K followed by an additional adsorption up to 873K. Increasing the total cycle number revealed a more pronounced SO_2 formation.

The dashed line in Fig. 5.5 represents the $Na/Mn/CaO\text{-}Al_2O_3$ material during the temperature cycles. No SO_2 could be detected in the first temperature cycle indicating the complete storage on the material. A similar pattern was observed in the second temperature cycle (only a small release of SO_2 until 473K). The SO_2 removal over the first two cycles was around 80% indicating a good

storage behavior. Performing the third cycle the material showed only a partial SO_2 adsorption while cooling down. A similar behavior was observed in the fourth cycle. The comparison of the two materials shows for the Na/Mn/CaO-Al_2O_3 material almost complete adsorption during two temperature cycles, and a far less pronounced SO_2 release while heating up from 323 - 473K with respect to the Mn/CaO-Al_2O_3.

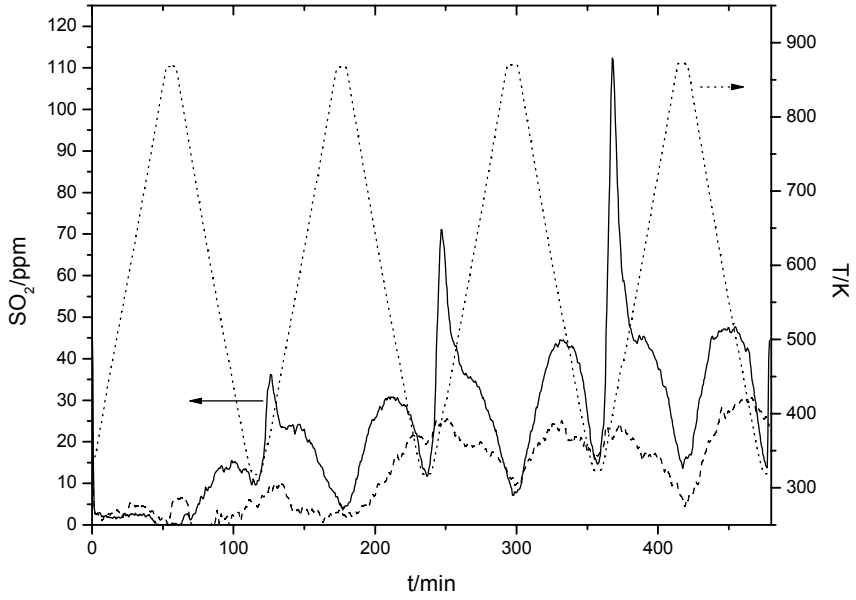

Fig. 5.5 : Temperature programmed reaction on the Mn/CaO-Al_2O_3 and Na/Mn/CaO-Al_2O_3 in 50ppm SO_2 + 100ppm NO + 6% O_2 + 5% CO_2 in He.

5.3.5 Physicochemical Characterization after SO_2 adsorption

The diffraction pattern for the samples exposed to SO_2 in absence and presence of H_2O are shown in Fig. 5.6A and B, respectively. On the pure support only the reflections assigned to Al_2O_3 (2Θ=46° and 66°) were observed. On the manganese impregnated material additional reflections were attributed to $CaSO_4$ located in the region between 25° < 2Θ < 32°. However, due to the low intensity of the reflections observed the $CaSO_4$ seems to be present in a highly dispersed form. The Na/Mn/CaO-Al_2O_3 material shows a small new reflection at 2Θ=29.4° after the SO_2 + O_2 treatment, which could not be clearly assigned to Na_2SO_4.

In the presence of water no extra reflections on the CaO-Al_2O_3 material could be detected. On Mn/CaO-Al_2O_3 three additional reflections located at 2Θ=25.5°, 30.4° (broad) and 37° were observed. They are assigned to $CaSO_4$ with higher intensity compared to the sample treated in absence of water. This

indicates that $CaSO_4$ is present as bigger particles. A similar behavior showed the Na/Mn/CaO-Al_2O_3 revealing new reflections in presence of water. They are between 2Θ=20-25° and could be attributed to Na_2SO_4 and at 2Θ=29° to $CaSO_4$. The comparison of the results shows the general trend of only a minor formation of bulk species in absence of H_2O. However in the presence of water especially on the Na containing sample higher bulk contribution are found.

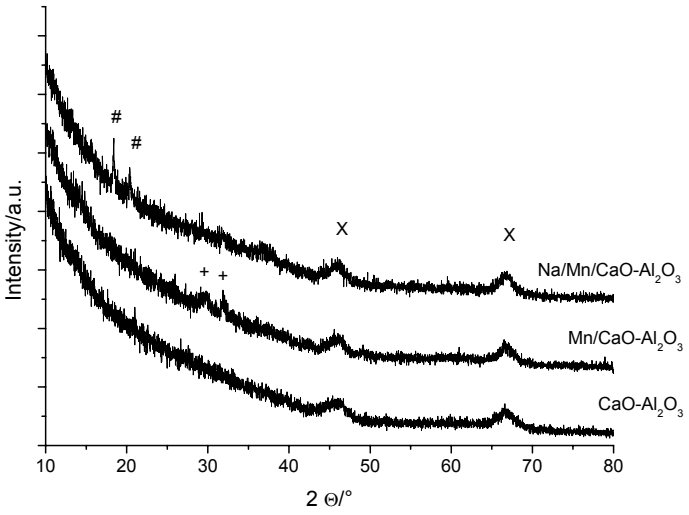

(A)

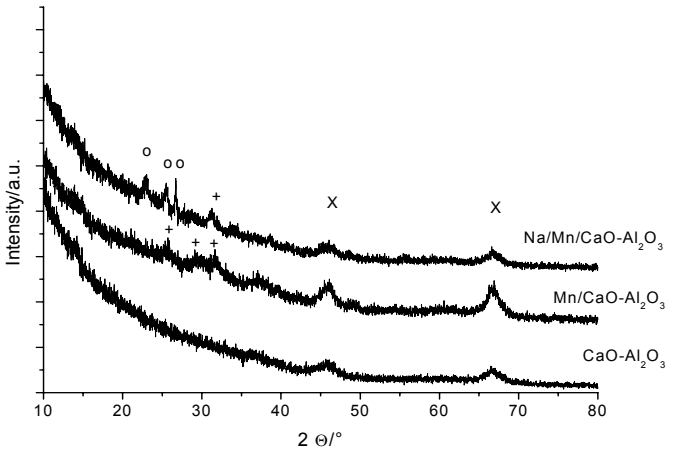

(B)

Fig. 5.6 : XRD pattern of the CaO-Al_2O_3, Mn/CaO-Al_2O_3 and Na/Mn/CaO-Al_2O_3 material exposed to 50ppm SO_2 + 12% O_2 (A) and 50ppm SO_2 + 12% O_2 + 10% H_2O (B) # = Na_2CO_3, o = Na_2SO_4, + = $CaSO_4$ x = Al_2O_3.

5.3.6 Infrared spectroscopy

The IR spectra of the fresh materials in the region of 3900cm^{-1}-3300cm^{-1} (hydroxyl groups) and 1800cm^{-1}-970cm^{-1} (carbonates/sulfates) are shown in Fig. 5.7. On the fresh CaO-Al_2O_3 sample the peak at 1490cm^{-1} and 1425cm^{-1} could be attributed to the ν_{3a} and ν_{3b} vibrations of $CaCO_3$ (Argonite) [38, 39] and the two bands located at 1515 and 1425cm^{-1} to $CaCO_3$. Note that the band 1515cm^{-1} is shifted about 35cm^{-1} to higher frequency compared to the pure support due to an influence of the various vibration modes for the carbonates present. This results in a variation in the intensity contribution as described by Andersen *et al.* indicating a slight influence of the impregnation procedure on the $CaCO_3$ present [38]. Four distinct peaks at 1545, 1474,1395, 1070cm^{-1} and a shoulder around 1660cm^{-1} could be observed in the fresh Na/Mn/CaO-Al_2O_3 material. The shoulder can be assigned to crystal bound water and the band at 1070cm^{-1} to the ν_1 vibration of CO_3^{2-} as present in $Na_2CO_3 \cdot xH_2O$ [40, 41]. The additional bands observed in the carbonate region can not be clearly assigned to calcium or sodium carbonates due to their strong overlapping [40, 41].

In the hydroxyl group region (see Fig. 5.7B) two distinct bands at 3726cm^{-1} and 3678cm^{-1} were observed on the fresh CaO-Al_2O_3 material and assigned to OH groups connected to tetrahedreally and octahedreally Al ions, respectively [42-44]. On the Mn impregnated material similar peaks were observed compared the CaO-Al_2O_3 material, the intensity of the peak at 3678cm^{-1} is slightly reduced indicating a partial depletion of this surface Al ion due to the additional impregnation [45]. The depositing of Na_2CO_3 led to the complete removal of bands assigned to hydroxyl groups indicating the complete coverage of surface.

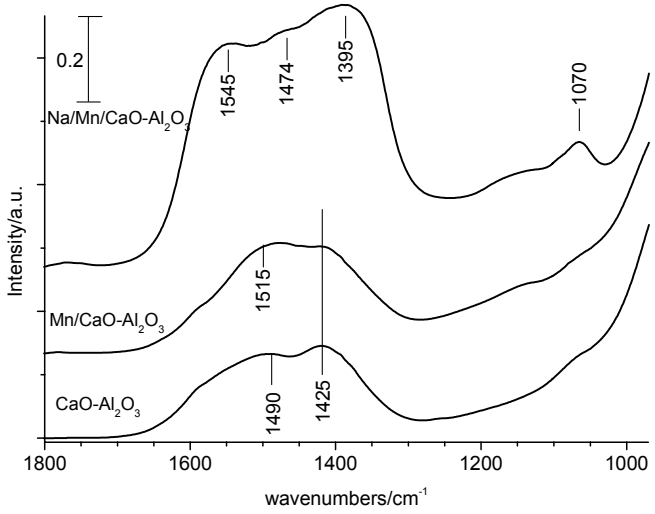

(A)

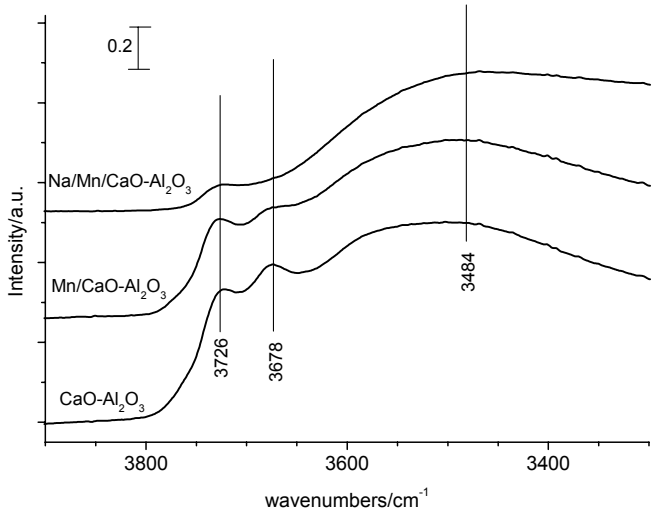

(B)

Fig. 5.7 : Infrared spectra of the fresh $CaO\text{-}Al_2O_3$, $Mn/CaO\text{-}Al_2O_3$ and $Na/Mn/CaO\text{-}Al_2O_3$ of the carbonate (A) and hydroxyl group region (B).

5.3.7 *In situ* Infrared spectroscopy in absence of H_2O

The IR spectra of the $CaO\text{-}Al_2O_3$ sample (dotted line = RT) during the exposure of 10ppm SO_2 + 12% O_2 at 523K on are shown in Fig. 5.8. For reasons of clarity, only 7 spectra (solid lines) measured with a time interval of 20min are shown. With increasing exposure bands at 1153cm^{-1} and 1070cm^{-1} are formed. The band at 1153cm^{-1}, which arises in the region typical for sulfates could be assigned to ν_3

vibration of $CaSO_4^{2-}$ (1153cm^{-1}) located at the surface (symmetric S-O stretching vibration) [12, 46, 47]. The band at 1070cm^{-1} was assigned by different authors to SO_3^{2-} formed on Al_2O_3/CaO [48-50].

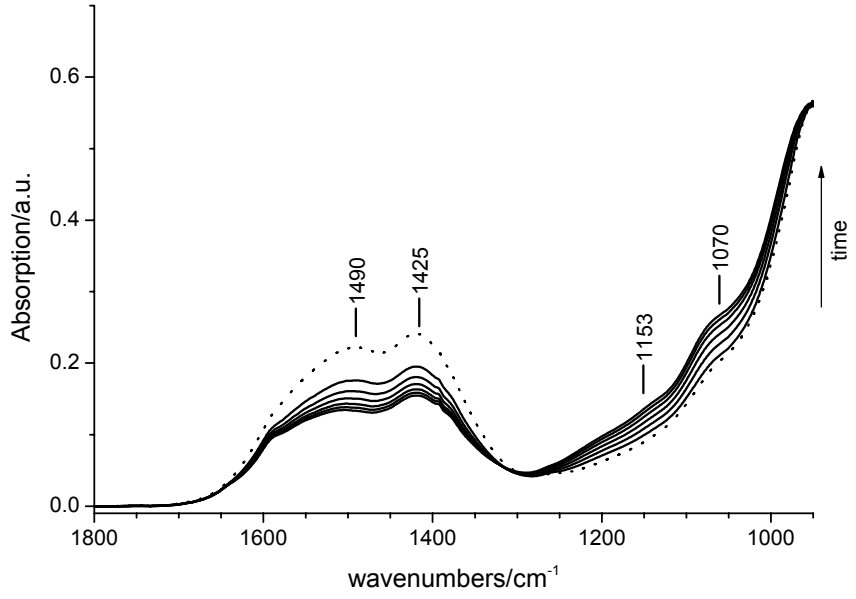

Fig. 5.8 : Time resolved IR spectra of CaO-Al_2O_3 sample during the exposure to 10ppm SO_2 + 12% O_2 at 523K (dotted line = fresh sample, full line Δt = 20min, first spectrum at 20min).

The spectra recorded for the Mn/CaO-Al_2O_3 material during exposure to 10ppm SO_2 + 12% O_2 are shown in Fig. 5.9. Four new bands at 1358, 1227, 1146 and 1070cm^{-1} arise accompanied by the decrease of the carbonate bands. The bands at 1146cm^{-1} and 1070cm^{-1} could be assigned to the $CaSO_4$ and to sulfite species, respectively, similar to the result obtained for the CaO-Al_2O_3 material. The additional bands at 1358cm^{-1} and 1227cm^{-1} appear in the typical range for organic sulfates. They are assigned to the symmetric and asymmetric vibration of a S=O bond (e.g. from $(Al_2O)_3S=O$) located on the surface of the material [10, 12, 51-53]. Alternatively Kijlstra *et al.* assigned this band to sulfate species on Mn, which could not be excluded for the samples investigated [54]. However, the presence of bulk $MnSO_4$ is unlikely as it should lead to an intense band around 1200-1180cm^{-1} [55].

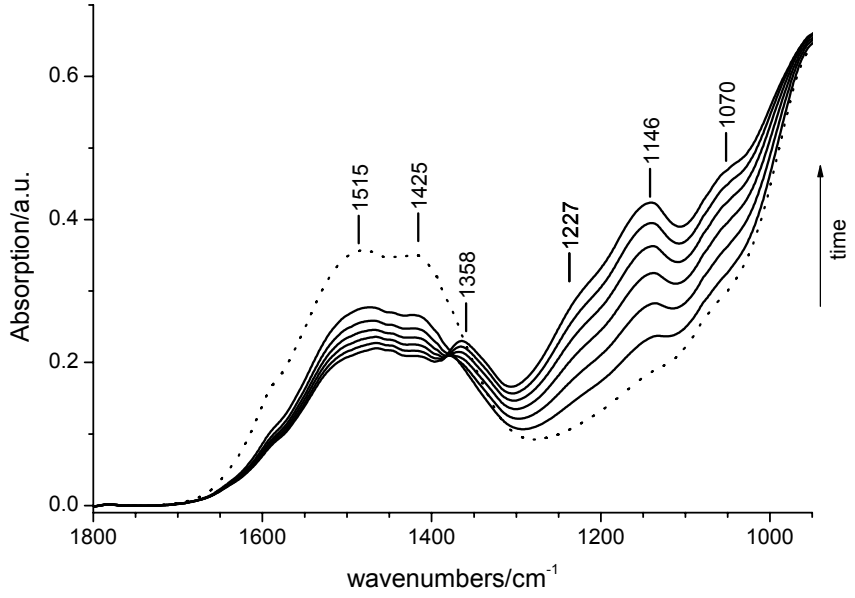

Fig. 5.9 : Time resolved IR spectra of $Mn/CaO-Al_2O_3$ sample during the exposure to 10ppm SO_2 + 12% O_2 at 523K (dotted line = fresh sample, full line Δt = 20min, first spectrum at 20min).

The time resolved IR spectra of the $Na/Mn/CaO-Al_2O_3$ material are depicted in Fig. 5.10. During the exposure to the SO_2 mixture bands located at 1151cm^{-1} and 1070cm^{-1} were observed, while the intensities of the bands in the carbonate region decreased. The broad band around 1151cm^{-1} is assigned to a bulk sulfate species however the bands of Na_2SO_4 and $CaSO_4$ are strongly overlapping in this region [56, 57].

The results obtained from the *in situ* IR measurement for the three materials investigated during exposure to SO_2/O_2 show a similar pattern. The peaks located in the carbonate region 1640cm^{-1}-1360cm^{-1} decreased whereas bands were formed in the region 1360cm^{-1}-1000cm^{-1}, typical for S-O/S=O vibrations indicating the formation of sulfate/sulfite species.

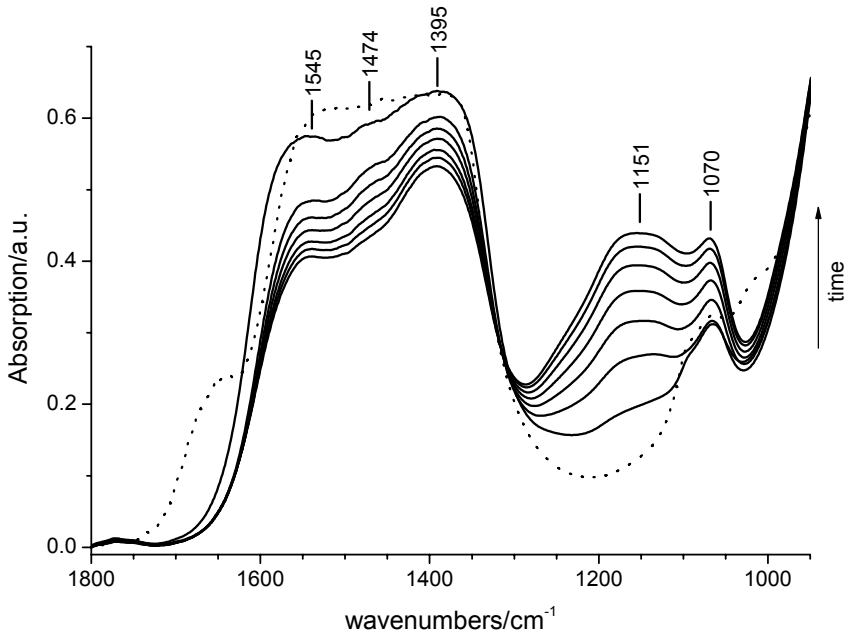

Fig. 5.10 : Time resolved IR spectra of Na/Mn/CaO-Al_2O_3 sample during the exposure to 10ppm SO_2 + 12% O_2 at 523K (dotted line = fresh sample, full line Δt = 20min, first spectrum at 20min).

5.3.8 *In situ* IR spectra in presence of H_2O

The materials have been investigated in presence of 10% water in air which is similar to 0.3% relative humidity at 523K. On all samples investigated a broad peak around 3300$cm^{-1}$and a small peak at 1640cm^{-1} were observed (graphs not shown) which could be assigned to physisorbed water on the surface [58]. The time resolved IR spectra recorded *in situ* for the CaO-Al_2O_3 material in presence of 10% H_2O, 12% O_2 and 10ppm SO_2 at 523K are shown in Fig. 5.11.

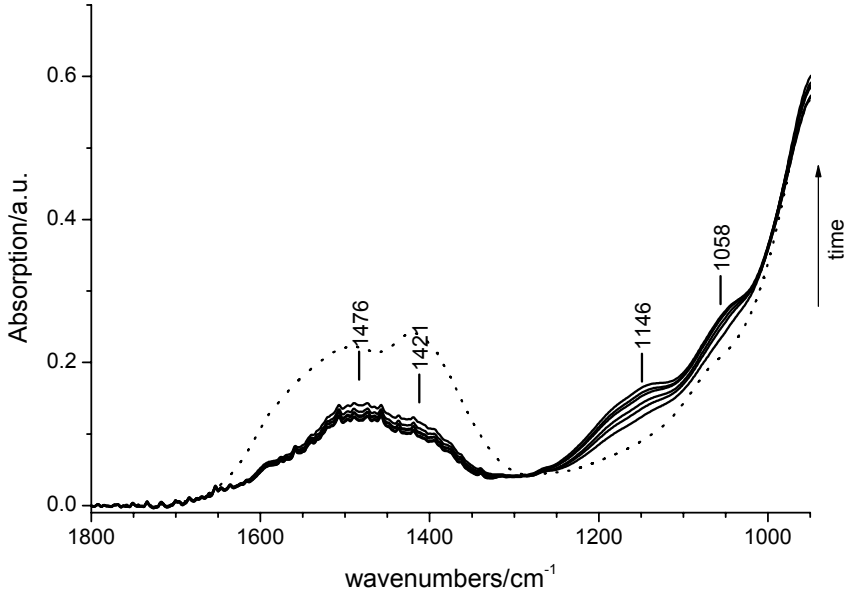

Fig. 5.11 : Time resolved IR spectra of $CaO\text{-}Al_2O_3$ sample during the exposure to 10ppm SO_2 + 12% O_2 + 10% H_2O at 523K (dotted line = fresh sample, full line Δt = 20min, first spectrum at 20min).

On the support two peaks assigned to $CaSO_4$ and sulfite type species (1058cm^{-1} and 1146cm^{-1}) were formed and, simultaneously, the peaks assigned to $CaCO_3$ (1476$cm^{-1}$and 1421cm^{-1}) decreased. It is important to note that a shift of ν=+7cm^{-1} with respect to the sample treated under dry conditions was observed for the band at 1058 cm^{-1} ($CaSO_4$).

Fig. 5.12 shows the time resolved IR spectra of the $Mn/CaO\text{-}Al_2O_3$ material exposed to SO_2 + O_2 + H_2O at 523K. Also for this material the bands assigned to carbonates are decreasing (fresh sample = dotted line), while the bands assigned to a sulfite and sulfate type species (1148cm^{-1} and1058cm^{-1}) are increasing. Note that surface sulfate species observed under dry conditions could not be identified on this material in presence of water. However, switching to dry helium leads to the formation of a band located at 1349cm^{-1} (not shown here). This band is located about 9cm^{-1} shifted to higher wavenumbers compared to the surface sulfate species observed under dry conditions (see Fig. 5.10).

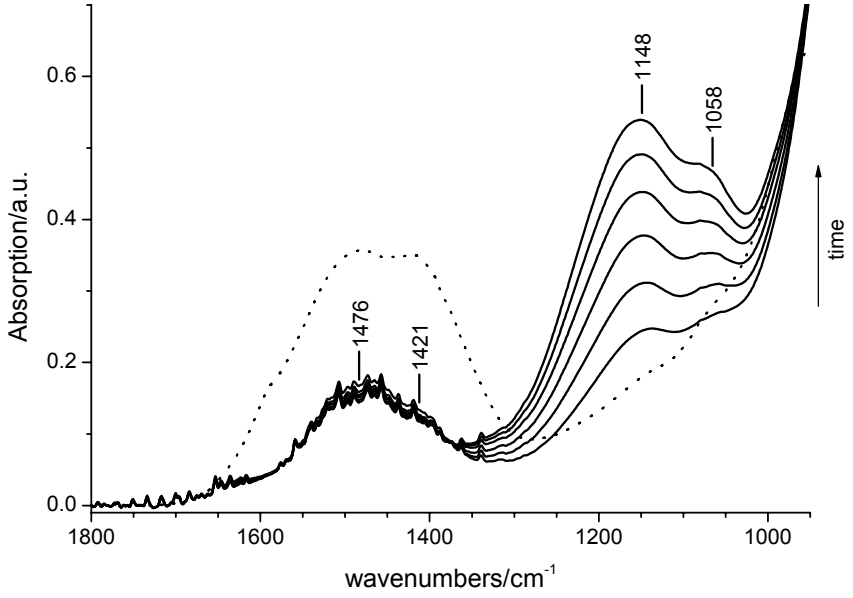

Fig. 5.12 : Time resolved IR spectra of Mn/CaO-Al_2O_3 sample while exposure to 10ppm SO_2 + 12% O_2 +10% H_2O at 523K (dotted line = fresh sample, full line Δt = 20min, first spectrum at 20min).

This indicates that the surface sulfate band is perturbed by the adsorbed water resulting in a frequency shift to higher wavenumbers and could be therefore covered by the intense carbonate band. Saur *et al.* found a similar behavior for Al_2O_3/Fe_2O_3 [10]. The sample Na/Mn/CaO-Al_2O_3 exposed to SO_2 + O_2 in presence of H_2O is shown in Fig. 5.13. The decrease of the carbonate peaks (1475 and 1404cm^{-1}- Na_2CO_3 and $CaCO_3$) is clearly observed. At low exposure time a shoulder at 1060cm^{-1} appears which could be attributed to the sulfite type species. With increasing exposure time a broad peak at 1125cm^{-1} is formed, which could not be clearly assigned to a single sorption site.

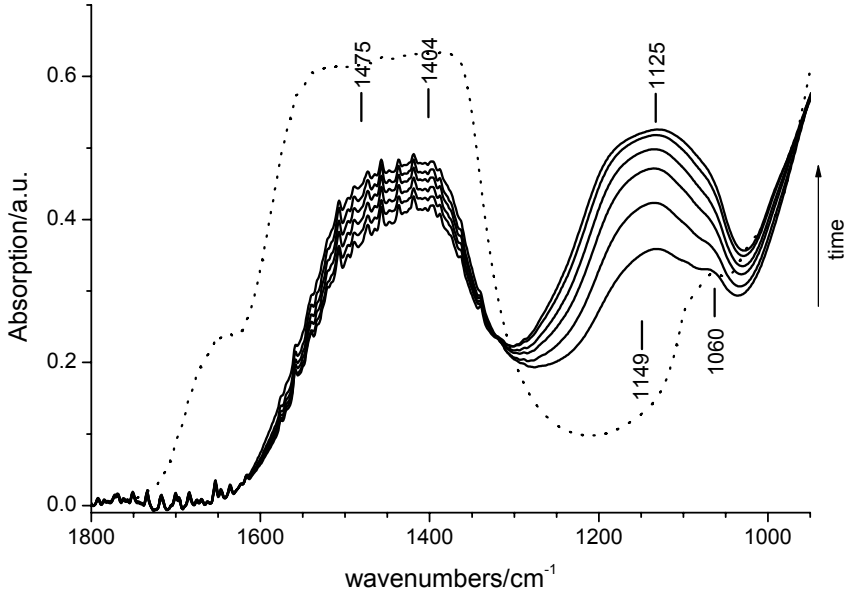

Fig. 5.13 : Time resolved IR spectra of Na/Mn/CaO-Al_2O_3 sample while exposure to 10ppm SO_2 + 12% O_2 +10% H_2O at 523K (dotted line = fresh sample, full line Δt = 20min, first spectrum at 20min).

The effect of water in the reaction mixture is summarized in Fig. 5.14 depicting the comparison of all samples in absence/presence of 10% water after exposure to the reaction mixture for 150 minutes. Note that similar molar extinction coefficients for the sulfates species on the various materials were assumed. The intensities of the spectral features in the region for sulfates is found to be in the order CaO-Al_2O_3 < Mn/CaO-Al_2O_3 < Na/Mn/CaO-Al_2O_3 indicating that the Na promoted material shows the highest sulfate loading on the sample (in presence and absence of water). Additionally on all samples studied the higher intensity of the sulfate bands under wet conditions indicates that water also acts as a promoter for the adsorption of SO_2. The strong increase of the bands is always accompanied by a faster decrease of carbonate species.

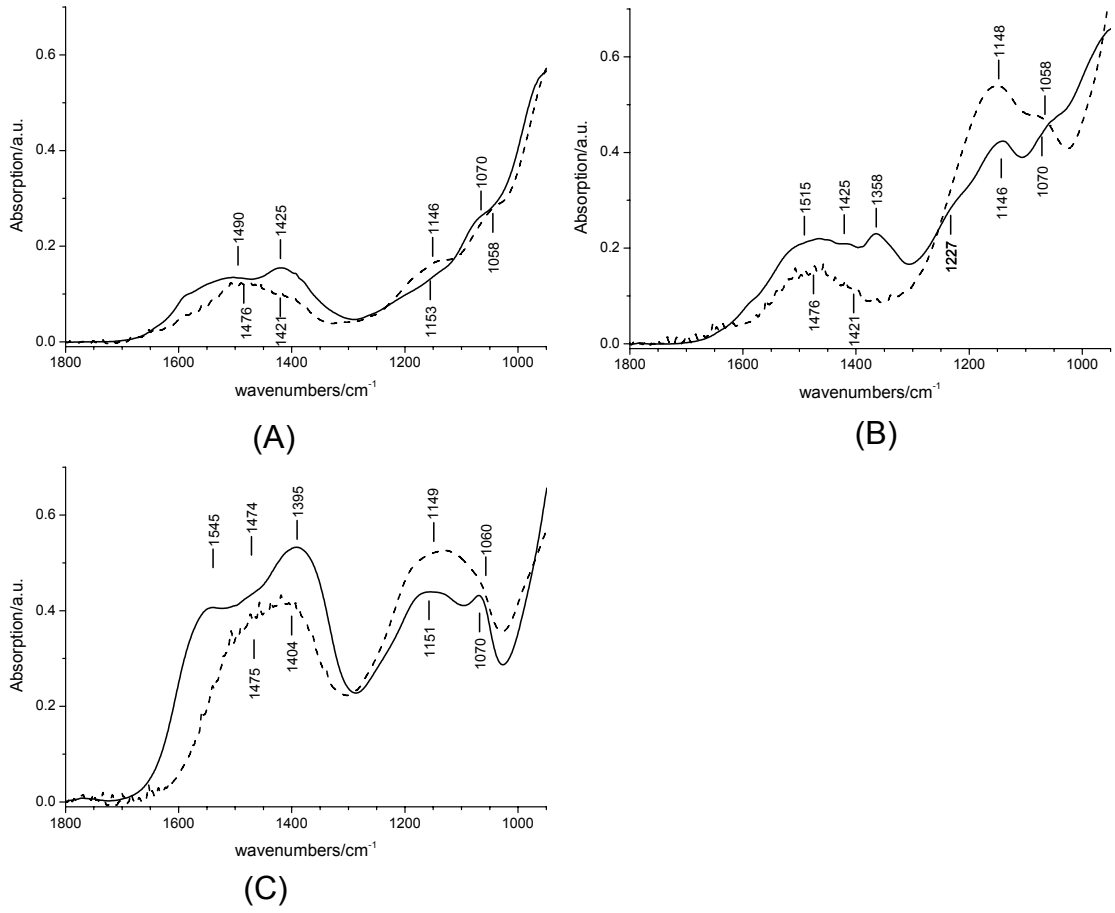

Fig. 5.14 : IR spectra of $CaO\text{-}Al_2O_3$ (A), $Mn/CaO\text{-}Al_2O_3$ (B) and $Na/Mn/CaO\text{-}Al_2O_3$ (C) after 150min exposure to 10ppm SO_2 + 12% O_2 (solid line) and in additional presence of 10% H_2O (dashed line).

5.3.9 2D Correlation analysis

However, from *in situ* infrared spectroscopy for the $Na/Mn/Al_2O_3$ material the two features located at 1358cm^{-1} and 1225cm^{-1} (see Fig. 5.15) found on $Mn/CaO\text{-}Al_2O_3$ are absent in this sample (see Fig. 5.10). From the spectra recorded under dry conditions, it seems possible that these features are obscured by the large peaks assigned to carbonate species located in the region from 1600cm^{-1}-1340cm^{-1} (see Fig. 5.10). Therefore, the time resolved *in situ* spectra were further analyzed by the 2D Correlation Analysis, leading to the contour plots as shown in Fig. 5.15. As already discussed the asynchronous plot obtained is especially useful in the determination of unrevealed, hidden features in 1D datasets. However, the numerous problems involved with the calculation of the asynchronous plot reported in literature require special precaution in the

application of this tool due to the increase of the artifact formation obtained by effects such as peak shifting or band broadening by using large datasets [15, 25, 59].

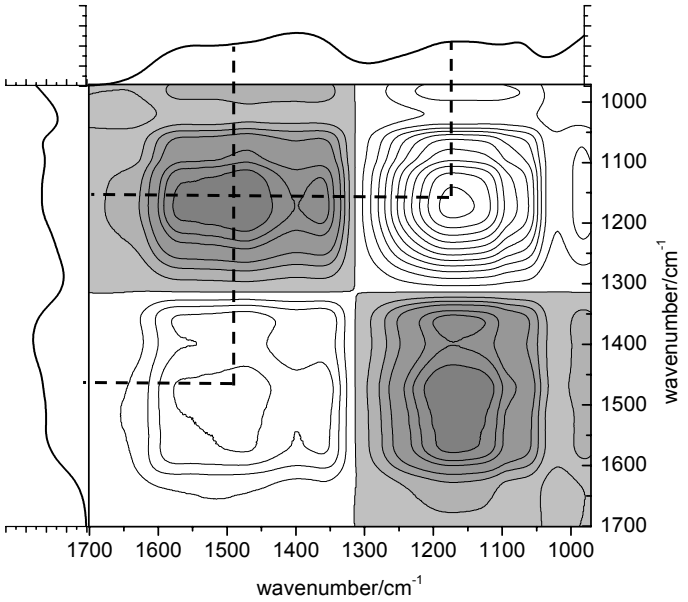

(A)

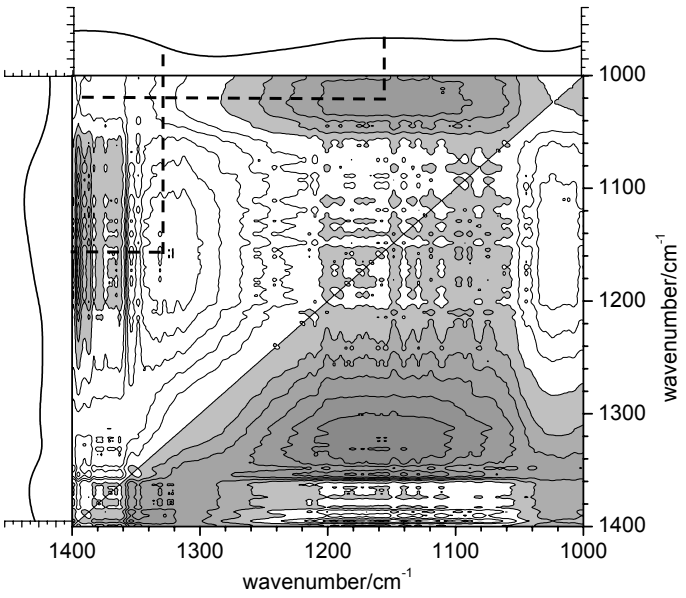

(B)

Fig. 5.15 : 2D correlation analysis plots calculated for the sample Na/Mn/CaO-Al_2O_3. (A) synchronous plot calculated from the whole dataset (see Fig. 5.10 total exposure time 150min), (B) asynchronous plots calculated for the sample exposed to 10ppm SO_2 + 12% O_2 at 523K (Δt=30min), shaded area represent negative values.

The time range for the asynchronous plot was therefore set to 30min to prevent the formation of misleading artifacts. The synchronous plot representing the changes occurring at the same time is depicted in Fig. 5.15. Two distinct auto-peaks centered at 1475cm^{-1} and 1150cm^{-1} that mark the regions of interest were observed. The negative sign of cross-peaks Φ(1475cm^{-1},1150cm^{-1}) gives evidence for a change of the bands in opposite direction. This indicates that the carbonates are consumed while the sulfates are formed, which is in good agreement with the observations from the 1D plots showing a decreasing intensity in these spectral regions (see Fig. 5.10). A small auto-peak at 1370cm^{-1} indicates an additional peak located there, however the closeness of the carbonate peak could result in a overlapping.

The asynchronous plot calculated from the dataset recorded under dry conditions (Fig. 5.15B) gives rise to two distinct cross-peaks located at the intersections Ψ(1321cm^{-1},1155cm^{-1}) and Ψ(1155cm^{-1},1080cm^{-1}) indicating that the intensity of the spectral features at 1321cm^{-1}, 1155cm^{-1} and 1080cm^{-1} changes at exposure time. If $\Psi(\nu_1,\nu_2)$ is positive (white area in the plot), a band at ν_1 grows prior to a band at ν_2, and if $\Psi(\nu_1,\nu_2)$ is negative (gray shaded area in the plot) , the increasing of a band at ν_1 is behind that of a band at ν_2. In Fig. 5.15B, the peak at Ψ(1321cm^{-1},1155cm^{-1}) has a positive sign, suggesting that the band at 1321cm^{-1} precedes the band at 1155cm^{-1}. On the other hand, the asynchronous peak at Ψ(1155cm^{-1};1080 cm^{-1}) has a negative sign, indicating that the band at 1155cm^{-1} follows the other band. No correlation was observed at the peak at Ψ(1321cm^{-1};1080cm^{-1}) indicating a similar time resolved behavior of the species.

These results would suggest 3 different species present. The band at 1321cm^{-1} could be assigned to the similar surface sulfate species as on the Mn/Al_2O_3 while the band at 1155cm^{-1} is assigned to a bulk sulfate species. This assignment is confirmed by the results from the asynchronous plot showing a prior formation of the surface species compared to the bulk species. It is important to note that the synchronous intersection shows a negative sign which would result in an inversion of the sequence. However it is very likely that the positive peak in the synchronous plot from the sulfate band is covered by broad contribution of the carbonate band which is decreasing throughout the experiment. The similar time resolved behavior of 1321cm^{-1} and 1080cm^{-1} could be explained by the simultaneous decomposition of carbonates while the surface sulfates are formed.

The strong carbonate band located at 1070cm^{-1} in the fresh material could influence this correlation slightly. The later formation of bulk sulfates compared to the carbonate decomposition is confirmed by a negative correlation of the intersection at Ψ(1155cm^{-1};1080cm^{-1}).

However, despite the equivocalness in the determination of the sequence in which the peak (1321cm^{-1}) changes the application of the 2D Correlation Analysis leads to an unambiguous identification of the surface species. The similar one observed at the Mn/CaO-Al_2O_3 material could be obscured by the broad carbonate peak (1600cm^{-1}-1300cm^{-1}) in this sample (depicted in Fig. 5.10). The small difference in the position is proposed to be caused by a smaller dataset used for the calculation of the asynchronous plots.

5.3.10 Sulfur K-edge X-ray absorption spectroscopy

Sulfur X-ray adsorption spectroscopy is a powerful tool to determine the oxidation states of the sulfur present and is depicted in Fig. 5.16. The spectra of Na_2SO_3 (S^{+4}) and $CaSO_4$ (S^{+6}) show a shift of the absorption maximum of +4.1eV in between. This result is in good agreement according to literature pointing out the strength of this tool [28, 60, 61].

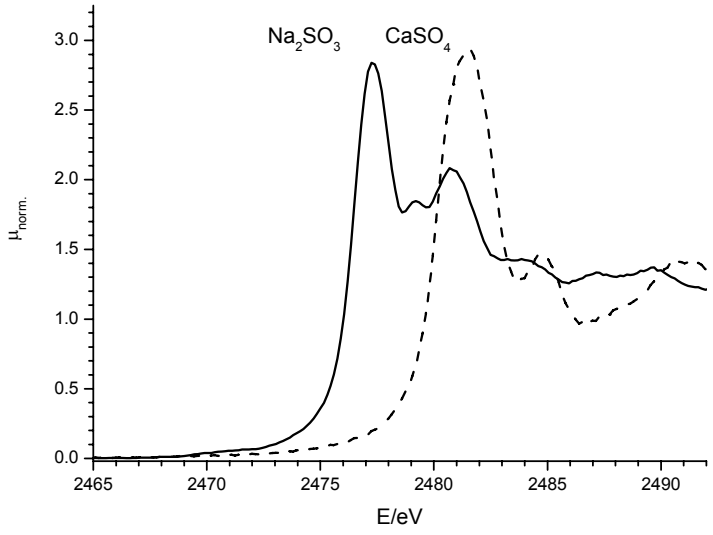

Fig. 5.16 : S K edge XANES of Na_2SO_3 and $CaSO_4$.

5.3.11 *In situ* S K-edge XANES

The time resolved S K-edge XANES during the exposure to 10ppm SO_2 + 12% O_2 as well as under reducing conditions (5% H_2 in He) is shown in Fig. 5.17. During exposure to SO_2, two distinct peaks at 2477.2eV and 2481.5eV indicate that sulfate S^{+4} and sulfite S^{+6} species are present [26, 62, 63].

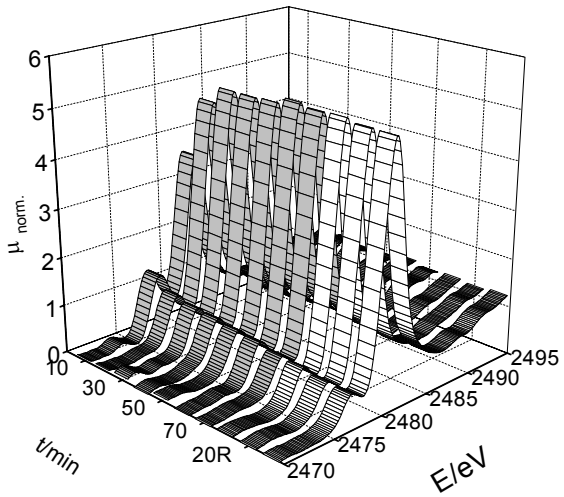

Fig. 5.17 : Time resolved *in situ* S K-edge XAFS of $CaO\text{-}Al_2O_3$ exposed to 10ppm SO_2 + 12% O_2 (dark grey bands) or 5% H_2 in He (white bands)

The time resolved behavior was revealed by applying a least square fitting procedure as described in the experimental section determining the fraction of sulfite and sulfates. Fig. 5.18 depicts an example fit. Note that the intensity of the peak assigned to the electron transitions strongly depends on the occupancy of the S p states and, therefore, the intensities of the peak for S^{+4} and S^{+6} can not directly be compared, as shown by Huffman *et al.* [64].

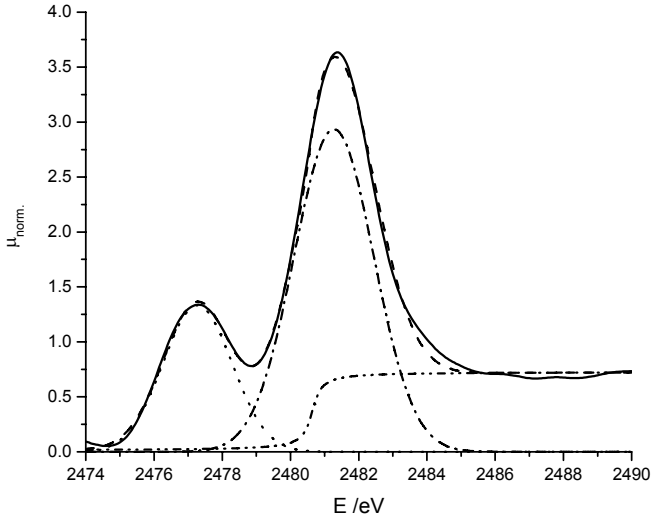

Fig. 5.18 : S K-edge spectra and least square fitted results of $CaO\text{-}Al_2O_3$ after 10min 10ppm SO_2 + 12% O_2 at 523K (full line = original spectra; dashed-dotted line = sulfate species; dotted line = sulfite species; dashed-double dotted line = arc tan function; dashed line = summed simulated spectra).

The relative fraction of the samples in dependence of the exposure time is shown in Fig. 5.19. After 10min of exposure to 10ppm SO_2 in 12% O_2 approx. 25% of the total sulfur on the $CaO\text{-}Al_2O_3$ material is in the form of sulfite. With increasing exposure time under oxidizing conditions the sulfite fraction remains almost constant at around 20%. After switching to reducing conditions a slight reduction could be observed. Increasing the reduction time shows only minor influence on the sulfite fraction. The sulfate fraction rises with increasing exposure time indicating that the sulfite is oxidized to sulfates. Switching to reducing conditions shows only small changes in the sulfate fraction indicating the formation of a stable sulfate species. The $Mn/CaO\text{-}Al_2O_3$ shows an initial relative sulfite fraction of 13% and sulfate fraction of 87% respectively. From 30min on the sulfite fraction remains stable at 10% and the sulfate at 90% respectively. Switching to reducing conditions showed no influence on the sulfite fraction. On the $Na/Mn/CaO\text{-}Al_2O_3$ material with 1% of relative sulfite fraction the lowest amount was detected. Practically all sulfur present is sulfate indicated by a 99% fraction.

In general the impregnation with Mn leads to a better oxidation indicated by a higher sulfate fraction compared to the $CaO\text{-}Al_2O_3$. Additional depositing of Na_2CO_3 leads to a further enhancement of the sulfate formation indicated by a almost complete sulfate fraction.

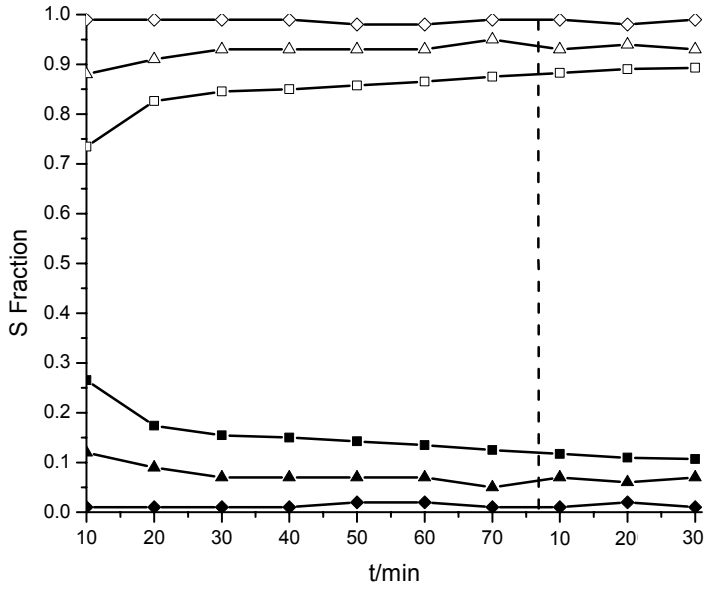

Fig. 5.19 : Relative fractions of sulfate (S^{+6}; open symbols) and sulfite (S^{+4}; bold symbols) present on $CaO\text{-}Al_2O_3$ (□), $Mn/CaO\text{-}Al_2O_3$ (Δ) and $Na/Mn/CaO\text{-}Al_2O_3$ (◊) while exposure to 10ppm SO_2 + 12% O_2 (left of the dashed line) and 5% H_2 in He (right of the dashed line) at 523K.

To monitor the effect of water on the SO_x storage process under oxidizing conditions the experiment was repeated in presence of water to gain deeper insight whether water inhibits or promotes the full oxidation of sulfur. Fig. 5.20 depicts the results obtained from the least square fitting procedure. On the $CaO\text{-}Al_2O_3$ after 10min exposure under oxidizing conditions in presence of water, sulfite represents 55% relative fraction and sulfate 45% respectively of all sulfur adsorbed. With increasing exposure time the sulfite fraction decreases continuously to a final level of 20%. Likewise the relative sulfate fraction increases until 80% after 70min. In contrast to this the $Mn/CaO\text{-}Al_2O_3$ and $Na/Mn/CaO\text{-}Al_2O_3$ samples show almost no sulfite present from the beginning on, pointed out by 99% relative sulfate fraction over the whole time investigated. No significant deviation between the additional impregnation with Na was observed implying that the main influence is carried out by an oxidation component present rather than Na as additional storage component.

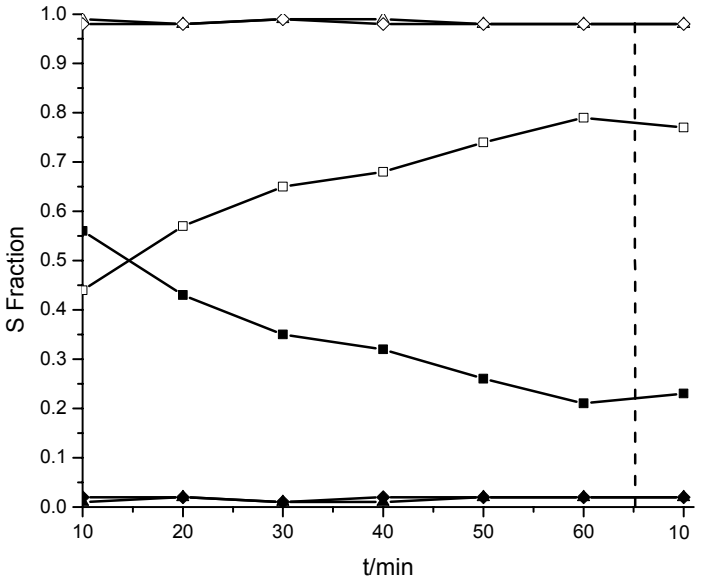

Fig. 5.20 : Relative fractions of Sulfate (S^{+6}; open symbols) and sulfite (S^{+4}; bold symbols) present on $CaO\text{-}Al_2O_3$ (□), $Mn/CaO\text{-}Al_2O_3$ (Δ) and $Na/Mn/CaO\text{-}Al_2O_3$ (◊) while exposure to 10ppm SO_2 + 12% O_2 +10% H_2O (left of the dashed line) and pure He (right of the dashed line) at 523K.

5.4 Discussion

Calcium based materials for removal of SO_x are well known for high temperature application [65-68, 69]. However there are a lot of limitations regarding the temperature range and the capacity of the materials investigated [70, 71]. In absence of a potential oxidation component it is well known that the SO_2 sorption mainly depends on the particle size and the state of the calcium in the material [72-74]. The results obtained from N_2 physisorption and XRD suggest that the support material $CaO\text{-}Al_2O_3$ is mainly amorphous with a mesoporous structure. Furthermore the lack of detection of CO_2 regarding the theoretical amount of calcium in the material indicates that Ca is only in a minor phase present as carbonate. The high temperature applied during the calcination of the precursor could lead to the formation of a $CaO\text{-}Al_2O_3$ phase, even at a relatively low temperature for this reaction, according to literature [75, 76]. As several authors showed a lower carbonate decomposition temperature result from the better heat transfer of small particles of $CaCO_3$ a highly dispersed carbonated species can be assumed regarding the TPD results [77, 78]. Moreover, the additional calcination after the Mn impregnation removes bulk-like carbonates stable until 873K.

However, a similar pattern for the release of CO_2 from Mn/CaO-Al_2O_3 is observed indicating the presence of the same carbonate containing species. Consequently this species must be located on the surface.

The further impregnation with Mn leads to a lower pore volume indicating a partial blocking of the pores. However the main pore structure seems to be preserved. The absence of additional reflexes in the XRD of the Mn/CaO-Al_2O_3 sample suggests the presence of Mn in small particles. According to the infrared spectrum only a partial coverage of the surface with this Mn can be assumed, as shown by a slight reduction in the intensity of the Al_2O_3 hydroxyl groups. The impregnation with Na, however, leads to the formation of big Na_2CO_3 particles which were observed by XRD. The decrease of the pore volume, which is higher compared to the theoretical volume of impregnated sodiumcarbonate, indicates that a pore blocking takes place due to the impregnation. These results are in perfect agreement with the IR spectrum representing a complete removal of the bands assigned to hydroxyl groups suggesting a major coverage of these. Additionally the higher decomposition temperature of the surface carbonates with respect to the CaO-Al_2O_3 indicates the coverage of these sites, as observed by TPD.

The results from all the physicochemical characterization suggest the presence of a highly dispersed potential storage component (Ca, Na) as well as a small particle size for the oxidation component (Mn). Furthermore, the CO_2 desorption profile indicates that at the operation temperature (523K) the $CaCO_3$ present on the material is mainly decomposed. Therefore the active storage component is rather CaO than $CaCO_3$.

After reaching the full SO_x saturation at 523K on the CaO-Al_2O_3 sample the absence of additional XRD reflections suggests the formation of a highly dispersed sulfur species on the material. The absence of the IR bands for $CaSO_3$ as well as the presence of sulfite type species obtained by means of *in situ* S K XANES could mean that the sulfite species is located on the Al_2O_3. This is supported by the findings of IR showing small contributions of sulfites probably located on Al_2O_3. According to literature the formation of $CaSO_4$ out of carbonates in absence of an oxidation component mainly depends on the particle size. The difference in the density of $CaCO_3$ and $CaSO_4$ results in a pore blocking during the storage process limiting the utilization [71, 79-81]. The prepared CaO-Al_2O_3 with a highly dispersed

Ca species integrated in the mesoporous structure seems therefore to be quite sufficient at this low temperature as indicated by a 57% utilization of the theoretical amount of calcium. This utilization is similar to the highest possible (57%), typically reached only at >1000K according to literature [82-84]. The rate limiting step at low exposure times seems to be the oxidation of SO_2 to SO_3, with respect to the results obtained from *in situ* S K-edge XANES. However, the S-shape of the breakthrough curve represents in the end the typical behavior of a limitation by diffusion, which is in good agreement according to literature on Ca-based sorbents [34, 85, 86]. The expected species obtained from the results are depicted in Fig. 5.21 and represent the formation of the sulfite (B) as well as the sulfate species (C) according to the results from the *in situ* IR and *in situ* S K-edge XANES.

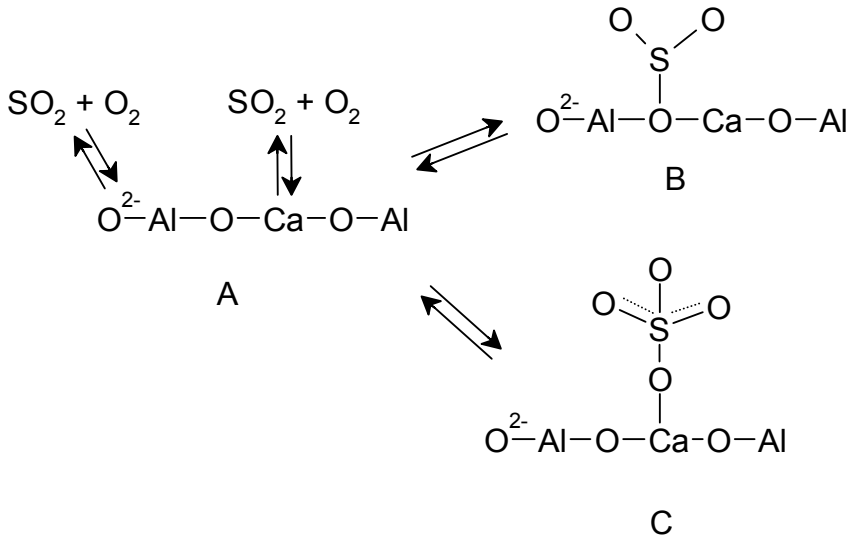

Fig. 5.21 : Formation of sulfur species on $CaO\text{-}Al_2O_3$ as obtained from *in situ* IR and *in situ* S K-edge XANES A = fresh material, B = sulfite type species, C = unidentate sulfate on the support.

The SO_2 adsorption in oxidizing conditions on the materials $Mn/CaO\text{-}Al_2O_3$ and $Na/Mn/CaO\text{-}Al_2O_3$ however, results in the formation of hardly reducible bulk species, $CaSO_4$ and Na_2SO_4, respectively, identified in the corresponding XRD pattern. The higher intensity of the $CaSO_4$ assigned bands in the infrared spectra on the $Mn/CaO\text{-}Al_2O_3$ indicates a higher amount of $CaSO_4$ present. Nevertheless, the absence of the IR bands of bulk $MnSO_4$ accompanied with an increasing storage capacity suggests that the surface sulfate on the Al_2O_3 or Mn contributes additional to the higher uptake. That Mn is rather a suitable oxidation component than a potential storage component, as shown by Li *et al.*, is supported by the findings of in situ S K-edge XANES showing a higher fraction of sulfates compared

to sulfites [8]. Only 65% of the theoretical amount of potential storage components (Mn, Ca) or 85% of the Calcium, respectively is used on the Mn/CaO-Al_2O_3 indicating even at high SO_2 loading the presence free oxidation and storage sites. Therefore it is assumed that the bulk diffusion limited the full utilization rather then the presence of potential oxidation sites. The results from the temperature programmed reaction showed only a complete sorption in the first heating up while at the second one a stronger penetration of the SO_2 occurs. This supports the finding that at low temperatures mainly the bulk transport seems to be limiting rather than the oxidation.

The extremely increased total SO_x uptake obtained for the Na/Mn/CaO-Al_2O_3 recommend sodium as a good promoter for high storage capacity, even at higher temperatures as shown by the TPR experiment. Furthermore the depositing of Na_2CO_3 leads to the formation of hardly reducible bulk sulfate species during the sorption revealed by XRD. Similar promoting results were obtained from Laursen and coworkers [87]. However the authors performed a calcination procedure up to 1000K, prior SO_2 sorption experiments,) leading to the formation of Na_2O. Therefore a direct comparison is not possible. The results obtained with the 2D Correlation Analysis suggest that the similar manganese surface sulfate species formed as on the Mn/CaO-Al_2O_3 suggesting the similar reaction network [54]. The reduction of the amount of surface sulfate species located on the Al_2O_3 in comparison to Mn/CaO-Al_2O_3 as shown by IR could result from the coverage of the surface due to the impregnation. However, the complete absence of these species could not be completely excluded due to the overlapping carbonate band at 1070cm^{-1}. The absence of sulfite type species as shown by *in situ* S K XANES suggest that the oxidation capacity is not affected by the impregnation. The final storage capacity reached on the sodium containing sample is equal to 25% with respect to the Na and Ca present, indicating that rather the transport into the bulk than the amount of potential storage component is the rate limiting step. Moreover the presence of big Na_2CO_3 particles could result in slower surface layer diffusion to the sorption sites as shown by Stelson *et al.* [88]. However, the presence of the excellent sulfate storage component sodiumcarbonate promotes in general the adsorption of SO_2, especially at low temperatures as shown in literature [89, 90].

The expected reaction network obtained from the results of IR and S K-edge XANES are summarized in Fig. 5.22. It is in good agreement with results

obtained by other authors for metal oxides materials as Al_2O_3, Fe_2O_3 or TiO_2 [10, 12].

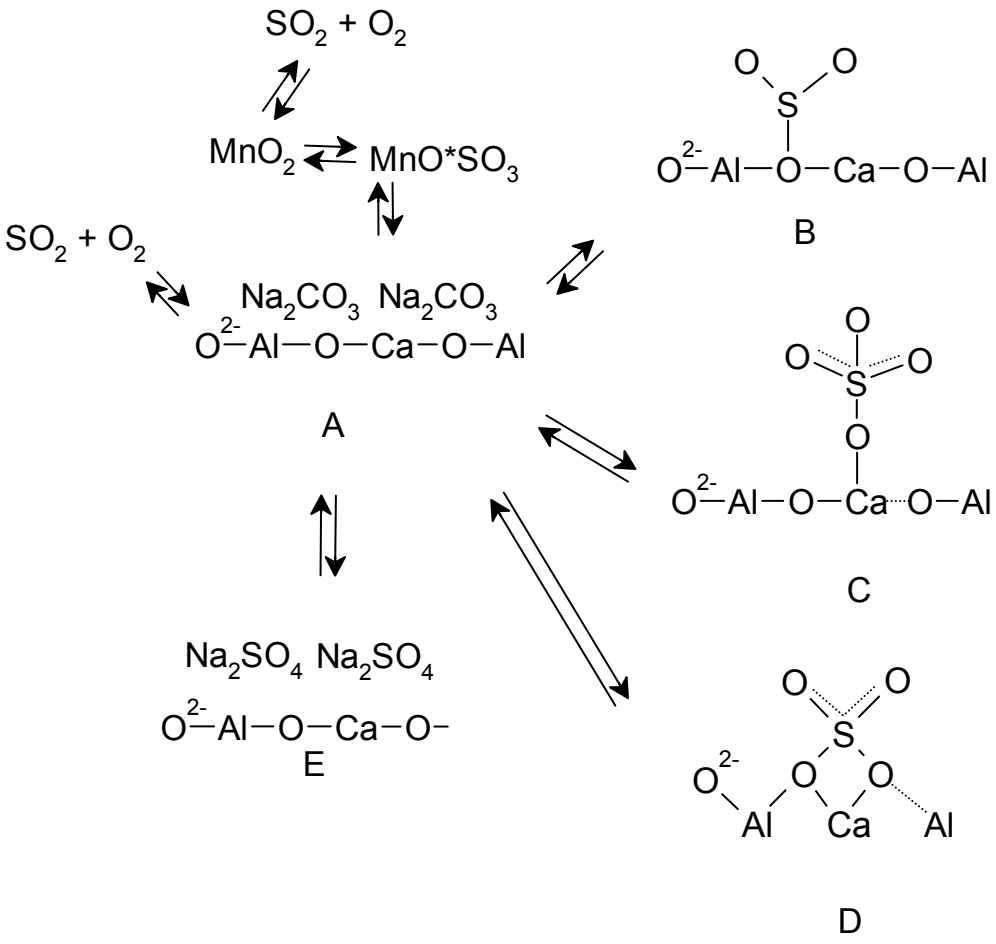

Fig. 5.22 : Formation of sulfur species on CaO-Al_2O_3 as obtained from *in situ* IR and *in situ* S K XANES, A = fresh material, B = sulfite type species, C = unidentate sulfate on the support, D = bridged sulfate on the support E = bulk sulfate on Na.

In addition to the promoting effects of Mn and Na, an increase in the uptake for all samples except the pure support CaO-Al_2O_3 were observed in presence of water. The wet conditions lead to the formation of a surface layer of water as shown by IR spectroscopy. On CaO-Al_2O_3 the higher fraction of sulfite species (*in situ* S K-edge XANES) indicates that the oxidation could be a limiting step. As the oxidation takes place on the surface the presence of the water layer hinders the formation of SO_3. Similar results for CaO/$Ca(OH)_2$ (formed from $CaCO_3$ in presence of water) were presented by several authors suggesting that the formation of $CaSO_3$ ½H_2O is being strongly influenced by the amount of H_2O on the surface [91, 92]. Furthermore the increasing sulfate fraction indicates that at long exposure times the product diffusion contributes additionally to the low

uptake. Nevertheless, the comparison to the final state of the sample showed almost similar fractions in absence and presence of water.

The *in situ* S K-edge XANES results reported here show clearly that in presence of water and Mn, the oxidation is accelerated and it is suggested not to be the rate limiting step. Chughtai *et al.* presented a mechanism of sulfate formation on MnO_2 including the adsorption of a H_2O*SO_2 on MnO_2 as the accelerating effect [36]. The surface sulfate species located on Mn as identified after switching to dry conditions by IR strongly suggest this meachnism. However, there was no direct experimental evidence of this species. Furthermore it is very likely that in presence of water and Mn the formation of sulfuric acid takes place leading to a faster conversion from surface to bulk species [93-95]. The higher amount of sulfates in the bulk phase was additionally shown by higher XRD reflections ($CaSO_4$). In presence of sodium, the small contribution of sulfite species identified by means of *in situ* S K-edge XANES suggests a very small hindrances of the oxidation of SO_2, which could be caused by the partial coverage of the surface as shown by IR spectroscopy and CO_2 desorption profile.

The enhancing effect of water observed was also shown by Al-Hosney and coworkers however the high relative humidity rules out a direct comparison [58]. According to literature on carbonates the presence of water leads to a reduction of the decomposition temperature accompanied with an increase of their decomposition rate. The so formed sorption centre could additionally facilitate the SO_2 adsorption [96, 97]. However, after the formation of the water layer the diffusion plays an important role [98].

5.5 Conclusions

With the combination of two different experimental *in situ* techniques (S K XANES and IR) and the application of 2D Correlation Analysis, various sulfate species could be clearly identified on the materials investigated. It has been shown that a sophisticated sulfur trapping support for low SO_2 concentrations at low temperatures in absence and presence of water was prepared by precipitation of calcium in presence of Al_2O_3. The physicochemical characterization (BET, XRD and TPD) revealed a mesoporous material with Calcium mainly present in oxide form. The sorption capacity was further improved by the additional impregnation with Mn and Na resulting in an excellent SO_x trapping material which could be

applied in diesel exhaust gas streams at low temperatures. Ca used as a storage component shows high weight advantages compared to conventional Ba based materials being important for a potential application in the automotive sector. The application of *in situ* S K-edge XANES could clearly reveal Mn as sufficient oxidation component at low SO_2 concentrations in absence and presence of water. The usage of a noble metal component is not necessary in this case. The combination of *in situ* IR and the 2D correlation technique lead to the identification of various surface and bulk type species which could be clearly assigned to the sorption sites. The influence of water on the storage capacity was investigated showing a higher sorption capacity accompanied with a faster bulk transport. The SO_2 sorption experiments showed that the total storage capacity as well as the time of complete SO_2 sorption was clearly increased compared to a second generation SO_x trapping material.

5.6 Acknowledgments

This work was supported by the European Union in the framework of project G3RD-CT2002 00793. We acknowledge the ANKA Angstroemquelle Karlsruhe for the provision of beamtime. Specially we would like to thank Stefan Mangold for the adaptation of the ANKA-XAS beamline for the experiments at the S K-edge and for the assistance during the experiments. The authors are also grateful to M. Neukamm for the BET measurements, Rolf Fricke and Ellen Schreier for providing the samples.

5.7 References

[1] P. Greening, *Topics in Catalysis,* 2001, **16**, 5.
[2] W. S. Epling, L. E. Campbell, A. Yezerets, N. W. Currier and J. E. Parks, *Catalysis Reviews-Science and Engineering,* 2004, **46**, 163.
[3] S. I. Matsumoto, *Catalysis Today,* 2004, **90**, 183.
[4] C. Sedlmair, K. Seshan, A. Jentys and J. A. Lercher, *Journal of Catalysis,* 2003, **214**, 308.
[5] C. Sedlmair, K. Seshan, A. Jentys and J. A. Lercher, *Research on Chemical Intermediates,* 2003, **29**, 257.
[6] L. Limousy, H. Mahzoul, J. F. Brilhac, F. Garin, G. Maire and P. Gilot, *Applied Catalysis B-Environmental,* 2003, **45**, 169.
[7] H. Mahzoul, L. Limousy, J. F. Brilhac and P. Gilot, *Journal of Analytical and Applied Pyrolysis,* 2000, **56**, 179.
[8] L. Y. Li and D. L. King, *Industrial & Engineering Chemistry Research,* 2004,
[9] J. H. Swisher and K. Schwerdtfeger, *Journal of Materials Engineering and Performance,* 1992, **1**, 399.
[10] O. Saur, M. Bensitel, A. B. M. Saad, J. C. Lavalley, C. P. Tripp and B. A. Morrow, *Journal of Catalysis,* 1986, **99**, 104.
[11] M. Waqif, M. Lakhdar, O. Saur and J. C. Lavalley, *Journal of the Chemical Society-Faraday Transactions,* 1994, **90**, 2815.
[12] T. Yamaguchi, T. Jin and K. Tanabe, *Journal of Physical Chemistry,* 1986, **90**, 3148.
[13] I. Noda, *Journal of the American Chemical Society,* 1989, **111**, 8116.
[14] I. Noda, A. E. Dowrey and C. Marcott, *Mikrochimica Acta,* 1988, **1**, 101.
[15] P. Haider, Y. Chen, S. Lim, G. L. Haller, L. Pfefferle and D. Ciuparu, *Journal of the American Chemical Society,* 2005, **127**, 1906.
[16] D. L. Elmore and R. A. Dluhy, *Applied Spectroscopy,* 2000, **54**, 956.
[17] I. Noda, *Vibrational Spectroscopy,* 2004, **36**, 143.
[18] J. Itoh, T. Sasaki, T. Ohtsuka and M. Osawa, *Journal of Electroanalytical Chemistry,* 1999, **473**, 256.
[19] I. Noda, *Applied Spectroscopy,* 2000, **54**, 994.
[20] I. Noda, A. E. Dowrey and C. Marcott, *Applied Spectroscopy,* 1993, **47**, 1317.
[21] I. Noda, A. E. Dowrey, C. Marcott, G. M. Story and Y. Ozaki, *Applied Spectroscopy,* 2000, **54**, 236A.
[22] P. D. Harrington, A. Urbas and P. J. Tandler, *Chemometrics and Intelligent Laboratory Systems,* 2000, **50**, 149.
[23] Y. Ozaki, S. Sasic, T. Tanaka and I. Noda, *Bulletin of the Chemical Society of Japan,* 2001, **74**, 1.
[24] S. J. Gadaleta, A. Gericke, A. L. Boskey and R. Mendelsohn, *Biospectroscopy,* 1996, **2**, 353.
[25] M. A. Czarnecki, *Applied Spectroscopy,* 1998, **52**, 1583.
[26] D. Solomon, J. Lehmann and C. E. Martinez, *Soil Science Society of America Journal,* 2003, **67**, 1721.
[27] G. N. George and M. L. Gorbaty, *Journal of the American Chemical Society,* 1989, **111**, 3182.
[28] A. Vairavamurthy, *Spectrochimica Acta, Part A: Molecular and Biomolecular Spectroscopy,* 1998, **54**, 2009.

[29] S. C. B. Myneni, *Reviews in Mineralogy & Geochemistry,* 2000, **40**, 113.
[30] V. Mazet, C. Carteret, D. Brie, J. Idier and B. Humbert, *Chemometrics and Intelligent Laboratory Systems,* 2005, **76**, 121.
[31] D. Adachi, Y. Katsumoto, H. Sato and Y. Ozaki, *Applied Spectroscopy,* 2002, **56**, 357.
[32] K. V. Klementev, *Journal of Physics D: Applied Physics,* 2001, **34**, 209.
[33] N. Orbey, G. Dogu and T. Dogu, *Canadian Journal of Chemical Engineering,* 1982, **60**, 314.
[34] T. Dogu, *Chemical Engineering Journal (Amsterdam, Netherlands),* 1981, **21**, 213.
[35] W. L. Duo, K. Laursen, J. Lim and J. Grace, *Powder Technology,* 2000, **111**, 154.
[36] A. R. Chughtai, M. E. Brooks and D. M. Smith, *Aerosol Science and Technology,* 1993, **19**, 121.
[37] V. Vadjic and M. Gentilizza, *Science of the Total Environment,* 1985, **44**, 245.
[38] F. A. Andersen and L. Brecevic, *Acta Chemica Scandinavica,* 1991, **45**, 1018.
[39] H. H. Adler and P. F. Kerr, *American Mineralogist,* 1962, **47**, 700.
[40] K. Buijs and C. J. H. Schutte, *Spectrochimica Acta,* 1961, **17**, 917.
[41] F. A. Miller and C. H. Wilkins, *Analytical Chemistry,* 1952, **24**, 1253.
[42] H. Knozinger and P. Ratnasamy, *Catalysis Reviews-Science And Engineering,* 1978, **17**, 31.
[43] C. Morterra and G. Magnacca, *Catalysis Today,* 1996, **27**, 497.
[44] P. O. Scokart, A. Amin, C. Defosse and P. G. Rouxhet, *Journal of Physical Chemistry,* 1981, **85**, 1406.
[45] C. Morterra, G. Magnacca, G. Cerrato, N. Delfavero, F. Filippi and C. V. Folonari, *Journal Of The Chemical Society-Faraday Transactions,* 1993, **89**, 135.
[46] A. Hezel and S. D. Ross, *Spectrochimica Acta,* 1966, **22**, 1949.
[47] J. M. Hunt, M. P. Wisherd and L. C. Bonham, *Analytical Chemistry,* 1950, **22**, 1478.
[48] M. A. Babaeva, A. A. Tsyganenko and V. N. Filimonov, *Kinetics and Catalysis,* 1985, **25**, 787.
[49] H. C. Yao, H. K. Stepien and H. S. Gandhi, *Journal of Catalysis,* 1981, **67**, 231.
[50] A. Datta, R. G. Cavell, R. W. Tower and Z. M. George, *Journal of Physical Chemistry,* 1985, **89**, 443.
[51] M. Waqif, O. Saur, J. C. Lavalley, S. Perathoner and G. Centi, *Journal of Physical Chemistry,* 1991, **95**, 4051.
[52] C. Sedlmair, K. Seshan, A. Jentys and J. A. Lercher, *Catalysis Today,* 2002, **75**, 413.
[53] K. C. Schreiber, *Analytical Chemistry,* 1949, **21**, 1168.
[54] W. S. Kijlstra, M. Biervliet, E. K. Poels and A. Bliek, *Applied Catalysis B-Environmental,* 1998, **16**, 327.
[55] F. Golinska, A. Lodzinska and F. Rozploch, *Polish Journal of Chemistry,* 1984, **58**, 31.
[56] R. A. Durie and J. W. Milne, *Spectrochimica Acta Part A-Molecular And Biomolecular Spectroscopy,* 1978, **34**, 215.
[57] E. Steger and W. Schmidt, *Berichte Der Bunsen-Gesellschaft Fur Physikalische Chemie,* 1964, **68**, 102.

[58] H. A. Al-Hosney and V. H. Grassian, *Physical Chemistry Chemical Physics,* 2005, **7**, 1266.
[59] A. Gericke, S. J. Gadaleta, J. W. Brauner and R. Mendelsohn, *Biospectroscopy,* 1996, **2**, 341.
[60] H. Sekiyama, N. Kosugi, H. Kuroda and T. Ohta, *Bulletin of the Chemical Society of Japan,* 1986, **59**, 575.
[61] D. A. McKeown, I. S. Muller, H. Gan, I. L. Pegg and W. C. Stolte, *Journal of Non-Crystalline Solids,* 2004, **333**, 74.
[62] A. Vairavamurthy, B. Manowitz, W. Q. Zhou and Y. S. Jeon, Determination of Hydrogen-Sulfide Oxidation-Products by Sulfur K-Edge X-Ray-Absorption near-Edge Structure Spectroscopy, American Chemical Society, Washington, p. 412.
[63] D. Li, G. M. Bancroft, M. Kasrai, M. E. Fleet, X. H. Feng and K. Tan, *Canadian Mineralogist,* 1995, **33**, 949.
[64] G. P. Huffman, S. Mitra, F. E. Huggins, N. Shah, S. Vaidya and F. L. Lu, *Energy & Fuels,* 1991, **5**, 574.
[65] M. Hartman and O. Trnka, *AIChE Journal,* 1993, **39**, 615.
[66] K. Svoboda, W. G. Lin, J. Hannes, R. Korbee and C. M. Vandenbleek, *Fuel,* 1994, **73**, 1144.
[67] A. Garea, J. R. Viguri and A. Irabien, *Chemical Engineering Science,* 1997, **52**, 715.
[68] P. A. Cengiz, J. Abbasian, N. R. Khalili, R. B. Slimane and K. K. Ho, *International Journal of Environment and Pollution,* 2002, **17**, 82.
[69] J. Cheng, J. H. Zhou, J. Z. Liu, Z. J. Zhou, Z. Y. Huang, X. Y. Cao, X. Zhao and K. F. Cen, *Progress In Energy And Combustion Science,* 2003, **29**, 381.
[70] M. Hartman and O. Trnka, *Chemical Engineering Science,* 1980, **35**, 1189.
[71] S. Zarkanitis and S. V. Sotirchos, *AIChE Journal,* 1989, **35**, 821.
[72] M. Hartman and R. W. Coughlin, *Industrial & Engineering Chemistry Process Design And Development,* 1974, **13**, 248.
[73] J. Klingspor, H. T. Karlsson and I. Bjerle, *Chemical Engineering Communications,* 1983, **22**, 81.
[74] P. Davini, *Fuel,* 2002, **81**, 763.
[75] B. S. Mitchell, K. Y. Yon, S. A. Dunn and J. A. Koutsky, *Journal of Non-Crystalline Solids,* 1993, **152**, 143.
[76] Y. M. Sung, *Journal of Materials Science,* 1997, **32**, 1069.
[77] G. Narsimhan, *Chemical Engineering Science,* 1961, **16**, 7.
[78] A. W. D. Hills, *Chemical Engineering Science,* 1968, **23**, 297.
[79] S. V. Sotirchos and S. Zarkanitis, *AIChE Journal,* 1992, **38**, 1536.
[80] M. Hartman, J. Pata and R. W. Coughlin, *Industrial & Engineering Chemistry Process Design And Development,* 1978, **17**, 411.
[81] D. C. Anderson, P. Anderson and A. K. Galwey, *Fuel,* 1995, **74**, 1018.
[82] R. B. Fieldes, N. A. Burdett and J. F. Davidson, *Transactions Of The Institution Of Chemical Engineers,* 1979, **57**, 276.
[83] J. D. Thibault, F. R. Steward and D. M. Ruthven, *Canadian Journal of Chemical Engineering,* 1982, **60**, 796.
[84] D. Kocaefe, D. Karman and F. R. Steward, *AIChE Journal,* 1987, **33**, 1835.
[85] A. B. Fuertes, G. Velasco, E. Fuente and T. Alvarez, *Fuel Processing Technology,* 1994, **38**, 181.
[86] R. H. Borgwardt, *Environmental Science and Technology,* 1970, **4**, 23.

[87] K. Laursen, A. A. Kern, J. R. Grace and C. J. Lim, *Environmental Science & Technology,* 2003, **37**, 3709.
[88] A. W. Stelson, *Japca-The International Journal Of Air Pollution Control And Hazardous Waste Management,* 1987, **37**, 830.
[89] D. H. McCrea, J. G. Myers and A. J. Forney, *Proc. Int. Clean Air Congr., 2nd,* 1971, 922.
[90] C. Guldur, G. Dogu and T. Dogu, *Chemical Engineering and Processing,* 2001, **40**, 13.
[91] J. Klingspor, A.-M. Stromberg, H. T. Karlsson and I. Bjerle, *Chemical Engineering and Processing,* 1984, **18**, 239.
[92] M. Bausach, M. Pera-Titus, C. Fite, F. Cunill, J. F. Izquierdo, J. Tejero and M. Iborra, *AIChE Journal,* 2005, **51**, 1455.
[93] J. C. Summers, *Environmental Science & Technology,* 1979, **13**, 321.
[94] J. L. P. Bernal and M. A. Bello, *Industrial & Engineering Chemistry Research,* 2003, **42**, 1028.
[95] T. Sydberger and N. Vannerberg, *Corrosion Science,* 1972, **12**, 775.
[96] B. S. Terry and G. McGurk, *Transactions Of The Institution Of Mining And Metallurgy Section C-Mineral Processing And Extractive Metallurgy,* 1994, **103**, C62.
[97] B. V. L'Vov, *Thermochimica Acta,* 1997, **303**, 161.
[98] S. E. Schwartz and J. E. Freiberg, *Atmospheric Environment,* 1981, **15**, 1129.

Chapter 6

Identification of transient sulfur species under lean-rich cycling conditions on potential SO_x storage materials

Abstract:

The influence of Pt and the reaction conditions during lean-rich cycling experiments were evaluated in plug flow experiments on a second generation SO_x trapping material. The combination of the Generalized 2D Correlation Analysis, 2D Sample-Sample Correlation Analysis and Factor Analysis using the MCR-ALS technique was applied to identify three different regimes present on the sample from in situ IR spectra. The combined application of these techniques led to the identification of carbonates, bulk and surface sulfate species. Transient surface sulfate species were diminished under reducing reaction conditions (rich operation mode) and formed under oxidative reaction conditions (lean mode).

The reduction of the surface sulfate species is proposed to be the main contribution to the SO_2 release observed under dynamic flow conditions. Pt facilitates the formation and reduction of the surface sulfate species leading to a higher amount of SO_2 released under rich conditions. The presence of water diminished this effect, which was found to be mainly a result of the suppressed formation of surface species due to the faster transport of SO_2 into the bulk phase ($BaCO_3$). Increasing the reduction time in the cycles leads to an enhanced reduction of the surface sulfates reduced during rich conditions. No influence in the bulk type species could be detected. It is proposed that for effective SO_2 storage materials with a high utilization, strong adsorption sites on the surface species, the presence of water and short reducing time is essential.

6.1 Introduction

A significant reduction of harmful substances emitted from automotive applications like CO, CO_2, unburned hydrocarbons, NO_x and SO_x has already been achieved [1]. However, due to tighter legislation restrictions (EURO IV), new techniques for the emission control are necessary, especially for NO_x. A promising approach to overcome the NO_x emissions from lean-burn engines can be found in the Nitrogen Storage-Reduction concept (NSR), which is based on a cycling operation mode of the engine [2-5]. During a long period of low fuel consumption in oxygen excess (lean mode) the NO_x species formed are trapped on the catalyst surface. The reduction occurs during a short period in reducing atmosphere, e.g. under fuel rich conditions (rich mode). Unburned hydrocarbons in addition to CO are used as a reducing agent for the NO_x species. However, the NSR catalysts are severely deactivated by the presence of SO_2 in the exhaust gas stream, which adsorbs irreversibly on the catalyst surface and leads to the blockage of the NO_x sorption sites by the formation of thermodynamically favored sulfate species [5-7]. A promising approach to overcome this limitation is the implementation of a SO_x trap before the NSR catalyst to remove the sulfur species present in the exhaust gas stream. The typical composition of S-trap materials should include a refractory support (e.g. Al_2O_3, CeO_2, ZrO_2), an oxidation component (e.g. Pt, Rh, Mn) and a sulfur storage component (e.g. Mg, Na, Ca, Ba) [8]. Further promising materials for such devices based on metal organic framework structures have been already described in Chapter 2 and 3. However, for a further improvement of the performance of such materials a deeper insight in the formation of stable sulfur species as well as their behavior under cycling operation conditions is essential. During lean reaction conditions (oxygen excess) a fast oxidation of SO_2 to SO_3 in combination with an instantaneous adsorption of SO_3 on the storage component should be realized. Apart from a high sulfur storage capacity, an essential feature of S-trap materials is the stability of the sulfur-species under fuel rich reactions conditions to avoid the release of SO_x in the regeneration cycles of the NSR catalyst [9, 10].

The application of *in situ* IR spectroscopy to study the formation of sulfate species on metal oxides is widely explored, however, strongly overlapping bands were typically observed [5, 11-13]. Time resolved *in situ* spectroscopy can

significantly benefit from the application of the Generalized 2D Correlation Analysis as introduced by Noda *et al.* [14-17]. This two-dimensional approach allows a better resolution of overlapping bands in a series of time resolved spectra and can reveal features not readily observable in the regular spectra. Additionally, it gives clearly an evidence for changes in the spectral intensities after a perturbation was applied to the system and allows establishing time sequences for changes in the spectral features allowing the identification of reaction intermediates and/or the determination of reaction mechanisms. The early methods of 2D Correlation Analysis were limited to sinusoidal perturbations, however, new theoretical developments broadened the possible applications for the 2D Correlation Analysis. In 1993, Noda introduced the concept of "Generalized 2D Correlation Analysis", including the calculation of the synchronous and asynchronous correlations with matrix multiplications as shown in Equation 6.1. Each column of the data matrix D being one corrected (i.e. mean centered, mean normalized) spectrum [16, 18]:

$$\Phi(\nu_1,\nu_2) = \frac{1}{n-1}\cdot DD^T$$

$$\Psi(\nu_1,\nu_2) = \frac{1}{n-1}\cdot DND^T \qquad with \qquad N_{jk} = \begin{cases} 0 & for \quad j = k \\ \dfrac{1}{\pi\cdot(k-j)} & for \quad j \neq k \end{cases}$$

Equation 6.1 : Generalized 2D Correlation Analysis involving matrix multiplications.

The synchronous 2D correlation intensity is regarded as the overall similarity between the two spectral intensity variations measured at different spectral variables (ν) at different times, while the asynchronous correlation represents sequential or successive changes in the spectral intensities measured at ν_1 and ν_2. Due to the major application of the synchronous technique in this work, the reader is referred to contributions from [16, 18-21] for the interpretation of asynchronous spectra.

The synchronous correlation evidences the simultaneous changes of spectral intensity variations measured at ν_1 and ν_2. Auto correlation peaks located on the diagonal line corresponding to $\nu_1 = \nu_2$ for $\Phi(\nu_1, \nu_2)$ are always positive [16][1], and form a square with two symmetric cross-peaks at the corresponding intersections. The sign of the cross-peaks indicates whether the changes are

[1] This is not necessarily true for heterospectral analysis.

directly or reversibly correlated, i.e., if the changes in intensity occur in the same (positive sign) or in different directions (negative sign)

Additional, the 2D Correlation Analysis in combination with other chemometric methods can be applied for revealing temporary effects in a dataset e.g. with the concept of Fixed-Size Moving Window Evolving Factor Analysis (FSMWEFA) [22, 23]. In this approach the information for the whole dataset are obtained by analyzing the dataset partially. Therefore e.g. fixed window size is defined to reveal the temporary effects.

As indicated by Equation 6.1 the calculation of the 2D Correlation Analysis results in two 2D plots (synchronous and asynchronous) ranging from ν_{MIN} to ν_{MAX}, thus monitoring the spectral variables (variable-variable correlation intensity). New theoretical contributions by Sasic *et al.* have suggested to calculate the so-called sample-sample correlation intensity [24, 25], which compares the spectral intensities between two spectra as shown in Equation 6.2. With this technique, a detailed investigation of the periodical behavior of the spectral intensities of interest can be performed following the concentration profiles directly. In other words the 2D Sample-Sample correlation can reveal the concentration dynamics in a spectral system through tracking spectral changes at all wavenumber points of interest. In the crossproduct matrix $\Phi(\nu_1, \nu_2)$ only positive peaks are obtained representing the correlations and disrelations between samples/spectra (i.e. between the different spectra of the dataset D). In comparison to the wavenumber-wavenumber 2D Correlation Analysis which explains the relations among the spectral features, the 2D Sample-Sample Correlation Analysis reveals the correlations among the concentration features of the components.

$$\Phi(\nu_1,\nu_2) = \frac{1}{n-1} \cdot D^T D$$

$$\Psi(\nu_1,\nu_2) = \frac{1}{n-1} \cdot D^T N D \qquad with \qquad N_{jk} = \begin{cases} 0 & for \quad j = k \\ \dfrac{1}{\pi \cdot (k-j)} & for \quad j \neq k \end{cases}$$

Equation 6.2 : Generalized 2D Sample-Sample Correlation Analysis.

Beside the identification of the spectral regimes influenced by the perturbation, the identification of the spectra of the pure components is important for a detailed characterization of the different contributions to the overall spectral intensity. Factor Analysis is a powerful tool to identify individual components

contained in a set of data as shown by Malinowski [26]. In classical Factor Analysis (FA), the Eigenvalues and Eigenvectors of the dataset present are separated into physically meaningful components and insignificant contributions attributed to noise only. Factor Analysis is in widespread use in analytical chemistry as it can be used to extract additional information from the dataset present, such as number of essential components and the corresponding concentration profile [26-29]. The fundamental hypothesis of Factor Analysis is that an original data matrix can be reconstructed from a limited number of significant loading vectors and scores. The scores (coefficients or concentration) and the loading vectors (Eigenvectors) rebuild the original dataset in a linear combination. In general, the raw data matrix consists of r spectra with c datapoints. Here, every row of the data matrix corresponds to one spectrum being a linear combination of the spectra of the pure components as shown in Equation 6.3 and Fig. 6.1.

$$A_{rc,raw} = C_{rn,abstract} \cdot S^{T}_{nc,abstract} + E_{rc} = A_{rc,PCA} + E_{rc}$$

Equation 6.3 : Generalized equation for Factor analysis.

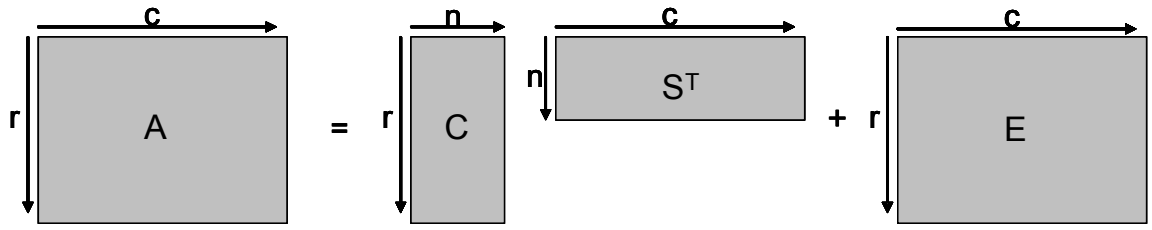

Fig. 6.1 : Scheme – matrix decomposition in Factor Analysis.

A critical point in every factor analysis is the determination of n, the number of essential components present in the sample. There are various approaches towards this problem [26]. The following statistical tests were used to unambiguously determine the number of factors in the dataset: reduced eigenvalue (REV), reduced eigenvalue ratio (REVR), variance and cumulative variance of each eigenvalue, F-Test and the corresponding significance level and Malinowski's IND-function [26]. After the number of components or significant eigenvalues has been calculated, it is possible to perform the calculation of the coefficient or concentration matrix C and the spectra matrix S, respectively (see Fig. 6.1). However, the coefficient matrix C and the matrix containing the spectra of the pure components, S^T, are only the so-called abstract matrices leading to a

mathematically correct but possibly physically meaningless result [27-32]. To obtain 'real' or physically meaningful coefficient and spectra matrices the 'abstract' solutions have to be transformed with the transformation matrix T (rotational ambiguity) as shown in Equation 6.4 [29, 31, 32]. The obtained matrices C_{real} and S_{real} are subject to the so-called intensity ambiguity as shown in Equation 6.5

$$\begin{aligned} A_{(rxc)} &= C_{rxn} \cdot S^T_{nxr} = C_{abstr.} \cdot S^T_{abstr.} \\ A &= C_{abstr.} \cdot S^T_{abstr.} = C_{abstr.} \cdot (T \cdot T^{-1}) \cdot S^T_{abstr.} \\ A &= (C_{abstr.} \cdot T) \cdot (T^{-1} \cdot S^T_{abstr.}) \\ A &= C_{real} \cdot S_{real} \end{aligned}$$

Equation 6.4 : Verification of the Rotational Ambiguity

$$A = \sum_{j=1}^{n} \left[\left(\frac{1}{k_j} \cdot \vec{c}_j \right) \cdot (k_j \cdot \vec{s}_j^{\,T}) \right]$$

Equation 6.5 : Verification of the Intensity Ambiguity

with k_j being n scalars [29]. The application of certain constraints to solve the equations above is indispensable – possible constraints are non-negativity for the spectra and the coefficient profile. For dealing with the Rotational Ambiguity, the Multivariate Curve Resolution with Alternating Least-Squares (MCR-ALS) concept was used. It was introduced in the late 1980s and transforms the abstract coefficient matrix C and the matrix containing the abstract spectra S^T in an alternating manner [33]. In the first step, S^T is calculated from an initial estimation for the coefficient profile. In each iteration step S^T and C can then be calculated by the following approach (see Equation 6.6 and Equation 6.7) [28, 34]:

$$\begin{aligned} A^* &= C \cdot S^T \\ C^T \cdot A^* &= C^T \cdot C \cdot S^T \\ (C^T C)^{-1} \cdot C^T \cdot A^* &= (C^T C)^{-1} \cdot C^T C \cdot S^T \\ S^T &= (C^T C)^{-1} \cdot C^T \cdot A^* \end{aligned}$$

Equation 6.6 : MCR-ALS – calculation of S^T

$$C = A^* \cdot S \cdot (S^T S)^{-1}$$

Equation 6.7 : MCR-ALS – calculation of C

One of the great advantages of MCR-ALS is the possibility to apply certain constraints concerning non-negativity or shape of the results at every step of the iterative process. To avoid physically meaningless solutions, a non-negativity

constraint was applied to the coefficient profile and the spectra, between each iteration step.

6.2 Experimental

6.2.1 Materials

A cogel $CuO\text{-}Al_2O_3$ was synthesized by a proprietary procedure of Venezia Tecnologia and calcined in air at 823K for 3h. The support was further impregnated with Ba and calcined again in air at 823K for 1h. Finally the impregnation with Pt followed by a recalcination at 823K for 1h was carried out. The catalysts are named VTNS3 for the Pt free sample and VTNS3 Pt for the sample impregnated with Pt.

6.2.2 *In situ* IR experiments

IR experiments were carried out in a flow cell in a transmission mode with a Perkin Elmer 2000 – FTIR spectrometer. For the IR measurements, the samples were pressed into self supporting wafers. The gas mixture typically contained 10ppm SO_2 and, in variable concentrations O_2, NO_2, CO_2, H_2 and C_3H_6 as shown in Table 6.1. All gases were balanced with helium to obtain a total flow of 200ml/min. All experiments were carried out at 523K. The SO_x uptake experiments were performed at the same temperature under dynamic conditions using a tubular reactor system described in Chapter 2. A typical material mixture contains 50mg of the sample with a particle size of 0.1-0.3mm and 100mg SiC (d < 0.3mm). Similar gas mixtures as used for *in situ* IR experiments were utilized. The SO_2 concentration in the exhaust gas stream was determined using an SO_2 analyzer (*Thermo Environmental Instruments, Model 43C*). The cycling times were typically set to 240s for lean operation mode and various times for rich operation mode.

Table 6.1 : Typical Gas composition applied under *in situ* IR and during plug flow experiments

Gas	Lean operation	Rich operation
O_2	12%	4%
CO_2	4%	8.5%
SO_2	10ppm	10ppm
NO_2	30ppm	50ppm
HC (C_3H_6)	0%	0.5%
H_2	0%	1%
H_2O	10%	10%
He	Balance to 200ml/min	Balance to 200ml/min

6.2.3 Matlab programs

The calculations of the synchronous and asynchronous correlation plot were performed using matlab programs applying the matrix multiplication approach (see Equation 6.1). The spectra were mean-centered before the calculation. The programs to compute the (Moving Window) 2D Correlation Analysis were written in Matlab 6.5. The number of principle components was selected using the program developed by Malinowski [26]. All calculations involving MCR-ALS were performed using matlab programs developed by Tauler *et al.* [35]. Prior to the calculations the background correction was performed using the concept by Mazet *et al.* [36]. A moving window approach involving 5 consecutive spectra was used as a dataset, hence the dataset covers either solely spectra recorded under lean operation mode or spectra recorded under lean and rich operation mode (Moving Window Fig).

6.3 Results

6.3.1 Properties of the materials

Only CuO, Al_2O_3 and $BaCO_3$ could be identified by XRD indicating the presence of agglomerates of $BaCO_3$ present on the CuO-Al_2O_3 support. N_2 physisorption carried out on the Pt free sample showed a BET surface area of 176m²/g with a sharp mean pore size distribution of 60Å. The subsequent impregnation with Pt did not affect the physicochemical properties of the support. Temperature

programmed desorption showed a release of 9.46mmol CO_2/g which is equal to 13% of Ba on the Pt free sample. This is in good agreement with the impregnated amount indicating that Ba is mainly carbonate. No deviations were detected on the Pt containing sample. Further details are shown in Chapter 5.

6.3.2 SO_2 uptake experiments

Fig. 6.2A shows the plug flow experiments carried out under lean-rich cycling conditions in absence of water on the Ba/CuO-Al_2O_3 material with and without Pt on the sample. The duration for reducing conditions for the sample was varied (18s, 36s, 72s and 144s) to determine the effect of the time under rich reaction conditions on the SO_x storage process. The time of oxidizing conditions was kept constant at t=240s. Fig. 6.2A depicts the SO_2 content in the exhaust gas under cycling conditions on the Pt free sample revealing the complete saturation of the materials after 1000min for all reduction times investigated. Fig. 6.2B shows the first 200min enhanced, indicating that under oxidizing conditions a complete SO_2 removal is observed during the first 100 minutes time on stream. However switching to rich operation condition leads to an increase in the concentration of SO_2 in the exhaust gas stream resulting from a release and/or decomposition of the sulfur species present on the sample. It is clearly observed that with increasing numbers of cycles an increasing amount of SO_2 was released under rich conditions. Furthermore, for longer time under reducing reaction conditions (from 18s up to 144s) an increase of the SO_2 released was clearly observed.

Fig. 6.2C and Fig. 6.2D shows the lean-rich cycling experiments carried out on the Pt containing sample. In comparison to the Pt free sample a constant SO_2 level in the exhaust gas stream was not reached even after 1000min. It is clearly observed that under oxidizing conditions SO_2 is completely removed from the exhaust gas stream, while switching to reducing conditions leads to a release of SO_2 (indicated by a higher intensity of the SO_2 detected). The increase of the total number of cycles is accompanied with an enlarged release of SO_2 under fuel rich conditions. Furthermore, during the whole time on stream a constant SO_2 release under these conditions was not reached as shown in Fig. 6.2C. At the constant increase of the SO_2 at 36s (B) only lean conditions were applied. This clearly a show that the SO_2 desorption is caused by the lean-rich conditions, whereas only lean conditions would lead to a constant uptake. The comparison of the area of the desorption peak between the Pt and Pt free sample is depicted in Fig. 6.3. It

shows that during low total cycling number (A) a slightly higher SO_2 release per cycle was observed on the Pt free sample. However, this effect is inversed and strongly pronounced on the Pt containing sample with increasing the total number of cycles indicating that Pt facilitates the reduction of sulfur species under rich conditions (see Fig. 6.3B).

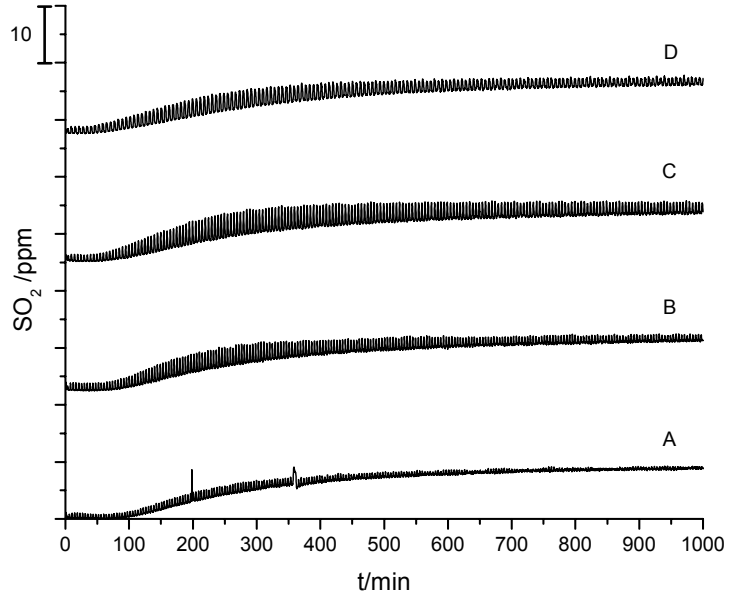

(A)

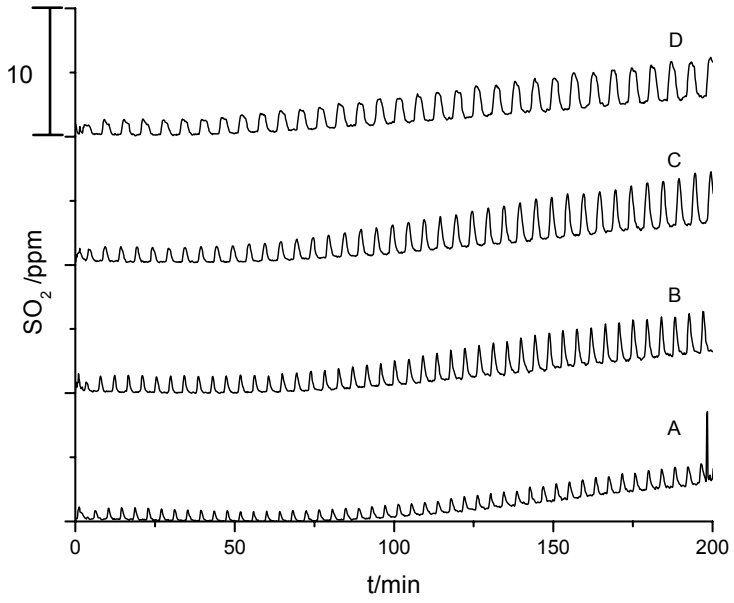

(B)

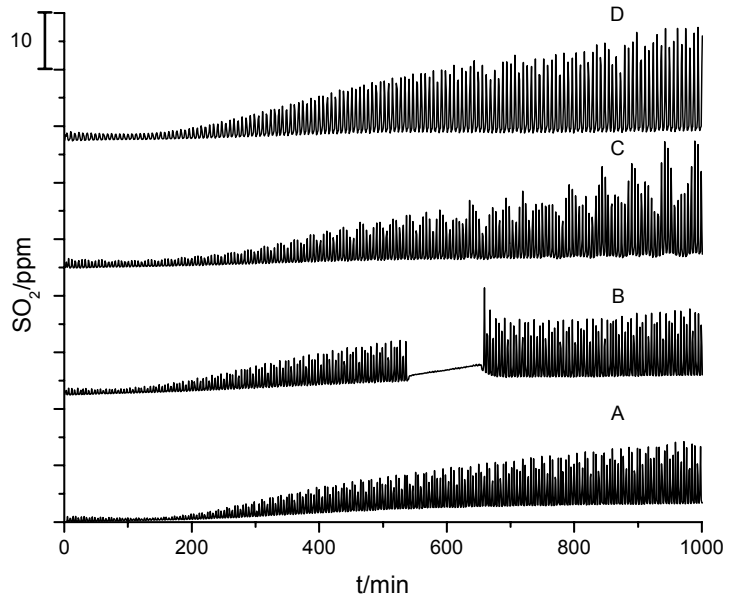

(C)

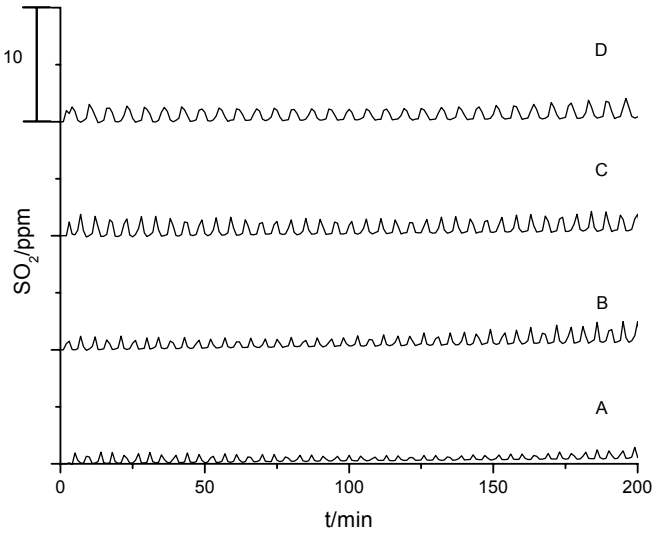

(D)

Fig. 6.2 : Plug flow experiments at lean-rich cycling conditions with gas compositions mentioned at Table 6.1 on VTNS3 (A + B) and VTNS3 Pt (C + D) at various times for rich conditions (A=18s, B=36s, C=72s, D=144s) at 523K; lower part show an enhanced area for t=200min.

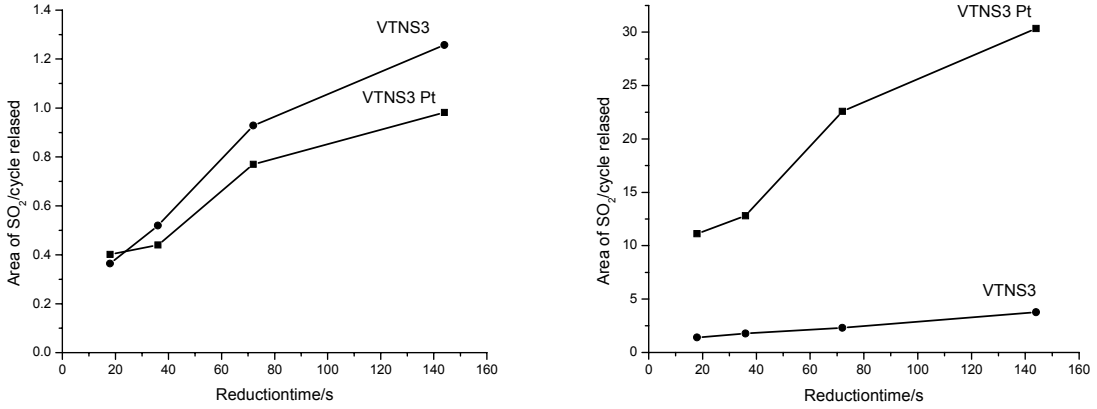

(A) (B)

Fig. 6.3 : Area of SO_2 per cycle in the breakthrough experiments released in dependence of rich cycling time on the VTNS3 and VTNS3 Pt t=0-60min (A), t=950-1000min (B)

The influence of 10% water present in the exhaust gas stream on the S-trapping process under lean-rich-cycling conditions was investigated. Fig. 6.4 shows the continuous lean-rich cycling experiment carried out with 72s reducing time in presence of 10% water additional to the gas composition summarized in Table 6.1. A similar behavior for the SO_2 storage was detected compared to dry conditions. A complete SO_2 adsorption is only observed during the first 100min time on stream under oxidizing conditions. Under reducing conditions a release of SO_2 was observed, however, strongly diminished compared to dry conditions. On the Pt containing material this effect is only observed at a low number of total cycles. Experiments carried out only under lean conditions (not shown here) in presence of water showed an overall enhanced SO_2 uptake capacity compared to dry conditions indicating the promoting effect of H_2O. Varying the time for reduction (experiments not shown here) a similar behavior compared to dry conditions was observed, indicating that a longer time under reducing conditions forces the SO_2 release. The influence of NO_2, C_3H_6, and CO_2 on the total SO_x storage capacity was investigated indicating no effect of C_3H_6, and CO_2 and minor effects of NO_2 with respect to the total sorption capacity.

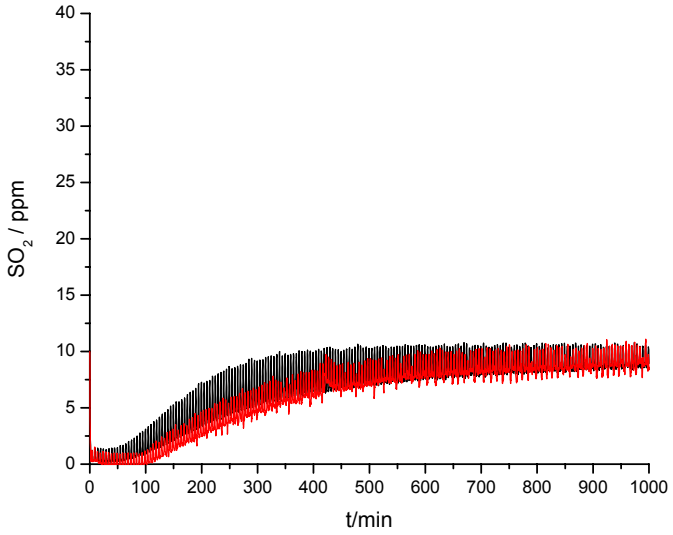

(A)

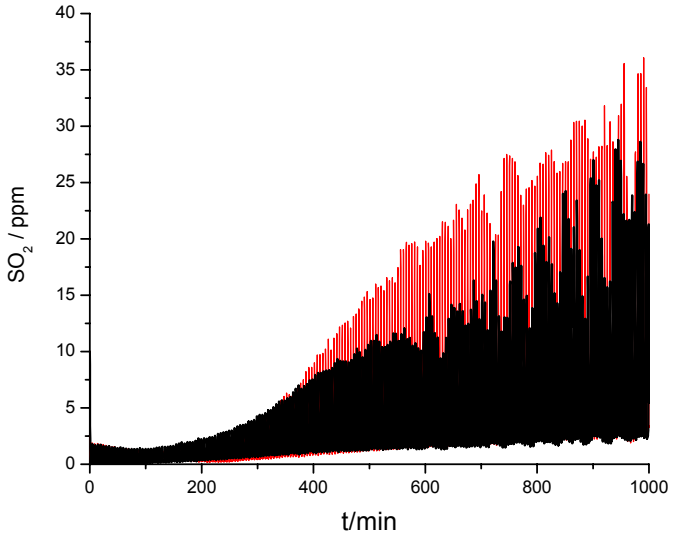

(B)

Fig. 6.4 : Plug flow experiments at lean-rich cycling conditions in absence (black line) and Table 6.1 in presence of 10% H_2O (red line) on VTNS3 (A) and VTNS3 Pt (B) at t=72s for rich conditions.

6.3.3 *In situ* IR experiments

6.3.3.1 Influence of NO_2 during lean-rich cycling conditions

The influence of NO_2 on the sorption process was investigated by means of *in situ* IR to assign the NO_x species formed. As known from literature the spectral region of nitrates and sulfates strongly overlaps, which makes this experiment necessary

for a latter clear assignment of the perturbation by the presence of SO_2 [37, 38]. For the experiments the time for rich reaction conditions was extended to 72s whereas in the lean mode 240s was kept.

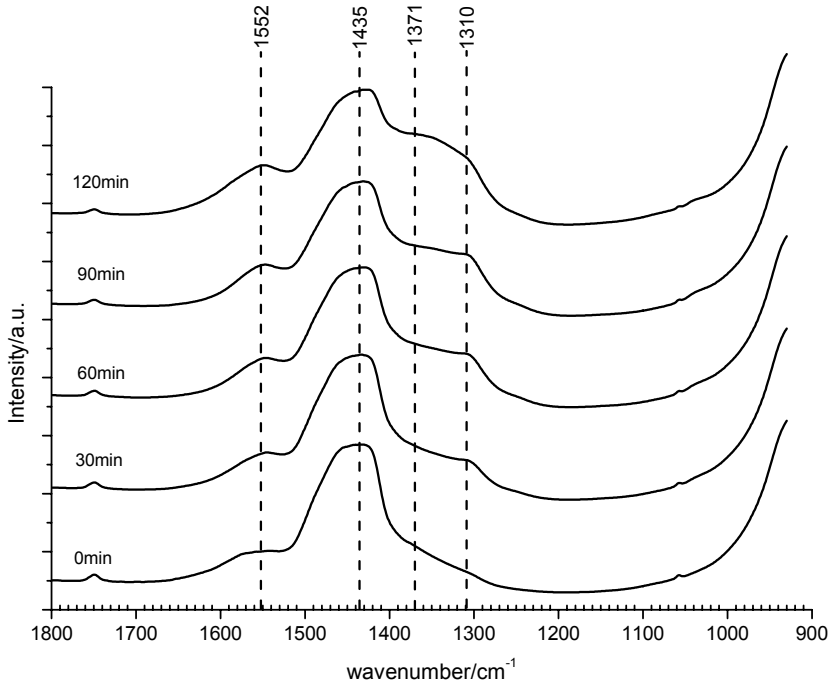

Fig. 6.5 : Time resolved IR spectra of VTNS3 under lean-rich conditions (240s lean, 72s rich) at mixtures shown in Table 6.1 in absence of SO_2 at 573K.

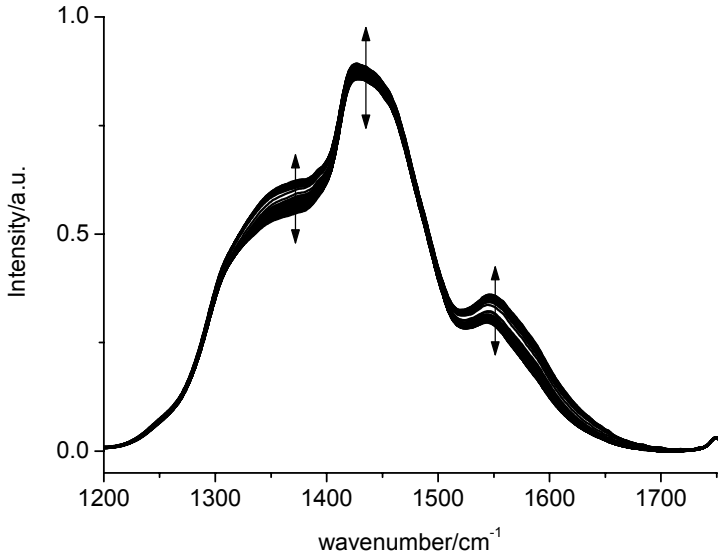

Fig. 6.6 : Time resolved IR spectroscopy at VTNS3 under lean-rich conditions (240s lean, 72s rich) in absence of SO_2 Δt=30min.

Fig. 6.5 shows the time resolved IR spectra recorded for VNTS3 during exposure to the typical gas mixture (Table 6.1) without SO_2. The band formed at 1310cm^{-1} during the first 30min can be assigned to Nitrato/Nitro species located on Cu [39, 40]. With increasing exposure time the formation of bands located at 1371cm^{-1}($Cu^{2+}(NO_3^-)_2$), 1435cm^{-1} (Ba-N<$^{O}_{O}$) and 1552cm^{-1}(Cu^{2+}<$^{O}_{O}$ > N–O) was observed, while the absence of bands assigned to NO_2^- on Al (around 1080cm^{-1}) indicates the formation of nitrates on Cu and Ba [5, 37, 41]. However due to the strong carbonate band located in this region masking other species the formation of other nitrates could not be excluded. After 2h under lean reaction conditions no further changes in the concentration and presence of surface species was observed, while under lean-rich cycling reaction conditions only the bands at 1371cm^{-1}, 1435cm^{-1}, 1552cm^{-1}, 1080cm^{-1} were affected.

As the 2D Sample-Sample Correlation reveals information about the concentration dynamic in a spectral system through tracking spectral changes at all wavenumber points of interest it was performed on the spectral range from 1650cm^{-1}-1300cm^{-1}, including all spectral features identified from the 1D plot. Fig. 6.7 depicts the 2D Sample-Sample Correlation over 25min starting from t=120min on.

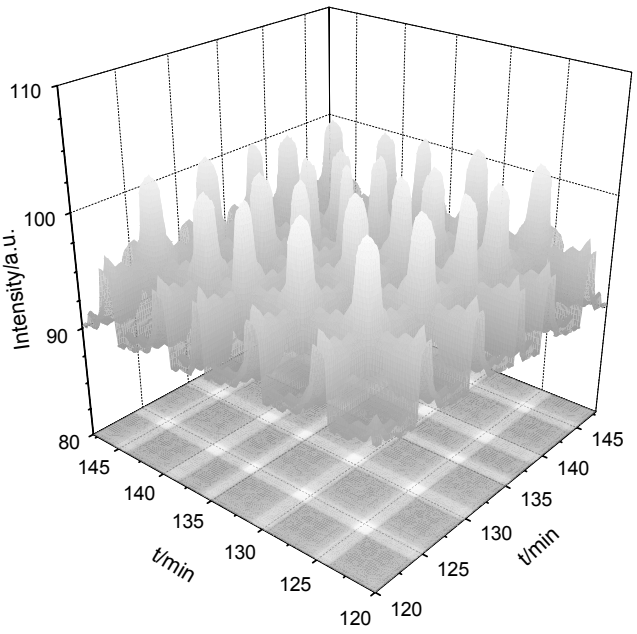

(A)

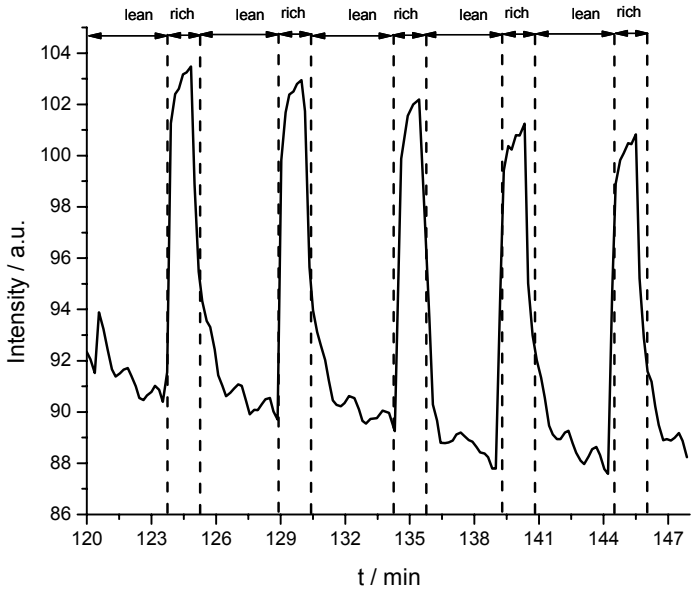

(B)

Fig. 6.7 : 2D Sample-Sample Correlation Analysis calculated for the dataset shown in Fig. 6.6 for five lean-rich cycles (A) 2D surface plot, (B) corresponding diagonal.

The diagonal line (see Fig. 6.7B) reflects the changes in the spectral intensity occurring in the wavenumber region selected and is plotted in addition to the 3D plots (see Fig. 6.7A) to allow a more thorough investigation of various positions of the peaks. Five well resolved peaks can be found at around 125, 130, 135, 140 and 145min while rich conditions are applied to the sample. The peaks can be assigned to an overall spectral intensity increase at these times. After the gas mixture is switched back to lean operation mode, the intensity of these features starts to level off again. The 2D Sample-Sample correlation reveals the time resolved behavior of summarized spectral regions and leads to the conclusion that the three peaks located at 1371cm^{-1}, 1435cm^{-1} and 1552cm^{-1} (see Fig. 6.5) are increasing during rich mode and decreasing in lean mode. As these bands are assigned to surface nitrate species this indicates a higher intensity (concentration) of these under rich conditions. This could result from their preferred formation which is in agreement to the findings for the NSR catalysts while the reduction of the nitrates (see Chapter 1). The trace extracted along the diagonal (plotted in Fig. 6.7B) indicates that the overall intensity decreases with increasing exposure to the reaction mixture. Note that in the region chosen for the 2D Sample-Sample correlation analysis carbonate and NO_x species appear,

therefore, a combination of two regimes that involve the reduction of the carbonate species and adsorption of NO_x species formed under lean conditions is observed.

It should also be mentioned that the calculation was performed with datasets consisting of only one of the three peaks proofing the consistence over the whole dataset (i.e. the datasets were shortened leading to ranges from 1400cm^{-1}-1300cm^{-1}, 1500cm^{-1}-1400cm^{-1} and 1600cm^{-1}-1500cm^{-1}). Moreover, it was found that the same pattern was obtained if the wavenumber region was set from 1000cm^{-1} to 1200cm^{-1} (see Fig. 6.5) although the pattern was less intense in this region (graphs not shown here). Similar experiments carried out at various reducing times showed the same trend but the time extension leads to a more vivid and clear pattern as more spectra can be recorded during rich mode.

6.3.3.2 SO_2 adsorption in absence of Pt during lean-rich cycling conditions

The plug flow experiments carried out under cycling conditions on the Ba/CuO-Al_2O_3 material showed sufficient long term stability, with a small release of SO_2 under rich conditions. *In situ* IR spectra Fig. 6.8 recorded during lean-rich cycling with a cycling time for lean conditions of 240s and a cycling time for rich conditions of 18s are shown in Fig. 6.8. The bands at 1770cm^{-1}, 1557cm^{-1} and 1437cm^{-1} are attributed to carbonate species [13, 42] and the bands observed at 1045cm^{-1}, 1158cm^{-1} and 1247cm^{-1} are attributed to sulfates. The different symmetries of the S-O vibrations (see Chapter 1) indicate the presence of surface and bulk sulfates as shown by numerous authors, nevertheless due to the strong overlapping bands of the various sulfates formed on the mixed metal material no clear assignment was possible [7, 12, 40, 43-46]. It is important to note that the interval ranging from 1350cm^{-1}-1290cm^{-1} was found to be affected by the lean-rich cycling. The 2D Sample-Sample correlation analysis is therefore a promising technique to identify the time resolved behavior.

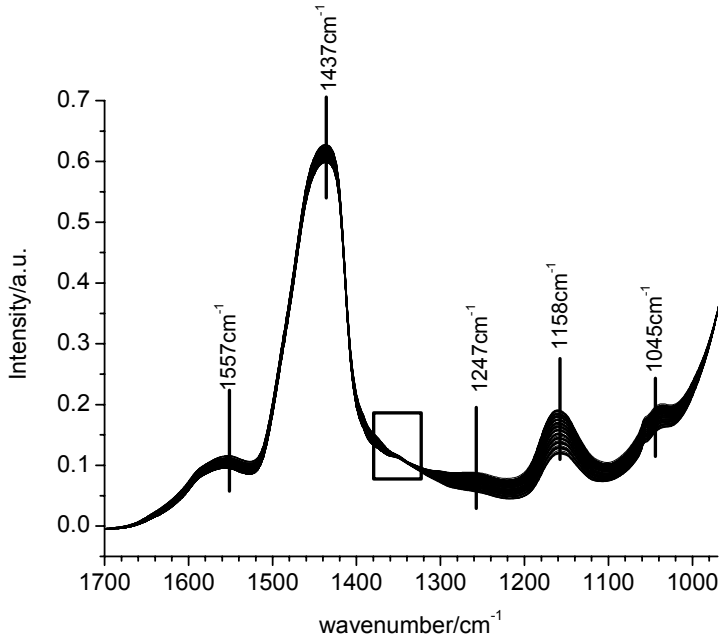

Fig. 6.8 : Time resolved IR spectra obtained for the sample VTNS3 recorded under lean-rich cycling conditions (see Table 6.1) at 523K.

For the entire dataset recorded only a total increase in the intensity of the bands assigned to sulfur species was observed (see Fig. 6.8). The spectral changes while switching between lean-rich can not be directly observed. Furthermore one complete lean-rich cycle consists of five spectra (e.g. 50s per spectra). When using 18s for reducing conditions, this would always lead to a strong overlapping of effects while recording at least one spectra caused by lean-rich switching.

As shown in the introduction the analysis of datasets to reveal the effects of perturbation could be more effective by analyzing it in sections, e.g. Fixed Window technique. We applied the Moving Window 2D Correlation as shown in the experimental section by selecting an appropriate amount of spectra to resolve spectral changes occurring while lean-rich cycling. The synchronous plot calculated from five spectra recorded under lean operation mode is depicted in Fig. 6.9. Three well defined auto-peaks appear at the diagonal at the locations 1247cm^{-1}, 1158cm^{-1} and 1045cm^{-1}. The positions as well as the signs of the cross peaks indicating the correlation of the spectral changes at the respective positions are compiled in Table 6.2. The variation at the peak centered at 1247cm^{-1} is shown by large distinct positive cross-peaks located at the intersections

Φ(1247cm^{-1},1158cm^{-1}) and Φ(1247cm^{-1},1045cm^{-1}) indicating a synchronous increase of these bands. The bands at 1247cm^{-1}, 1158cm^{-1} and 1045cm^{-1} are assigned to sulfate species [13, 47]. The small negative changes observed at the intersection of the peak centered at 1442cm^{-1} (carbonate species) with the sulfate species indicate the replacement of carbonates with sulfates under lean conditions.

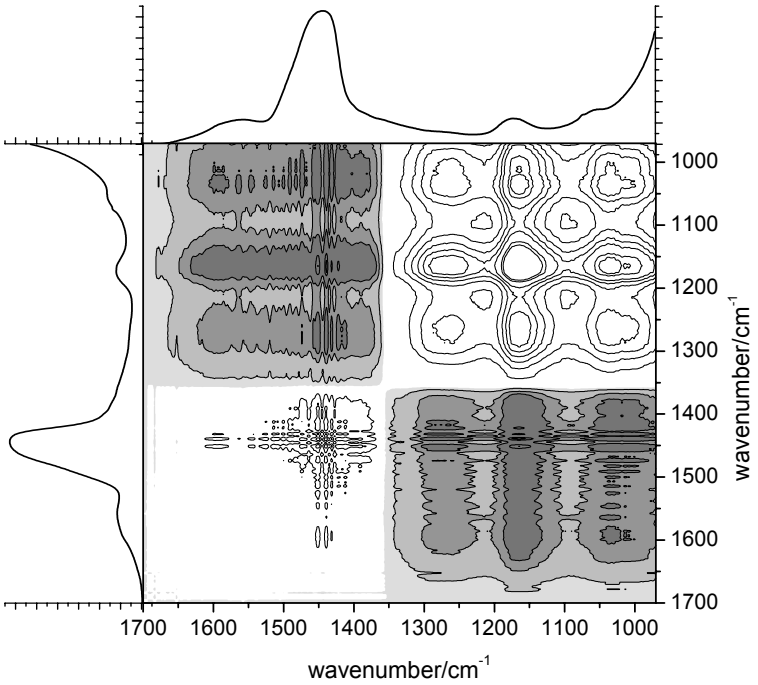

Fig. 6.9 : Synchronous Correlation contour plots calculated by means of Moving Window correlation analysis from a dataset consisting of 5 spectra recorded under lean conditions at 523K at VTNS3.

Table 6.2 : Peak positions and peak signs determined for the synchronous 2D correlation plots including spectra recorded in lean mode.

Location	Peak sign	Direction of change
1158cm^{-1}-1045cm^{-1}	Positive	Increasing
1158cm^{-1}-1295cm^{-1}	Positive	Increasing
1158cm^{-1}-1350cm^{-1}	Positive	Increasing
1158cm^{-1}-1442cm^{-1}	Negative	Decreasing
1158cm^{-1}-1557cm^{-1}	Negative	Decreasing

Fig. 6.10 shows the synchronous plot obtained from 5 consecutive spectra, 4 spectra recorded under lean and 1 spectrum recorded under rich conditions. The position of the bands obtained from the spectra collected under lean and rich reaction conditions from the synchronous plot is shown in Table 6.3. The cross-peak at the intersection Φ(1158cm^{-1},1350-1290cm^{-1}) is negative indicating that the bands in the region 1350cm^{-1}-1290cm^{-1} are decreasing while the band at 1158cm^{-1} increases. The band located at 1442cm^{-1} (attributed to the continuously decreasing carbonate species) is increasing under rich operation conditions indicated by a positive cross-peak appearing at the intersection 1160cm^{-1}-1442cm^{-1}.

Table 6.3 : Peak positions and peak signs determined for the synchronous 2D correlation plots including spectra recorded in rich mode for the VTNS3 at 523K.

Location	Peak sign	Direction of change
1158cm^{-1}-1045cm^{-1}	Positive	Increasing
1158cm^{-1}-1295cm^{-1}	Negative	Decreasing
1158cm^{-1}-1350cm^{-1}	Negative	Decreasing
1158cm^{-1}-1442cm^{-1}	Positive	Increasing
1158cm^{-1}-1557cm^{-1}	Negative	Decreasing

However, taking into consideration the experiments in absence of SO_2 (see Fig. 6.7), it is proposed that this slight increase in the region at 1442cm^{-1} results from the adsorption of NO_x species formed during rich mode. The peak identified in the position 1557cm^{-1} – also attributed to carbonate species – shows two negative cross-peaks (1557cm^{-1},1158cm^{-1} and 1557cm^{-1},1045cm^{-1}). This indicates that this spectral intensity is changing in the opposite direction compared to the sulfate peaks centered at 1158cm^{-1} and 1045cm^{-1} under these conditions.

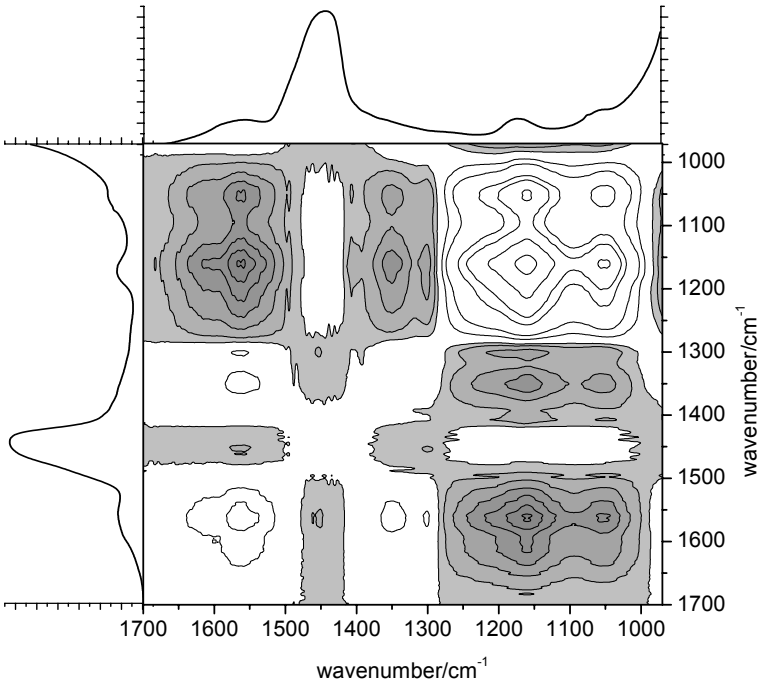

Fig. 6.10 : Synchronous Correlation plots calculated by means of Moving Window Correlation analysis from a dataset (Fig. 6.8) consisting of 5 spectra recorded (4 under lean and 1 rich conditions) at 523K for the VTNS3.

To confirm the results obtained for a single cycle the calculations (2D Moving Window Correlation Analysis with a selection of five spectra) were performed on each of the 20 cycles showing similar results. During lean operation mode, the sulfate bands centered at 1247cm^{-1}, 1158cm^{-1}and 1045cm^{-1} were increasing whereas the carbonate bands located at 1557cm^{-1} and 1442cm^{-1} were found to decrease. During rich operation mode, the sulfate bands centered at 1158cm^{-1} and 1045cm^{-1} were found to remain almost at a constant level under reducing conditions whereas two new bands present at 1350cm^{-1} and 1295cm^{-1} were found to be decreasing in rich operation mode. The carbonate species located at 1557cm^{-1} continuously decreased throughout the experiment. However, for the carbonate species centered at 1442cm^{-1} the decrease under lean and increase under rich conditions could be possibly caused by an interaction of the S-trapping material with the NO_x species formed under rich operation mode. After the identification of the position of the IR band of species changing in intensity during the lean-rich cycling conditions, the quantification in dependence of the number of cycles was investigated by means of 2D Sample-Sample Correlation Analysis.

The regions selected were 1650cm^{-1}-1350cm^{-1} (assigned to carbonate species), 1350cm^{-1}-1290cm^{-1} (assigned to transient sulfate species) and 1290cm^{-1}-1000cm^{-1} (assigned to bulk-like sulfate species). It is important to note that several authors assigned bands in the latter region to surface sulfate species. However, by means of Moving Window 2D Correlation Analysis no difference in the time behavior was observed, which indicates that these species are more likely bulk-like than surface species due to the reducibility under rich conditions. The dataset utilized for the calculation consisted of spectra for Δt=55min recorded 40min after the sample was exposed to SO_2. The spectra used here represent a snapshot of the whole dataset.

The 2D Sample-Sample correlation calculated for the wavenumber range of 1650cm^{-1}-1350cm^{-1} is shown in Fig. 6.11 A as well as the trace along the diagonal in Fig. 6.11 B. The general decrease in the intensity with increasing exposure time to the gas mixture indicates that the intensity of the peaks located at 1437cm^{-1} and 1557cm^{-1} is continuously decreasing throughout the experiment. It can be clearly seen that after switching to rich conditions, a slight increase in the spectral intensity occurs leading to the characteristic spike pattern similar to the one depicted in Fig. 6.7; which might result from the reversibly adsorbed NO_x species formed during rich mode (see Fig. 6.7).

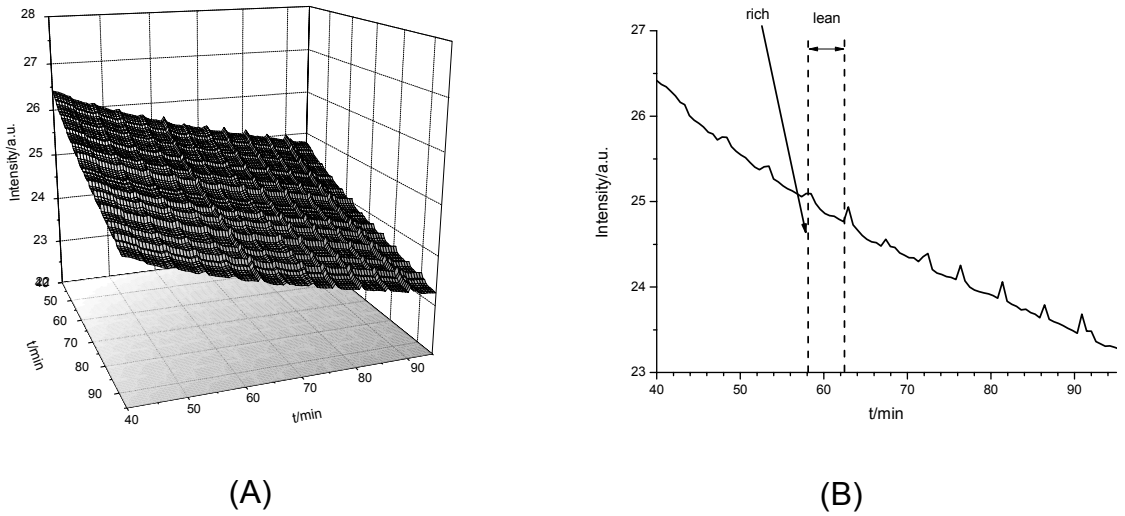

Fig. 6.11 : 2D Sample-Sample Correlation Analysis of the vibrations attributed to carbonates (1650cm^{-1}-1350cm^{-1}) at Δt=55min recorded 40min after the experiment was started. The surface plot is depicted in (A), the corresponding diagonal in (B).

The 2D Sample-Sample correlation analysis for the region of 1350cm^{-1}-1290cm^{-1} is shown in Fig. 6.12A. It is clearly observed that the intensity in the surface plot at the time location X,Y=40min,40min is much smaller than the intensity at the spectra X,Y=95min,95min indicating that the vibrations located in this region are increasing with time during the experiment. The trace along the diagonal shown in Fig. 6.12B contains a very characteristic pattern obtained during the lean-rich cycling which can be best described as a saw-tooth pattern. This pattern is characteristic for the changes in concentration of transient species which is strongly diminished under rich conditions and formed under lean conditions.

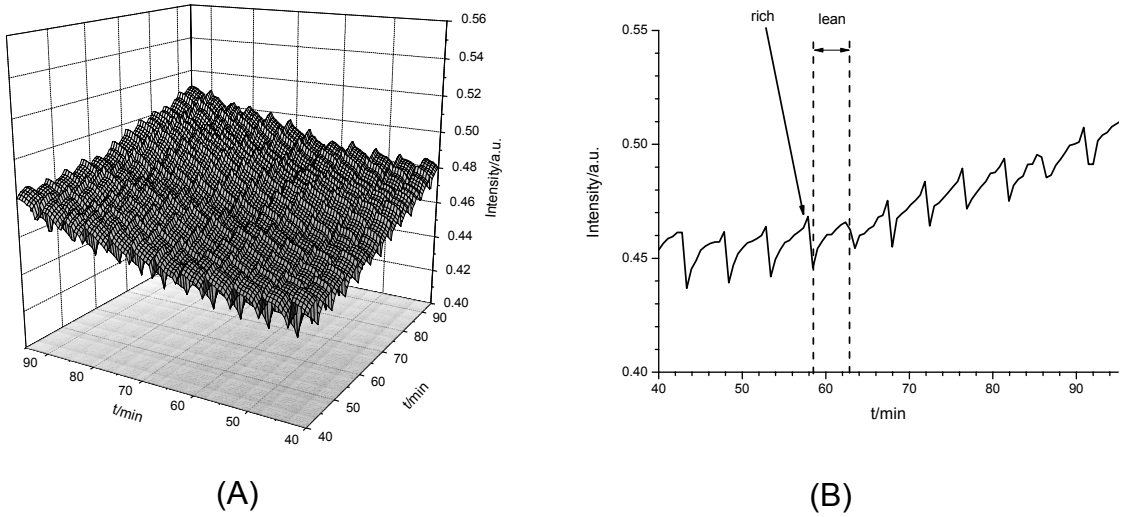

(A) (B)

Fig. 6.12 : 2D Sample-Sample Correlation Analysis of the vibrations attributed to a transient species (1350cm^{-1}-1290cm^{-1}) at Δt=55min recorded 40min after the experiment was started. The surface plot is depicted in (A), the corresponding diagonal in (B).

Fig. 6.13 shows the 2D Sample-Sample Correlation applied to the region from 1290cm^{-1}-1000cm^{-1} attributed to S-O vibrations. The intensity in the surface plot at the time location X,Y=40min,40min is much smaller than the intensity at the spectra X,Y=95min,95min indicating that the vibrations located in the region 1290cm^{-1}-1000cm^{-1} are increasing with time during the experiment due to the adsorption of SO_2 and the formation of sulfate species. However, the spike type pattern observed is similar to the NO_2 adsorption shown in Fig. 6.13B.

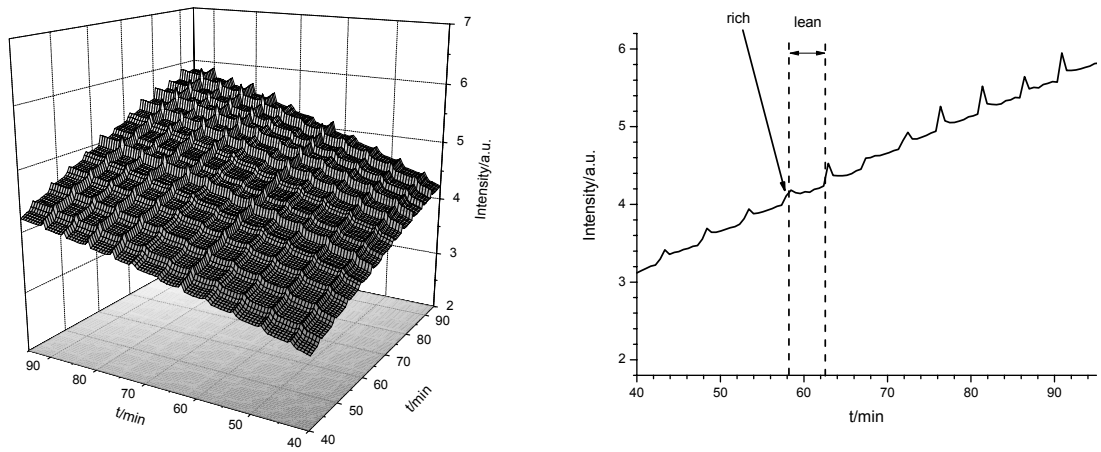

(A) (B)

Fig. 6.13 : 2D Sample-Sample Correlation Analysis of the region (1290cm^{-1}-1000cm^{-1}) at Δt=45min recorded 40min after the experiment was started. The surface plot is depicted in (A), the corresponding diagonal in (B).

After the identification of the spectral regions as well as the time resolved concentration behavior under lean-rich conditions, the MCR-ALS technique was used for the determination of the spectra of the pure components. First the number of significant components (shown in Table 6.4) was determined by a statistical analysis of the eigenvalues calculated for the dataset depicted in Fig. 6.8.

Table 6.4 : Analysis of eigenvalues calculated fort the spectra depicted in Fig. 6.8.

No.	EV	Var	CumVar	REV	REVR	F-Test	RE
1	7117.905	0.999938	0.999938	0.26331	16064.38	240428.5	2.53E-05
2	0.4283	0.00006	0.999999	1.64E-05	41.9264	593.3299	4.02E-06
3	0.00986	1.39E-06	1	3.91E-07	34.3226	284.9148	8.96E-07
4	2.77E-04	3.89E-08	1	1.14E-08	6.1338	18.3208	6.04E-07
5	4.35E-05	6.11E-09	1	1.86E-09	1.2398	3.5326	5.55E-07
6	3.38E-05	4.74E-09	1	1.50E-09	1.3083	3.3502	5.12E-07
7	2.48E-05	3.48E-09	1	1.14E-09	1.2511	2.9481	4.78E-07
8	1.90E-05	2.67E-09	1	9.15E-10	1.5165	2.675	4.48E-07
9	1.20E-05	1.68E-09	1	6.03E-10	1.2552	1.8969	4.33E-07
10	9.13E-06	1.28E-09	1	4.81E-10	1.1096	1.5893	4.22E-07

The first and second eigenvalues are clearly found to be physically meaningful eigenvalues due to the significantly larger value compared to the others. Also, the third eigenvalue is considered to be a significant eigenvalue being more than one order of magnitude larger than the fourth eigenvalue. Moreover, the error in the real part (RE) obtained for the remaining spectra is still approximately 50% larger than the value obtained for the fourth eigenvalue. The values obtained for the reduced eigenvalue ratio (REVR = 34.3226) and the F-Test (284.9148) clearly indicate that the third eigenvalue can be attributed to physically relevant contributions in the spectra. The fourth eigenvalue shows a variance being two orders of magnitude smaller than the third eigenvalue. Also, the REVR is one order of magnitude smaller than the REVR values obtained for the eigenvalues 2 and 3. Additionally, the RE in the remaining dataset differs only of ≈10% from the value obtained for the fifth eigenvalue. Thus, the fourth eigenvalue is attributed to noise and the number of components in the present dataset is chosen to be three.

As mentioned in the introduction, an initial coefficient matrix is necessary for the MCR-ALS technique. In the present contribution, the diagonals of the matrices obtained from the 2D Sample-Sample Correlation Analysis were used as the initial input for the coefficient matrix in the MCR-ALS calculation. Non-negativity constraints were applied to both coefficient and spectra matrix. The spectra were normalized to the same length. The resulting spectra of the components and the coefficient matrix representing the time resolved behavior of the pure components is depicted in Fig. 6.14 and Fig. 6.15 respectively.

The spectra of the pure components shown in Fig. 6.14 reveals three clear distinguishable species located at 1557cm^{-1} and 1442cm^{-1} at 1045cm^{-1}, 1247cm^{-1} and 1158cm^{-1} and, at 1350cm^{-1} and 1295cm^{-1}. The two peaks at 1557cm^{-1} and 1442cm^{-} (solid line) can be assigned to carbonate species, most likely $BaCO_3$ [13, 42]. The three peaks at 1247cm^{-1},1158cm^{-1} and 1045cm^{-1} indicated by the dotted line can be assigned to bulk sulfate species located on Cu, Ba or Al [12, 47-51]. A clear assignment is not possible due to the strong overlapping regions of the sulfates. In general, these species are located in the spectral region for SO stretching vibrations from uni- and bidentate sulfate species on the metal atom according to literature [10, 43]. The transient species, indicated by the dashed line, show two distinct peaks at 1295cm^{-1} and 1350cm^{-1}. This is located in the typical

region for surface sulfate species e.g. on Al_2O_3 as shown by several authors [45, 46, 52-54]. Moreover, Waqif *et al.* assigned at low sulfate coverage on Al_2O_3 a band at 1350cm^{-1} to a single S-O vibration resulting from a Al-(O_3)S-O species, where a second band appearing at 1290cm^{-1} revealing at slightly higher coverage [55]. This is in perfect agreement with the positions for the transient species identified here.

From the coefficient matrix (representing a time resolved concentration profile) the carbonate and bulk sulfate species were the dominant species showing an increasing intensity over time. Taking into consideration that the spectra matrix was normalized, it can be concluded that the carbonates and the bulk sulfate species show a contribution about 9 times larger than the contribution of the saw-tooth pattern like species. Therefore these intensities could not be readily observed from the 1D plots, while the application of the moving window 2D Correlation Analysis and MCR-ALS calculations allowed a clear identification of these (obscured) features.

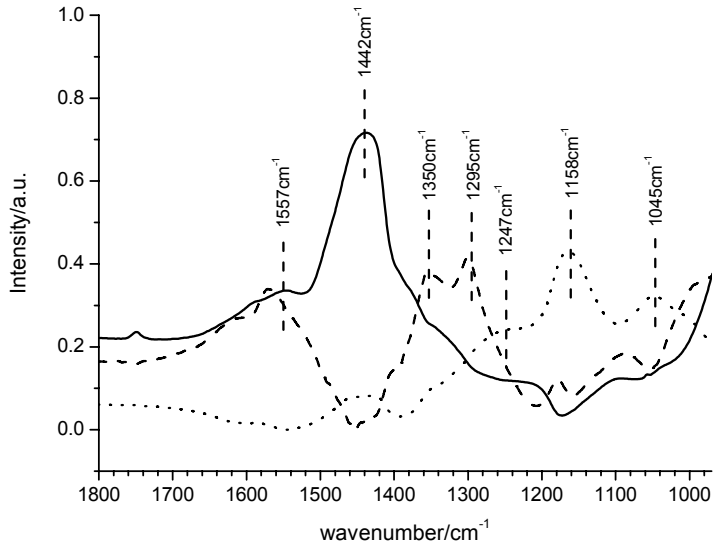

Fig. 6.14 : Spectra of the pure components obtained from the spectra depicted in Fig. 6.8 by means of MCR-ALS.

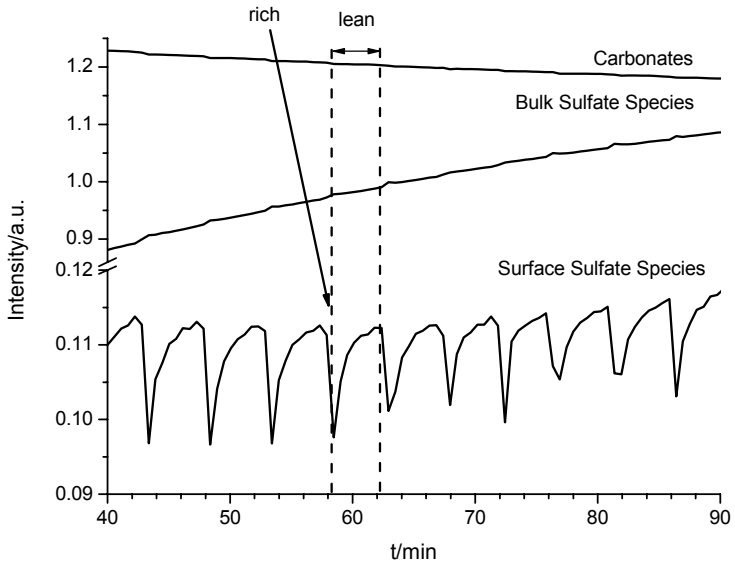

Fig. 6.15 : Coefficient matrix representing the concentration profile obtained from the spectra depicted in Fig. 6.14 by means of MCR-ALS.

6.3.3.3 Influence of Pt on the SO_2 adsorption during lean-rich cycling conditions

To identify the influence of Pt on the SO_x storage process similar in situ IR experiments were carried out on the Pt/Ba/CuO-Al_2O_3. The time resolved spectra are depicted in Fig. 6.16 showing a similar pattern with respect to the Pt free sample (see Fig. 6.8). Two well defined bands attributed to bariumcarbonate were found at 1447cm^{-1} and 1552cm^{-1}. Furthermore the arising of bands at 1040cm^{-1}, 1162cm^{-1} and 1251cm^{-1} was assigned to bulk sulfate species on the Ba/CuO-Al_2O_3. The formation of surface sulfate species identified on the parent material was observed in a similar region from 1290cm^{-1}-1350cm^{-1} (marked with a rectangle). In general, the positions of the bands on the Pt containing materials are similar to those on the Pt free sample (see Fig. 6.8).

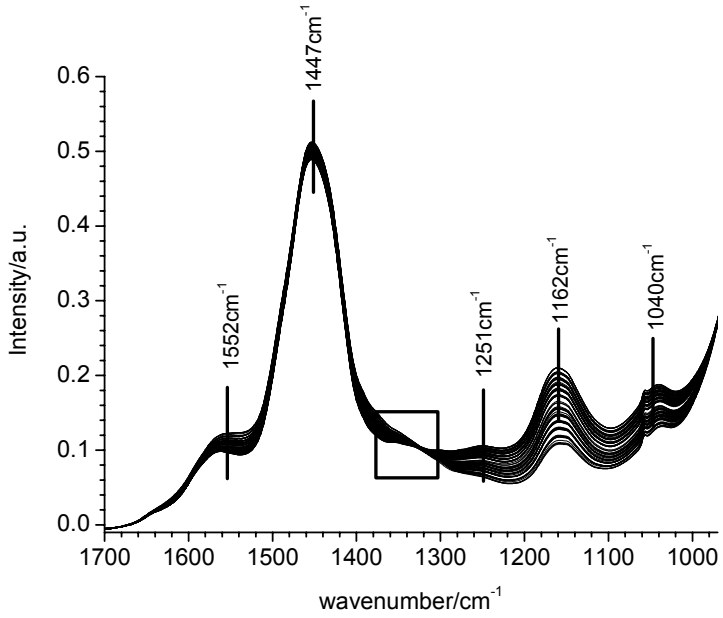

Fig. 6.16 : IR spectra obtained for the sample VTNS3 Pt recorded during lean (240s)-rich (18s) cycling at 523K at the conditions shown in Table 6.1.

To identify the spectral regions changing during the lean-rich cycling the Moving Window 2D Correlation Analysis was applied. The synchronous contour plot obtained for lean and lean-rich conditions are depicted in Fig. 6.17. Under lean conditions (see Fig. 6.17A) three well defined auto-peaks located on the diagonal at 1251cm^{-1},1162cm^{-1} and 1040cm^{-1} were found. All three auto-peaks are forming a square with cross peaks at the corresponding intersections with a positive sign. This indicates that the bands at these wavenumbers are increasing during lean operation mode. The negative peaks at the intersections of 1040cm^{-1}, 1162cm^{-1} and 1251cm^{-1} with 1447cm^{-1} indicate that the carbonate species decrease during the exposure to the lean conditions. Note that the spectral intensities attributed to carbonate species are increasing on the Pt free sample during the exposure to NO_2 containing gases in reducing conditions, possibly due to the interaction of the sample with the different NO_x-species formed. The result derived from the data-analysis of the *in situ* NO_x experiments for the sample containing Pt showed that this effect is diminished (not shown here). The positive cross-peaks at the intersections of the sulfates with the band at 1442cm^{-1} indicate that the intensity of this peak is found to be increasing during rich mode. Fig. 6.17B depicts the synchronous contour plot obtained for lean and rich conditions. It can be clearly seen that the intersections of 1162cm^{-1} and 1040cm^{-1} with the

carbonate species located at 1447cm^{-1} are centered in a negative area (gray) indicating that the intensity of the peak located at 1447cm^{-1} is decreasing also during rich operation mode, unlike at the Pt free sample (see Fig. 6.10 **:**).

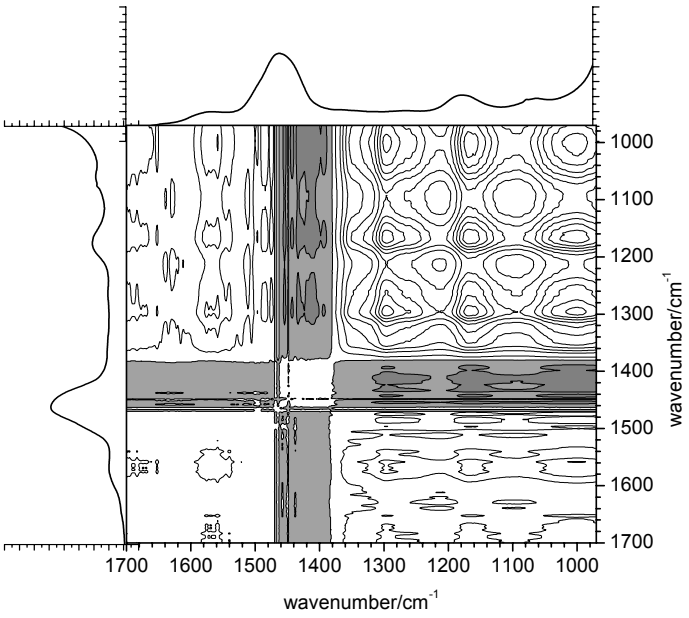

(A)

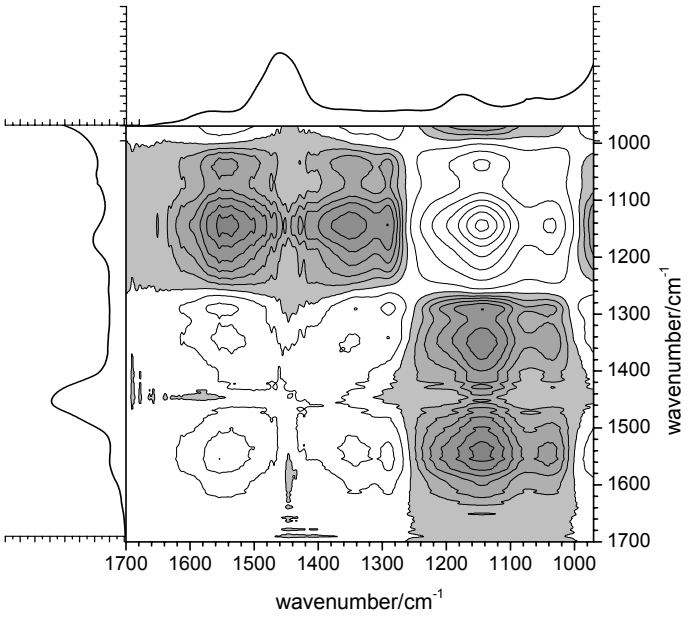

(B)

Fig. 6.17 : Synchronous plots calculated with the moving window concept: (A) is calculated from spectra entirely recorded under lean conditions, (B) depicts the effect of a reducing atmosphere (rich operation mode) on VTNS3 Pt.

After the identification of the perturbed spectral regions applying MCR-ALS to the dataset using the 2D Sample-Sample matrix as initial concentration matrix revealed similar species (bulk carbonates, bulk sulfates and surface sulfates (transient)) compared to the Pt free sample. To compare the time resolved behavior of the spectral intensities, the 2D Sample-Sample Correlation was carried out on the same spectral regions as on the Pt free sample. The results are shown in Fig. 6.18. The dashed lines represent the sample containing Pt, the solid lines picture the Pt free sample. Only the traces along the diagonal of the 2D Sample-Sample Correlation Analysis are plotted here (Note that an offset was applied to all spectral intensities to simplify the comparison).

The spectral intensities attributed to carbonate species (Fig. 6.18A, decreasing lines) and bulk sulfate species (Fig. 6.18A, increasing lines) for both materials show a similar trend with a slightly higher slope for the bulk sulfate species on the Pt containing material indicating a higher amount of sulfates present on the material. It is important to note, that the intensity of the spikes observed while switching to the rich operation mode are less pronounced for the Pt containing sample, possibly due to a faster reduction of NO_2 species to N_2 rather than to NO_x.

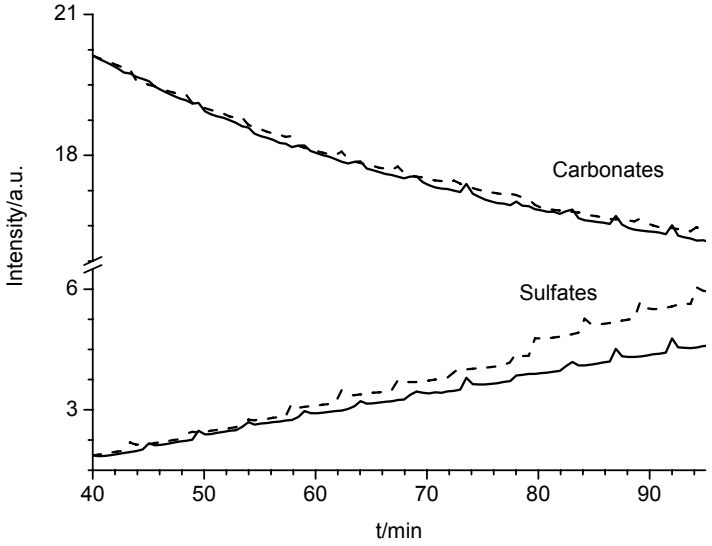

(A)

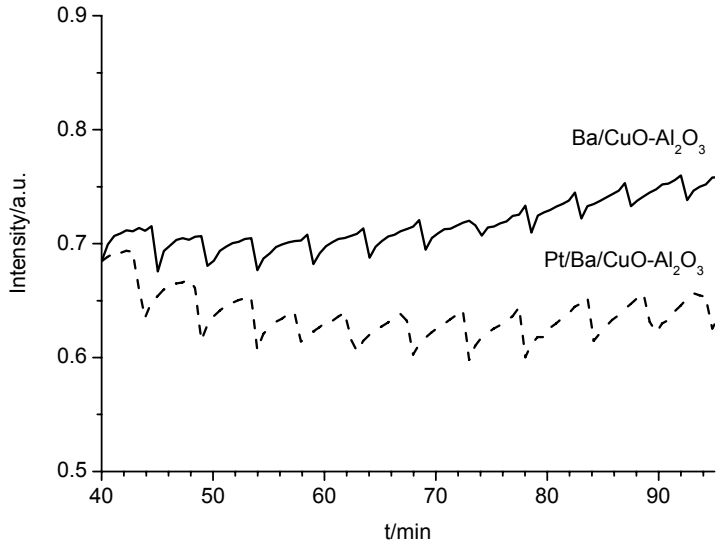

(B)

Fig. 6.18 : Diagonal traces obtained from the 2D Sample-Sample Correlation Analysis of the carbonate and sulfate species (A) and surface species (B). The Pt containing samples are marked as dotted line. Note that all graphs were forced to the same intensity at the first point.

The pattern obtained for the transient sulfate species (see Fig. 6.18B) shows that on both materials, the reduction of the surface species during the rich operation mode leads to the characteristic saw-tooth pattern. Moreover, for the Pt free sample the increasing intensity indicates that the concentration of surface sulfate species increases over time, while for the Pt containing sample the slight decrease indicates a smaller amount of surface species being present. However, the intensity of the oscillations during the lean-rich cycling shows that the amplitude of the oscillations is approximately twice as high for the Pt containing sample compared to the Pt free sample, which strongly suggests that Pt facilitates the reduction of the transient sulfate species.

6.3.3.4 SO_2 adsorption in presence of H_2O during lean-rich cycling conditions

The presence of H_2O diminishes the SO_2 release under rich conditions as shown by the plug flow experiments (see Fig. 6.4). On all samples investigated a small peak at 1641cm^{-1} and a broad peak around 3300cm^{-1} were observed (graphs not shown) which could be assigned to physisorbed water on the surface [56]. During *in situ* IR experiments carried out in the presence of 10% water similar bands for the bulk sulfate species and the carbonate species were observed. However, the

intensity of the bulk sulfate species is higher and the intensity of the carbonates is decreasing faster in presence of water compared to dry conditions (not shown here). The comparison of the concentration profiles obtained by 2D Sample-Sample Correlation over the region from 1350cm^{-1}-1290cm^{-1} for the Pt containing and Pt free material in absence and presence of water is shown in Fig. 6.19. The strong effect of water is clearly observed. The saw-tooth pattern of the transient sulfate species obtained under dry conditions was almost completely removed (see Fig. 6.19 solid and dashed line), which indicates only a small reduction of this species in presence of water on the Pt/Ba/CuO-Al_2O_3 material. However, the overall intensity of the band under lean conditions is not strongly affected by the presence of water on the Pt containing sample indicating a similar concentration of the surface species present. On the Ba/CuO-Al_2O_3 material the saw-tooth pattern completely disappeared in presence of water (dotted line) and the increasing intensity of the surface sulfate species suggests an accumulation of this species. It is important to note that under dry conditions the oscillatory behavior is approximately two times higher in the presence of Pt compared to the Pt free sample.

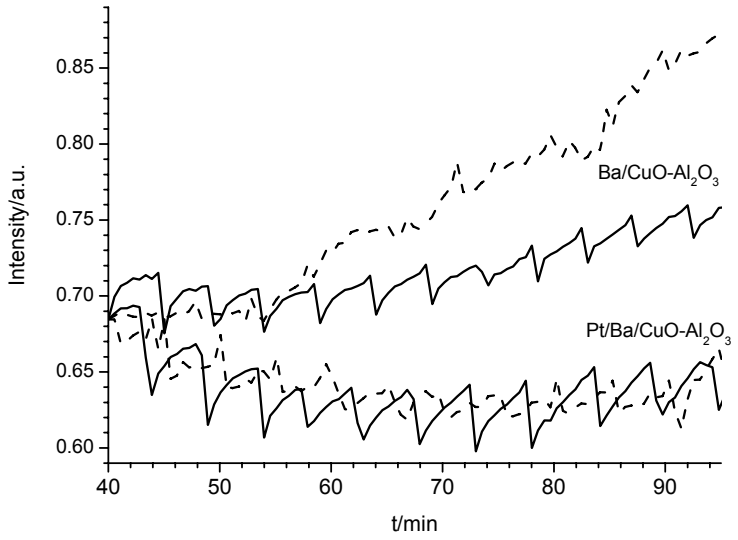

Fig. 6.19 : Diagonal trace of the 2D Sample-Sample correlation (1350cm^{-1}-1290cm^{-1}). The dashed graph represents the under wet conditions, the solid plot the same under dry conditions.

6.3.3.5 Influence of rich conditions time on the SO_2 adsorption during lean-rich cycling conditions

The influence of the time under rich conditions in absence of water was investigated to determine the increasing SO_2 release observed under plug flow conditions (see Fig. 6.2). The graphs depicted in Fig. 6.20 represent the diagonal traces from the 2D Sample-Sample Correlation Analysis performed on a dataset obtained from the Pt free sample (240s lean / 72s rich). For the carbonate species a decreasing intensity was observed overlaid by a characteristic step-like pattern during switching to rich conditions. The spike pattern observed at shorter reduction time is transformed into a step-like pattern possibly due to the prolonged exposure to a reducing atmosphere. The overall concentration of bulk sulfate species is increasing also showing sharp step-like signals during the changes in gas composition In comparison to the shorter cycling time two clearly defined and equilibrated surface concentrations were established

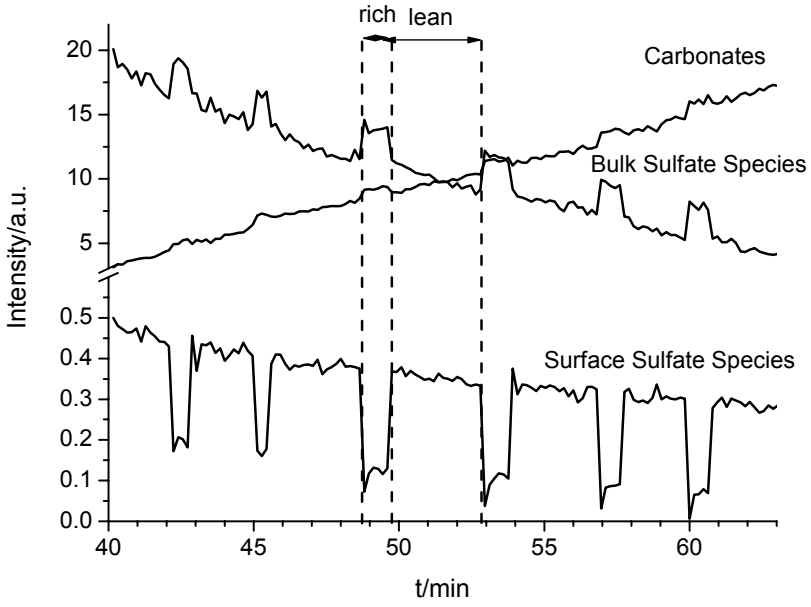

Fig. 6.20 : Diagonal lines obtained from the 2D Sample-Sample Correlation Analysis of the surface species and carbonate and sulfate species on the VTNS3 with t=240s (lean) t=72s (rich) with the conditions shown in Table 6.1 at 523K.

6.4 Discussion

The physico-chemical characterization of the sol-gel derived $CuO\text{-}Al_2O_3$ based material impregnated with Barium and Pt suggests the presence of $BaCO_3$ particles on an amorphous $CuO\text{-}Al_2O_3$ support. The SO_2 uptake experiments carried out under cycling conditions showed the release of SO_2 under rich conditions, which is far more pronounced for the Pt containing material. This strongly suggests that Pt has an accelerating effect on the reducibility of the sulfur species formed on the material.

In situ XANES experiments at the S K-edge (see Chapter 4) showed the formation of sulfite type species under reaction conditions, which were easily reduced in presence of Pt and could lead to the formation of SO_2 under rich conditions. However, the impact of various sulfate type species could not be distinguished due to the limitations of the XANES for the distinction of sulfur species of the same oxidation state. *In situ* IR spectroscopy experiments carried out under typical exhaust gas compositions at 523K showed the formation of various sulfate species present on the surface and in the bulk during the lean-rich cycling conditions.

The spike pattern observed under cycling conditions by *in situ* IR in presence of NO_2 revealed the interaction of the sample with the NO_x species. Typically under rich conditions this leads to an increase in the spectral intensity resulting in a spike pattern on the 2D Sample-Sample Correlation Analysis. This pattern masks all experiments and therefore the spike is referred to the interaction with the NO_x species.

6.4.1 Identification of the sulfur species

The Factor Analysis (FA) performed on the *in situ* IR spectra gives evidence for three spectral contributions present during lean-rich cycling conditions. The extremely short time under rich conditions allowed the collection of only one spectrum under reducing conditions, representing a snapshot of the species formed. However, applying the Generalized 2D Correlation Analysis using the Moving Window approach, individual spectral regions could be identified. The synchronous correlation plot calculated from spectra recorded under lean operation mode only shows an increase in the peaks attributed to sulfate species (positive cross-peaks), which indicates the formation of bulk as well as surface

sulfate species under oxidizing conditions. This increase was accompanied by the simultaneous decomposition of the carbonate species indicated by the negative cross peaks between carbonate and sulfate bands. In contrast the synchronous correlation plot calculated from spectra recorded under lean and rich operation mode gives clear evidence for two new features located at 1295cm^{-1} and 1350cm^{-1}, which appear in the region for surface sulfate species [12, 43].

The intensities of the carbonate species were decreasing during rich reaction conditions (negative correlation with the bulk sulfate species) which imply their removal. However, species located in the typical region for carbonates were found to increase under rich conditions, which would suggest a highly unlikely formation of carbonates under reducing conditions. Regarding the experiments carried out in absence of SO_2 as mentioned above this is caused by an interaction of the sample with the NO_x species formed under reducing conditions rather than formation of new carbonate species.

Factor Analysis and the Moving Window 2D Correlation Analysis suggest the presence of three different species or spectral regimes, while applying the 2D Sample-Sample Correlation on the spectral regimes allows the quantitative time resolved description of the species located in this region. The decreasing intensity for the carbonates suggests their decomposition, which was accompanied by an increasing overall intensity of the bulk sulfate species indicating the conversion of carbonates to sulfates. The spectral intensities located in the region of 1350cm^{-1}-1290cm^{-1} are found to follow a saw-tooth pattern suggesting a reduction of the concentration under rich operation mode and a new formation under lean conditions.

The application of the MCR-ALS technique utilizing an initial coefficient matrix obtained from the 2D Sample-Sample Correlation leads to the determination of the spectra of the pure components and the corresponding time resolved coefficient profiles. The species located in the carbonate region could be clearly identified as $BaCO_3$. The bulk sulfate species are rather assigned to Ba and Cu than on Al_2O_3. The bands in the spectra of the pure components for the transient species suggest the formation mainly on the surface of Al_2O_3 with low coverage rather than on the Ba or Cu. The saw-tooth concentration pattern under the cycling conditions suggests the partial reduction and therefore could lead to a release of SO_2 which was macroscopically observed in the plug flow SO_x uptake

experiments. However the total contribution of the reduced surface species to the SO_2 released could not be clearly determined.

6.4.2 Influence of Pt on the SO_2 storage process

After the successful determination of the concentrations of sulfate and carbonate species formed under cycling conditions, the influence of Pt was investigated. The 2D Sample-Sample-Correlation Analysis showed a higher amplitude of the changes in the surface concentration of the transient species on the Pt containing material while cycling between rich and lean reaction conditions of the surface sulfate species formed. This strongly suggests that the formation as well as the reduction of this species on the surface of the SO_x trap is mainly affected by the presence of Pt rather than by the formation of bulk species.

This result is supported by the lower intensity in the spikes observed for this material on the concentration profile of NO_x species indicating a higher reduction/oxidation behavior of Pt regarding NO/NO_2 which was already described for $DeNO_x$ catalysis [5, 57-59]. This leads to the conclusion that the presence of Pt enhances the formation of the sulfates as well as the reduction of the nitrates. The higher amount of SO_2 released under dynamic conditions therefore could result from the reduction of more surface sulfates under rich conditions. Pieplu *et al.* suggested a kinetic model for the sulfation of pure Al_2O_3 involving the formation of free Al sites during the sulfate formation [60]. The accelerating effect of Pt could lead therefore to a higher amount of free Al sites resulting in a higher formation of surface sulfate species which are reduced under rich conditions. For a complete protection and a long term durability of the NSR catalyst it seems to be sufficient to have a Pt free sample resulting in a lower SO_2 amount released under rich conditions [8, 10].

6.4.3 Influence of water on the SO_x storage

A promoting effect of H_2O on the total SO_2 storage capacity as well as a lower SO_2 release under rich conditions was observed under dynamic flow conditions. *In situ* IR spectroscopy shows that in presence of water only carbonates, bulk and surface were present. However, in presence of water, the oscillations in the concentration of surface species during periodic lean-rich cycling were found to be less pronounced for the sample containing Pt compared to absence of water. This indicates that the lower amount of SO_2 released in presence of water could result

from a lower concentration of surface sulfate species. Therefore, we propose that the surface sulfate species identified on Al_2O_3 are mainly affected by the presence of water [61]. The higher total SO_2 sorption capacity could result from the formation of sulfuric acid, where at 523K thermodynamic limitations do not exist. This could lead to a faster transport of surface sulfates into the bulk phase of the material, as already shown in Chapter 5 for a similar material. However, *in situ* XANES at the S K-edge indicated that in presence of 10% water (see Chapter 4) a reduced relative fraction of sulfites is present on both samples compared to dry conditions. This indicates that the oxidation is additionally facilitated by the presence of water. A higher rate of carbonate decomposition in presence of water is reported which could result in a higher concentration of Ba sites present able to form bulk species thus lowering the coverage of the surface due to a faster bulk transport. This is in perfect agreement with the findings of higher bulk sulfate fraction detected by IR spectroscopy [62, 63]. The interaction of surface sulfate species on Al_2O_3 in presence of water was already discussed, however the determination of the pure component spectra is to the best of our knowledge not reported [54, 60, 64].

6.4.4 Influence of the time of rich conditions

Beside the presence of water, the release of SO_2 is mainly influenced by the time period under reducing conditions. The results showed that the general trend of the concentration changes of the bulk carbonate and sulfate species is enlarged at longer cycles under reducing reaction conditions. This suggests that longer cycle times would lead to a higher NO_x conversion on the NSR catalyst. However, higher reduction times also lead to an unfavorable increase in fuel consumption diminishing the advantage of a lean burning engine. A strong influence on the surface sulfate species was detected by increasing the reduction time to 72s. The spikes observed for the spectral intensities attributed to carbonates and bulk sulfates are transformed into step shaped features due to the enlarged reduction period. Nevertheless, the general trend, i.e. the formation under reducing conditions and the removal after switching back to lean operation mode of 240s, is still observed. The results obtained for the surface species being located in the region from 1350cm^{-1}-1290cm^{-1} are also in perfect agreement with the saw-tooth pattern found for these spectral intensities. It is observed that the amount to which

the surface species are reduced is far more pronounced than for a reducing period of 18s.

Fig. 6.21 summarizes the results in a simplified reaction network. Generally, in presence of O_2 the SO_2 is oxidized to SO_3 (1) and afterwards trapped on the storage sites (2, 3), whereas the Ba sites are more stable compared to the Al sites [49, 65]. The lean-rich cycling experiments under plug flow conditions showed clearly that Cu is a sufficient oxidation component for the first step, moreover the lower reduction potential even leads to less SO_2 under rich conditions [66]. The formation of the surface sulfate species (2) as well as the bulk-like ones (3) could be shown by the results obtained from the MCR-ALS. The removal of the surface sulfate (2) was additionally proved while applying lean-rich conditions indicating a labile bonding. This reaction was accelerated in the presence of Pt [61]. The absence of the surface species leads consequently to no further bulk sulfates, therefore a complete removal (as partially obtained by longer reduction time) should be prevented.

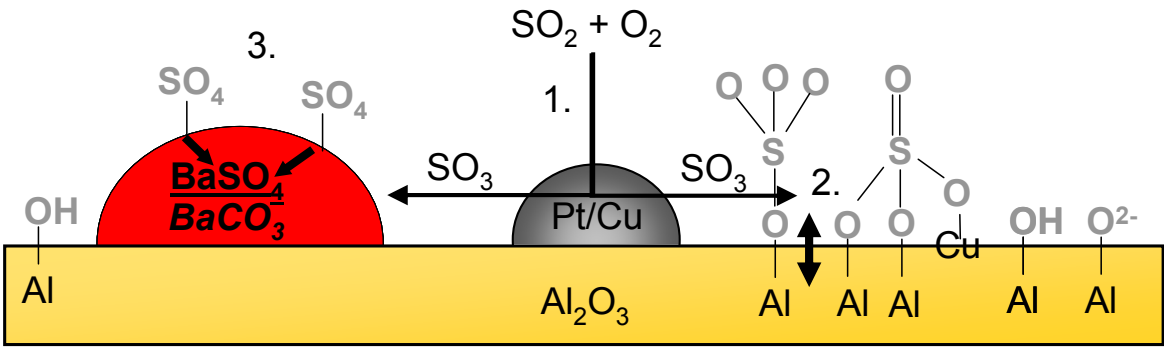

Fig. 6.21 : Simplified reaction network for the SO_x storage process.

Furthermore it should be taken into account that a low SO_2 content (10ppm) in the gas phase additionally the desorption under rich conditions is favored. The quantification of the sulfur content on a monolith coated with these materials (not shown here) clearly showed a higher sulfur contribution in the end of the monolith. Furthermore the maximum storage capacity obtained under lean conditions was not reached. This led us to assume that the surface is mainly sulfated and the species is slightly mobile, according to literature [12, 67, 68]. The continuous formation and reduction makes it possible to spill over the sorbents surface. The removal of the species consequently leads to a lower bulk sulfate formation resulting in a low utilization of the theoretical storage amount. It is speculated that this effect could contribute to the high stability of NSR catalyst at low sulfur

contents. The formation of highly stable bulk sulfate (3) in presence of water was shown by IR. Therefore water seems to be essential for a high storage capacity.

6.5 Conclusions

A transient species present under lean-rich conditions imperceptible in the conventional spectra could be identified by applying innovative and powerful chemometric techniques.

With the combination of the Generalized 2D Correlation Analysis, 2D Sample-Sample Correlation Analysis und Factor Analysis using the MCR-ALS technique the three different regimes present on the sample have been clearly identified, separated and characterized. The multiple and combined application of these techniques led to the identification of three spectral regimes showing characteristic patterns: (i) carbonates showing a decreasing, (ii) bulk sulfates are showing an general increasing (iii) surface sulfate species showing a characteristic saw-tooth pattern. A spike pattern in the concentration profiles was found to be from the reduction of NO_x species. It is proposed that the reduction of the transient surface sulfate species contributes mainly to the SO_2 release observed under dynamic flow conditions. Pt as noble metal facilitates the formation and reduction of this species leading to a higher amount of SO_2 released under rich conditions. Consequently noble metal free storage materials are preferred. The promoting effect of water concerning a diminished SO_2 release under rich operation mode could clearly be identified. In presence of water a suppression of the reduction of the surface species were observed resulting in a faster transport into the bulk phase ($BaCO_3$). Increasing the reduction time at these temperatures mainly leads to a higher amount of surface sulfates reduced, contributing to a higher SO_2 release. A direct influence on the concentration and type of the bulk type species formed could not be clearly detected. For developing effective SO_2 storage materials with a high utilization a stronger adsorption on the surface species has to be reached.

6.6 Acknowledgments

This work was supported by the European Union in the framework of project G3RD-CT2002 00793.

6.7 References

[1] P. Greening, *Topics in Catalysis,* 2001, **16**, 5.
[2] W. S. a. H. Epling, Gar B, *Journal of Catalysis,* 1999, **182**, 5.
[3] S. I. Matsumoto, *Catalysis Today,* 2004, **90**, 183.
[4] T. Kreuzer, E. S. Lox, D. Lindner and J. Leyrer, *Catalysis Today,* 1996, **29**, 17.
[5] C. Sedlmair, K. Seshan, A. Jentys and J. A. Lercher, *Journal of Catalysis,* 2003, **214**, 308.
[6] W. S. Epling, L. E. Campbell, A. Yezerets, N. W. Currier and J. E. Parks, *Catalysis Reviews-Science and Engineering,* 2004, **46**, 163.
[7] C. Sedlmair, K. Seshan, A. Jentys and J. A. Lercher, *Research on Chemical Intermediates,* 2003, **29**, 257.
[8] L. Limousy, H. Mahzoul, J. F. Brilhac, P. Gilot, F. Garin and G. Maire, *Applied Catalysis B-Environmental,* 2003, **42**, 237.
[9] O. H. Bailey, D. Dou and M. Molinier, *Society of Automotive Engineers, [Special Publication] SP,* 2000, **SP-1533**, 257.
[10] H. L. Fang, J. C. Wang, R. C. Yu, C. Z. Wan and K. Howden, *Society of Automotive Engineers, [Special Publication] SP,* 2003, **SP-1801**, 185.
[11] M. Waqif, A. M. Saad, M. Bensitel, J. Bachelier, O. Saur and J. C. Lavalley, *Journal of the Chemical Society-Faraday Transactions,* 1992, **88**, 2931.
[12] M. Waqif, O. Saur, J. C. Lavalley, S. Perathoner and G. Centi, *Journal of Physical Chemistry,* 1991, **95**, 4051.
[13] F. Rohr, S. D. Peter, E. Lox, M. Kogel, A. Sassi, L. Juste, C. Rigaudeau, G. Belot, P. Gelin and M. Primet, *Applied Catalysis B-Environmental,* 2005, **56**, 201.
[14] I. Noda, *Journal of the American Chemical Society,* 1989, **111**, 8116.
[15] I. Noda, A. E. Dowrey and C. Marcott, *Mikrochimica Acta,* 1988, **1**, 101.
[16] I. Noda, *Applied Spectroscopy,* 1993, **47**, 1329.
[17] I. Noda, A. E. Dowrey, C. Marcott, G. M. Story and Y. Ozaki, *Applied Spectroscopy,* 2000, **54**, 236A.
[18] I. Noda, *Applied Spectroscopy,* 2000, **54**, 994.
[19] M. A. Czarnecki, *Applied Spectroscopy,* 1998, **52**, 1583.
[20] S. J. Gadaleta, A. Gericke, A. L. Boskey and R. Mendelsohn, *Biospectroscopy,* 1996, **2**, 353.
[21] P. Haider, Y. Chen, S. Lim, G. L. Haller, L. Pfefferle and D. Ciuparu, *Journal of the American Chemical Society,* 2005, **127**, 1906.
[22] H. R. Keller and D. L. Massart, *Chemometrics and Intelligent Laboratory Systems,* 1992, **12**, 209.
[23] M. Thomas and H. H. Richardson, *Vibrational Spectroscopy,* 2000, **24**, 137.
[24] S. Sasic, A. Muszynski and Y. Ozaki, *Journal of Physical Chemistry A,* 2000, **104**, 6380.
[25] S. Sasic, A. Muszynski and Y. Ozaki, *Journal of Physical Chemistry A,* 2000, **104**, 6388.
[26] E. R. Malinowski, Factor Analysis in Chemistry, John Wiley & Sons Ltd., New York.
[27] J. H. Jiang and Y. Ozaki, *Applied Spectroscopy Reviews,* 2002, **37**, 321.
[28] T. H. Jiang, Y. Liang and Y. Ozaki, *Chemometrics and Intelligent Laboratory Systems,* 2004, **71**, 1.

[29] A. de Juan and R. Tauler, *Analytica Chimica Acta,* 2003, **500**, 195.
[30] P. J. Gemperline, *Journal of Chemical Information and Computer Sciences,* 1984, **24**, 206.
[31] M. Fernandez-Garcia, C. M. Alvarez and G. L. Haller, *Journal of Physical Chemistry,* 1995, **99**, 12565.
[32] C. MarquezAlvarez, I. RodriguezRamos, A. GuerreroRuiz, G. L. Haller and M. FernandezGarcia, *Journal of the American Chemical Society,* 1997, **119**, 2905.
[33] E. J. Karjalainen, *Chemometrics and Intelligent Laboratory Systems,* 1989, **7**, 31.
[34] R. Tauler and E. Casassas, *Chemometrics and Intelligent Laboratory Systems,* 1992, **14**, 305.
[35] R. d. J. Tauler, A., *roma@quimio.qui.ub.es,* 2003,
[36] V. Mazet, C. Carteret, D. Brie, J. Idier and B. Humbert, *Chemometrics and Intelligent Laboratory Systems,* 2005, **76**, 121.
[37] K. I. Hadjiivanov, *Catalysis Reviews-Science and Engineering,* 2000, **42**, 71.
[38] T. Yamaguchi, T. Jin and K. Tanabe, *Journal of Physical Chemistry,* 1986, **90**, 3148.
[39] A. W. Aylor, S. C. Larsen, J. A. Reimer and A. T. Bell, *Journal of Catalysis,* 1995, **157**, 592.
[40] K. Nakamoto, Infrared and Raman spectra of inorganic and coordination compounds, Wiley-Interscience, New York.
[41] Y. W. Chi and S. S. C. Chuang, *Journal of Catalysis,* 2000, **190**, 75.
[42] F. A. Miller and C. H. Wilkins, *Analytical Chemistry,* 1952, **24**, 1253.
[43] T. Yamaguchi, *Applied Catalysis,* 1990, **61**, 1.
[44] S. Iretskaya and M. B. Mitchell, *Journal of Physical Chemistry B,* 2003, **107**, 4955.
[45] M. A. Babaeva, A. A. Tsyganenko and V. N. Filimonov, *Kinetics and Catalysis,* 1985, **25**, 787.
[46] H. C. Yao, H. K. Stepien and H. S. Gandhi, *Journal of Catalysis,* 1981, **67**, 231.
[47] C. Sedlmair, K. Seshan, A. Jentys and J. A. Lercher, *Catalysis Today,* 2002, **75**, 413.
[48] R. A. Schoonheydt and J. H. Lunsford, *Journal of Catalysis,* 1972, **26**, 261.
[49] G. Centi, N. Passarini, S. Perathoner and A. Riva, *Industrial & Engineering Chemistry Research,* 1992, **31**, 1947.
[50] J. C. Decius, E. H. Coker and G. L. Brenna, *Spectrochimica Acta,* 1963, **19**, 1281.
[51] A. Hezel and S. D. Ross, *Spectrochimica Acta,* 1966, **22**, 1949.
[52] C. P. Hubbard, K. Otto, H. S. Gandhi and K. Y. S. Ng, *Catalysis Letters,* 1995, **30**, 41.
[53] W. S. Kijlstra, M. Biervliet, E. K. Poels and A. Bliek, *Applied Catalysis B-Environmental,* 1998, **16**, 327.
[54] O. Saur, M. Bensitel, A. B. M. Saad, J. C. Lavalley, C. P. Tripp and B. A. Morrow, *Journal of Catalysis,* 1986, **99**, 104.
[55] M. Waqif, O. Saur, J. C. Lavalley, Y. Wang and B. A. Morrow, *Applied Catalysis,* 1991, **71**, 319.
[56] H. A. Al-Hosney and V. H. Grassian, *Physical Chemistry Chemical Physics,* 2005, **7**, 1266.

[57] A. Amberntsson, E. Fridell and M. Skoglundh, *Applied Catalysis B-Environmental,* 2003, **46**, 429.
[58] E. Fridell, M. Skoglundh, B. Westerberg, S. Johansson and G. Smedler, *Journal of Catalysis,* 1999, **183**, 196.
[59] Y. Su and M. D. Amiridis, *Catalysis Today,* 2004, **96**, 31.
[60] A. Pieplu, O. Saur, J. C. Lavalley, M. Pijolat and O. Legendre, *Journal of Catalysis,* 1996, **159**, 394.
[61] J. C. Summers, *Environmental Science & Technology,* 1979, **13**, 321.
[62] B. S. Terry and G. McGurk, *Transactions Of The Institution Of Mining And Metallurgy Section C-Mineral Processing And Extractive Metallurgy,* 1994, **103**, C62.
[63] B. V. L'Vov, *Thermochimica Acta,* 1997, **303**, 161.
[64] M. Y. Smirnov, A. V. Kalinkin, A. V. Pashis, A. M. Sorokin, A. S. Noskov, V. I. Bukhtiyarov, K. C. Kharas and M. A. Rodkin, *Kinetics and Catalysis,* 2003, **44**, 575.
[65] G. Centi, N. Passarini, S. Perathoner and A. Riva, *Industrial & Engineering Chemistry Research,* 1992, **31**, 1956.
[66] S. A. Kent, J. R. Katzer and W. H. Manogue, *Industrial & Engineering Chemistry Fundamentals,* 1977, **16**, 443.
[67] K. S. Yoo, S. M. Jeong, S. D. Kim and S. B. Park, *Industrial & Engineering Chemistry Research,* 1996, **35**, 1543.
[68] K. S. Yoo, S. D. Kim and S. B. Park, *Industrial & Engineering Chemistry Research,* 1994, **33**, 1786.

Chapter 7

Summary

7.1 Summary

Vehicles equipped with exhaust gas catalysts have been commercialized for over twenty years, but the growing number of vehicles in use (over 600 million units world-wide of which about one third are in Europe) and the increasing concerns about the global environment have created a demand for lower CO_2 emissions, in addition to further reductions in CO, HC and NO_x emissions. Current three way catalysts require the engine to operate in a very narrow air/fuel (A/F) range near the stoichiometric value (A/F = 14.7), because only at that A/F ratio simultaneous removal of CO, HC and NO_x is possible. However, at A/F = 14.7 the engine is not operating at the economical optimum with regard to the fuel consumption. Significant fuel economy can be obtained when the engine operates under lean conditions (A/F about 20-25), especially when diesel engines are used.

However, due to the large excess of O_2 in the exhaust gas stream the addition of a reducing agent is necessary for effective NO_x reduction, which requires the development of new approaches for the removal of pollutants. A promising approach for the reduction of NO_x is the NO_x-Storage/Reduction (NSR) concept, which has already demonstrated a high potential to meet the EURO IV requirements for emissions from diesel and lean-burn gasoline engines. The NSR process utilizes a periodic change in the exhaust gas composition between lean and fuel rich conditions. During the lean operation conditions NO_x is stored as nitrate on the NSR catalyst. After the NO_x storage capacity of the NSR catalyst is close to be exceeded the nitrates are removed by switching to fuel rich atmosphere for a short period of time. Under these reaction conditions the nitrates are decomposed to N_2 + CO_2 + H_2O.

The major drawback for a successful industrial application is the deactivation of the catalyst by sulfur present in the fuel. As the NO_x storage components are typically based on Ba, sulfates are formed in presence of SO_x that are thermodynamically more stable then nitrates and ,therefore, the NSR catalysts looses its storage capacity for NO_x during a few cycles. The decreasing levels of sulfur tolerated in diesel and petrol (10ppm or less) allows to use disposable or ex-situ regenerable sulfur traps for on-site removal of sulfur from emissions prior to contact with NSR catalyst to avoid the irreversible deactivation of the systems.

The main goal of the thesis was to develop an understanding of the key parameters of the SO_x storage process, which should lead to the development of new and innovative nanostructured materials to realize disposable or ex-situ regenerable sulfur traps to protect NSR catalysts. The SO_x storage process was studied for various gas compositions mixtures and the presence of noble metals, as well as the influence of the process conditions was investigated.

In Chapter 2 metal organic framework materials were evaluated as host materials for depositing a second SO_x storage component for novel high capacity SO_x traps. Metal organic framework materials with Cu^{2+} as central cation and benzene-1,3,5-tricarboxylate (BTC) as linker were prepared via hydrothermal synthesis. Barium, used as secondary storage component, was impregnated in various forms (chloride, nitrate, acetate) to explore the role of the Ba^{2+} counter ion on the total SO_2 uptake capacity. The physicochemical characterization showed that the impregnation of the metal organic framework materials with barium salts led to a decrease of pore volume through the (intra pore) formation of small Ba – salt crystals. The sample impregnated with $BaCl_2$ exhibited a higher fraction of Cu^{2+} species, as indicated by Cu K-edge XANES, compared to the other Ba/Cu-BTC samples.

The SO_2 uptake capacity of the $BaCl_2$ impregnated Cu-BTC sample was the highest at temperatures below 673K among all materials prepared and exceeded that of a commercial $BaCO_3/Al_2O_3$/Pt based material. The partial destruction of the BTC structure, observed at temperatures above 573K, led to the presence of highly dispersed CuO species. EXAFS analysis on the Cu K-edge in Ba/Cu-BTC, described in Chapter 3, indicates the opening of the majority of the Cu-Cu pairs present in the parent Cu-BTC. Compared to Cu-BTC, the $BaCl_2$ loaded material had a lower micropore volume and were disordered, but the better accessibility of the Cu^{2+} cations led to the formation of additional active centers for SO_2 oxidation and SO_x storage. The comparison of the theoretical uptake (based on the stoichiometric formation of $BaSO_4$) with the maximum SO_x uptake achieved on the Ba/Cu-BTC samples clearly points out that a fraction of the SO_x is stored on the Cu species being part of the metal organic framework structure. On all samples investigated, decomposition of the framework was observed with increasing temperature, leading to the formation of additional highly dispersed Cu species,

which could act as additional not additional again SO_x storage sites in the high temperature region.

After the successful preparation of the MOF materials, the elementary reaction steps during the oxidative chemisorption of SO_2 on the $BaCl_2$ impregnated Cu-BTC were investigated in Chapter 3. As shown in Chapter 2, the SO_2 uptake in oxidative atmosphere was higher for the Ba/Cu-BTC samples compared to the $BaCO_3/Al_2O_3$/Pt based material. XRD showed that on Ba/Cu-BTC the formation of $BaSO_4$ and $CuSO_4$ occurs in parallel to the destruction of the crystalline structure. On $BaCO_3/Al_2O_3$/Pt, the disappearance of carbonates was accompanied by formation of Ba- and Al-sulfates. XANES at the S K-edge was successfully applied to determine the oxidation states of sulfur and to (quantitatively) differentiate between the various sulfate species formed. It was clearly shown that at low temperatures (473K) $BaSO_4$ was preferentially formed, while at higher temperatures (and higher sulfate loading) $CuSO_4$ was the most abundant species. In contrast, on the $BaCO_3/Al_2O_3$/Pt based material the relative concentration of the sulfate species (i.e., $BaSO_4$ and $Al_2(SO_4)_3$) as a function of temperature remained constant.

To gain a deeper insight in the sulfur present under reaction conditions in the SO_x storage process, an *in situ* S K-edge XANES method was developed and described in Chapter 4. The experiments were carried out on second generation SO_x trapping materials containing Ba on a $CuO\text{-}Al_2O_3$ support under oxidizing and reducing conditions.

Plug flow experiments performed on the materials showed the release of SO_2 under rich (reducing) conditions. The *in situ* S K-edge XANES experiments clearly indicated that a contribution to the strong release of SO_2 under rich conditions was caused by the facilitated reduction of sulfite species on Pt. In the absence of Pt the sulfite species were stable under reducing conditions, while maintaining a similar total SO_2 uptake capacity. Therefore, it is concluded that noble metal-free SO_x trapping materials are clearly a better option. The presence of water leads to an enhanced formation of sulfate species on the samples. The results obtained in Chapter 4 clearly indicate that the application of the *in situ* S K-edge XANES technique revealed new information and insights on the behavior of sulfur in the trapping process compared to the ex situ measurements.

A third class of materials containing Na and Mn on a mesoporous CaO-Al_2O_3 support were evaluated in Chapter 5. All materials showed far higher total SO_x storage capacity compared to the second generation material investigated in Chapter 4 at 523K. Therefore, the prepared Na/Mn/CaO-Al_2O_3 mesoporous material seems to be an excellent SO_x trapping material, which can be applied in diesel exhaust gas streams at low temperatures. With the combination of various experimental *in situ* techniques (S K-edge XANES and IR) and the application of 2D Correlation Analysis the key parameters in the storage process were identified in relation to the chemical composition.

Ca proved to be a sufficient storage component, exhibiting a high weight advantage compared to the conventional Ba-based material, which is important for a potential application in the automotive sector. Mn was identified as a suitable oxidation component, even at low SO_2 concentrations. The enhanced SO_x uptake capacity after an additional impregnation with Na allows to upgrade potential sorbents for low temperature SO_2 storage.

In situ IR experiments indicated that Mn acts rather as an oxidation component than as a SO_x storage site in the absence and presence of water. The combination of *in situ* IR and the 2D Correlation Analysis clearly revealed the presence of the same surface sulfate species on the Na containing sample as on the Mn/CaO-Al_2O_3 material, which was strongly covered by the carbonate bands. The positive influence of water on the total SO_x sorption capacity of the materials was investigated by *in situ* S K-edge XANES. A transport limitation of SO_2 to the sorption centers was identified as rate limiting step.

Chapter 6 deals with the identification of the influence of Pt, water and the rich time on lean-rich cycling experiments on the second generation SO_x trapping material. The combination of the Generalized 2D Correlation Analysis, 2D Sample-Sample Correlation Analysis and Factor Analysis using the MCR-ALS technique was applied on time resolved *in situ* IR spectra. Three different species present on the sample were identified: carbonates, bulk sulfates and transient surface sulfate species connected to the Al sites. The surface species were reduced in rich operation mode and were formed under lean conditions, represented by a characteristic saw-tooth pattern. The reduction of these species is proposed to be a second contribution to the SO_2 release observed under dynamic flow conditions, whereas the first one was already described in Chapter 4. It was found that Pt as

noble metal facilitates the formation and reduction of this species, leading to a higher amount of SO_2 released under rich conditions.

The diminished SO_2 release under rich operation mode in presence of water was found to be mainly a result of the suppressed formation of surface species. This indicates a faster transport of SO_x into the bulk phase, replacing $BaCO_3$. This is in good agreement with the findings on the CaO-Al_2O_3 based material, as shown in Chapter 5. It was clearly shown that the increase of the reduction time at these temperatures leads mainly to a higher amount of surface sulfates reduced under rich conditions. No influence in the bulk type species was detected.

In general, the key steps in the SO_x storage process on metal oxide based materials could be identified by the combination of various *in situ* methods (S K-edge XANES, IR) with advanced chemometric techniques. It was found that the presence of a noble metal on the trap is not necessary and even detrimental for the complete protection of the NO_x storage catalyst. The presence of water proved to be essential for a high SO_x storage capacity, accompanied with a diminished SO_2 release under lean-rich conditions. This promoting effect results probably from the formation of sulfuric acid leading to an enhanced bulk transport. Additionally, the presence of water accelerates the decomposition of carbonates, leading to additional sorption sites.

7.2 Zusammenfassung

Kraftfahrzeuge werden seit 20 Jahren serienmäßig mit Abgaskatalysatoren ausgestattet. Die stetig ansteigende Menge an Fahrzeugen (über 600 Mill. weltweit) und das gesteigerte Bewusstsein für die Umwelt und das globale Klima führte zu immer strikteren Emissionsgrenzwerten bezüglich CO, HC and NO_x. Derzeitige 3-Wege-Katalysatoren benötigen für einen optimalen Betrieb ein nahezu stöchimetrisches Luft / Kraftstoff-Verhältnis. Jedoch arbeitet bei diesem Luft / Kraftstoff-Verhältnis der Motor nicht mit optimalem Wirkungsgrad. Eine deutlich höhere Energieeffizienz kann erreicht werden, wenn der Motor mit Luftüberschuss betrieben wird, wie dies etwa bei Dieselfahrzeugen der Fall ist.

Die dadurch fehlenden Reduktionskomponenten im Abgas ermöglichen keinen Einsatz von 3-Wege-Katalysatoren und machen neue Ansätze notwendig. Ein viel versprechender Ansatz zur Reduzierung von NO_x ist der NO_x-Speicher-Reduktionskatalysator (NSR) um die strikten Emissionsgrenzwerte einhalten zu können. Am Speicherkatalysator wird während einer langen Periode unter mageren Bedingungen NO_x als Nitrate gespeichert. Diese werden anschließend in einer sehr kurzen fetten Periode in Verbindung mit den jetzt vorhandenen Kohlenwasserstoffen zu N_2, CO_2 und H_2O zersetzt. Mit dieser Technik wird eine fast vollständige Reinigung des Abgases erreicht. Ein großes Problem für die erfolgreiche industrielle Anwendung ist die Deaktivierung des Katalysators durch den im Kraftstoff vorhandenen Schwefel.

Die immer geringeren Schwefelgehalte (< 10ppm) im Kraftstoff, ermöglichen jedoch eine alternative Strategie. Eine möglichst regenerierbare Schwefelfalle zur Entfernung der Schwefelverbindungen vor dem NSR Katalysator.

Das Hauptziel dieser Arbeit war die Identifikation der Schlüsselparameter/-prozesse während des SO_x-Speicherprozesses. Aufbauend darauf sollten neue innovative nanostrukturierte Materialien als potentielle Schwefelfallen entwickelt werden. Das detaillierte Verständnis des Speicherprozesses bezüglich verschiedener Gaszusammensetzungen, der Anwesenheit von Edelmetallen auf den Materialien und des Einflusses der Zeit unter fetten Bedingungen bei der zyklischen Betriebsweise sind daher essentiell.

In Kapitel 2 wurden Metallorganische Netzwerkverbindungen (MOF) als Trägermaterialien als potentielle Schwefelfallen getestet, in welche zusätzliche Speicherkomponenten integriert wurden. Dafür wurden MOF Materialien mit Kupfer als Zentralatom und Benzoe-1,3,5-tricarboxylat (BTC) als „Linker“ mittels hydrothermaler Synthese präpariert. Barium als zweite Speicherkomponente wurde mittels Imprägnierung eingebracht und der Einfluss der Bariumquelle (Chlorid, Nitrat, Acetat) auf die SO_x-Aufnahmekapazität evaluiert. Die Charakterisierung mittels verschiedener physikochemischer Methoden zeigte, dass sich durch die Imprägnierung das Porenvolumen verringert, verursacht durch die Bildung von Bariumkristallen. Cu-Röntgenabsorptionsspektroskopie zeigte eine erhöhte Fraktion an Cu^{2+}-Ionen im Material nach der Imprägnierung mit $BaCl_2$. Die Imprägnierung mit Nitrat/Acetat zeigte keinen signifikanten Einfluss auf die MOF Struktur, so das eine teilweise Zerstörung durch die Imprägnierung im Beisein von Chlorid wahrscheinlich ist.

Die komplette Aufnahmekapazität des mit $BaCl_2$ imprägnierten Materials war die höchste unter 673K, sogar höher als eine zum Vergleich untersuchte kommerzielle Schwefelfalle. Dies lässt vermuten, dass die teilweise Zerstörung der MOF-Struktur einen positiven Einfluss hat, ausgelöst durch die daraus resultierende hoch disperse CuO Spezies. Dies zeigte auch die Analyse mittels Röntgenabsorptionsspektroskopie, wie in Kapitel 3 dargestellt, welche eine Öffnung der Cu-Cu Bindungspaare in der Ausgangsstruktur aufzeigte. Im Vergleich zum Ausgangsmaterial zeigte die imprägnierte Probe nur wenige Mikroporen und eine hohe strukturelle Unordnung aber auch dadurch besser zugängliche Cu^{2+}-Zentren. Der Vergleich der theoretischen Aufnahmekapazität (basierend auf der stöchiometrischen Bildung von $BaSO_4$) mit der für die Ba/Cu-BTC(Cl^-) maximal erreichten zeigt deutlich, dass die Kupferspezies als Teil der Netzwerkstruktur ebenfalls SO_x speichert. Bei allen untersuchten Proben zeigte sich mit ansteigender Temperatur eine Zersetzung des organischen Netzwerkes, welches zur Bildung von hoch dispersen Cu-Spezies führt. Diese können anschließend als zusätzliche SO_x-Speicherzentren agieren.

Nach der erfolgreichen Präparation der Netzwerkverbindungen wurden die Reaktionen während des Speicherprozess in Kapitel 3 näher untersucht. Wie in Kapitel 2 gezeigt, wies die mit $BaCl_2$ imprägnierte Probe eine höhere Speicherkapazität im Vergleich zur industriellen $BaCO_3/Al_2O_3$/Pt Probe auf. Mittels

XRD konnte auf den metallorganischen Materialien die Bildung von $CuSO_4$ und $BaSO_4$ parallel zur Zerstörung des organischen Gitters beobachtet werden. Eine Quantifizierung war jedoch nicht möglich. Auf dem industriellen Material konnte die Bildung von $BaSO_4$ und $Al_2(SO_4)_3$ zeitgleich mit einer Abnahme an $BaCO_3$ beobachtet werden.

Um den Oxidationszustand des Schwefels zu bestimmen wurden Röntgenabsorptionsspektroskopiemessungen an der Schwefel K-Kante durchgeführt. Dies ermöglichte eine quantitative Bestimmung der verschiedenen Sulfatspezies auf dem metallorganischen Netzwerkmaterial. Die bevorzugte Bildung von $BaSO_4$ bei niedrigen Temperaturen auf diesen Materialien konnte eindeutig gezeigt werden. Mit höheren Temperaturen, und damit höheren Schwefelbeladungen wurde $CuSO_4$ als hauptsächliche Spezies identifiziert. Im Vergleich dazu wurde auf dem $BaCO_3/Al_2O_3$/Pt basierenden Material keine signifikante Änderung der Sulfatspezies in Abhängigkeit von der Temperatur festgestellt.

Der Oxidationszustand des Schwefels im SO_x-Speicherprozess unter Reaktionsbedingungen wurde mittels Röntgenabsorptionsspektroskopie an der Schwefel K-Kante untersucht (Kapitel 4). Eine apparative Methode wurde dabei erfolgreich an einem SO_x Speichermaterial der zweiten Generation unter oxidierenden und reduzierenden Bedingungen angewendet.

Untersuchungen im Durchflussreaktor zeigten die Bildung von SO_2 unter fetten (reduzierenden) Bedingungen. Die Röntgenabsorptionsspektroskopieuntersuchungen unter Reaktionsbedingungen an der Schwefel K-Kante zeigten deutlich, dass ein Teil des beobachteten SO_2 unter reduzierenden Bedingungen durch einen Zersetzung einer Sulfitspezies verursacht wird. Die relative Konzentration dieser Spezies ist in Anwesenheit von Pt unter oxidativen Bedingungen geringer als ohne Pt. Weiterhin wird die Sulfitspezies in Abwesenheit von Pt unter reduktiven Bedingungen kaum beeinflusst. Deshalb scheint eine Pt freie Schwefelfalle die klar bessere Option zu sein. Der unter Durchflussbedingungen als positiven Effekt identifizierte Einfluss von Wasser auf die SO_2-Speicherkapazität wurde mittels Röntgenabsorptionsspektroskopie unter Reaktionsbedingungen an der Schwefel K-Kante einer höheren Bildung von Sulfaten zugeschrieben. Begründet wird dies durch die deutlich geringere Konzentration an sulfitischen Spezies im Vergleich zu

trockenen Bedingungen. Die im Kapitel 4 beschriebenen Resultate zeigten deutlich die Vorteile der Anwendung der Röntgenabsorptionspektroskopie an der Schwefel Kante unter Reaktionsbedingungen. Die neuen Informationen bezüglich des SO_x-Speicherprozesses im Vergleich zu Proben welche nicht unter Reaktionsbedingungen gemessen wurden führen dabei zu einem besseren Verständnis.

In Kapitel 5 wurden Sorbentien mit Na und Mn geträgert auf mesoporösen $CaO\text{-}Al_2O_3$ - eine dritte Klasse an Materialien evaluiert. All diese zeigten eine deutlich höhere SO_x-Speicherkapazität bei 523K im Vergleich zu der industriellen Schwefelfalle der zweiten Generation (siehe Kapitel 4). Dies zeigt, dass diese Materialien exzellente Optionen für Niedrigtemperatur SO_x-Sorbentien in Dieselabgasen sind. Mit der Kombination aus verschiedenen *in situ* Techniken (Röntgenabsorptionsspektroskopie und IR) und der Anwendung von 2D Korrelations Analyse konnten die Schlüsselparameter der Materialien im Bezug auf den Speicherprozess identifiziert werden.

Calcium, als gute Speicherkomponente zeigt hierbei durch sein geringeres molares Gewicht im Vergleich zu Barium besondere Gewichtsvorteile, was entscheidend für eine erfolgreiche Anwendung im Automobilbau ist. Mn wurde als gute Oxidationskomponente identifiziert, sowohl bei niedrigen SO_2-Konzentrationen als auch in An- bzw. Abwesenheit von Wasser. Der positive Effekt der zusätzlichen Imprägnierung mittels Natrium macht dieses sehr interessant für eine zusätzliche Verbesserung vorhandener Schwefelfallen.
In situ IR Experimente zeigten, dass Mn vorrangig als Oxidations- und nicht als Speicherkomponente agiert. Mittels 2D Korrelations-Analyse der *in situ* IR-Messungen konnte hierbei an der $Na/Mn/CaO\text{-}Al_2O_3$ Probe die gleiche Oberflächenspezies wie an $Mn/CaO\text{-}Al_2O_3$ nachgewiesen werden. Dies war mit Standardmethoden nicht möglich. Der positive Effekt des Wassers auf die Speicherkapazität der Materialien wurde mittels *in situ* Röntgenabsorptionsspektroskopie an der Schwefel K-Kante untersucht. Diese zeigten, dass eine Transportlimitierung zu den Speicherplätzen und nicht eine Limitierung der Oxidationskapazität in Anwesenheit von Mn vorliegt.

In Kapitel 6 wird der Einfluss von Pt, Wasser und Reduzierzeit unter zyklischen Operationsbedingungen an Materialien der zweiten Generation diskutiert. Die Kombination aus der allgemeinen 2D KorrelationsAnalyse, 2D

Sample-Sample KorrelationsAnalyse und Hauptkomponentenanalyse (MCR-ALS) wurde hierbei erfolgreich auf *in situ* IR-Messungen angewendet. Die Resultate zeigten dabei deutlich das Vorhandensein von drei unterschiedlichen spektralen Regimes welche drei Spezies auf der Probe repräsentieren. Basierend auf den Resultaten konnten in Kombination mit den chemometrischen Methoden eindeutig diese Spezies identifiziert werden. Hierbei konnte die gleichzeitige Zersetzung von Carbonaten mit der Bildung von Sulfaten im Volumen gezeigt werden. Zusätzlich konnte eine kurzlebige Oberflächensulfatspezies gebunden an die Aluminium-Zentren zweifelsfrei identifiziert werden. Es zeigte sich, dass diese unter oxidativen Bedingungen an der Oberfläche gebildet wird. Unter reduzierenden Bedingungen jedoch zersetzt sie sich sehr leicht.

Dieser Konzentrationsverlauf, durch Standardanalysemethoden nicht nachweisbar, zeigte dabei ein typisches Sägezahnmuster. Die Zersetzung dieser Spezies wurde daraufhin eindeutig als weiterer Beitrag zur Bildung von SO_2 unter reduzierenden Bedingungen identifiziert (siehe Kapitel 4). Es konnte gezeigt werden, dass Pt sowohl die Bildung als auch die Zersetzung der Oberflächenspezies begünstigt, welches zu einer höheren SO_2-Bildung unter reduktiven Bedingungen führt.

Der positive Einfluss des Wassers auf die verminderte SO_2-Bildung unter zyklischen Operationsbedingungen wurde hauptsächlich auf eine geringere Konzentration an Oberflächenspezies zurückgeführt. Dies könnte aus einem schnelleren Transport in das Volumen resultieren, wo $BaCO_3$ durch $BaSO_4$ ersetzt wird. Die Ergebnisse aus Kapitel 4 unterstützen diese Resultate.

Eine Erhöhung der fetten Operationszeit unter zyklischen Bedingungen, welche zu einer erhöhten SO_2-Bildung führt, konnte der erhöhten Reduktion der Oberflächenspezies zugeordnet werden. Die Sulfate im Volumen wurden dadurch nicht beeinflusst.

Im Allgemeinen lässt sich zusammenfassen, dass die Schlüsselschritte des SO_x-Speicherprozesses für die Metalloxid-basierenden Materialien mit der Kombination aus *in situ* spektroskopischen Methoden (Schwefel K-Kanten Röntgenabsorptionsspektroskopie, IR) und fortgeschrittenen chemometrischen Methoden identifiziert wurden.

Es wurde gezeigt, dass die Anwesenheit von Edelmetallen auf die Sorbentien nicht notwendig sondern sogar nachteilig für einen kompletten Schutz

des NSR Katalysators ist. Die Anwesenheit von Wasser zeigte deutlich positive Effekte bezüglich der Gesamtspeicherkapazität, als auch der geringeren SO_2-Bildung unter zyklischen Bedingungen. Dieser Effekt wurde hauptsächlich auf die Bildung von Schwefelsäure zurückgeführt welches in einem schnelleren Transport ins Volumen resultiert. Zusätzlich wird die Zersetzung von Carbonaten beschleunigt, was neue Zentren zur Schwefelspeicherung bereitstellt.

Curriculum vitae

Hendrik Dathe was born on April 12, 1978 in Leipzig, Germany (former GDR). After graduating from high school in 1996 and civil service he started hi study in chemistry at the University Leipzig, Germany. He worked on his diploma thesis, entitled "*Mechanistic Investigation on SCR - DeNOx with propane*" at the Institute for Technical Chemistry at the University Leipzig under supervision of Prof. H. Papp. In April 2002 he received his master degree (Diplom-Chemiker).

After graduation he started to work as a PhD student in the group of Prof. J.A. Lercher at the Technical University of Munich., Germany and started a research on sulfur traps for the protection of high performance NOx storage/reduction catalysts in low emission engine applications in 2002. The results are described in this thesis.

Wissenschaftliche Präsentationen

2005

08/05 Europäische Katalysekonferenz, Sofia, “2D IR correlation spectroscopy and in situ XANES at the Sulfur K – edge – to identify the key parameter in sulfate formation on SO_x trapping materials”, H. Dathe, A. Jentys, J.A. Lercher, Vortrag

08/05 Europäische Zeolithkonferenz, Prag, “Adsorption of SO_2 on Ba impregnated metal organic framework material”, H. Dathe, A. Jentys, J.A. Lercher, Vortrag

06/05 Internationale Konferenz für Umweltkatalyse, Heidelberg, “Sulfate formation on advanced SO_x trap materials based on metal organic framework materials”, H. Dathe, A. Jentys, J.A. Lercher, Poster

05/05 Treffen der nordamerikanischen Katalysevereinigung, Philadelphia, “New approaches to identify the key parameter in sulfate formation on SO_x trapping materials”, H. Dathe, A. Jentys, J.A. Lercher, Poster

03/05 Deutsche Zeolithtagung, Giessen, “Sulfur K – edge and correlation spectroscopy - tools for new insights in sulfate formation on various SO_x trapping materials”, H. Dathe, A. Jentys, J.A. Lercher, Vortrag

03/05 Deutsche Katalysetagung, Weimar, “Combined sulfur K – edge and 2 - D IR spectroscopy as tool for new insights in sulfate formation on SO_x trapping materials”, H. Dathe, A. Jentys, J.A. Lercher, Poster

2004

04/04 Internationale Zeolithkonferenz, Kapstadt, “Adsorption of SO_2 on different metal impregnated zeolites”, H. Dathe, C. Sedlmair, A. Jentys, J.A. Lercher, Poster

03/04 Deutsche Zeolithtagung, Dresden, “New material for the adsorption of SO_2 in oxygen rich atmosphere”, H. Dathe, E. Peringer, A. Jentys, J.A. Lercher, Vortrag

03/04 Deutsche Katalysetagung, Weimar “Formation of Sulfate Species on Metal Oxide Based SO_x Trap Materials”, H. Dathe, A. Jentys, J.A. Lercher, Poster

2003

08/03 Europäische Katalysekonferenz, Innsbruck, “Adsorption of SO_2 on different metal impregnated zeolites”, H. Dathe, C. Sedlmair, A. Jentys, J.A. Lercher, Poster

03/03 Deutsche Katalysetagung, Weimar, “Elementary Steps of NO_x adsorption and surface reaction on a commercial storage-reduction catalysts”, H. Dathe, A. Jentys, C. Sedlmair, J.A. Lercher, Poster

03/03 Deutsche Zeolithtagung, Kaiserslautern, “Adsorption of SO_2 on different metal impregnated zeolites”, H. Dathe, A. Jentys, J.A. Lercher, Poster

Wissenschaftliche Publikationen

H. Dathe, C. Sedlmair, A., J.A. Lercher, *Studies in Surface Science and Catalysis*, „Adsorption of SO_2 on different metal impregnated zeolites“,154, **2004,** 3003-3009

H. Dathe, E. Peringer, V. Roberts, A. Jentys, J.A. Lercher, *Comptes Rendue Chime,* „Metal organic frameworks based on Cu^{2+} and benzene-1,3,5-tricarboxylate as host for SO_2 trapping agents “, 8, **2005,** 753-763**.**

H. Dathe, A. Jentys, J.A. Lercher, *Physical Chemist Chemistry Physics*, “Sulfate formation on SO_x trapping materials studied by Cu and S K edge XAFS”, 7, **2005**,1283-1292.

H. Dathe, A. Jentys, J.A. Lercher, *Studies in Surface Science and Catalysis*, “Adsorption of SO_2 on Ba impregnated metal organic framework materials”, **2005**, akzeptiert

H. Dathe, A. Jentys, J.A. Lercher, *Journal of Physical Chemistry B*, ‘In situ S K-edge X-ray absorption spectroscopy for understanding and developing SO_x storage catalysts’, **2005**, akzeptiert

H. Dathe, P. Haider, A. Jentys, J.A. Lercher, R. Fricke, E. Schreier ‘On the trapping of SO_x on Ca-Al based novel high capacity sorbents’, **2005**, eingereicht

H. Dathe, P. Haider, A. Jentys, J.A. Lercher, ‘Identification of transient sulfur species with IR spectroscopy under lean-rich cycling conditions on potential SO_x storage materials’, **2005**, in Bearbeitung